THE ELECTROCHEMISTRY OF SURFACTANTS ON GOLD SINGLE-CRYSTALS AND OF PLATINUM-GOLD NANORODS

By

JOHN FENNELL

A thesis submitted to

The University of Birmingham

for the degree of

DOCTOR OF PHILOSOPHY

School of Chemistry

College of Engineering and

Physical Sciences

The University of Birmingham

September 2012

ABSTRACT

The electrochemistry of the cationic surfactants CTAF, CTAC, CTAB and BDAC on Au (100) and Au (111) was investigated using cyclic voltammetry, differential capacitance, and chronocoulometry. These techniques showed that the aggregation of CTAF, CTAC and CTAB is driven by the adsorption or co-adsorption of their halide counter-ions on the Au-substrate. The benzyl group of BDAC strongly interacted with the gold surface and did not desorb, even at the negative potential limit.

A series of Pt-coated gold nanorod (Au NR) electrocatalysts were prepared. STEM images showed that Pt nanodots grew epitaxially on the Au NR surface. A CO blocking technique was used in order to coat Pt in a more controlled, uniform manner. The nanorods were characterised using UV-visible spectroscopy and, after being immobilised onto a supported glassy carbon electrode, with cyclic voltammetry. The CO blocking technique was crucial in enhancing CO electrooxidation and oxygen reduction reaction activity of the nanorods, not only because of the higher coverage of Pt nanodots but also because of their electrocatalytically more active nature.

To my wonderful family

ACKNOWLEDGEMENTS

First and foremost my supervisor Sarah Horswell for the tireless support, the belief in me and the amazing help, which I cannot be grateful enough.for

Stuart Arkless, Steve Williams, Steve West and Cheryl Powell for the generous technical support

Ziyou Li and group for helpful suggestions, and in particular Donsheng He for STEM images

The financial support from the School of Chemistry, University of Birmingham, and the EPSRC (DTA Award Reference EP/P504678/1)

Birmingham Science City:Innovative Uses for Advanced Materials in the Modern World (West Midlands Centre for Advanced Materials Project 2), Advantage West Midlands (AWM) and the European Regional Development Fund (ERDF) for the use of the UV-visible spectrometer.

Andy Logsdail, Dave Lewis, Melanie Britton and Roy Johnson for useful ideas

Andrea Mulas and other JHRT group members for excellent help with the surfactant synthesis and purification

The ELCAT network for providing opportunities for learning more about electrocatalysis, and especially for memorable discussions

My group, especially Goy for the invaluable tips, and Anicitus for beginning my enthusiasm for gold nanorods

My family for their great support and care throughout; a particular mention to my grandmother Babushka and my aunt Lina

My parents without whom none of this would have been possible

Donya for giving me pride in everything

Contents

1. Introduction

1.1 Preface

Gold nanorods (AuNRs) have been the subject of much research in the past. Au NRs have longitudinal plasmon excitation, meaning they have a wide variety of uses, for example as contrasting agents in medical imaging,[1] drug delivery[2] and photothermal destruction of cancer cells and pathogenic bacteria.[3 4]

The cationic surfactant cetyltrimethylammonium bromide (CTAB) is used to synthesise Au NRs. However, the yield of Au NRs produced and their aspect ratio are not consistent when only CTAB is used. $AgNO_3$ is often added during synthesis to improve monodispersity.[5] (see section 1.8.4) Another way that is more beneficial in the long term, to improve monodispersity of Au NRs is to obtain a better idea of the role of CTAB in Au NR synthesis. This is the first objective of this work: to investigate the CTAB adlayer structure by using electrochemical techniques on the two facets most commonly found on Au NRs, Au (111) and Au (100). The electrochemical techniques can also show how the adlayer structure changes with bulk concentration and applied potential, depending on which single-crystal surface it is adsorbed on. In order to get a better idea of the role of the Br^- counter ion in the bonding of CTAB to the gold substrate surface, Cl^- and Br^- adsorption are investigated on Au (111) and Au (100). The aggregate structures of CTA^+ surfactant molecules with different halide counter ions Cl^- and F^- (thus CTAC and CTAF) were also investigated.

The second objective of this work is to study at the feasibility of Pt-coated Au NRs as electrocatalysts in fuel cells. Au-Pt electrocatalysts have been previously found to have high activity for the oxygen reduction reaction[6 7] and have been found to have high CO tolerance in direct methanol fuel cells.[8 9] However, in the past, coating gold nanoparticles with Pt has proved to be problematic.[5 10] One of the main objectives of preparing Pt-Au nanorod electrocatalysts is finding a method of controlled deposition of Pt on the Au NR surface for optimum electrocatalytic properties.

1.2 The Electrical Double Layer

An electrode and an electrolyte are in contact in the region of the electrochemical interface. This chapter focuses on the electric double layer (EDL) region, defined as 'an electrically neutral system that occurs at an interface or surface, in which a layer of positive charges opposes a layer of negative charges'.[11]

Various models for the EDL have been proposed over the last 159 years. Helmholtz proposed the first concept, a double layer for a metal-metal interface, in 1853.[12] In 1879, he proposed a double layer for the metal-electrolyte interface.[13] In this model, the charge at the electrode surface is balanced by ions from the electrolyte. This would give rise to a rigid double layer region. A diagram of this model is given in Figure 1.1.

Figure 1.1 The Helmoltz model of the Electric Double layer

According to this model, the interfacial capacity is constant, regardless of the potential applied to the electrode. This rigid double layer is described as a parallel plate capacitor, and the relationship between the stored charge density (σ), and the voltage drop (v) between the plates can be described with Equation (1).[14]

$$\frac{\partial \sigma}{\partial v} = C_d = \frac{\varepsilon \varepsilon_0}{d} \qquad (1)$$

Here, C_d is the specific differential capacitance, ε is the dielectric constant, ε_0 is the permittivity of free space, and d is the inter-plate spacing.

In the early twentieth century, Gouy and Chapman developed a double layer model, in which the thermal motion of ions, the applied potential of the electrode and the electrolyte concentration were taken into consideration.[15] These factors are said to influence the value

of the double layer capacity.[16] According to this model, known as the Gouy-Chapman model, these is less of a compact layer at the electrode interface, but the double layer would be of variable thickness, and its ions would be free to move in the solution. Figure 1.2 gives a diagram of the Gouy-Chapman model.

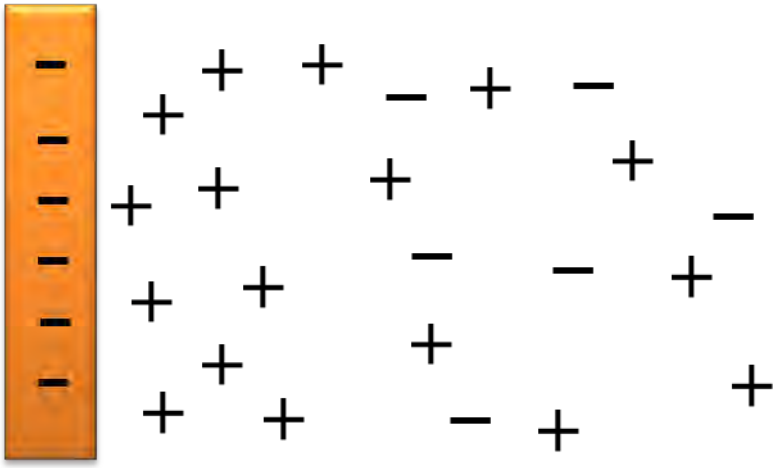

Figure 1.2 The Gouy-Chapman model of the Electric Double layer

In the Gouy-Chapman model, which is schematically represented in Figure 1.2, the capacitance would be a function of the electrode potential and would vary according to the concentration and temperature. Based on this model, the capacitance of the interfacial region can be calculated according to Equation (2).[14]

$$C_d = \left(\frac{2z^2e^2\varepsilon\varepsilon_0 n^0}{kT}\right)^{\frac{1}{2}} \cosh\left(\frac{ze\phi_0}{2kT}\right) \qquad (2)$$

Here, C_d is the differential capacitance in the double layer, z is the magnitude of charge of each ion, e is the electronic charge, ε is the dielectric constant of the medium, ε_0 is the permittivity of free space, n is the bulk concentration, k is the Boltzmann constant, T is the

absolute temperature, ϕ is the electrostatic potential. The Gouy-Chapman model predicts larger capacities than those given by experimental values because this model assumes that ions are point charges with no size.

Stern proposed a combination of the Helmoltz and the Gouy-Chapman models in 1924.[17] According to the Stern model, electrolyte ions would have a finite size, with a charge located in the centre. In this model, the double layer is divided into two regions: the first is the compact ion layer, similar to that found in the Helmoltz model, in close proximity to the electrode surface; the second is the diffuse layer extending into the bulk solution (similar to that of the Gouy-Chapman model). A schematic representation of this model is given in Figure 1.3.

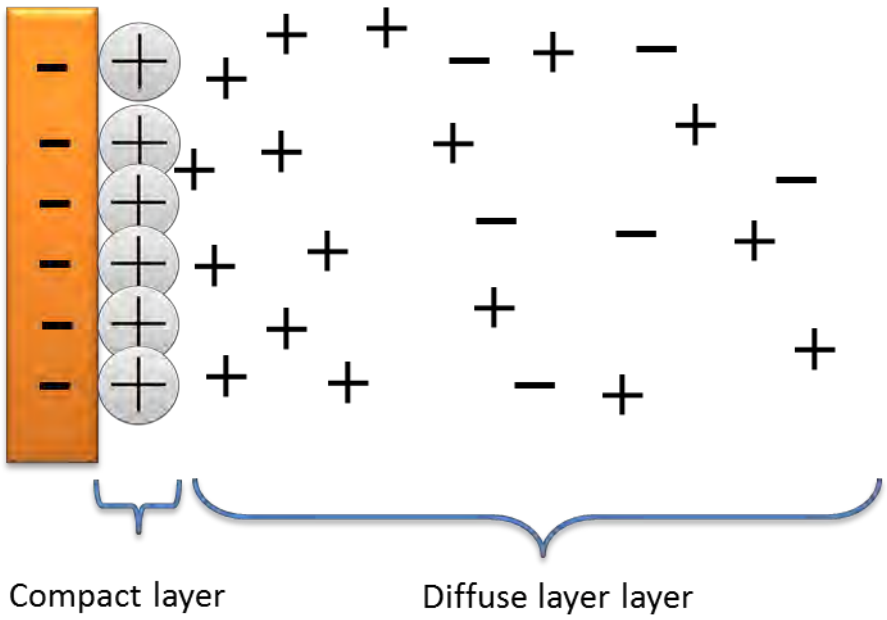

Figure 1.3 The Stern model of the Electric Double layer

In 1947, Grahame added further details to the Stern model, by dividing the inner layer into two regions.[18] In this model, the ions have a solvation layer. The closest approach of the diffuse ions is in the outer Helmholtz plane (OHP), and the layer of specifically adsorbed ions at the electrode is designated the inner Helmholtz plane (IHP). The IHP consists of specifically adsorbed ions and ions which have lost part of their solvation shell. These ions are closer to the electrode surface. The OHP comprises solvated and non-specifically adsorbed ions. These ions are attracted to form an OHP by long-range coulombic forces. A diagram of the Grahame model is given in Figure 1.4.

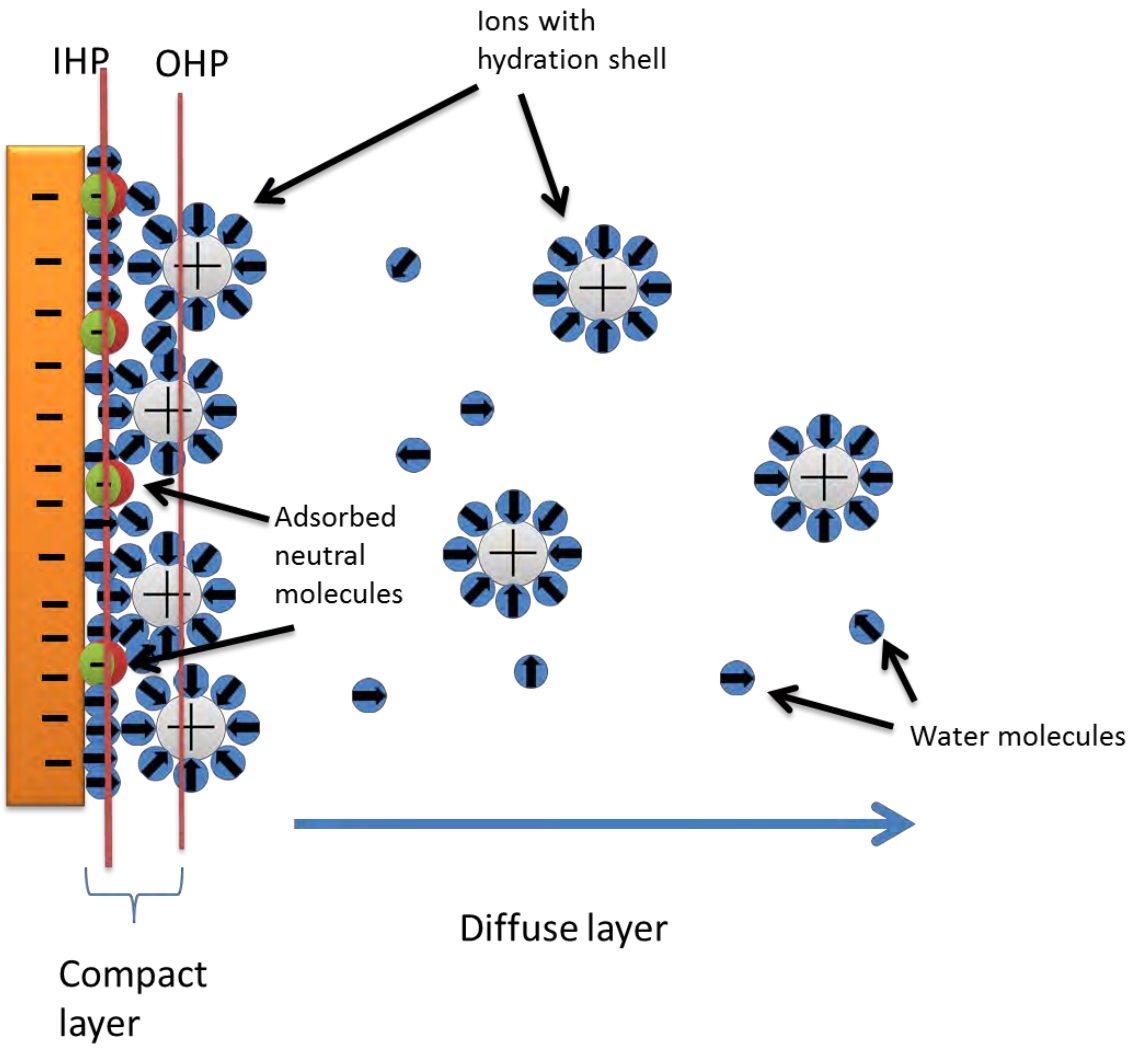

Figure 1.4 Diagram of the Grahame model for the EDL

According to this model, in the absence of specific adsorption on the electrode surface, the capacitance of the inner and outer layer can be modelled as two parallel plate capacitors in a series. The total double layer capacitance can be calculated using Equation (3).[14]

$$\frac{1}{C_d} = \frac{1}{C_H} + \frac{1}{C_D} = \frac{d}{\varepsilon\varepsilon_0} + \frac{1}{\left(\frac{2\varepsilon\varepsilon_0 z^2 e^2 n^0}{kT}\right)^{\frac{1}{2}} \cosh\left(\frac{ze\phi_0}{2kT}\right)} \qquad (3)$$

Here, C_d is the differential capacitance in the double layer, C_H and C_D represent the capacitance of the capacitance of the Helmoltz region and the capacitance of the diffuse regions of the double layer, respectively.

Bockris et al. further refined the Grahame model by suggesting that a layer of water is present within the IHP.[19] The dipoles of water molecules are aligned owing to the electrode charge.

An important parameter in electrochemistry is the electrode potential representing the electrochemical potential of the electrons in the electrode.[20] The electrode potential is thus directly related to the work function of the metal's Fermi energy. Charging the electrode potential by 1 V in the positive direction results in the Fermi energy of the electrode having work function values 1 eV higher. Similarly, charging the electrode potential by 1 eV in the negative direction means that the Fermi energy of the electrode has a work function 1 eV lower.[21]

At a given electrode potential, all electrodes, irrespective of their material, have the same Fermi energies, and hence identical electrochemical work functions. The difference in the individual work function of a metal is compensated by potential-induced surface excess charges. Solvated ions provide the excess charge, but have no chemical interaction with the surface of the electrode. As a result, the electrochemical work function of an electrode can change over a large potential range while the chemical nature of the surface remains the same. [21]

1.3 Water at the Electrode Interface

Although in most cases water is used to carry out electrochemical experiments, there is little emphasis on its interactions with the electrode surface and with other adsorbates. According to a study by Thiel and Madey, water bonds to the electrode surface through oxygen atoms to the surface.[22] Water is said to have a relatively low adsorption energy of between 0.4 and 0.7 eV. By comparison, the adsorption energy of a chemisorbed molecule on an electrode surface in the IHP is several eV.[133] The relatively low adsorption energy of water on the electrode surface is a result of water molecules hydrogen bonding with each other. This hydrogen bonding lowers their adsorption energy because the intramolecular interactions are strong. The structure, with its hexagonal hydrogen-bonded network, is similar to that found in ice. The first layer is bound to the metal electrode surface, and the second is held by hydrogen bonding with the first layer. Figure 1.5 is a diagram of this structure.

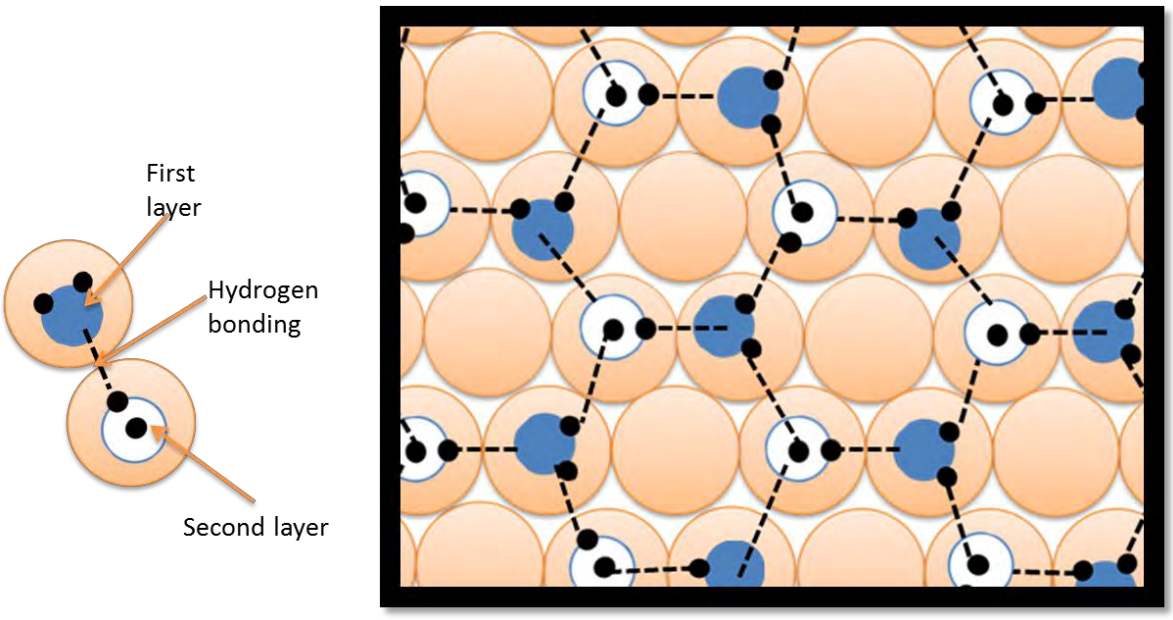

Figure 1.5 Schematic representation, reproduced from Thiel and Madey, of the adsorbed water bilayer over an Au (111) surface. [22]

The stability of the hexagonal structure is relative to its superimposition over the single-crystal electrode surface. This structure is further complicated when there is an applied electric field. According to x-ray diffraction (XRD) experiments studying the water-Ag (111) interface, water molecules form three layers over the electrode surface.[23] According to these experiments, when the electrode surface is positively charged, the density of the surface water molecules is greater than when the surface is negatively charged. This is because water interacts more strongly with a positively charged surface, owing to the partial negative dipole charge from the oxygen in the water.

Using surface-enhanced infrared adsorption spectroscopy (SEIRAS), whereby the relative intensity of the bending modes of water molecules in an interface with an Au (111) electrode is measured as a function of applied potential, the following is deduced: water molecules are nearly parallel to the surface when the substrate is neutrally charged; they change from

'oxygen up' to 'oxygen down' relative to the surface as the surface goes from being negatively to positively charged. Simulations produce similar results to these findings, although details vary amongst different models used to describe the water-metal interactions.[24]

1.4 Change of Au (111) electrode surface structure at the interface

In electrochemical conditions, the Au surface charge can vary by as much as 0.5 electrons per surface atom in the double-layer region.[25] At room temperature, a negatively charged gold single-crystal electrode surface reconstructs such that the Au surface atoms are arranged in an ordered pattern with different symmetry and periodicity from the underlying bulk layers.[21] This reconstruction lifts as the gold single-crystal surface becomes positively charged. Hamelin introduces the possibility of electrochemically induced reconstruction on an Au surface.[26] [27] This conclusion is based on changes observed in differential capacitance curves and peaks in CVs occurring at the same potential. *Ex-situ* low-energy-electron diffraction (LEED) studies[28] on an Au (111) single-crystal electrode after it has been immersed in an electrochemical cell, *in-situ* STM studies [29] [30] and *in-situ* second harmonic generation (SHG) measurements [31] [32] have shown that the surface atoms of an Au (111) single-crystal forms a $(23 \times \sqrt{3})$ symmetry when the electrode is negatively charged. This is known as a striped structure. When the potential is sufficiently positive, the striped or 'herringbone' reconstruction is said to vanish and the surface atoms are said to have the symmetry of the underlying lattice, and thus a (1×1) symmetry.[31]

Various vacuum techniques such as LEED,[33] transition electron diffraction (TED),[34] helium scattering,[35] surface x-ray diffraction[36] and STM[37] have characterised the reconstructed $(23 \times \sqrt{3})$ phase on an Au (111) electrode. It has been found from these techniques that there is an uniaxial compression so that 24 surface atoms are in the place of 23 underlying atoms in the <100> direction; the compression is thus 24/23 -1 = 4.4 %. A diagram of the in-plane hexagonal structure of the negatively charged, reconstructed $(23 \times \sqrt{3})$ phase on an Au (111) electrode is given in Figure 1.6. The dark orange circles represent the underlying Au atoms and the light orange circles represent the surface Au atoms.

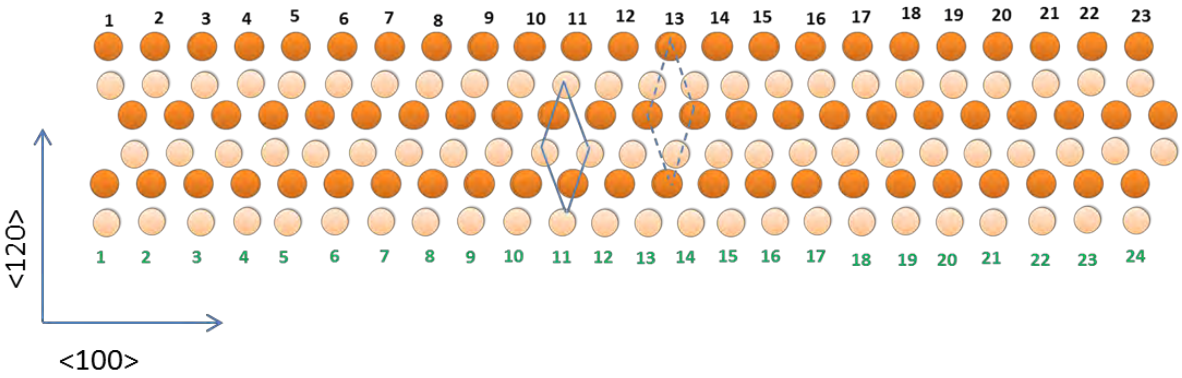

Figure 1.6 In-plane hexagonal structure of the reconstructed $(23 \times \sqrt{3})$ Au (111) surface. The dark orange circles correspond to the underlying Au atoms and the light orange circles to the Au surface atoms. In the far left and far right-hand sides of Figure 2, the surface atoms are in undistorted hexagonal sites, where there is an ABC stacking sequence. In the centre of the figure, the atoms are in faulted sites and there is an ABA stacking sequence. The black numbers at the top of Figure 2 represent the number of second layer Au atoms, and the green numbers at the bottom of it represent the number of surface Au atoms. As there are 24 surface atoms in place of 23 underlying Au atoms in the <100> direction, there is a uniaxial compression of 4.4 %.

Diagram adapted from Huang, D. Gibbs et al. [36]

The effect of changes in the surface charge density on the stability of reconstructed surfaces can be related to the electronic origin of spontaneous reconstruction at noble metal surfaces. According to theoretical studies, delocalised sp-electrons in the metals can

accumulate into regions between the surface atoms.[38] According to a study by Smoluchowski in 1941 on the electronic work function of metals, the excess electron density of a negatively charged metal surface gathers in the valleys between the surface atoms so that a flat termination of the electronic charge is obtained.[39] This excess electron density would result in smoothing and would lead to an increase in sp-electron density between the surface atoms. There would therefore be an increased attraction between these atoms, which form a densely packed reconstruction.[40] When the electrode is positively charged, the loss of mobile sp-electron density causes a weakened attraction between the surface atoms. Thus the (1×1) phase is more stable than the reconstructed phase.

1.5 Change of the Au (100) electrode surface structure at the interface

Au (100) has a four-fold symmetrical (1×1) structure. When it is heat treated, the Au (100) surface reconstructs from this (1×1) structure to form a pseudo hexagonal (5×20) structure, with a three-fold symmetry.[41] [42] The reconstructed structure will be referred to as Au (100)-(hex). This reconstruction occurs in order to lower the surface energy of the atoms. An energy diagram of this reconstruction is given in Figure 1.7.

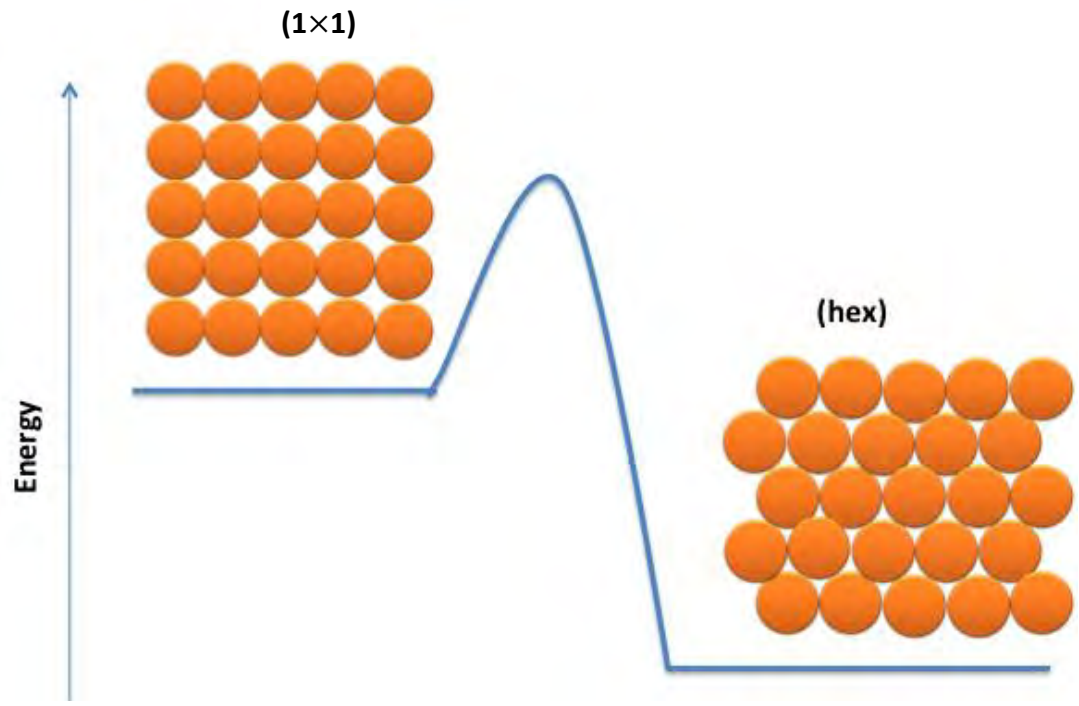

Figure 1.7 An energy diagram of the unreconstructed Au (100)- (1×1) surface, and the reconstructed, more compressed Au (100)-(hex) structure.

As can be seen in Figure 1.7, there is a significant difference between the reconstructed (hex) structure and the structure of the underlying planes of atoms (which have the (1×1) structure). The misfit between the top and underlying layer of atoms cause the (hex) structure to be slightly buckled with a corrugation length of 14.5 Å and depths of 0.3 Å.[43] As a result of this buckling, the reconstructed Au (100) surface has different properties to a conventional Au (111) single-crystal surface. Although a clean, reconstructed Au (100)-(hex) surface is thermodynamically more stable than an unreconstructed Au (100)-(1×1) surface, a high activation barrier prevents spontaneous reconstruction from occurring at room temperature. The activation barrier is high for (100) single-crystal surfaces because the reconstruction to a hex configuration involves bond breaking and transport of atoms.[44] The

Au (100) electrode surface thus needs to be heated in order to restore the reconstructed state.

Since the surface reconstruction of an Au (100) electrode is caused by the lateral displacement of atoms, the mobility of surface atoms is important for reconstruction kinetics. For gold surfaces, it has been found that anions adsorbing specifically can enhance the mobility of steps.[45] This occurs for strong anion-gold interactions. The anion interactions with gold increases to the order (F^-< Cl^-< Br^-). Such enhanced mobility, as a result of this specific adsorption, can cause the Au (100)-(hex) reconstruction to lift.

Only 5% of a monolayer of Cl^- or Br^- on the Au surface is required to remove reconstruction.[46] This suggests that the lifting of the surface Au (100)-(hex) reconstruction is anion-induced rather than charge driven as it is with the lifting of the reconstruction of the Au (111) surface. The kinetics of the (hex) →(1×1) has been found to depend strongly on the electrode potential.[47] At high overpotentials (relative to the equilibrium potential of the (hex) → (1×1) transition), the structure transition occurs in mere milliseconds. Analysis of the current transients by Au (100)-(hex) has led to the conclusion that if a reconstructed Au (100)-(hex) surface is in a solution containing specifically adsorbing anions at high overpotentials, instantaneous nucleation occurs. Submersion of a reconstructed Au (100)-(hex) surface in a solution containing specifically adsorbing anions at an open circuit potential gives rise to a mechanism with a constant transition rate.[47] It has been concluded that the lifting of the Au (100) reconstruction occurs via a nucleation-growth process. According to STM images, the lifting of the Au (100)-(hex) reconstruction starts at the surface defects, such a monoatomically high steps, or at defects of the (hex) overlayer.[48]

Figure 1.7 shows that the reconstructed Au (100) surface has around 25% more atoms than the unreconstructed (1x1) surface. Surface atoms are expelled from the reconstructed surface when the reconstruction lifts, causing surface roughening. According to STM studies, the transition from the (hex) → (1 × 1) results in the formation of small monoatomic islands.[49] [50] These 'islands' can coalesce via surface diffusion. It has been shown that when a potential positive of the pzc is applied to an Au (100) surface straight after a (hex) → (1 × 1) transition in a chloride containing electrolyte solution, the monoatomic gold islands disappear quickly. The resulting surface is an ideal, island-free unreconstructed (1 × 1) surface possessing different properties to that of an Au (100) surface which has not been electrochemically annealed.[51] [52] The monoatomic ad-islands are removed by anion adsorption because, according to STM measurements, anions preferentially adsorb on step sites.[53] This anion adsorption on the monoatomic ad-islands weakens the Au-Au bond and allows enhanced surface diffusion of gold atoms.

Although Br^- and I^- adsorb more strongly onto the Au surface, Cl^- is preferred for electrochemical annealing because Br^- and I^- ions have impurities difficult to remove after the annealing process.[44]

In this study, the flame-annealed Au (100) electrode was submerged in NaCl solution in order to lift the Au (100)-(hex) reconstruction. It was submerged for several minutes in an attempt to remove the monoatomic adislands. The aim was to have a clean, unreconstructed Au (100) surface before every electrochemical measurement.

1.6 Halide adlayers on Au (111) and Au (100) surfaces

Solvated OHP ions have only electrostatic interactions with the electrode and are therefore non-specifically adsorbed. Cations and F^- anions have strongly bonded solvation shells. Since other ions, such as Cl^- or Br^-, have a comparatively weakly bound solvation layer, their solvation shell in the double-layer region can partially strip and the ions can form a direct chemical bond with the electrode surface. These ions are 'specifically bonded' and are found in the IHP. The coverage of solvated F^- ions rarely exceeds 0.1-0.2 of a full monolayer. The coverage of specifically adsorbed ions can be significantly higher and form a close-packed configuration.[54] The coverage of specifically adsorbed ions varies depending on the crystallographic orientation of the substrate.[55]

The degree of specific halide adsorption on a metal surface increases in the order $F^- < Cl^- < Br^-$, reflecting the decreasing solvation energy of the anions.[56] The influence on the solvation layer is crucial. Theoretical studies on the adsorption geometry and binding energy of halides or halogens have been performed using density functional theory (DFT) for (100)-type surfaces by Ignaezak and Gomez,[57] and on (111)-type surface by Koper and van Santen.[58] Both studies found that the halide's adsorption energy is in the order Br< Cl < F. This is an opposite trend to the one observed for halide ions.

During specific anion adsorption, a chemical bond is believed to be formed involving a redistribution of the anion's electronic charge, known as a partial charge transfer.[59] In quantum mechanical terms, the partial charge transfer is associated with filling the orbital resonances of the adsorbate.[60] Above a critical potential, E_0, ordered halide adlayers have been observed on Au (111) and Au (100) surfaces. An ordered halide layer occurs at high

anion coverage. At a lower coverage of halides, the anion adlayer is disordered. The ordered phase forms instantaneously once the critical potential (resulting in a critical coverage) is reached. A combination of an ordered and disordered adlayer phase has never been observed, indicating that the driving force for ordered adlayer formation is the repulsive adsorbate-adsorbate interactions. The value of this critical potential depends on the potential of the metal's zero charge (pzc) and the strength of the metal-halide interaction.[61]

On an Au surface, the adsorbate-adsorbate and adsorbate-substrate interactions affect the adlayer structure. This causes complex phase behaviour on the Au single-crystal surfaces.[62 63] If the average ad-lattice spacing of the halide layer on an Au surface is different from that of the substrate atomic spacing, the adlayer is a compromise between a commensurate structure (see Figure 1.8A), where the interfacial energy is minimised, and a compressed incommensurate phase (Figure 1.8B), which is driven by the elastic lateral interactions between the ad-atoms.[61] According to previously proposed one-dimensional models of halide adsorption on a metal substrate,[64 65] the lowest energy of a compressed adlayer structure is a system with commensurate regions separated by misfit dislocations, otherwise known as domain walls, whose adsorbates are displaced from the preferential surbstrate sites. A schematic representation of this structure is given in Figure 1.8C.

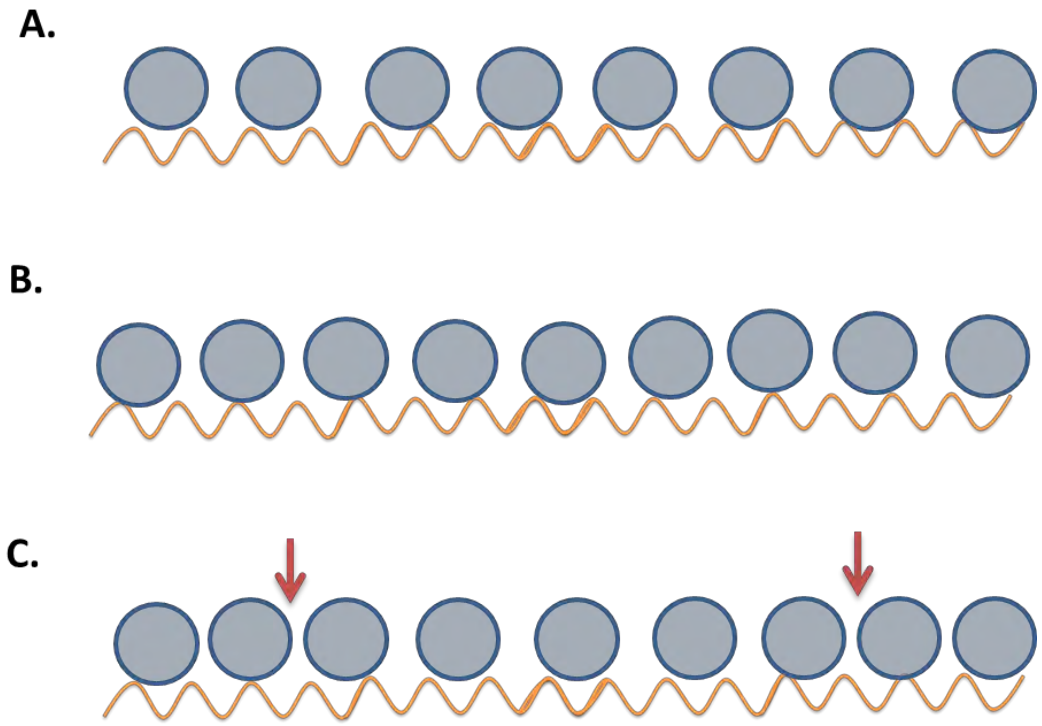

Figure 1.8 Schematic representations of **A.** a simple commensurate structure, **B.** a uniformly compressed structure and **C.** a domain-wall adlayer structure. The domain walls in **C.** are indicated by red arrows.

Adapted from Magnussen [61]

As the adlattice structure becomes increasingly compressed, the domain wall spacing decreases and the domain walls increasingly overlap. The adlayer structure becomes uniformly compressed. This is referred to in literature as a 'floating two-dimensional solid'.

1.6.1 Halide adlayer structures on Au (111) surfaces

The hitherto most extensive and detailed studies on halide adsorption on (111) substrates have concerned iodide ions, probably owing to their larger molecular size than Cl^- and Br^-. Their larger size leads to clearer experimental data, though the adlayer structures by iodide ions on (111) surfaces also can occur with Cl^- and Br^-.

SXS studies by Magnussen et al.[66] and STEM and LEED studies by Yamada et al.[67] have shown how halide adlayer structures vary with potential. At negative electrode potentials, halides form a disordered commensurate ($\sqrt{3} \times \sqrt{3}$) R30° structure at a halide coverage of θ = 0.33. A schematic representation of this structure is given in Figure 1.9A. As the (111) electrode potential becomes more positive, the ($\sqrt{3} \times \sqrt{3}$) R30° structure uniaxially compresses along the [110] direction of the metal substrate, resulting in a centred rectangular unit cell. In this structure, the halide ions adsorb on the three-fold hollow, bridge, or intermediate sites, with the top-most sites unoccupied. This adlayer structure is known as the c(p × $\sqrt{3}$) structure, a schematic representation of which is given in Figure 1.9B. At an even more positive potential region, a completely incommensurate adlayer phase is observed, which has a rotated hexagonal phase. This adlayer structure is schematically represented in Figure 1.9C. The rotation angle between the adsorbate and substrate is 1°-2.5° and depends on the potential.[66]

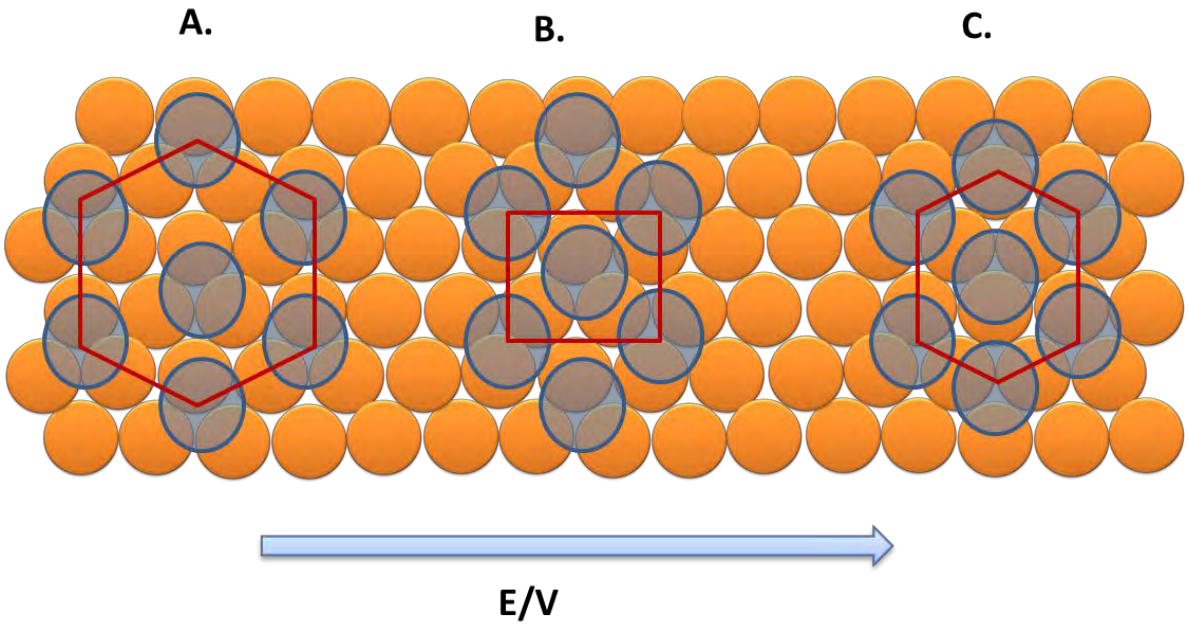

Figure 1.9 Structure of halide layers on an Au (111) surface as the applied potential increases, where **A.** is the commensurate ($\sqrt{3} \times \sqrt{3}$) R30° structure, **B.** is the incommensurate c(p × $\sqrt{3}$) phase and **C.** is a schematic representation of the compressed incommensurate rotated-hexagonal phase.
Adapted from Magnussen et al. [61]

According to the SXS measurements, the commensurate ($\sqrt{3} \times \sqrt{3}$) R30° structure (Figure 1.9A) occurs in a narrow potential range of around only 40 mV. The phase occurring at such a small potential range is due to the coverage of halides on a (111) surface constantly varying with potential. This adlayer structure only occurs when the coverage, θ, is around 1/3. The c(p × $\sqrt{3}$) structure (Figure 1.9B), on the other hand, is present over the considerably larger potential range of 560 mV because its coverage on the (111) surface can increase from 0.355 to 0.4.[66] The variation of this adlayer structure's density is as a result of the incommensurate ad-atoms uniaxially changing position. The rotated hexagonal structure, which is schematically represented in Figure 1.9C is found to be continually compressed as the potential becomes more positive, up to the positive potential limit.[66]

Magnussen et al.[66] and Yamada et al. [67] have found the structures suggested in Figure 1.9 by studying I^- adsorption Ag (111). Au (111) has an identical substrate geometry to Ag (111) as it has similar lattice spacing. Thus the incommensurate c(p × $\sqrt{3}$) (Fig 1.9B) and rotated hexagonal phases (Fig 1.9C) have been observed on an Au (111) surface using STM measurements,[68] SXS[69] and LEED.[70] The commensurate ($\sqrt{3} \times \sqrt{3}$) R30° (Fig 1.9A) phase has been observed with STM and LEED,[68 71] but not in SXS measurements.[72] This is due to the structure existing over an even smaller potential range.

SXS studies have shown that Cl^- anions form only an aligned hex-structure on the Au (111) surface with a coverage, θ, of 0.508 to 0.527.[66] STM studies have shown that Br^- anions form a commensurate ($\sqrt{3} \times \sqrt{3}$) R30° phase on the Au (111) surface at negative potentials, also with a coverage of 1/3.[73] SXS and STM studies have shown that there is a rotated hex-adlayer structure at more positive potentials, with the Br^- coverage, θ, between 0.41 and 0.52.[73 74 66]

1.6.2 Halide adlayer structures on an Au (100) surfaces

Owing to the square nature of the Au (100) surface lattice sites, four-fold hollow adsorption sides with a higher coordination than the three-fold sites found on Au (111) surfaces, are available. For this reason, the halide-substrate interactions, of the hollow sites are stronger on (100) surfaces than on (111) surfaces. Thus a stable commensurate halide adlayer structure such as that schematically represented in Figure 1.10A should theoretically form on (100) single-crystal surfaces. The structure in Figure 1.10A is known as the c(2 × 2) structure which in situ SXS studies have shown c(2 × 2) structure to be formed by Cl^-, Br^- and I^- on Ag (100).[75 76 77] However, the c(2 × 2) structure has not been found on the Au (100) surface.[78 79 80] A reason could be that although the c(2 × 2) structure is favourable in terms of adsorbate-substrate interactions, it is unfavourable in terms of adsorbate-adsorbate interactions. The corrugation potential (ad-atom–substrate interactions) is weaker for halides on Au (100) than on Ag (100). Thus, rather than forming this c(2 × 2) commensurate structure, at a coverage of θ=0.5, Cl^-, Br^- and I^- ad-atoms form a more isotropic, quasihexagonal c($\sqrt{2} \times 2\sqrt{2}$) R45° structure,[81 79 82] the structure of which is schematically represented in Figure 10B. The formation of this structure is driven by the unfavourable adsorbate-adsorbate interactions. Crystallographic analysis of X-ray peak intensities show that all the halide ad-atoms of this structure adsorb on bridge sites rather than a mixture of hollow or top sites.[79 82] This has been confirmed by in situ STM studies, where the height of two halide adsorbates in a c($\sqrt{2} \times 2\sqrt{2}$) R45° unit cell have been found to be the same.[81]

The c($\sqrt{2} \times 2\sqrt{2}$) R45° structure on an Au (100) surface can be uniaxially expanded along the $\sqrt{2}$ direction at lower halide coverages; this structure is schematically represented

in Figure 1.10C, and is known as the c($p \times 2\sqrt{2}$) R45° structure. At higher halide coverages (as a result of more positive applied potentials), uniaxial compression occurs in the $2\sqrt{2}$ direction and forms the c($\sqrt{2} \times p$) R45° structure, which is schematically represented in Figure 1.10D.

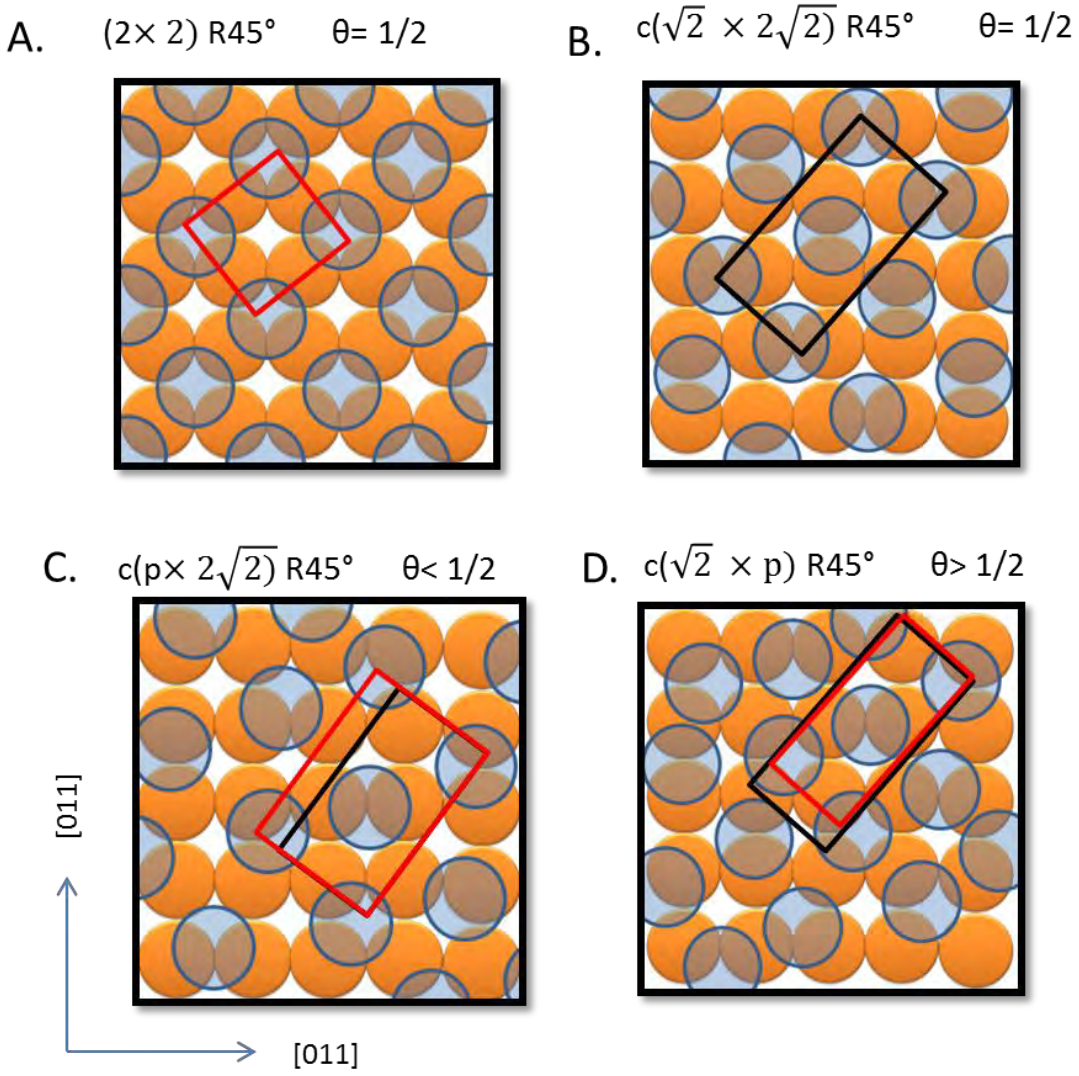

Figure 1.10 Halide adlayer phases on (100) surfaces: **A.** is the c(2x2) structure, **B.** is the c($\sqrt{2} \times 2\sqrt{2}$) R45°stucture, **C.** is the c($p \times 2\sqrt{2}$) R45°structure and **D.** is the c($\sqrt{2} \times p$) R45° structure. The adlayer unit cells are represented by red rectangles. The c($\sqrt{2} \times 2\sqrt{2}$) R45°unit cell is represented with by a black rectangle, and is also included in C. and D. as a comparison.

Adapted from Magnussen [66]

For the c($p \times 2\sqrt{2}$) R45° and c($\sqrt{2} \times p$) R45° structures shown in Figures 1.10C and 1.10D, the ad-atoms are bonded between the bridge sites and the energetically more favourable

hollow sites, giving the two structures extra stability. A transition from the c($\sqrt{2} \times 2\sqrt{2}$) R45° structure to the more densely packed c($\sqrt{2} \times p$) R45° structure has been observed for Cl^- and Br^- on Au (100) surfaces as the halide coverage increases because of the electrode potential becoming more positive,[83] [79] probably owing to a screening effect provided by the positively charged substrate. At the most positive potentials, the halide adlayer on Au (111) has been found to have an undistorted hexagonal structure.[79] This compressed undistorted halide structure is similar to that of the rotated hexagonal phase on Au (111), hence the halide-substrate interactions are similar on both the Au (111) and Au (100) surfaces, even though there is a difference in the crystallographic plane symmetry of these two surfaces. These compressed phases are therefore mainly driven by the unfavourable adsorbate-adsorbate interactions.

1.7 The structure of surfactants at the electrode interface

The cationic surfactants examined are amphiphilic molecules. Cetyltrimethyl ammonium bromide (CTAB) is the cationic surfactant which is used to synthesise gold nanorods (Au NRs).A diagram of CTAB is given in Figure 1.11. CTAB consists of: a hydrophobic hydrocarbon tail group, which is $C_{16}H_{33}$ (highlighted in red in Figure 1.11); a hydrophilic, cationic head group, which is trimethyl ammonium (highlighted in green in Figure 1.11) and a bromide counter-ion (highlighted in black in Figure 1.11).

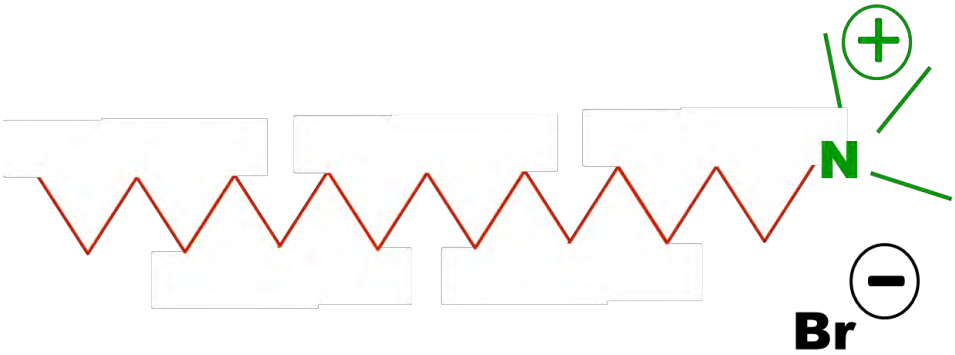

Figure 1.11 The chemical structure of cetyltrimethylammonium bromide (CTAB), which has a $C_{16}H_{33}$ hydrophobic tail group (shown in red), a trimethylammonium cationic head group (shown in green) and a bromide counter ion (shown in black)

1.7.1 The structure of surfactants in a bulk electrolyte solution

At low bulk concentrations, surfactant molecules are present in aqueous solutions as solvated monomers.[84] When the bulk concentration exceeds a critical value, known as the critical micelle concentration (CMC), the hydrophobic tails segregate from the aqueous solution, and aggregate into colloidal micelles which have a hydrophobic interior and a hydrophilic surface.[85] Figure 1.12 gives a schematic representation of a cross-section of a surfactant micelle. The red dots are the polar head groups, and the blue lines represent the hydrophobic tail groups of the surfactant molecules.

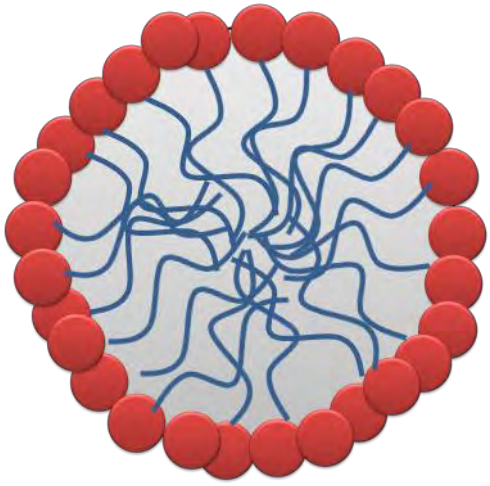

Figure 1.12 Schematic representation of a cross section of a surfactant micelle in bulk solution. The red dots represent the polar head group, and the blue lines represent the hydrophobic tail group of the surfactant molecule.

A delicate balance of forces controls the stability of cationic micelles: the more stable the cationic micelle, the lower the concentration at which it spontaneously forms. For the surfactants studied in this section, aggregate formation is driven by the hydrophobic nature of the hydrocarbon tail group.[86] Phase separation between the surfactants and the aqueous solution is prevented by the surfactant head groups and counter-ions retaining their contact with the aqueous phase. A micelle has a liquid-like hydrocarbon core filled with surfactant tails surrounded by an interfacial region containing the surfactant head groups and a large fraction of the surfactant counter-ions between 50-90%. The remaining counter-ions are 'free' in the surrounding aqueous solution.[86]

1.7.2 The adlayer Structure of Surfactants on a gold electrode surface

Theoretical modelling of surfactant structure at the electrode-liquid interface is more complicated than modelling surfactant structure in bulk solution because there are added complications of substrate-surfactant interactions. Figure 1.13 gives a schematic representation of various structures that have been proposed for surfactants on a gold surface.

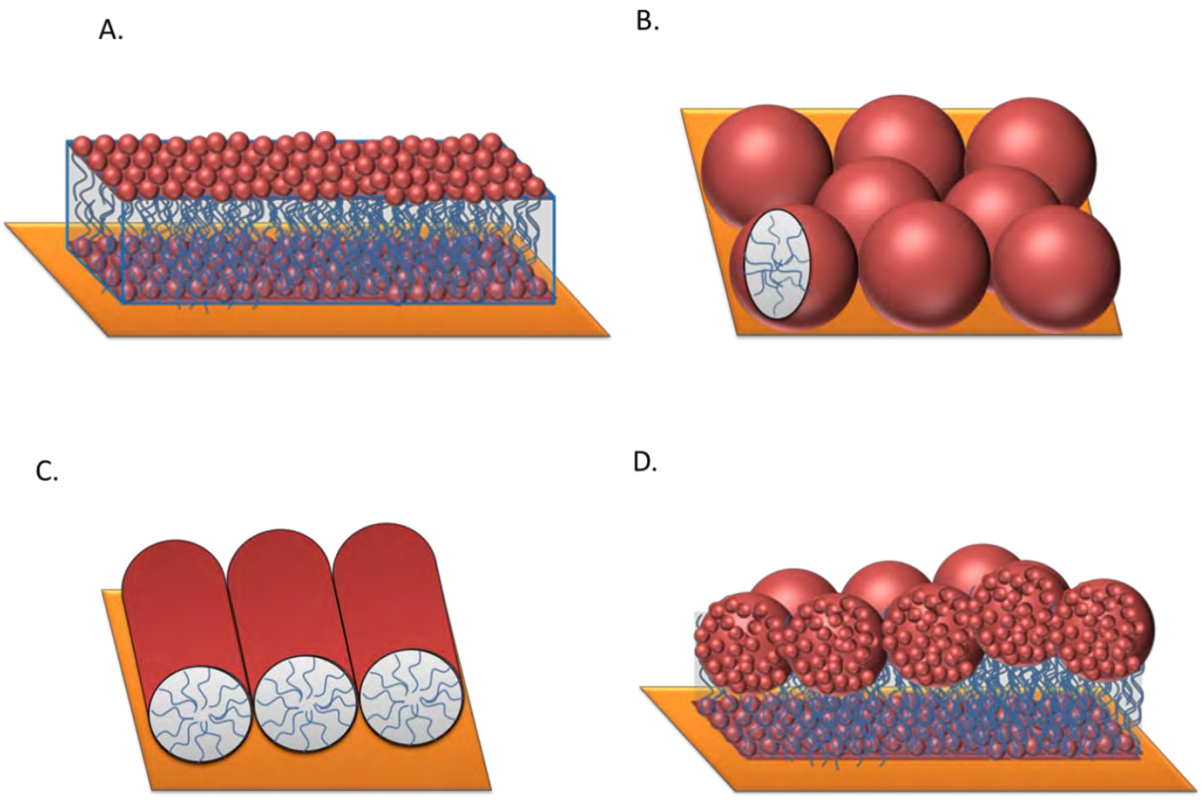

Figure 1.13 Various proposed structures for surfactants on a gold surface. The following surfactant structures are schematically represented: **A.** bilayer structure, **B.** micelle structure, **C.** cylindrical structure and D. Composite micelle/bilayer structure.

Diagram adapted from Chen et al. [107]

According to theoretical modelling, only a bilayer of adsorbed surfactants can form on hydrophilic surfaces when the concentration of the surfactant is greater than or equal to the CMC.[87] A schematic representation of this structure is given in Figure 1.13A.

In 1955, Gaudin and Fuerstenau suggested a different model, in which surfactants form micellar structures on the substrate surface.[88] A diagram of this structure is given in Figure 13B. However, there was no direct experimental evidence of this theory and the bilayer structure, Figure 1.13A, was accepted as being the aggregate structure of micelles on a substrate.

In 1995, Manne and Gaub [89] gave experimental evidence through atomic force microscopy (AFM) that at the substrate-liquid interface, surfactants adsorb as micelles (Figure 1.13B), or cylindrical micellar structures, a diagram of which is given in Figure 1.13C. A combination of a bilayer (1.13 A) with micelle/hemicylindrical micelle structures has also been proposed.[87] A schematic representation of these structures is given in Figure 1.13D.

Proving that these structures exist is nonetheless experimentally difficult because it is hard to distinguish between ad-micellar structures such as those represented in Figures 1.13B and 1.13C, and composite hemispherical/micelle bilayer structures such as the one represented in Figure 1.13D.[84] Since the interaction between the substrate surface and the polar head group of the surfactant could alter the spacing between the surfactant head groups, the surface area per surfactant molecule may change. A change in the area per surfactant molecule would also change the packing parameter. This would subsequently cause the shape of the adsorbed micelle to change from its shape in the bulk solution.[90 91] The shape of the ad-micelle depends not on the chemical properties of the substrate

surface, but on the electrostatic factors such as the composition of the electrolyte and the charge of the substrate surface.[84] Unless there is a strong, specific adsorptive interaction.

On hydrophobic surfaces, such as graphite [92], or silica treated with dimethyldichlorosilane, [93] surfactants can also aggregate and form hemispherical, hemicylindrical, or monolayer structures directly on its surface.[94] [95] [96] A schematic representation of these structures is given in Figure 1.14.

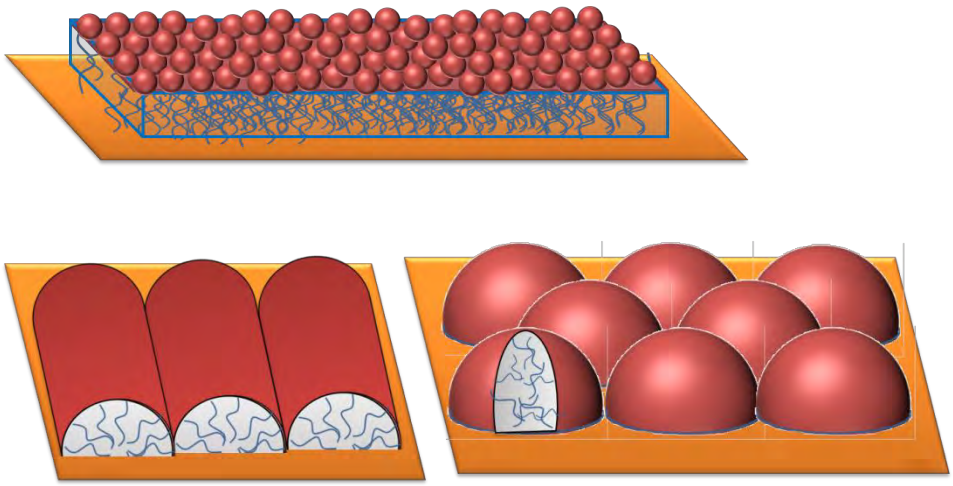

Figure 1.14 Monolayer, hemicylindrical and hemispherical surfactant structures formed on hydrophobic surfaces.

On gold, which is a hydrophobic surface, it is also possible for surfactants to aggregate and form hemispherical, hemicylindrical, or monolayer structures directly on the gold surface.[94] [95] [96] Surfactant molecules are said to aggregate on this surface when the bulk concentration of the surfactant is around ten times less than the CMC. This concentration is known as the critical aggregation concentration (CAC).[87] The crystallographic structure of the

gold single-crystal surface is said to act as an aggregation template of the surfactant molecules.[92 97]

1.7.3 Electric field driven aggregation of surfactants on Au single-crystal surfaces.

In this section, previous findings on the adsorption of anionic, zwitterionic and cationic surfactants are discussed. This is because, although CTAB is a cationic surfactant (i.e. it has a positively charged head group), it also has a strongly adsorbing negatively charged counter ion and could have similar adsorption characteristics to anionic surfactants. Moreover, there could be coupling between the anionic head group and the cationic surfactant, giving CTAB zwitterionic properties at the gold-liquid interface.

The type of structure the surfactant forms on the gold surface very much depends on the charge of the gold (or applied potential) and the type of head group and counter-ion the surfactant has. For example, at concentrations of lower than the CMC, a surfactant with a negatively charged head group has two states of adsorption; when the electrode is at a negative potential, it has one state, when it is at a positive potential, the surfactant is in another adsorption state, in which double the amount of surfactant molecules adsorb on the electrode surface.[98] The transition between these two states corresponds to the number of molecules in the interfacial region doubling. This has been ascribed to the positive charge on the metal surface screening the electrostatic repulsions between the headgroups of the surfactants.

For neutral or zwitterionic surfactants, the surfactant coverage is said to be considerably larger than with surfactants with negatively charged headgroups. Instead of two states being

observed, as the potential is swept positively, the concentration of surfactants at the interface gradually increases and there are multiple adsorption states.[99]

For the cationic surfactant *N*-Decyl-*N,N,N*-trimethyl ammonium trifluoromethane sulfonate (DeTATf), which has a non-adsorbing counter-ion, the surfactant concentration at the gold-liquid interface is much lower than in the case of the coverage which can be expected for a monolayer of vertically adsorbed surfactant molecules.[100]

The phase of the surfactant film on a gold substrate also depends on the bulk concentration of the surfactant. Figure 1.15 gives a summary of how the structure of the surfactant film over the gold surface varies according to the bulk surfactant concentration and applied potential of the Au (111) electrode. These structures are suggested according to images obtained through atomic force microscopy (AFM) and scanning tunnelling microscopy (STM). Burgess et al. reported images of the anionic surfactant sodium dodecyl sulphate (SDS) on Au (111) with varying concentrations and potentials.[95 98] Xu et al. reported images for the zwitterionic surfactant, N-dodecyl-N, N, -dimethyl-3-ammonio-1-propanesulfonate (DDAPS) on Au (111), with varying concentrations and potentials.[99] Information as detailed is not possible to obtain for a cationic surfactant on Au (111) because because there are attractive, rather than repulsive forces between the AFM tip and the cationic surfactant molecules.[84] Nonetheless, STM images over a range of applied potentials on the Au (111) surface with the cationic surfactant DeTATf have previously been recorded.[101] The square in Figure 1.15 becomes progressively darker green as applied potential on the Au electrode becomes more positive and/or the bulk concentration of surfactant increases.

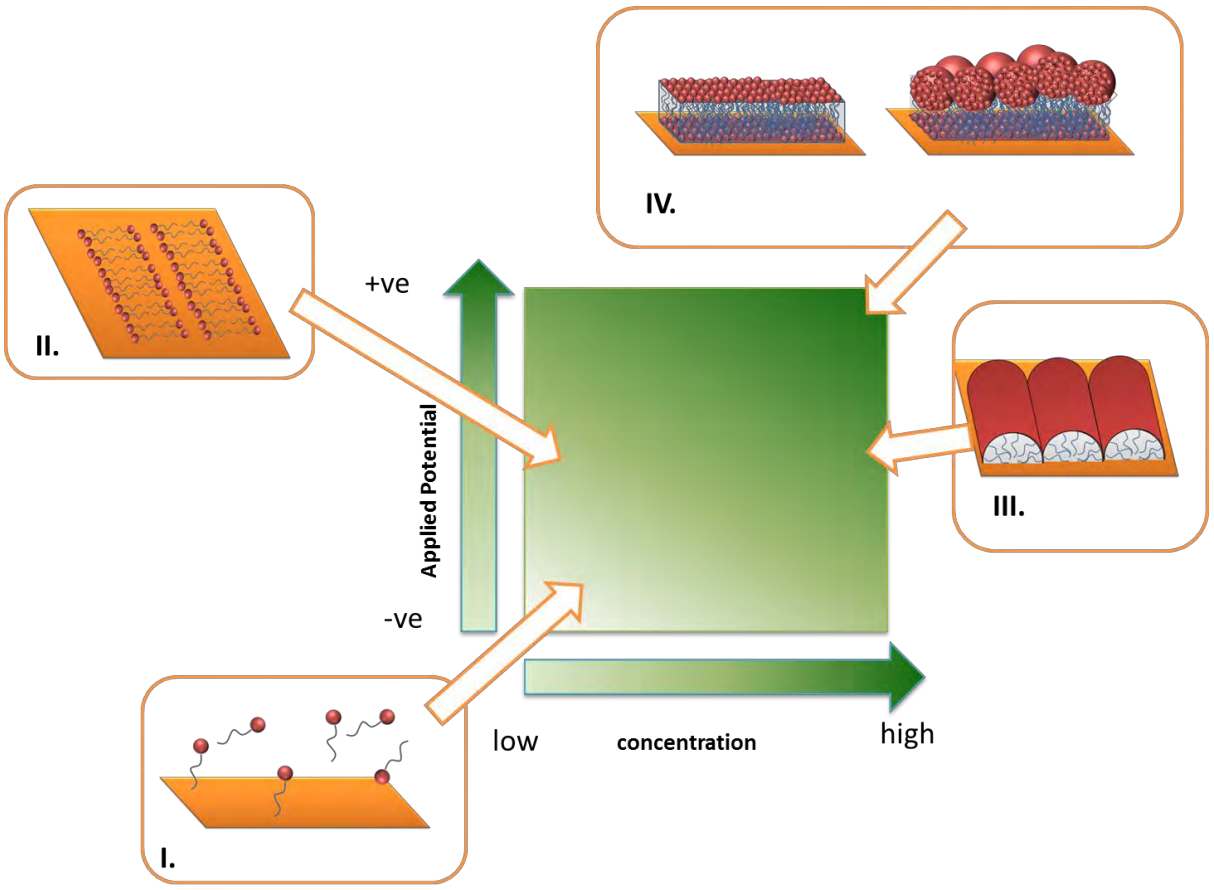

Figure 1.15 Diagram of how surfactant structures on a gold surface change with concentration (x axis) and applied potential (y axis). Diagram I represents surfactant structure at low concentration and negative potential; II is more positive potential and low concentration; III is more positive potential and higher bulk concentration, and IV is at the surfactant structure at the most positive potential and high bulk concentration. This diagram is based on the interactions of the anionic surfactant SDS and the zwitterionic surfactant DDAPS with a gold substrate, though these potential induced structure changes could apply to any surfactant.

Diagram adapted from Chen et al. [84]

Diagram I of Figure 1.15 represents the gold-liquid interface when the applied potential to the substrate surface is -800 mV. Here there is no surfactant adsorption on the surface.

When the gold surface is moderately charged and at a bulk concentration lower than the CMC and CAC, a film of flat-lying molecules packed side-to-side and tail-to-tail is said to form. Diagram II, Figure 1.15, schematically represents this structure, which is known as a striped structure. The alkyl chain tail groups of the surfactants are orientated along the [011] direction of the Au (111) surface. This structure is a result of van der Waals chain-chain and chain-substrate interactions. The arrangement of the gold atoms on the single-crystal surface act acts as a template for surfactant aggregate structures.[102]

Previous literature has highlighted the trend whereby the packing of the structure (Diagram III, Figure 1.15) depends on the polar head group of the surfactant molecule. According to high resolution STM images of molecules of the anionic surfactant SDS, when this 'striped' configuration is formed on the Au (111) surface, water molecules are said to stabilise the head group by bridging neighbouring sulphate ions through hydrogen bonding.[95] In the case of the zwitterionic surfactant molecule DDAPS, when this striped configuration forms, surfactant molecules are closely packed, with the average width per molecule row found to be around 4.2 nm.[99] This value is smaller than the hydrodynamic radius of a hydrated bulk surfactant micelle, which, according to Foucompre and Lindman, is around 4.8 nm.[103] The packing of the two-dimensional adlayer structure of the zwitterionic surfactant molecules is similar to that of n-alkanes on an Au (111) surface.[104] This close packing occurs because the positively charged quaternary ammonium centre of the head group screens the negatively charged sulphonate group, which is also at the surfactant head group. For the cationic surfactant DeTATf, the density of surfactant molecules in this structure is low and less than that of surfactants with anionic and zwitterionic head groups.[101] This is due to the repulsive forces between cationic head groups. The spacing

between each set of stripes is also larger, a fact which has been attributed to the adsorption, or co-adsorption of the large trifluoromethane sulphonate (triflate) counter-ion between stripes.

For this 2D adlayer structure, cationic and zwitterionic head groups face each other in a zip-like configuration.[101 99] With this configuration, the polar head groups are orientated antiparallel to each other, in a ($\sqrt{3} \times \sqrt{3}$) arrangement. Thus for a cationic surfactant, the counter-ion on one side of the 'zip' stabilises the cationic head group on the other side. A schematic representation of this structure is given in Figure 1.16. The surfactant in this diagram is CTA^+. The counter-ion of CTA^+ is represented by a pink circle.

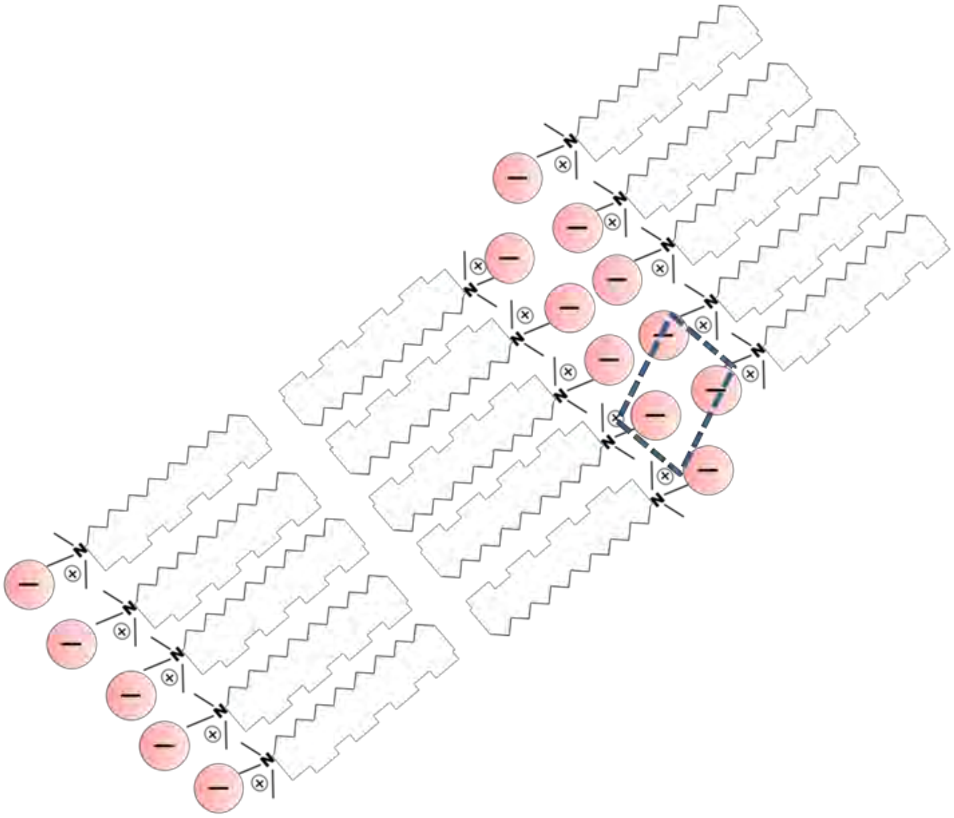

Figure 1.16 Schematic representation of the possible 2D $\sqrt{3} \times \sqrt{3}$ structure of a CTA^+, halide surfactant structure on a gold electrode. The pink circles represent the halide counter-ions.

For surfactants and zwitterionic surfactants, when the electrode is at the same potential, but the bulk surfactant concentration increases, and approaches the CMC, this flat lying aggregate 2D- adlayer structure acts as a template for a hemicylindrical aggregate.[98 99] This structure is represented by diagram III in Figure 1.15. However, for the cationic surfactant DeTATf, the aggregation has been found not to occur, with the large size of the co-adsorbed triflate counter-ion being the reason for this.[84] However, if the counter-ion of the cationic

surfactant is different, an aggregate structure such as the one observed in diagram III in Figure 6 could also occur for cationic surfactants. At positive potentials, a phase change occurs for the anionic, cationic and zwitterionic surfactant films. For the cationic surfactant DeTATf, though it is evident that there is a phase change at positive potentials, it is unclear as to what structure is formed.[101] For the surfactant with an anionic head group, at bulk concentrations near CMC, according to neutron reflectivity (NR) measurements, the thickness of this structure after the phase change is thicker than the hemicylindrical aggregate structure at more negative potentials.[98] From this experimental evidence, it has been suggested that that a transformation from a hemicylindrical aggregate structure to an interdigitated bilayer structure occurs, with the negative charge of the anionic head group being screened by the positive charge of the metal surface. When zwitterionic surfactants are in the solution, at positive potentials, and bulk concentrations are near the CMC, the hemicylindrical micelles transform into disc shaped structures. Due to the apparent multilayer thick film structure of the surfactant film at positive potentials, a composite structure similar to that in Figure 4D has been proposed, where the surfactant layer is capped by micellar/hemicylindrical structures.[99] A schematic representation of these types of surface structures is given in diagram IV of Figure 1.15.

Although this structure is unlikely to form for a cationic surfactant with a large, non-adsorbing counter-ion, if an adsorbing counter-ion such as bromide is present instead, it is possible that the cationic surfactant forms phases such as those given in diagram IV at positive potentials, because if the counter ion couples with the cationic head group of the surfactant, the surfactant could have properties similar to those of surfactants with anionic or zwitterionic head groups.

1.8 The synthesis of gold nanorods

1.8.1 An overview of the synthesis of gold nanoparticles

Colloidal gold has been used since the Ancient Roman times to colour glass intense shades of yellow, red or purple. In 1857, Michael Faraday prepared the first pure samples of colloidal gold, where he used phosphorus to reduce a solution of gold chloride.[105] Since this discovery, in situ-chemical reduction of tetrachloroauric acid is the most popular route for synthesis of gold nanoparticles. Reducing agents commonly used in the reduction of metal ions are potassium borohydride, nitric/hydrochloric acid,[106] hydrazine[107] and ascorbic acid.[108] When a reducing agent is added to a solution containing a metal salt, the metal ions are reduced and the metallic solid particles nucleated. As nanoparticles are unstable in solutions, precautions need to be taken in order to avoid precipitation, or aggregation.[109] The most common means of preventing aggregation of metal nanoparticles is the use of surfactants as capping agents. Using surfactants also results in functionalised and stabilised nanoparticles.[110] Surface active agents such as cysteine,[111] ionic and non-ionic surfactants,[112] CS_2,[113] sodium citrate,[114] and nitrotriacetate[115] have previously been used to bind to gold nanoparticles, limiting particle growth and creating a colloidal dispersion. The type of surfactant and the synthesis conditions used determine the shape of the gold nanoparticle. For example, citrate-stabilised gold nanoparticles prepared according to the Grabar procedure are spherical in shape and have an average diameter of 18nm.[116]

1.8.2 The role of CTAB during Au NR synthesis

The cationic surfactant hexadecyl (or cetyl) trimethyl bromide (CTAB) (see diagram of a CTAB molecule in Figure 1.11) allows colloidal gold to grow into rod shaped nanoparticles during synthesis. It has been found through thermo-gravimetric analysis[117] and zeta-potential analysis[118] that during gold nanorod (AuNR) synthesis, CTAB molecules form a bilayer on the gold nanoparticles. The CTAB bilayer consists of two surfactant layers. For the first layer, the quaternary ammonium headgroup binds to the Au surface; for the second, the quaternary ammonium headgroup faces the aqueous media.[119] Between these two head groups the hydrophobic tail groups pack together. Figure 1.17 is a diagram of the CTAB bilayer on a gold nanoparticle surface.

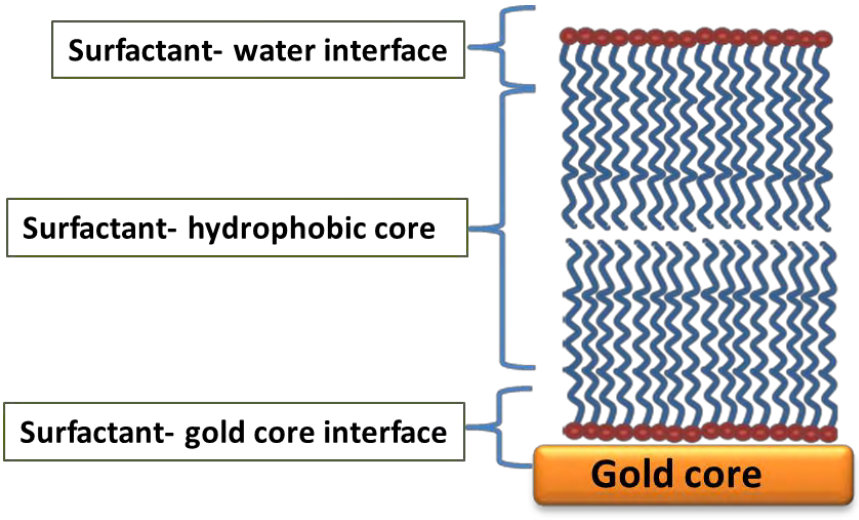

Figure 1.17 Diagram showing the CTAB bilayer on the surface of a gold nanorod. The small red circles represent the hydrophilic quaternary ammonium head group. The blue wavy lines represent the hydrophilic $C_{16}H_{33}$ tail groups. Three distinct regions are labelled: the surfactant- water interface, the surfactant- hydrophobic core, and the surfactant-gold core interface.

Diagram adapted from C. J. Murphy et al. [119]

It has been found through zeta potential analysis that the surface-water interface has a net positive charge, such that the Br^- counter-ions are loosely associated with the particles in the water. The hydrophobic region is considered as an organic solvent layer with the ability to concentrate hydrophobic molecules from the aqueous bulk.[120] Although the gold-surfactant interface is not clearly understood, it is accepted that there are electrostatic interactions between the cationic head group and anionic sites on the Au surface.[121]

1.8.3 The seed mediated growth mechanism for the synthesis of AuNRs

Au NRs are synthesised using the seed-mediated growth method which was proposed by Nikoobakht et al.[117] A strong reducing agent is used to prepare Au (0) seed particles from gold salts, then a weak reducing agent is used to reduce more gold salt onto the seed particles. The bilayer-micelle structure CTAB formed around the gold nanoparticles causes these seeds to grow epitaxially and thus into rod-shaped nanoparticles. With the CTAB as a growth-directing agent the gold seeds can grow into rod-shaped nanoparticles over 100 nm in length.[121]

Au seeds are made when Au^{3+} (from $HAuCl_4$ salt) is reduced to Au (0) using a strong reducing agent, $NaBH_4$. The solution of the resulting small Au nanoparticles is known as the seed solution. The seeds are kept dispersed with micelles from CTAB. A growth solution is then prepared. It also contains CTAB and $HAuCl_4$ but a weaker reducing agent, ascorbic acid (AA), is used. AA reduces the Au^{3+} in the growth solution twice. First, it reduces Au^{3+} to Au^{1+}, according to reaction (1).[122]

$$CTA^+AuCl_4^- + C_6H_8O_6 \rightarrow CTA^+AuCl_2^- + C_6H_6O_6 + 2H^+ + 2Cl^- \qquad (1)$$

In reaction (1), $AuCl_4^-$ is bound to the CTA^+ micelles and is reduced to form $CTA^+AuCl_2^-$ micelles. After the seed solution is added, the $CTA^+AuCl_2^-$ complex binds to the CTAB-capped seed particles through collisions. The growth-limiting step is the collision rate between the CTAB-protected seed particles, and the $CTA^+AuCl_2^-$ complexes.[123] The collision rate is higher on the tips than on the sides of the seeds, causing rod-shaped growth.

$$2CTA\text{-}AuCl_2 + 3C_6H_8O_6 \rightarrow 2Au + C_6H_6O_6 + 2CTA^+ + 6H^+ + 4Cl^- \qquad (2)$$

According to high resolution Transmission Electron Microscopy studies (HRTEM), Au NR particles (synthesised without $AgNO_3$) have a penta-twinned structure with {111} end faces, and {100} side faces. The common five-fold axis of elongation is [100].[124] A schematic representation of this model is given in Figure 1.18.

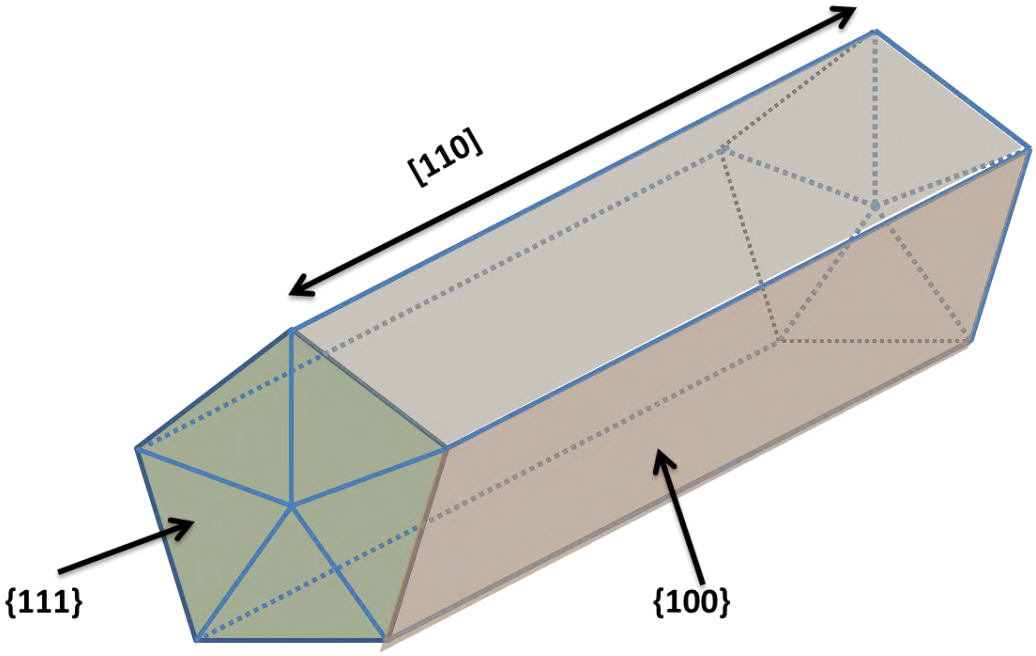

Figure 1.18 Proposed model of Au NR particle that has been synthesised without $AgNO_3$. The Au NR particle has a penta-twinned structure with {111} end faces, and {100} side faces. The common five-fold axis of elongation is [100].

Adapted from Johnson et al [124]

1.8.4 The role $AgNO_3$ during Au NR synthesis

For the Au NRs used in this study, $AgNO_3$ is added to the growth solution, providing Ag^+ ions. These Ag^+ ions restrict the growth of the Au NRs to less than 70 nm. However, they increase the yield of rod-shaped particles and their presence causes the Au NRs produced to be of a more uniform size (more monodisperse). [118] The ascorbic acid present in the growth solution cannot fully reduce Ag^+ ions to metallic silver during synthesis.[121] However, Ag^+ can be reduced to bulk silver onto a metal substrate in the form of a metal monolayer at a potential less negative than bulk reduction. This is known as underpotential deposition (UPD).[125] Whether Ag is present on the Au surface in the form of Ag (0) or Ag^+, or in the form of an AgBr monolayer has still not been determined. [126 127]

Ag deposits on different single-crystal facets of the gold seeds at different rates. It can thus direct growth along the facets on which it deposits slowest. CTAB-capped seeds have spherical symmetry broken into different facets with preferential binding of CTAB on the (110) facet. Silver ions deposit on the (110) side facet at a faster rate than they do on the (100) end facet.[128] This results in particle growth in the [110] direction. Complete deposition of Ag ions on the (100) end facet stops particle growth, restricting the length of Au NRs to under 100 nm. The proposed structure for AuNRs using Ag ions is 4 Au (110) faces on the sides and one Au (100) face on the ends.[121] Figure 1.19 shows a schematic representation of this Au NR particle structure.

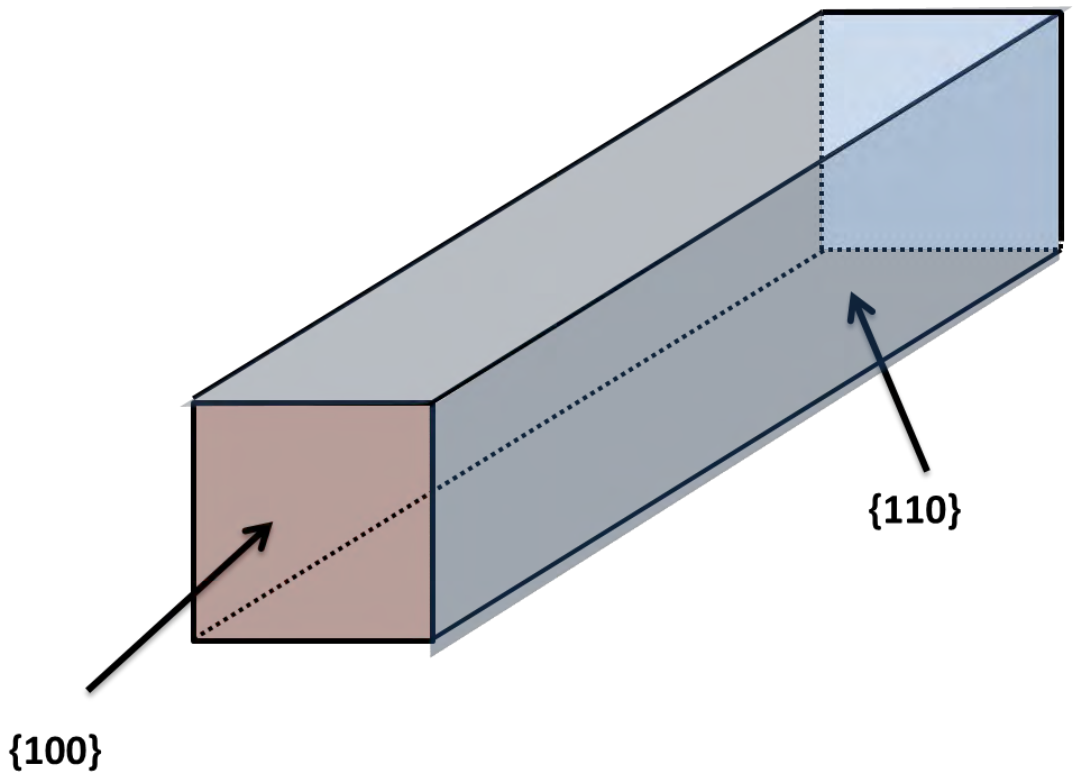

Figure 1.19: Diagram an Au NR molecule synthesised with Ag^+ present in the growth solution. The nanorods are single-crystals bearing {110} faces on the sides and {100} on the ends.

From Orendorff et al. [124]

1.8.5 Optical properties of Au NRs

Optical properties of Au NRs arise from their localised surface plasmons. When an electromagnetic field interacts with the gold conduction band electrons it induces an oscillation of electrons.[129] This oscillation causes a strong absorption of Ultraviolet and visible light, and is the reason why a colloidal suspension of Au NRs is red to purple in colour. This is discussed in detail in Section 2.6.

1.9 Pt coating onto Au nanoparticles

The two most commonly used methods for depositing Pt on Au nanoparticles are the underpotential deposition of Cu, followed by a redox exchange with Pt ions, and the direct deposition of Pt using a reducing agent.

1.9.1 Cu underpotential deposition, followed by redox exchange with Pt ions.

A monolayer of Pt can be deposited on an Au working electrode surface using the Cu_{UPD} followed by the Pt redox exchange technique. The Au-Cu bond is stronger than Cu-Cu and Au-Au bonds. This allows copper to be deposited at potentials more positive than the Nernst potential, where bulk deposition takes place (or underpotentially deposit) on the Au surface.[130] When an Au working electrode is held at a suitable potential for UPD in an electrochemical cell containing $CuSO_4$ solution, a monolayer, or sub-monolayer, of copper can form on the Au surface, allowing a controlled and reproducible deposition.

Brankovic et al. have demonstrated a spontaneous irreversible redox replacement process, in which the underpotentially deposited Cu adlayer on Au is oxidised by more noble metals, e.g. Pd^{2+}, Ag^{+}, Pt^{2+} ions.[131] These noble metal cations are reduced and deposited on the Au surface simultaneously. Pt-Au electrocatalysts having a monolayer of Pt on Au nanoparticles have since been studied using this method.[132] A diagram summarising the Cu_{UPD} Pt deposition procedure is presented in Figure 1.20.

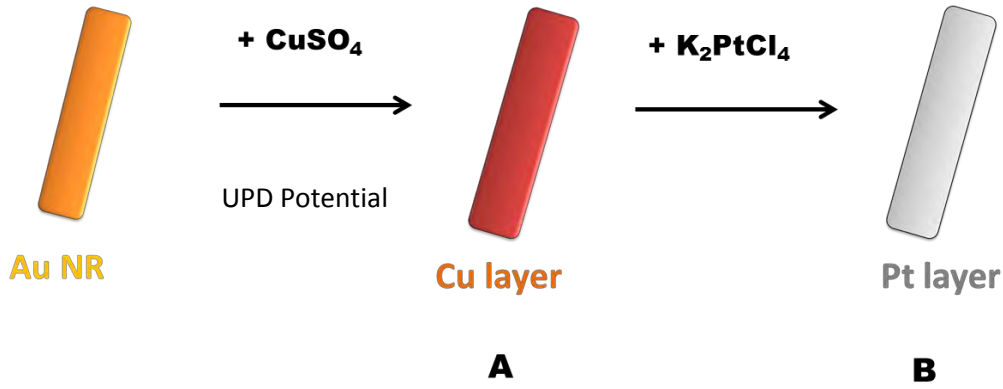

Figure 1.20 A schematic representation of a Pt monolayer deposition on a working electrode containing immobilised Au NR through Cu_{UPD} followed by Pt redox exchange. **A.** A copper layer is formed on the Au NRs after the working electrode is put in a cell solution containing $CuSO_4$ solution and held at a desired UPD potential. **B.** A monolayer of Pt is formed on the Au NRs after the copper-coated Au NR electrode is put in a solution of K_2PtCl_4, wher bulk Cu is redox exchanged with Pt^{2+} in the solution.

1.9.2 Direct Pt deposition

Pt^{2+} ions from a Pt salt (e.g. K_2PtCl_4) can be reduced onto an Au substrate to form a bulk Pt layer, using a reducing agent to provide the electrons.

$Pt^{2+} + 2e^- \rightarrow Pt\ (0)$ (3)

This method allows Pt to be deposited on to AuNRs in a colloidal suspension. Pt deposition on Au NRs could happen in a similar fashion to Au NR growth, where there is an electric field-directed mechanism.[123] The Pt salt complexes onto CTA^+ micelles. This Pt-CTA^+ complex approaches the surface of the Au NRs, with excess electrons provided by the reducing agent. The reduction rate depends on the collision frequency between the Pt micelle complexes and gold nanorods. An increase in the amount of Pt salt with respect to the amount of Au^0 concentration leads to an increase in the collision frequency between $CTA^+PtCl_4^{2-}$ micelles and AuNRs.[122]

1.10 Normalisation of active surface area of Pt on Au NRs

After Pt-coated Au NRs are immobilised onto a carbon working electrode (see section 3.9) cyclic voltammetry allows the determination of the active surface area of Pt on an electrode surface. In catalysis, the active area is limited to the metal surface. Determination of the quantity of active sites allows a good understanding of the effectiveness of the electrocatalyst. Moreover, it is a necessary step to obtain the turnover frequency (TOF), which gives information of how many times each catalyst site is used per second during the reaction.[133] Cyclic voltammetry where the charge is measured as a result of hydrogen and the CO adsorption are two common methods to look at the active surface area of Pt; they are used in this work to find the active surface area of Pt on the Au NRs. A cyclic voltammogram of polycrystalline Pt is looked at in detail in Appendix A.

1.10.1 Hydrogen adsorption method

During cyclic voltammetry of Pt on a working electrode surface in an acidic electrolyte, hydrogen from the electrolyte underpotentially deposits on the Pt surface during the negative sweep. To a first approximation, hydrogen deposits on all the active Pt sites present on the surface and forms a monolayer. The ratio of Pt: hydrogen is assumed to be 1:1. At the corresponding potentials on the anodic sweep, the hydrogen monolayer desorbs from the

monolayer surface. Figure 1.21 presents the hydrogen adsorption peaks (A) and the corresponding desorption peaks (B) of polycrystalline Pt in a 0.05 M H_2SO_4 electrolyte.

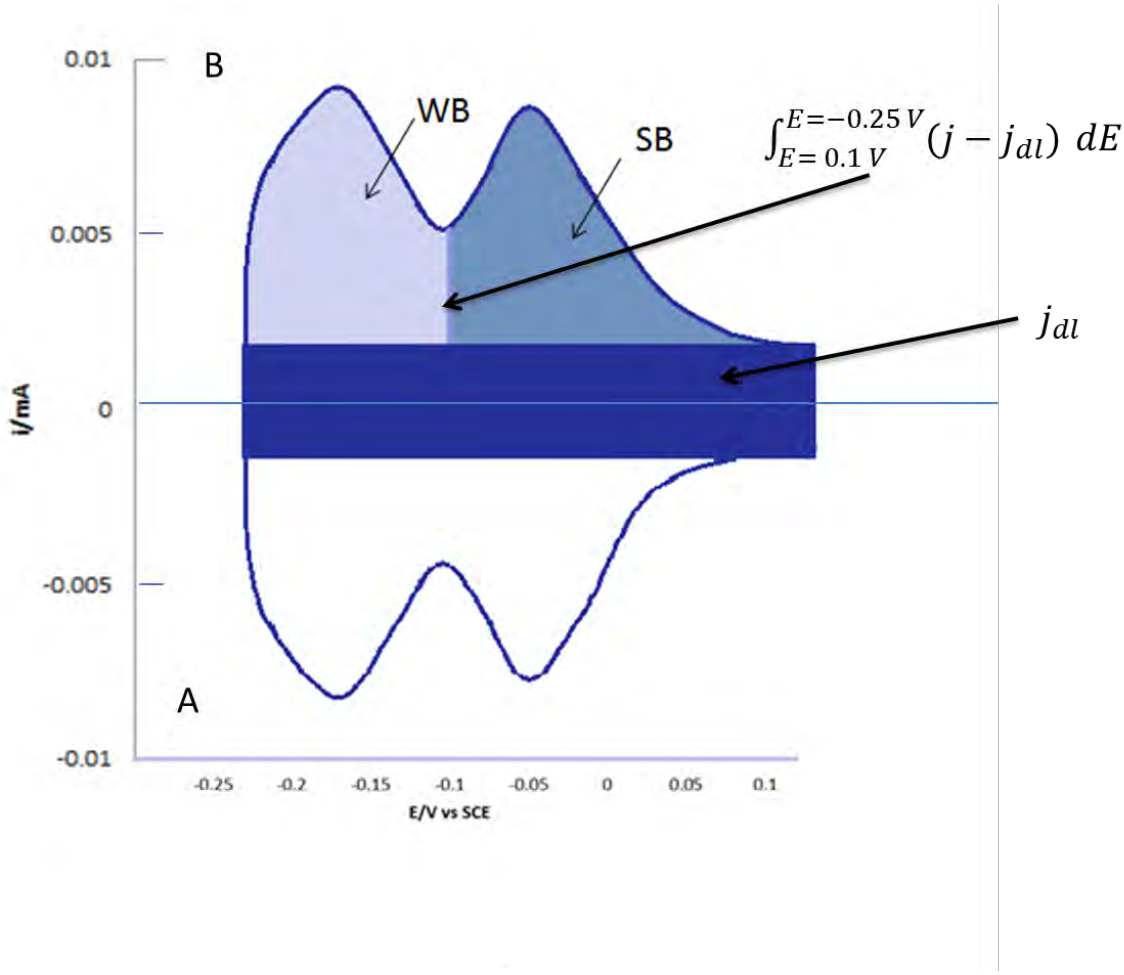

Figure 1.21 Cyclic voltammogram of a smooth polycrystalline Pt electrode in 0.05 M H_2SO_4 solution. A. represents the hydrogen adsorption region, B. the hydrogen desorption region. The dark blue rectangle is the estimated double-layer charge, used to correct the charge due to the hydrogen adsorption-desorption. The region shaded blue represents the strongly bonded (SB) hydrogen sites; the region shaded lighter blue represents the weakly bonded (WB) hydrogen sites. The principal method to integrate the electric charge of the hydrogen desorption is also shown.

Sweep rate 100 mV s^{-1}

In Figure 1.21 there are clearly two major peaks in the hydrogen desorption region. The peak at the more negative potential is caused by desorption of hydrogen from disordered (110) types of sites; this represents weakly bonded (WB) hydrogen on Pt. The peak at a more

positive potential is associated with hydrogen from disordered (100)-type sites and represents strongly bonded (SB) hydrogen on Pt. Both peaks contain mixed contributions from (111)-type sites. The general position and shape of the hydrogen adsorption and desorption peaks is attributed to a family of energetically similar sites.[134 135]

The hydrogen adsorption method determines the amount of charge to remove the adsorbed full hydrogen monolayer on the Pt surface of the electrode. The amount of charge required to remove one hydrogen atom is 1 electron or 1.602×10^{-19}C. It is important to consider the charge related to the charging of the double layer. This is represented by the dark blue area in Figure 1.21. It is small for pure electrodes, but higher for carbon-dispersed electrodes.

The integration of the hydrogen desorption region in Figure 5 can be carried out according to Equation (12):

$$Q_H = \frac{1}{v}\int_{E=0.1}^{E=-0.25}(j - j_{dl})\ dE \qquad (12)$$

Here v is the voltammetric sweep rate, j is the electric current, j_{dl} is the current caused by double layer charging and dE is the change in potential.[133]

The amount of electric charge to remove a monolayer of adsorbed hydrogen on Pt is considered to be 209 μC cm^{-2}, which is the amount of charge for a monolayer of hydrogen on the unreconstructed Pt (100) surface.[136] This surface is used as a standard because of the small amount of step sites, and because the reversible peak for the hydrogen adsorption-desorption is far from the onset of hydrogen evolution. The calculated charge of the hydrogen desorption region divided by this number gives the active surface area of Pt.

1.10.2 CO stripping voltammetry

A monolayer of CO can be deposited onto all the Pt sites of an electrode when the electrode is immersed in a CO-saturated electrolyte solution and held at a suitable potential for a monolayer of CO to form on the surface. This CO layer is subsequently anodically removed from the Pt surface in an argon-saturated solution with no CO present. A cyclic voltammogram of the anodic removal of a CO monolayer on a polycrystalline Pt surface in Ar-saturated H_2SO_4 solution is shown in Figure 1.22. This is known as a CO-stripping voltammogram.

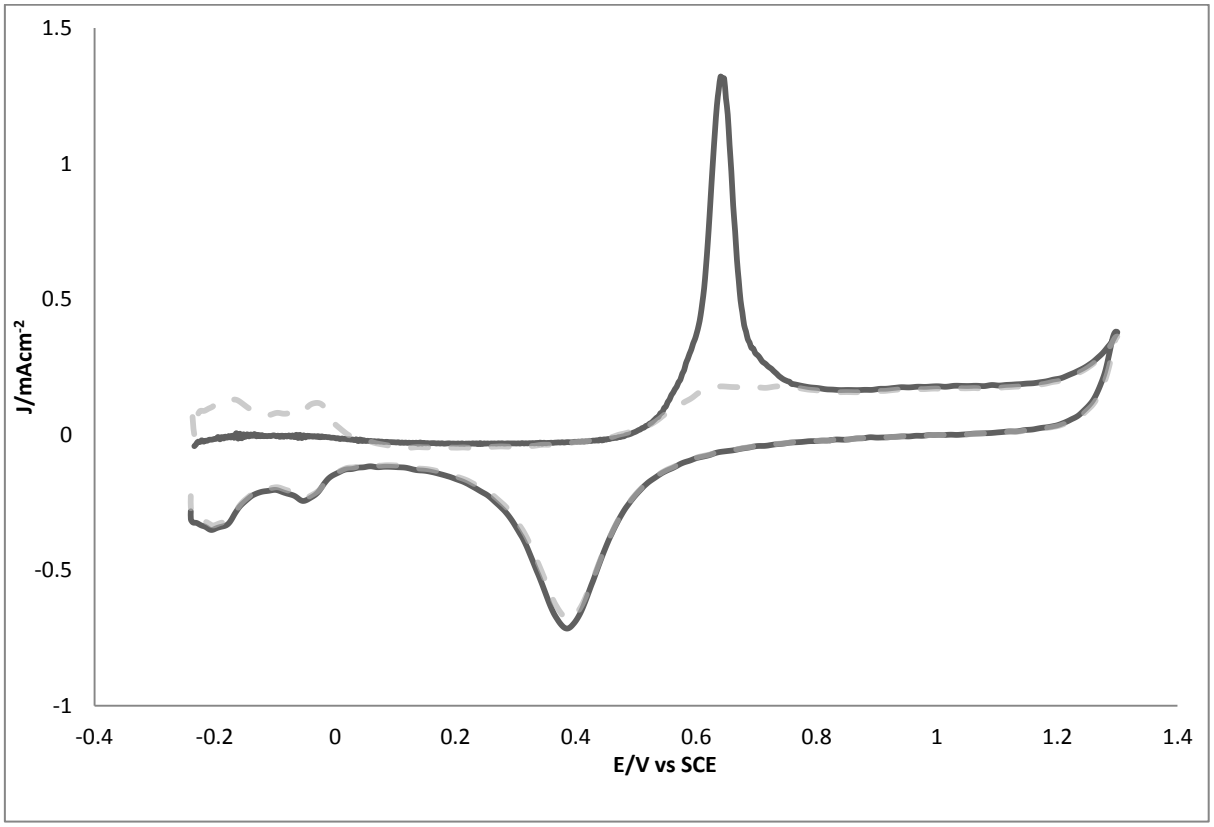

Figure 1.22 Cyclic voltammogram of oxidative desorption of CO on polycrystalline Pt in Ar saturated 0.05 M H_2SO_4 (solid line). Dashed line of polycrystalline Pt after CO removal.

Sweep rate 100 mV s^{-1}

In Figure 1.22, there are no hydrogen desorption peaks present between -0.24 V and 0 V, which shows that CO blocks all the Pt sites and prevents hydrogen from being adsorbed. The oxidative removal of the CO monolayer is represented by the sharp peak on the anodic sweep beween 0.5 V and 0.75 V. The charge of the CO oxidation peak, as with the hydrogen desorption peaks, gives an estimate of the surface area of Pt. The active surface area of Pt can be calculated by integrating and thus finding the charge of the CO oxidation peak. The

charge to remove a monolayer if there is 100% coverage of CO on Pt on the surface (θ_{CO} = 1.0) is 537 μC cm^{-2} .[137] If θ_{CO} = 1.0, it is assumed that the CO molecule is on-top (or linearly) bonded to the Pt sites. However, studies using in situ IR spectroscopy have identified two types of CO bonding on a polycrystalline Pt electrode: on-top and bridge adsorption [138] The frequency of C-O stretching is higher for on-top bonded CO than bridge bonded CO. As the bridge bonded CO has π-back bonding to two Pt atoms rather than one Pt atom, the C=O bond of the bridge bonded CO is weaker than the C=O bond of the linear bonded CO. As an estimate, voltammetric determination of the amount of CO on polycrystalline Pt shows that the saturation layer of CO on Pt is 90 % of one monolayer.[139] The charge to remove a monolayer of CO would thus be 480 μC cm^{-2}.

1.11 The Mechanism of CO electrooxidation on Pt

An adsorbed CO atom (CO_{AD}) on a Pt surface is oxidatively removed by water molecules from the double layer. After electron and proton transfer steps, CO_2 is formed.[140] It has been proposed that during oxidative removal of CO, H_2O attacks the CO_{AD} directly.[141] However, as can be seen in Figure 1.22, the CO the onset of the electrooxidation is at a similar potential to the onset of Pt-OH formation. It is generally agreed that there is a correlation between the potential of OH_{ads} formation and the potential of CO_{ads} removal. [142 143] Therefore OH_{ad} is the oxidant. The overall reaction for the oxidative desorption of CO_{ad} is:

$$CO_{AD} + OH_{AD} \rightarrow CO_2 + H^+ + e^- \qquad (4)$$

This oxidative removal of CO_{AD} happens via the Langmuir-Hinshelwood mechanism.[144] The mechanism suggested in this section is adapted from a theoretical model proposed by Anderson et al.[145] Initially, there is an interaction between the carbon atom atom of CO_{AD} with the oxygen OH_{AD} on an adjacent site. The CO_{AD}, which is strongly bonded to the Pt surface, remains on its Pt site, while the OH_{AD} leaves its site to bond with the carbon on the CO, forming a formic acid-type Pt –COOH structure, via an intermediate where the oxygen is semi-bonded to the Pt it was adsorbed on and the carbon atom of the CO. A schematic representation of the step of this mechanism is shown in Figure 1.23.

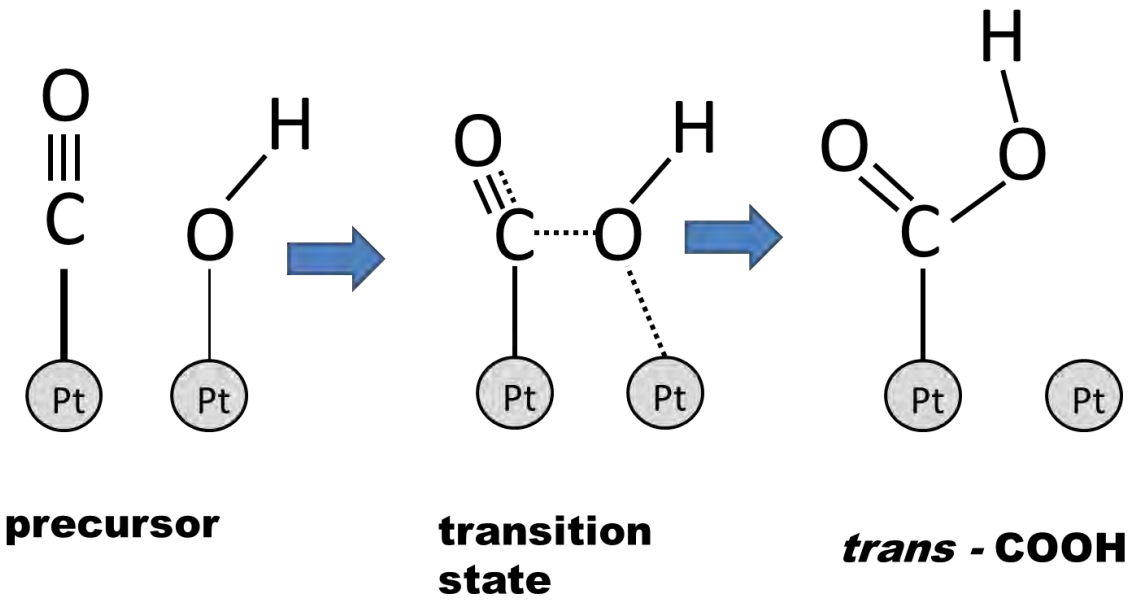

Figure 1.23 Schematic representation of the first step of electrooxidation of CO; the formation of the -COOH intermediate via interactions between CO_{AD} and adjacent OH_{AD} molecules.

Initially, the Pt-COOH is a *trans*- structure, because this is the most stable state of formic acid.[146] However, hydrogen bonding interactions of the hydrogen in COOH to the adjacent Pt atom means that when COOH is bonded to a Pt surface, *cis*-COOH is the more stable structure. The hydrogen therefore swings around from a *trans*- to *cis*- structure. A schematic representation of this process is shown in Figure 1.24.

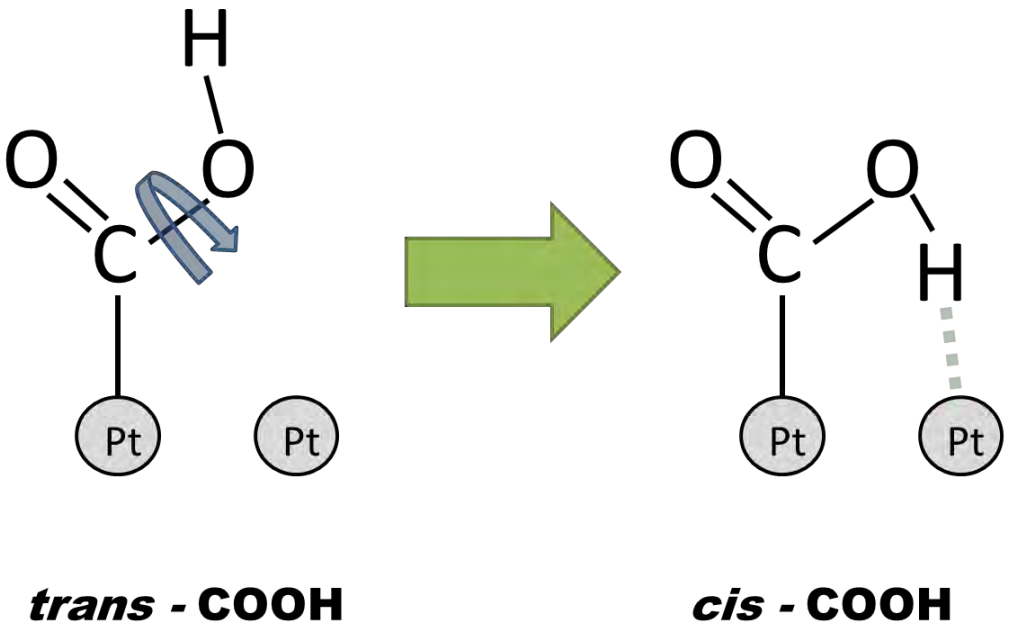

Figure 1.24 Diagram of the *trans*-COOH Pt intermediate interconverting to *cis*-COOH, owing to the hydrogen bonding interaction between the hydrogen in COOH and an adjacent Pt atom.

Cis-COOH becomes hydrogen-bonded to an adjacent OH, owing to the hydrogen-bonding interactions between the hydrogen of the COOH and the oxygen of the OH_{ADS}. This leads to the oxidative deprotonation of –COOH $_{ADS}$ because the hydrogen on the COOH forms a bond with the OH and causes the COO-H bonds to break. CO_2 is now formed, which desorbs from the Pt surface:

$$\text{-COOH}_{ADS} + OH_{ADS} \rightarrow CO_2 + H_2O_{ADS} \qquad (5)$$

A schematic of the intermediate species formed during the deprotonation of –COOH, followed by the desorption of CO_2 is presented in Figure 1.25.

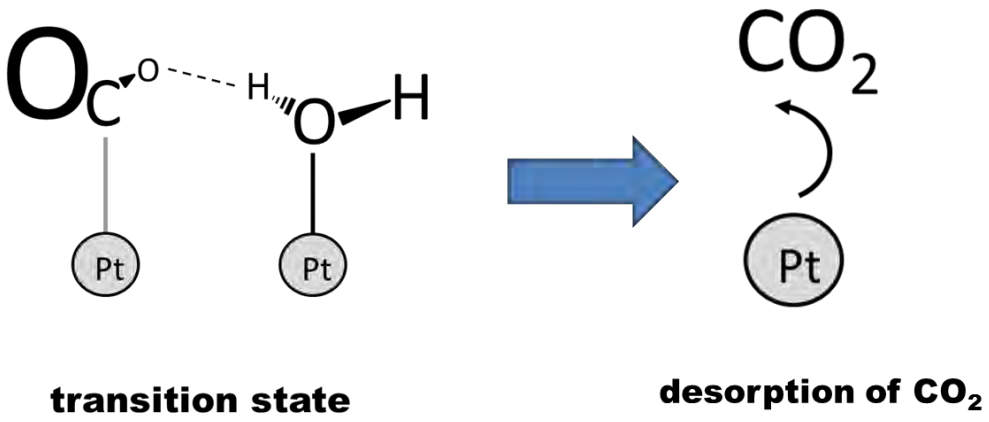

Figure 1.25 Schematic representation of the transition state of the deprotonation of COOH during electrooxidation of CO with Pt, which leads to desorption of CO_2. The transition state is caused by hydrogen bonding interactions between the hydrogen in –COOH and the oxygen in –OH.

If the Pt-COOH intermediate has the Au surface in close proximity, it would remain in a *trans* configuration. Hydrogen-Au interactions are considerably weaker than hydrogen-Pt interactions[133], therefore, it would be less likely that the H in the –COOH intermediate would flip round to form a *cis*-COOH configuration. Owing to its *trans* position, COOH is more likely to be deprotonated from H_2O from the double layer. An H_2O layer subsequently forms on the OH through hydrogen bonding interactions. A schematic of this step in the mechanism is represented in Figure 1.26.

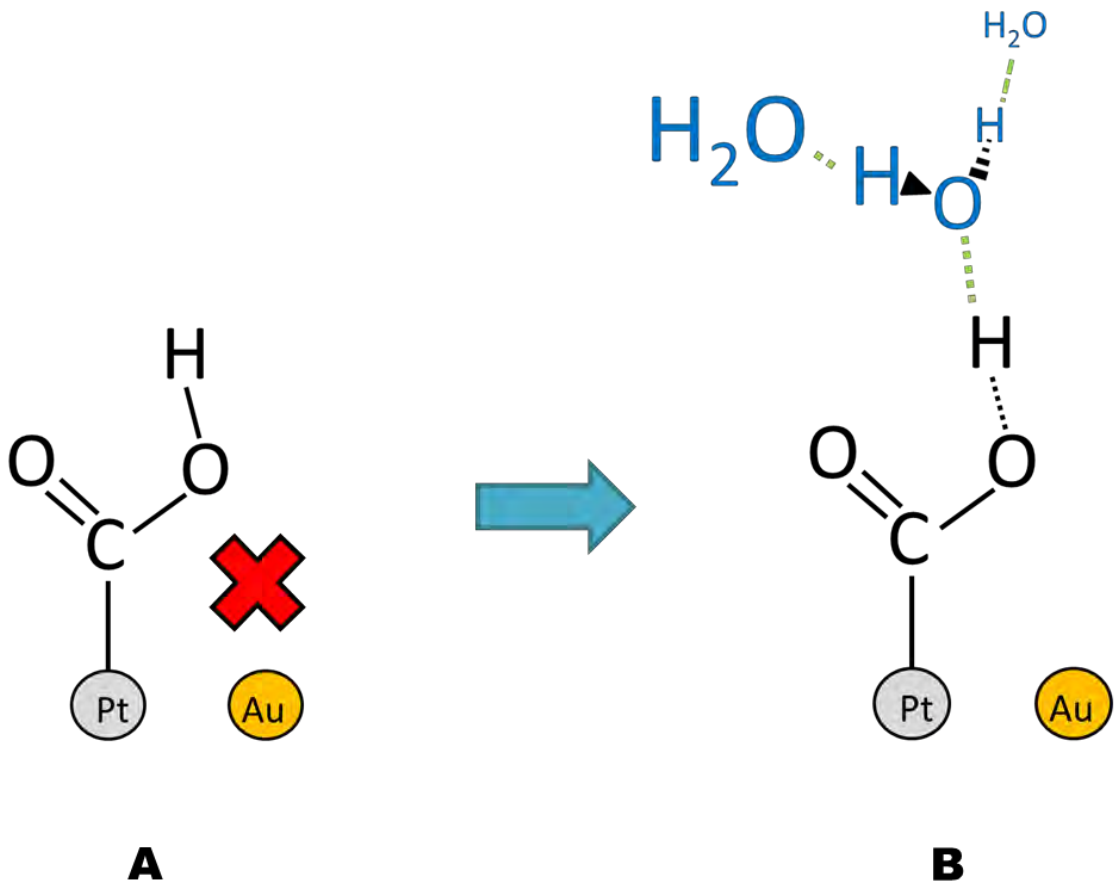

Figure 1.26 Schematic representation of Pt–COOH with an adjacent Au atom. **A** there is only a very small interaction between the COO-H and the adjacent Au atom, therefore Pt–COOH remains in a *trans*-configuration. **B** *trans*-Pt-COOH is deprotonated through the H_2O in the double layer, an H_2O layer can subsequently form on top of the –COOH intermediate, via hydrogen bonding interactions.

1.12 The oxygen reduction reaction

The oxygen reduction reaction (ORR) is a multi-electron process which involves several steps, where there are different reaction intermediates. A simplified version of the mechanism, proposed by Markovic et al., is given in Figure 1.27:[147]

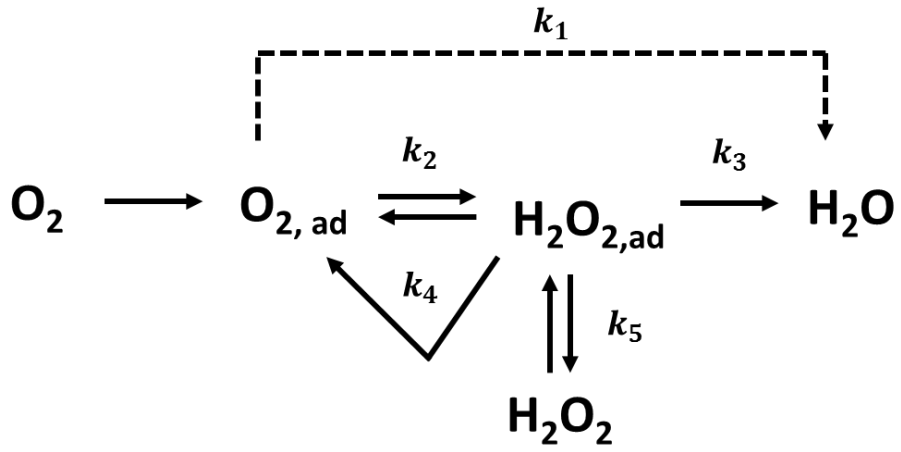

Figure 1.27. A simplified mechanism for the oxygen reduction reaction on Pt.

Adapted from Markovic et al. [147]

According to the reaction scheme, Figure 1.27, O_2 can be electrochemically reduced directly to H_2O. This reaction is referred to as the direct $4e^-$ reduction, and has the rate constant, k_1. O_2 can also be reduced to H_2O_2, with a rate constant is k_2; this reaction is referred to as the $2e^-$ series reduction. The $H_2O_{2\,AD}$ can be further reduced to H_2O; this is referred to as the $4e^-$ 'series' reduction; here the rate constant is k_3. $H_2O_{2\,AD}$ can also catalytically decompose back to $O_{2\,AD}$ with rate constant k_4 , or desorb into the bulk solution.

1.12.1 The direct 4 electron reduction

In order for it to reduce to H_2O via the direct $4e^-$ path, oxygen has to dissociate before the transfer of the first electron.[148] The mechanism for the direct 4 e^- reduction for this reaction path would be:

$$O_2 \rightarrow 2\bullet O_{ADS} \qquad (6.1)$$

$$2\bullet O_{ADS} + H^+ + 2e^- \rightarrow 2OH_{ADS} \qquad (6.2)$$

$$2OH_{ADS} + 2H^+ + 2e^- \rightarrow 2H_2O \qquad (6.3)$$

The dissociation energy of O_2 is very large (498.3 kJ mol^{-1}); it is energetically unfavourable unless there be a strong bond between the oxygen and the electrode surface.[149] However, metals forming very strong bonds with oxygen are said to have poor activity for the ORR because the ORR would stop at reaction (6.2) at the formation of OH_{AD}.[150] Pt is the only metal surface on which the direct $4e^-$ reduction is possible: it forms a bond with the oxygen strong enough for O_2 dissociation to occur, but not too strong, for it allows OH_{AD} further to be reduced to H_2O.

1.12.2 Indirect reduction of oxygen

The reduction of O_2 to H_2O via the peroxide intermediate is energetically more favourable because during this mechanism the first electron is transferred to the O_2 molecule before it dissociates. The bonding in oxygen is represented in Figure 1.28 using a molecular orbital (MO) diagram:

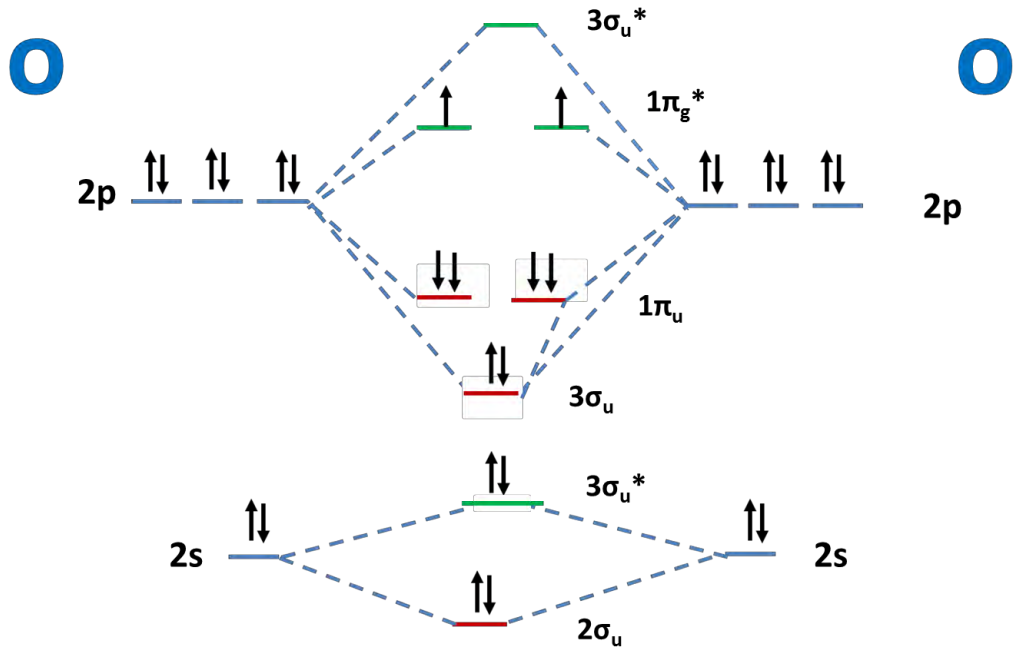

Figure 1.28 Molecular orbital diagram of the ground state of an O_2 molecule.

The MO diagram of O_2 in its ground state shown in Figure 1.28 shows that there are four more bonding than antibonding electrons. This explains the high stability and low reactivity of an O_2 molecule. However, there are two unpaired electrons on the doubly degenerate π^* antibonding orbital. Owing to these unpaired electrons, it possible to weaken the O-O bond.

If an extra electron is donated to the antibonding orbital of the oxygen during the ORR, the bond order of the O-O bond decreases form 2 to 1.5. This would increases the O-O bond length and the vibrational frequency. On its own, it has been said that O_2 has a dissociation of 494 kJ mol^{-1}. The dissociation energy of the O-O bond in H_2O_2, on the other hand, is less than a third of that of O_2, at 147 kJ mol^{-1}.[151]

The proposed mechanism for the reduction of O_2 to H_2O via an $H_2O_{2\ AD}$ intermediate is:

$$O_2 \rightarrow O_{2\ AD} \qquad (7.1)$$

$$O_{2\ AD} + e^- + H^+ \rightarrow HO_{2AD} \qquad (7.2)$$

$$HO_{2AD} + H^+ + e^- \rightarrow H_2O_{2\ AD} \qquad (7.3)$$

$$H_2O_{2\ AD} + e^- + H^+ \rightarrow H_2O + HO_{AD} \qquad (7.4)$$

$$OH_{AD} + H^+ + e^- \rightarrow H_2O \qquad (7.5)$$

It is unclear whether or not Pt reduces O_2 directly to H_2O_2 or via the $H_2O_{2\ AD}$ intermediate. It has been assumed in previous literature that all oxygen reductions proceed via the rate constant k_2, where a H_2O_2 intermediate is produced.[152] It is agreed that the rate-determining step (RDS) of the oxygen reduction reaction on all electrode surfaces, and through all mechanisms, is the transfer of the first electron to oxygen.[153]

1.12.3 The adsorption of O2 on a Pt surface

Figure 1.29 presents the ways in which O_2 has been proposed adsorb onto a metal surface. Here (a) is on-top end-on adsorption, where a single oxygen atom from the O_2 molecule is adsorbed onto a single Pt atom; (b) is bridge end-on adsorption where one oxygen atom is

adsorbed onto two or more Pt atoms; (c) shows on-top side-on adsorption and (d) shows hollow adsorption.

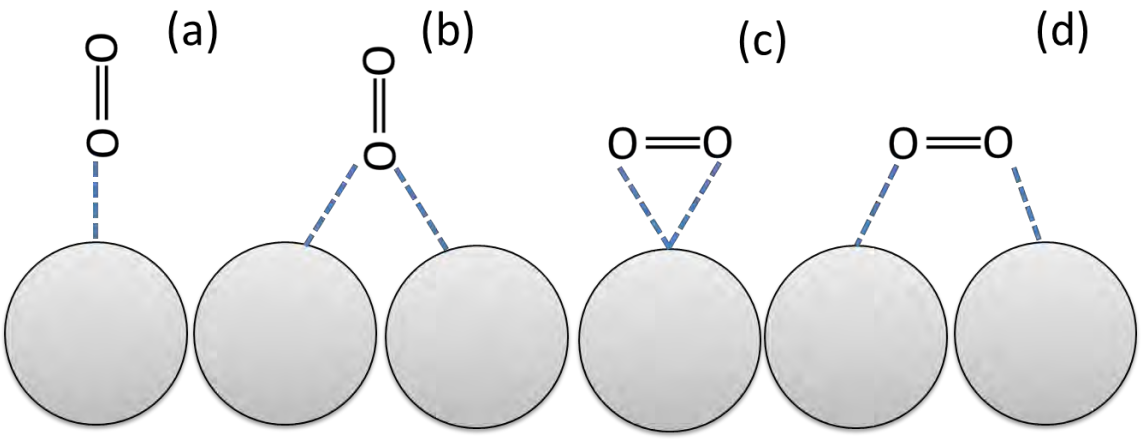

Figure 1.29 Adsorption of O_2 on Pt via the following configurations: (a) on-top end-on, (b) bridge end-on, (c) on-top side-on and (d) hollow

According to semi-empirical quantum calculations of O_2 adsorption on Pt (100) and Pt (111) by Zinola et al., the bridge adsorption on two or more Pt atoms (Figure 1.29B) is most stable on both the single-crystal surfaces.[154] The type of bonding on Pt is crucial to the rate of the ORR. The more stable the Pt-O interaction, the more readily the rate determining step occurs, and the more likely the oxygen will eventually reduce to H_2O. If there are ad-atoms such as surface oxides[155] or halides[156] on the Pt surface which block O_2 adsorption, the rate of O_2 reduction is significantly lower than it is on it is on a surface with no ad-atoms present. A reason for this lower activity is that stable bridge bonding involving an oxygen molecule being adsorbed on two or more Pt atoms is less likely to occur on a partially blocked Pt

surface. According to Markovic et al., the decrease in ORR activity on a Pt surface caused by ad-atoms is due to the loss of adsorption sites which break the O-O bond.[157]

Bridge end-on bonding, being the most stable adsorption for oxygen on Pt, could also indicate that the ORR on Pt proceeds via the H_2O_2 intermediate, rather than proceeding via a direct four-electron reduction. This is likely to be because direct four-electron reduction is more feasible if the oxygen is side-on or hollow-adsorbed. If an oxygen molecule were to dissociate before the transfer of the first electron, the oxygen-oxygen bond would have to be weakened by the interaction of the Pt surface with the π antibonding orbitals of O_2. This can occur via π back-bonding. When the O_2 molecule is side-on or hollow-adsorbed, more of the O_2 molecule is in contact with the Pt than if the O_2 molecule were end-on adsorbed. There would therefore be more interactions of the π anti-bonding orbitals with the Pt surface than there would be if the O_2 were side-on adsorbed. This means that there would be more of an orbital overlap.

1.12.4 The oxygen reduction reaction on other metal surfaces

According to electronic structure calculations by Nørskov et al., metals with either stronger or weaker bonding of oxygen than Pt are poorer catalysts for oxygen reduction.[158] Ni in these calculations, for example, is found to have such a strong bond to the O and OH intermediates that, during the ORR, the proton transfer steps become strongly activated, and therefore very slow. For an Au surface, on the other hand, the proton transfer is described as an exothermic process and should thus be a fast process. However, owing to

the weak bond of oxygen on the Au surface, oxygen adsorbed on an Au surface is said to be considerably less stable than O_2 in the gas phase. Therefore the transfer of protons and electrons to oxygen from an Au surface would happen less easily than it would to oxygen from a Pt surface. The weak binding of oxygen on an Au surface would indicate that the barrier for oxygen dissociation is large because it has been shown that there is a linear dependence between oxygen binding energy and the barrier for oxygen dissociation.[159]

On metal surfaces where the interactions with O_2 are weaker or stronger than they are with Pt, O_2 is reduced with fewer than four electrons. On surfaces that have weak interactions with O_2 and a high barrier for O_2 dissociation, such as Au, O_2 is reduced with one or two electrons, through a reaction mechanism where O_2 dissociation does not occur. For a one-electron reduction, the ORR would stop at reaction (7.2), with the formation of $HO_{2\ AD}$. Subsequently, a radical dissimulation reaction occurs where O_2 and H_2O_2 are formed from adjacent OH_2 molecules:[160]

$$2HO_2 \rightarrow O_2 + H_2O_2 \qquad (8)$$

The driving force of this reaction is the stability of the O_2 molecule.

If two electrons are transferred, the reaction stops at reaction (7.3). The adsorbed peroxide is desorbed back into the electrolyte solution. The $2e^-$ mechanism is common for electrode surfaces such as Au.[40] For a hydrogen fuel cell, the $2e^-$ reduction is unfavourable because the H_2O_2 is corrosive and hence damaging to fuel cell parts. The $2e^-$ reduction of oxygen is used in the manufacture of H_2O_2.

For metals forming a bond with the O_2 stronger than it is with Pt, the intermediates would be more stable than they are on Pt. Thus when O_2 adsorbs on these surfaces, the full $4e^-$ reduction is less likely to occur. The ORR on these surfaces is said to be desorption rate-limiting.[161]

[1] Durr, N.J. Larson, T., Smith, D.K., Korgel, B.A., Sokolov, K. and Ben-Yakar, A. (2007), *Nano Lett*, 7 (4), p. 94.
[2] Chen, C.C., Lin, Y.P., Wang, C.W., Tzeng, H.C., Wu, C.H., Chen, Y.C., Chen, C.P., Chen, L.C. and Wu, Y.C. (2006), *J Am Chem Soc*, 128, p. 3709.
[3] Huang, X., El-Sayed, I.H., Qian, W. and El-Sayed, M.A. (2006), *J Am Chem Soc*, 128, p. 2115
[4] Norman,R.S., Stone, J.W.;Gole,A.;Murphy,C. J.; Sabo-Attwood, T. L. Nano Lett. 2008, 8, p. 302.
[5] Grzelczak, M., Pérez-Juste, J., Rodriguez-Gonzalez, B. and Liz-Marzán, L.M. (2006), *J Mater Chem*, 16, p. 3946.
[6] Hernandez-Fernandez, P., Rojax, S., Ocon, P., de Frutos, A., Figueroa, J.M., Terreros, P., Pena, M.A, Fierro, J.L.G. (2009), *J P Sources* 177 p. 9.
[7] Liu, C-W., Wei, Y-C., Wang, K-W (2009), *J Col Inter Sci* 336 p. 654.
[8] Yiu, M., Huang, Y., Liang, L., Liao, J., Liu, C., Xing, W. (2011), *Chem Commun* 47, p. 8172.
[9] Choi, J-H., Park, K-W., Park, I-S., Kim, K, Lee, J-S., Sung, Y-E. (2006), *J Electrochem Soc* 153 (10), p. A1812.
[10] Feng, L., Wu, X., Ren, L., Xing, Y., He, W., Zhang, K., Zhong, W., Xie, S (2008), *Chem Eur J* 14 p. 9764.
[11] Sparnaay, M. (1972), *Characterization and Modeling of the Ionomer-Conductor Interface in Ionic Polymer Transducers*, Vol. 4, 1st Edition, Sydney: Pergamon Press (Australia), Pty. Ltd.
[12] Helmholtz, H. (1853), *Pogg Ann*, LXXXIX, p. 211.
[13] Helmholtz, H. (1879), *Weidemann Annalen der Physik u Chemie*, 3rd Ser., 7, p. 337.
[14] Bard, A.J and Faulkner, L.R. (2001), *Electrochemical Methods: Fundamentals and Applications*, New York: John Wiley & Sons, Inc.
[15] Gouy, G. (1913), *J Phys*, 4, 9, p. 457 (1910),; Chapman, D.L. *Phil Mag*, 6, 25, p. 475.
[16] Kitahara A. and Watanabe, A. (1984), *Electrical phenomena at interfaces: fundamentals, measurements, and applications*, Vol. 15, New York: M. Dekker.
[17] Stern, O. (1924), *Z Electrochem*, 30, p. 508.
[18] Grahame, D.C. (1947), *Chem Rev*, 41 (3), p. 441.
[19] Bockris, J., Devanathan, M. and Müller, K. (1963), *Proc R Soc London A*, Vol. 274, p. 55.
[20] Gerischer, H., Kolb D.M. and Sass, J.K. (1978), *Adv Physics*, 27, p. 437.
[21] Kolb, D.M. (1996), *Progress in Surface Science*, Vol. 51, N° 2, p. 109.
[22] Thiel, P.A. and Madey, T.E. (1987), *Surf Sci Rep,* 7, p. 211.
[23] Gordon, J.G., Melroy, O.R. and Toney, M.F. (1995), *Electrochim Acta*, 40, p. 3.
[24] Guidelli, R. and Schmickler, W. (2000), *Electrochim Acta,* 45, p. 2317.
[25] Wang, J., Ocko, M., Davenport, A.J. and Isaacs, H.S. (1992), *Phys Rev B,* Vol. 46, p. 16.
[26] Hamelin, A. (1982), *J. Electroanal Chem*, 142, p. 299.
[27] Bellier J.P. and Hamelin, A. (1975), *C R Acad Sci Ser*, C 280, p. 1489.
[28] Kolb D.M. and Schneider, J. (1986), *Electrochim Acta*, 31, p. 929.
[29] Tao N.J. and Lindsay, S.M. (1991), *J Appl Phys*, 170, p. 143.
[30] Gao, X., Hamelin, A. and Weaver, M.J. (1991), *J Chem Phys*, 95, p. 6993.
[31] Friedrich, A., Pettinger, B., Kolb, D.M., Lupke, G., Steinhoff, R. and Marowsky, G. (1989), *Chem Phys Lett*, 163, p. 123.
[32] Lupke, G., Marowsky, G., Steinhoff, R., Friedrich, A., Pettinger, B. and Kolb, D.M. (1991), *Phys Rev* B41, p. 6913.
[33] Perdereau, J., Biberian, J.P. and Rhead, G.E. (1974), *J Phys*, F4, p. 1978.
[34] Yamazaki, K., Takayamagi, K., Tanishiro, Y. and Yagi, K. (1988), *Surf Sci*, 199, p. 595.
[35] Harten, U., Lahee, A.M., Peter Toennies, J. and Wöll, Ch. (1985), *Phys Rev Lett* 54, p. 2619.
[36] Huang, K.G., Gibbs, D., Zehner, D.M., Sandy, A.R. and Mochrie, S.G.J. (1990), *Phys Rev Lett*, 65, p.3317.

[37] Barth, J.V., Brune, H., Ertl, G. and Behm, R.J. (1990), *Phys Rev*, B 42, p. 9307.
[38] Heine, V. and Marks, L.D. (1986), *Surf Sci*, 165, p. 65.
[39] Smoluchowski, R. (1941), *Phys Rev*, 60, p. 661.
[40] Kolb, D.M. and Schneider, J. (1985), *Surf Sci*, 162, p. 764.
[41] Fedak, D.G. and Gjostein, N.A. (1967), *Surf Sci*, 8, p. 77.
[42] Van Hove, M.A., Koestner, R.J., Stair, P.C., Biberian, J.P., Kesmodel, L.L., Battos I. and Somorjai, G.A. (1981), *Surf Sci*, 103, p. 189.
[43] Binnig, G., Rohrer, H., Gerber, Ch. and Stoll, E. (1984), *Surf Sci*, 144, p. 321.
[44] Kolb, D.M. (1996), *Prog Surf Sci*, Vol. 51, N^{o} 2, p. 109.
[45] Nichols, R.J., Magnussen, O.M., Hotlos, J., Tomey, T., Behm R.J. and Kolb D.M. (1990), *J Electroanal Chem*, 21, p. 290.
[46] Kolb, D.M. and Schneider, J. (1986), *Electrochim Acta*, 31, p. 929.
[47] Skoluda, P. and Kolb, D.M. (1992), *Surf Sci*, 260, p. 229.
[48] Kolb D.M. and Schneider, J. (1985), *Surf Sci*, 162, p. 764.
[49] Hosler, W., Ritter, E. and Behm, R.J. (1986), *Ber Bunsenges Phys Chem*, 90, p. 205.
[50] Nichols, R.J., Magnussen, O.M., Hotlos, J., Twomey, T., Behm R.J. and Kolb, D.M. (1990), *J Electroanal Chem*, 290, p. 21.
[51] Goetting, L.B., Huang, B.M., Lister, T.E. and Stickney, J.L. (1995), *Electrochim Acta*, 40, p. 143.
[52] Holzle, M.H., Wandlowski, Th. and Kolb, D.M. (1995), *J Electroanal Chem*, 394, p. 271.
[53] Magnussen, O.M., Hotlos, J., Beitel, G., Kolb, D.M. and Behm, R.J. (1991), *J Vat Sci Technol*, B9, p.969.
[54] Magnussen, O.M., Ocko, B.M., Adzic, R.R. and Wang, J.X. (1995), *Phys Rev*, B51, p. 5510
[55] Valette, G., Hamelin, A. and Parsons, R. (1978), *Z Phys Chem N F*, 113, p. 71.
[56] Habib, M.A. (1980), in: *Comprehensive Treatise of Electrochemistry*, Bockris, J. O'M., Conway, B.E. and Yeager, E., (eds.), New York: Plenum Press, Vol. 1
[57] Ignaczak, A. and Gomes, J.A.N.F. (1997), *J Electroanal Chem*, 420, p. 71.
[58] Koper, M.T.M. and van Santen, R.A. (1999), *Surf Sci*, 422, p. 118.
[59] Lorenz, W.J. and Salié, G.Z. (1963), *Phys Chem*, 218, p. 259.
[60] Schmickler, W. (1996), *Interfacial Electrochemistry*, New York-Oxford: Oxford University Press.
[61] Magnussen, O.M. (2002), *Chem Rev*, 102, p. 679.
[62] Abraham, F.F. (1981), *Phys Rep*, 80, p. 339.
[63] Bak, P. and Paczuski, M. (1994), in: *The Chemical Physics of Solid Surfaces*, King, D.A. and Woodruff, D.P. (eds.), Amsterdam-London-New York-Tokyo: Elsevier.
[64] Frenkel, Y.I. and Kontorowa, T. (1938), *Zh Eksp Teor Fiz*, 8, p. 1340.
[65] Frank, F.C., van der Merwe, J.H. (1949), *Proc R Soc Lond*, 198, p. 205.
[66] Magnussen, O.M., Ocko, B.M., Adzic, R.R. and Wang, J. (1995), *Phys Rev B*, 51, p. 5510.
[67] Yamada, T., Ogaki, K., Okubo, S. and Itaya, K. (1996), *Surf Sci*, 369, p. 321.
[68] Gao, X. and Weaver, M.J. (1992), *J Am Chem Soc*, 114, p. 8544.
[69] Ocko, B.M., Watson, G.M. and Wang, J. (1994), *J Phys Chem*, 98, p. 897.
[70] Batina, N., Yamada, T. and Itaya, K. (1995), *Langmuir*, 11, p. 4568.
[71] Yamada, T., Batina, N. and Itaya, K. (1995), *Surf Sci*, 335, p. 204.
[72] Ocko, B.M., Watson, G.M. and Wang, J. (1994), *J Phys Chem*, 98, p. 897.
[73] Tao, N.J. and Lindsay, S.M. (1992), *J Phys Chem*, 96, p. 5213.
[74] Magnussen, O.M., Wang, J.X., Adzic, R.R., Ocko, B.M. (1996), *J Phys Chem*, 100, p. 5500.
[75] Ocko, B.M., Wang, J.X. and Wandlowski, T. (1997), *Phys Rev Lett*, 79, p. 1511.
[76] Ocko, B.M. and Wandlowski, T. (1997), *Mater Res Soc Symp Proc*, 451, p. 55.
[77] Teshima, T., Ogaki, K. and Itaya, K. (1997), *J Phys Chem B*, 101, p. 2046.
[78] Gao, X., Edens, G.J., Liu, F.-C., Hamelin, A. and Weaver, M.J. (1994), *J Phys Chem*, 98, p. 8086.
[79] Ocko, B.M., Magnussen, O.M., Wang, J.X. and Wandlowski, T. (1996), *Phys Rev B*, 53, p. R7654.

[80] Cuesta, A. and Kolb, D.M. (2000), *Surf Sci*, 465, p. 310.
[81] Gao, X., Edens, G. J., Liu, F.-C., Hamelin, A., Weaver, M. J. (1994), *J.Phys. Chem.*, 98, p. 8086.
[82] Wandlowski, T., Wang, J.X., Magnussen, O.M. and Ocko, B.M. (1996), *J Phys Chem*, 100, p. 10277.
[83] Ocko, B.M., Magnussen, O.M., Wang, J.X. and Adzic, R.R. (1996), *Physica B*, 221, p. 238.
[84] Chen, M., Burgess, I. and Lipkowski, J. (2009), *Surface Science*, 603, p. 1891.
[85] Tanford, C. (1980), *The Hydrophobic Effect: Formation of Micelles and Biological Membranes*, 2nd Ed., New York: Wiley-Interscience.
[86] Romsted, L.S. (2005), *Adsorption and Aggregation of Surfactants in Solution*, New York: Marcel Dekker.
[87] Johnson, R.A. and Nagarajan (2000), *Colloids Surf*, A 167, p. 21.
[88] Gaudin, A.M. and Fuerstenau, D.W. (1955), *Trans A,* 202, p. 958.
[89] Manne, S. and Gaub, H.E., (1955), *Science*, 270, p. 1480.
[90] Lamont, R.E. and Ducker, W.A. (1998), *J Am Chem Soc*, 120, p. 7602.
[91] Ducker, W.A. and Wanless, E.J. (1999), *Langmuir*, 15, p. 160.
[92] Ducker, W.A. and Grant, L.M. (1996), *J Phys Chem*, 100, p. 11507.
[93] Wolgemuth, J.L., Workman, R.K. and Manne, S. (2000), *Langmuir*, 16, p. 3077.
[94] Manne, S. (1997), S. *Progr Colloid Polym Sci*, 103, p. 226.
[95] Burgess, I., Jeffrey, C.A., Cai, X., Szymanski, G., Galus, G. and Lipkowski, J. (1999), *Langmuir*, 15, p.2607.
[96] Schniepp, H.C., Shum, H.C., Saville, D.A. and Aksey, I.A. (2007), *J Phys Chem*, B111, p. 8708.
[97] Grant, L.M., Tiberg, F. and Ducker, W.A. (1998), *J Phys Chem*, B102, p. 42888.
[98] Burgess, I., Zamlynny, V., Szymanski, G., Lipkowski, J., Majewski, J., Smith, G., Satija, S. and Ivkov, R. (2001), *Langmuir*, 17, p. 3355.
[99] Xu, S., Chen, M., Cholewa, E., Szymanski, G. and Lipkowski, J. (2007), *Langmuir,* 23, p. 6937.
[100] Brosseau, C.L., Sheepwash, E., Burgess, I., Cholewa, E., Lipkowski, J. and Roscoe, S.G. (2007), *Langmuir,* 23, p. 1784
[101] Sek, S., Chen, M., Brosseau, C.L. and Lipkowski, J. (2007), *Langmuir,* 23, p. 12529.
[102] Jaschke, M., Butt, H.-J. and Gaub, H.E. (1997), *Langmuir*, 13, p. 1381.
[103] Foucompre, B. and Lindman, B. (1987), *J Phys Chem*, 91, p. 383.
[104] Uasaki, K. and Yamada, R. (1999), *J Am Chem Soc*, 121, p. 4090.
[105] Faraday, M. (1857), *Philos Trans*, 36, p. 147.
[106] Liu, Y., Male, K.B., Bouvrette, P. and Luong, J.H.T. (2003), *Chem Mater*, 15, p. 4180.
[107] Chen, D.-H. and Chen, C.-J. (2002), *Chem Mater*, 12, p. 1562.
[108] Velikov, K.P., Zegers, G.E. and van Blaaderen, A. (2003), *Langmuir*, 19, p. 1389.
[109] Yong, K.T., Swihart, M.T., Ding, H.P. and Prasad, N. (2009), *Plasmonics*, 4, p. 93.
[110] Zhao, X., Mai, Z., Kang, X., Dai, Z. and Zou, X. (2008), *Electrochim Acta*, 53, p. 4739.
[111] Ma, Z. and Han, H. (2008), *Colloids Surf A Physicochem Eng Asp*, 317, p. 233.
[112] Wang, W., Chen, X. and Efrima, S.J. (1999), *Phys Chem B*, 103, p. 7246.
[113] Jiang, X., Xie, Y., Lu, J., Zhu, L., He, W. and Qian, Y. (2001), *Langmuir*, 17, p. 3799.
[114] Neiman B., Grushka, E. and Lev, O. (2001), *Anal Chem*, 73, p. 5227.
[115] Zhu, J., Liu, S., Palchik, O., Koltypin, Y. and Gedanken, A. (2000), *Langmuir*, 16, p. 6399.
[116] Grabar, K.C., Freeman, R.G., Hommer, M.B. and Natan, M.J. (1995), *Anal Chem*, 67, p. 735.
[117] Nikoobakht, B. and El-Sayed, M. (2001), *Langmuir*, 17, p. 6368.
[118] Sau, T.K. and Murphy, C.J. (2005), *Langmuir*, 21, p. 2923.
[119] C. J. Murphy, L.B., Thompson, A.M., Alkilany, P., Sisco, N.S., Boulos, P., S.T. Sivapalan, Yang, J.A., Chernak, D.J. and Huang, J. (2010), *Phys Chem Lett*, 1, p. 2867.
[120] Wu, J.Y., Harwell, J.H. and Orear, E.A. (1987), *Langmuir*, 3, p. 531.
[121] Orendorff, C.J., Alam, T.M., Sasaki, D.Y., Bunker, B.C. and Voigt, J.A. (2009), *ACS Nano*, 3, p. 971.
[122] Sharma, V., Park, K. and Srinivasarao, M. (2009), *Mat Sci Eng*, R65, p. 1.

[123] Pérez-Juste, J., Liz-Marzán, L.M., Carnie, S., Chan, D.Y.C. and Mulvaney, P. (2004), *Adv Funct Mater*, 14, p. 571.
[124] Johnson, C.J., Dujardin, E., Davis. S.A., Murphy. C.J. and Mann, S. (2002), *J Mater Chem*, 12, p. 1765.
[125] Herrero, L.E., Buller, J. and Abruna, H.D. (2001), *Chem Rev*, 101, p. 1897.
[126] Hubert, F., Testard, F. and Spalla, O. (2008), *Langmuir*, 24, p. 9219.
[127] Liu, X.H., Luo, X.H., Lu, S.X., Zhang, J.C. and Cao, W.L. (2007), *J Colloid Interface Sci,* 307, p. 94.
[128] Liu, M. and Guyot-Sionnest, P. (2005), *J. Phys Chem*, 109, p. 22192.
[129] Papavassiliou, G.C., (1980), *Prog Solid State Chem*, 12, p. 185.
[130] Magnussen, O.M., Hotlos, J., Bettel, G., Kolb, D.M. and Behm, R.J. (1991), *J Vac Sci,* 9, p. 969.
[131] Brankovic, S.R., Wang, J.X. and Adzic, R.R. (2001), *Surf Sci*, 474, p. L173.
[132] Zhang, J., Lima, F.H.B., Shao, M.H., Sasaki, K., Wang, J.X., Hanson, J. and Adzic, R.R. (2005), *J Physl Chem B*, 109, p. 22701.
[133] Vielstich, W., Lamm, A., Gasteiger, H.A. (eds.), *Handbook of Fuel Cells*, Vol. 2, Chichester: John Wiley & Sons..
[134] Markovic, N.M., Marinkovic, N.S. and Adzic, R.R. (1991), *J Electrochem,* 314, p. 289.
[135] Grugur, B. and Ross, P. (1997), *J Phys Chem B*, 101, p. 5405.
[136] Clavilier, J., Rodes, A., El Achi, K. and K, Zamakhchari. (1991), *J Chim Phys*, 88, p. 1291.
[137] Orts, J.M., Fernandez-Vega, Feliu, A., J.M. Aldaz, A. and Clavilier, J. (1992), *J Electroanal Chem*, 327, p. 278.
[138] Iwasita T. and Nart, F.C. (1995), in: Gerischer, H. and Tobias, C.W. (eds.), *Advances in Electrochemical Science and Engineering*, Mannheim: VCH, Vol. 4
[139] Gasteiger, H.A., Markovic, N., Ross, Jr, P.N. and Cairns, E.J. (1994), *J Phys Chem*, 98, p. 617.
[140]Gilman, S. (1964), *J Phys Chem,* 68, p. 70.
[141] Wieckowski, A. (1977), *J Electroanal Chem,* 78, p. 229.
[142] Anderson, A.B. and Neshev, N.M. (2002), *J Electochem Soc* 149, 10, p. E388.
[143] Strmcnik, D.S., Tripkovic, D.V., van der Vliet, D., Chang, K.C., Komanicky, V., You, H., Karapetrov, G., Greeley, J.P., Stamenkovic, V.R. and Markovic, N.M. (2008), *J Am Chem Soc*, 130, p. 15339.
[144] Saravanan, Chandra, Markovic, N.M., Head-Gordon, M. and Ross, P.N. (2001), *J Chem Phys*, 114, p. 6404.
[145] Anderson, A.B. and Neshev, N. M. (2002), *J Electochem Soc*, 149 (10), p. E388.
[146] Pettersson, M., Lundell, J., Khriachtchev, L. and Rasanen, G.M. (1997), *J Am Chem Soc,* 119, p. 11715.
[147] Markovic, N.M. and Ross, P.N. (2002), *Surf Sci Rep*, 45, p. 229.
[148] Yeager, E., Razaq, M., Gervasio, D., Razaq A. and Tryk, D. (1992), 'Structural Effects in Electrocatalysis and Oxygen Electrochemistry' in: Scherson, D., Tryk, D., Daroux, M. and Xing, X. (eds.), *The Electrochemical Society*, New Jersey: Pennington.
[149] Ross Jr, P.N., (2003), 'Oxygen reduction reaction on smooth single-crystal electrodes', in: *Handbook of Fuel Cells*, Vol. 2, Vielstich, W., Lamm, A., Gasteiger, H.A. (eds.), Chichester: John Wiley & Sons.
[150] Appleby, A.J. (1970), *Catal Rev*, 4, p. 221.
[151] Zagal, , J.H. (1992), *Coord Chem Rev,* 119, p. 92.
[152] Grgur, B.N., Markovic, N.M. and Ross Jr, P.N. (1997), *Can J Chem*, 75, p. 1465.
[153] Ramaswamy, N. and Mukerjee, S. (2012), *Adv Phys Chem*, Vol. 2, Article ID 491604.
[154] Zinola, C.F., Arvia, A.J., Estia, G.L. and Castro, E.A. (1994), *J Phys Chem*, 98, p. 7576.
[155] Maillard, F., Martin, M., Gloaguen, F. and Leger, J.-M. (2002), *Electrochimica Acta*, 47, p. 3440.
[156] Gasteiger, H.A., Markovic, N.M. and Ross, P.N. (1996), *Langmuir,* 12, p. 1414.
[157] Markovic, N.M., Gasteiger, H.A. and Ross Jr, P.N. (1995), *J Phys Chem,* 99, p. 11.

[158] Nørskov, J.K., Rossmeisl, J., Logadottir, A., Lindqwist, L., Kitchin J.R. and Johsson, H. (2004), *J Phys Chem B,* 108, p. 17892.
[159] Nørskov, J.K., Bligaard, T., Logadottir, A., Bahn, S.R., Hansen, L.B., Bollinger, M.V., Bengaard, H.S., Hammer, B., Sljivancanin, Z., Mavrikakis, M., Xu, Y., Dahl, S. and Jacobsen, C.J.H. (2002), *J Catal*, 209, p. 275.
[160] Adzic, R.R., Strbac S. and Anastasijevic, N. (1989), *Mats Chem Phys*, 22, p. 375.
[161] Ross Jr, P.N. (2003), 'Oxygen reduction reaction on smooth single-crystal electrodes' in: Vielstich, W., Lamm, A., Gasteiger, H.A. (eds.), *Handbook of Fuel Cells*, Vol. 2, Chichester: John Wiley & Sons.

2. Experimental techniques

2.1 Cyclic voltammetry

Owing to the development in 1955 of the electronic potentiostat, cyclic voltammetry techniques (CV) can be applied to a 3-electrode cell.[1] A schematic diagram of a simplified potentiostatic circuit is shown in Figure 2.1.[2]

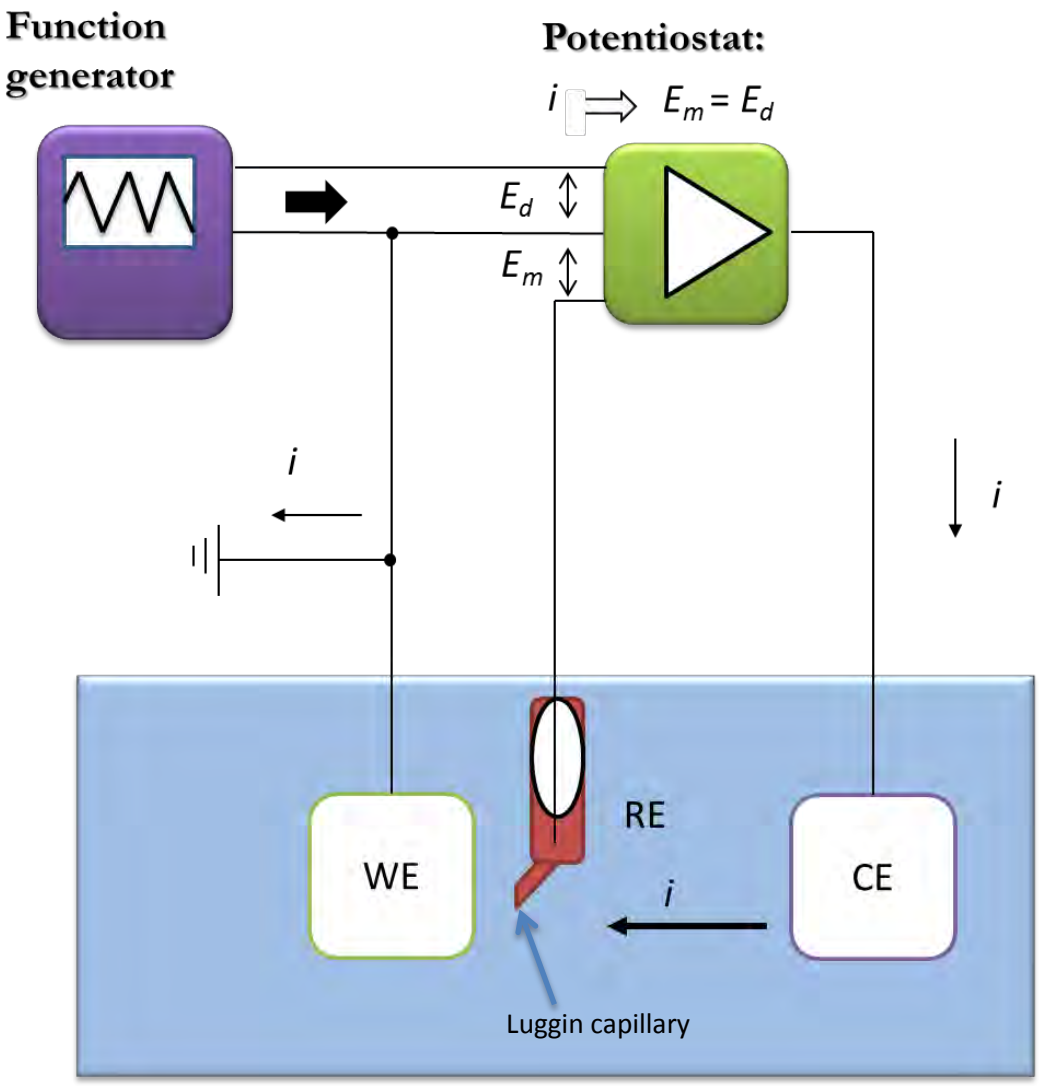

Figure 2.1: Basic potentiostatic circuit showing the working electrode (WE), counter-electrode (CE) and reference electrode (RE) of the electrochemical cell. E_d is the applied driving voltage; E_m the measured voltage. The potentiostat delivers a current equalising E_d and E_m.
Adapted from Vielstich [2]

The electrode potential is controlled by an applied potential difference, E_d, located between the Luggin capillary and the working electrode. A Luggin capillary is a small tube at the end of the reference electrode compartment; it defines a sensing point for the reference electrode near the working electrode.[3] In a potentiostatic circuit, the central electronic component is the comparator circuit. Its first function is to equalise the measured effective potential difference, E_m, between the working electrode, (WE), and the reference electrode, (RE), with the required voltage, E_d. E_d, which can be derived from a function generator. The comparator circuit's second function is to convert the current passing through the WE and the counter electrode, (CE), to a voltage signal, using a resistor, R. to enable the current to flow exclusively between the WE and CE electrodes, the RE connections must have a very high input impedance. The voltage drop over the resistor, R, and voltage, E_d, are plotted on an x/y recorder and stored digitally on a computer.

In CV, the potential is swept over a defined period to and from selected reversing points,[4] which are shown in Figure 2.2.

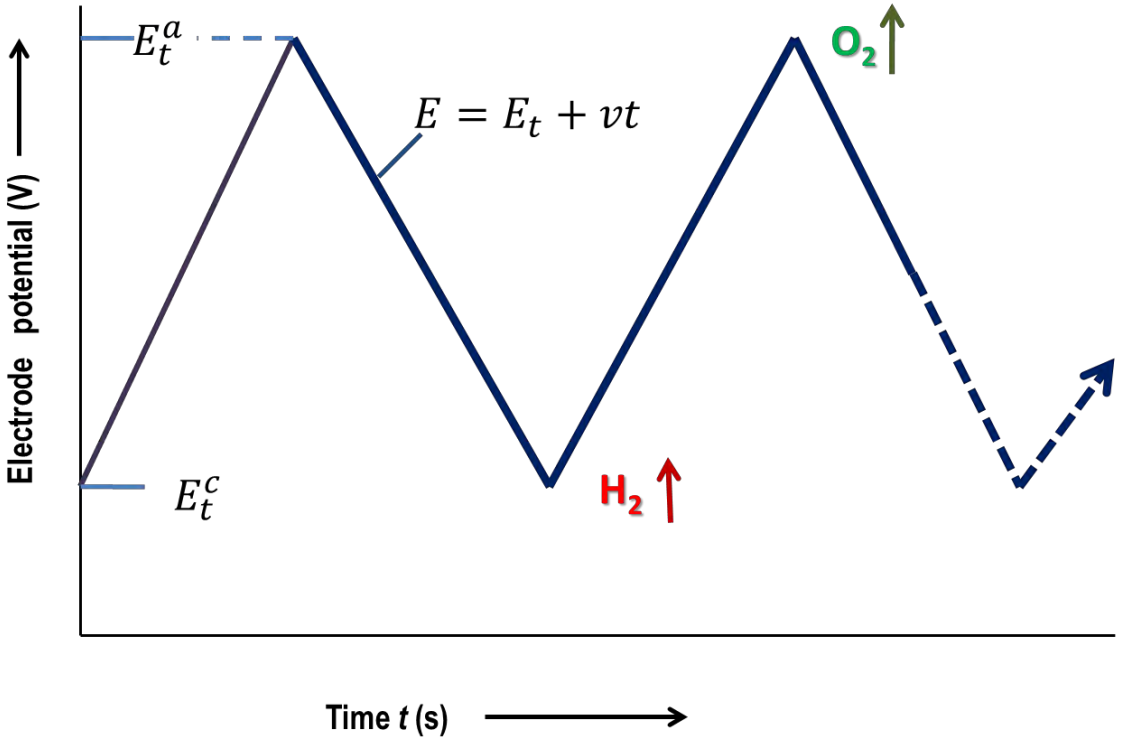

Figure 2.2: Change in electrode potential with time, going from the negative reversing point, hydrogen evolution, to the positive reversing point, oxygen evolution.
Adapted from Hamann et al [4]

Cyclic voltammetry allows the formation of highly reproducible surfaces for many metal surfaces, especially for gold and platinum. The desired sweep rates are generally between 20-500 mV s^{-1}; should they be below 5-10 mV s^{-1}, the surface is likely to be deactivated.[2] If a faster scan rate is used, it is possible to remove adsorbed impurities, possibly inhibiting the electrode process of interest either through electrochemical oxidation or reduction. This is an effective way of cleaning the working electrode surface.

CV is highly sensitive to what is present in the electrolyte solution. A CV for a working electrode in an electrolyte containing no active species produces current/potential relations characteristic of the electrode material used. Firstly, there is a contribution because of the

charging of the double layer. The double layer capacity is not a function of scan rate because equilibrium is reached quickly, despite its dependence on the potential. Secondly, charging a pseudo-capacitor of value C_p produces a larger contribution. Faradaic reactions cause some capacity effects, such as the formation and dissolution of hydride and oxide layers on the surface. Should this layer rapidly form or dissolve, the capacity, C_p, will scale with the sweep rate v (mV s^{-1}). Faradaic reactions also give rise to currents resulting from charge transfer (faradaic currents). The current response is a function of the kinetics of charge transfer and diffusion of reactive species to and from the surface. For fast kinetics, where Nersian equilibrium is maintained, the current in a potential sweep can be determined by the diffusion coupling within the fast charge transfer at the surface. The coupling makes the current peak, as the surface concentration of the reacting species falls with time, owing to the slow diffusion from the bulk solution. Although for the reactions with fast kinetics, the peak potential is independent of the sweep rate, the peak current increases linearly, albeit with the square root of the sweep rate. At increased sweep rates, the peaks become sharper. For a slow charge transfer coupled with linear diffusion, there is also a current maximum. However, the potential of the maximum is no longer independent of the scan rate. The potential peak shifts to positive values with increasing scan rate; and since the surface concentration changes at a slower rate, the maximum of the concentration gradient is reached at more positive potentials.

The active surface of metal electrocatalyst can be reproducibly prepared by cycling in base electrolyte solutions. Through CV, it is also possible to have an idea of the reactions taking place between the WE and the solution at given potentials.

2.2 Differential capacitance

Differential capacitance is used to characterise electrochemical interfaces. It can also be used to measure the excess charge at an electrode surface in the interface[5] and can give detailed information about microscopic properties of an electrode interface.[6]

The double-layer region in the metal-electrolyte interface can be described as a condenser of molecular dimensions, on one side of which is the metal surface, and on the other, a build-up of solvated electrolyte ions.[7] These ions are held in place by electrostatic forces and the position of these solvated electrolyte ions makes up the outer Helmoltz plane (OHP) (see Section 1.2). In the absence of a redox system in the DL region, no current passes through the interface. Owing to the small inter-plate distance, the radius of a solvated ion (around 3 Å), there is a high capacity of around 50 μF cm^{-2}, a value which changes with the applied potential.[8] The metal surface and potential dependent polarisability of the electron tail also contribute to the double-layer capacity.[9] Charging the double-layer results in high electric fields and large surface charges with excesses of up to 20-40 μ F cm^{-2}, corresponding to 0.1-0.2 electrons per surface atoms.[8]

The capacitance with specific adsorption on the electrode relates the charge on the metal surface, σ_M, to the applied potential, E, using Equation (2):

$$C = \frac{\partial \sigma_M}{\partial E} \qquad (2)$$

The charge on the metal surface can be expressed as a function of the Gibbs excess, Γ, and as a function of applied potential, E, according to Equation (3):

$$d\sigma_M = \left(\frac{\partial \sigma_M}{\partial \Gamma}\right)_E d\Gamma + \left(\frac{\partial \sigma_M}{\partial E}\right)_\Gamma dE \qquad (3)$$

According to Equation (2), Equation (3) can be differentiated with respect to *E* in order to obtain the capacitance of an electrode surface:

$$C = \left(\frac{\partial \sigma_M}{\partial \Gamma}\right)_E \frac{d\Gamma}{dE} + \left(\frac{\partial \sigma_M}{\partial E}\right)_\Gamma = C_{pseudo} + C_{true} \qquad (4)$$

Equation (4) shows the two contributions to the capacitance. The first is C_{true}, which is the true capacitance, the capacitance of an interface at constant adsorbate coverage. The second is C_{pseudo}, which is the pseudo capacitance, arising from changes in the phase state of the adsorbed molecule/ion layer. In a DC plot, an increase in pseudo-capacitance can be seen by an increase in the differential capacitance or a differential capacitance maximum.

A differential capacitance experiment uses phase selective alternating current (AC) voltammetry: a sinusoidal voltage at a fixed frequency is superimposed on the DC voltage of the cyclic voltammetry.[10 11] The in-phase and quadrature components of the resulting AC current are measured as functions of the DC voltage, and the measured parameters are converted to (potential dependent) differential capacitance.

A lock-in amplifier is used to measure the in- and out-phase of phase components of the AC current. Differential capacitance is calculated using the equation:

$$C = \frac{i_q}{E_{ac}\,\omega}\left[1 + \left(\frac{i_R}{i_Q}\right)^2\right] \qquad (5)$$

Here, C is the differential capacity, i_R is the real component of the current, i_Q is the quadrature (or imaginary) component of the measured current, E_{ac} is the root mean square AC voltage and ω is the angular frequency of the alternating current perturbation.[12]

2.3 Chronocoulometry

In 1834, Faraday proposed a fundamental law of electrolysis, according to which the amount of material deposited or evolved during electrolysis is directly proportional to the current and the time, i.e. the quantity of electricity passing through the solution.[13] This law is the basis of coulometry.

In chronocoulometry, the charge density of a working electrode can be determined at a given potential, E_i.[14] The potential-time profile of a chronocoulometry experiment is given in Figure 2.3.

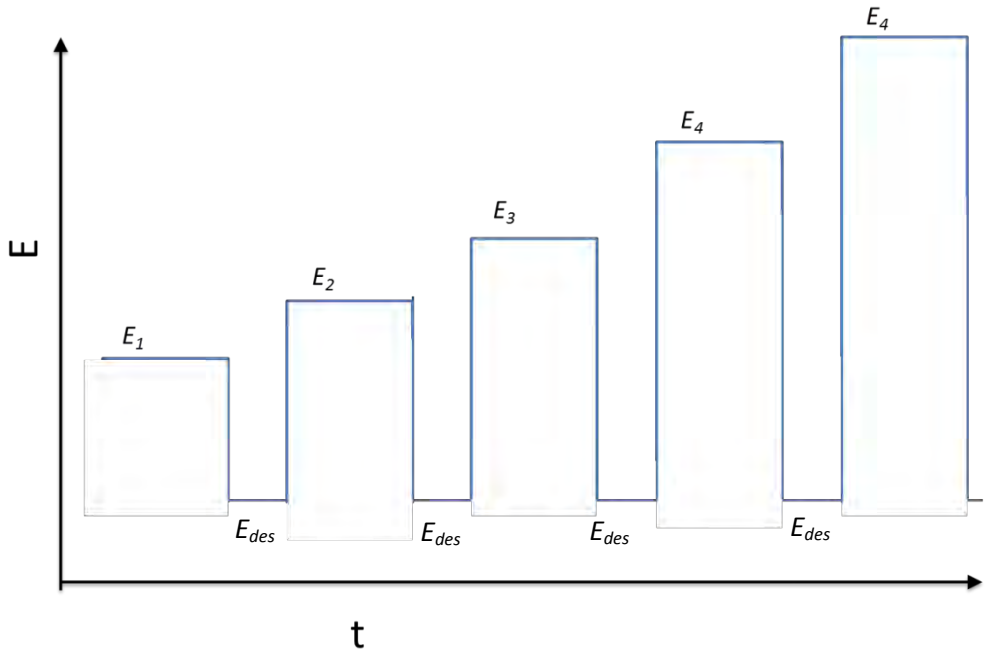

Figure 2.3 Potential-time profile for a chronocoulometry experiment

The potential is held at value, E_i, long enough to establish adsorption equilibrium. The potential is then stepped to E_{des}, the potential at which no molecules are present on the electrode surface. The double-layer charging currents are then recorded. The current-time transient at E_i is subsequently integrated digitally to give a charge-time transient; $\Delta\sigma_M$-t. $\Delta\sigma_M$ (E_i) is the relative charge density, which can be defined by the equation:

$$\Delta\sigma_M(E_i) = \sigma_M(E_i) - \sigma_M(E_{des}) \qquad (6)$$

Here, σ_M is the absolute charge density on the electrode surface. The measured charge density value $\Delta\sigma_M$ allows the absolute charge density σ_M to be calculated if the potential of zero charge (pzc) of the electrode is known (this is usually determined from a differential capacitance measurement of the electrode in a 5 mM NaF solution, where the diffuse layer

contributes most to the overall capacitance and a minimum in the capacitance can be observed at the pzc). From Equation (6), $\sigma_M(E_{des})$ can be determined according to the equation:[14]

$\Delta\sigma_M$ (pzc) = σ_M (pzc) - σ_M (E_{des}) = -σ_M (E_{des}) (7)

Once σ_M (E_{des}) is calculated, values of $\sigma_M(E_i)$ can be calculated over the whole potential range of the experiment from equation (6). This allows a charge vs. potential plot to be obtained for the working electrode in only the baseline electrolyte solution. Subsequently, charge vs. potential plots ($\Delta\sigma_M(E_i)\ vs.\ E_i$) are recorded for the working electrode in the baseline electrolyte solution containing molecules or ions whose adsorption on the electrode surface is studied at a measured concentration. Absolute charge density is calculated by equating σ_M (E_{des}) in the presence and absence of the molecules or ions under study (E_{des} is determined from differential capacity measurements: capacity should be equal in the presence and absence of molecules if molecules are desorbed). The surface pressure due to the adsorption of the molecules or ions in the electrolyte on the working electrode interface is calculated by integrating the charge density versus the electrode potential plots, according to the equation:

$$\pi = \gamma_0 - \gamma = \left(\int_{E_{des}}^{E} \sigma_M\, dE\right)_{[molecules/ions]} - \left(\int_{E_{des}}^{E} \sigma_M\, dE\right)_{[molecules/ions]=0} \quad (8)$$

Here, γ_0 and γ represent the specific surface energy of the molecule/ion-free surface and the molecule/ion-covered electrode, respectively. This equation is derived by integrating the Lippmann equation.[15] By differentiating the polynomial fit from a plot of the surface

pressure versus the natural logarithm of the bulk molecule/ion concentration at a constant *E*, the relative Gibbs surface excess, Γ, can be determined. Thus:

$$\Gamma = \left(\frac{\partial \pi}{RT\ \partial \ln c_{Cl^-}}\right) \qquad (9)$$

2.4 Electrode kinetics

In the electrochemical reaction

$$O\ (aq) + e^-\ (m) \rightleftharpoons R\ (aq) \qquad (1)$$

two chemical species are interconverted by a single electron transfer reaction. When the applied potential (*E*) is equal to the equilibrium potential, (E_e), no current will flow through the cell. For any other value of *E*, however, Electrode Reaction (1) will no longer be at equilibrium with the electrode potential. Whether or not any current flows depends on the kinetics of the particular reaction under investigation. The deviation of *E* from the equilibrium is called the overpotential, η, where:

$$\eta = E - E_e \qquad (10)$$

The Butler-Volmer equation is fundamental to electrode Kinetics.[16] It is given in Equation (11):

$$i = i_0 \left(\exp\left\{\frac{(1-a)Fn}{RT}\right\} - \exp\left\{\frac{-aFn}{RT}\right\}\right) \qquad (11)$$

The oxidative process is highlighted in red; the reductive process, in green. i is the net current flowing at the working electrode, i_0 is the exchange current density, *F* is the Faraday

constant and R is the gas constant. α is the symmetry factor (or transfer coefficient). The value of α ($0< \alpha <1$) reflects the sensitivity of the transition state of an electrochemical reaction to the drop in electrochemical potential between the metal and the solution. If α is close to zero, the transition state is similar to that of the reactant. When α is close to 1, the transition state behaves in a product-like manner; when α is 0.5, the transition state behaves as a combination of both reactants and products.[17]

The Butler-Volmer equation predicts how the net current varies as a function of the overpotential, the exchange current density and the symmetry factor α. Figure 2.4 shows the variation in current as a function of overpotential according to the Butler Volmer equation for two extreme cases, (a) and (b).

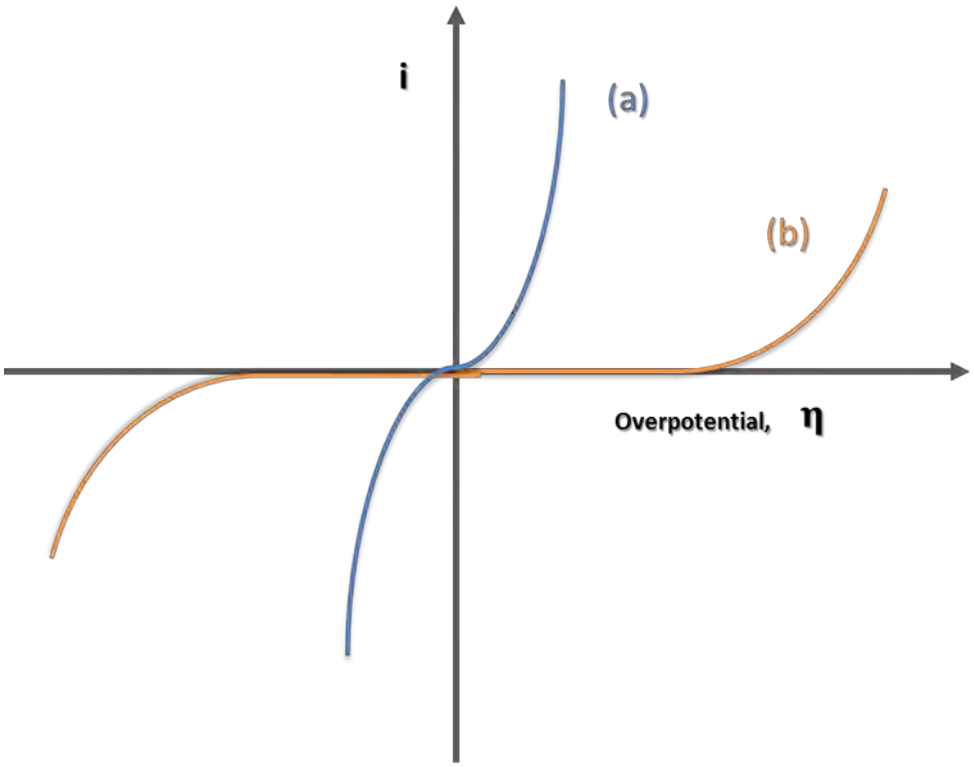

Figure 2.4 The variation of current as a function of overpotential according to the Butler Volmer equation for (a) a reversible, and (b) an irreversible electrode reaction.

Adapted from Bard and Faulkner [16]

Case (a) corresponds to a reversible electrode reaction with a large exchange current density, i_0; Case (b) corresponds to an irreversible electrode reaction, whose exchange current density, i_0, is low. Figure 4 shows that for both Cases (a) and (b), no current flows when the overpotential is η= 0. However, when small overpotentials are applied, both cases act very differently.

For Reversible Reaction (a), extremely little applied overpotential is needed to drive the reaction and the current can readily flow in the cathodic or anodic directions. For the

Irreversible Reaction (b), on the other hand, a high overpotential is required to induce current flow. Figure 4 shows that if the overpotential is increased to a value that drives the anodic oxidative process, the reductive component becomes negligible. In this case, the Butler-Volmer equation simplifies to:

$$\ln i = \ln i_0 + \frac{(1-a)F}{RT}\,\eta \qquad (12)$$

Likewise, at overpotentials where the cathodic reductive process is driven, negligible oxidation current flows:

$$\ln(-i) = \ln i_0 - \frac{aF}{RT}\,\eta \qquad (13)$$

The symmetry factor, a, and the exchange current density, i_0, can be calculated for the irreversible electrode reactions using Equations (12) and (13) by plotting $\ln i$ against η. This is known as Tafel analysis. Examples of Tafel Plots for oxidative and reductive reactions are given in Figure 2.5.

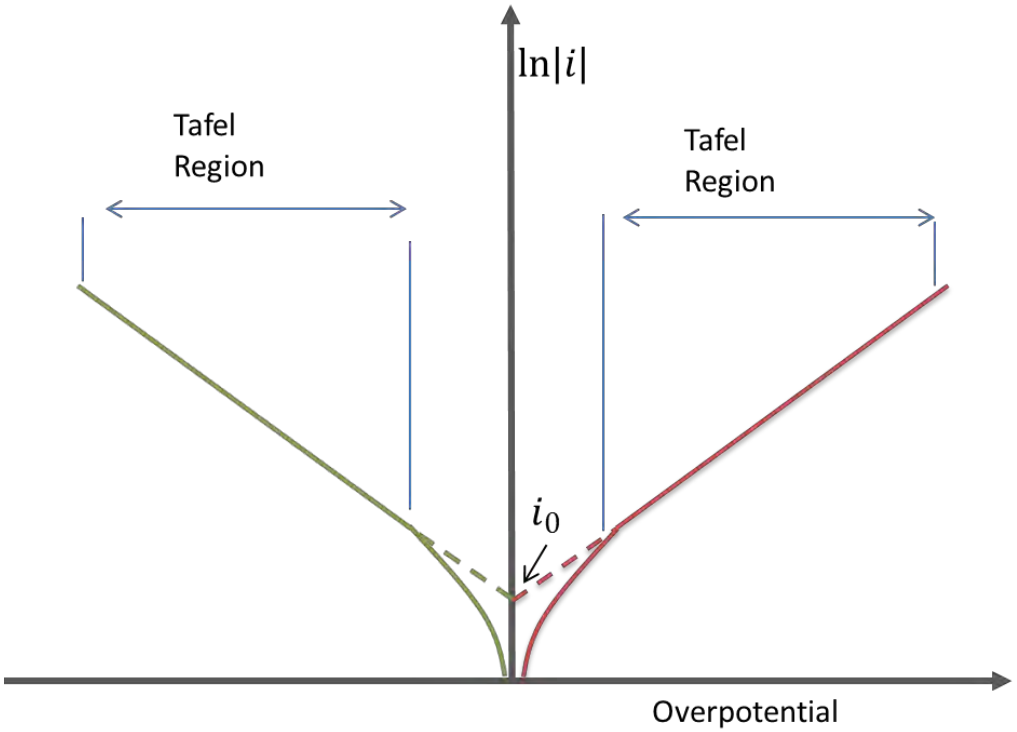

Figure 2.5 Tafel analysis of oxidative and reductive reactions.

Adapted from Bard and Faulkner [16]

Figure 2.5 and equations (12) and (13) show that the symmetry factor, a, is found from the gradient of the Tafel slope (given that *F, R* and *T* are constants*)*, and the exchange current density is calculated from the y-intercept of the Tafel plots. It is noteworthy that Tafel analysis cannot be carried out on a reversible reaction, (e.g. Case (a), Figure 4) because both anodic and cathodic components contribute significantly except at extreme overpotentials.

2.5 Mass transport and the rotating disc electrode

2.5.1 Mass transport

As mentioned in Section 2.4, the reversibility/irreversibility of an electrochemical reaction depends on whether the exchange current density is small or large. The measured current also depends on the rate of flux of material in and out of the interfacial region. In order for the rate of an electron transfer reaction to be accurately measured, the transport of material in and out of the interfacial has to be controlled/quantified. According to experimental conditions, the most significant ways in which materials are transported to the interface are diffusion, convection and migration.[17]

Diffusion occurs as a result of uneven concentration distribution and acts to maximise entropy. Convection arises from the action of mechanical forces on the solution. Natural convection is caused by thermal gradients and density differences in the solution; forced convection is achieved via external forces such as stirring or gas bubbling through a solution. Migration occurs as a result of the external electric field, which exists at the electrode/solution interface caused by the development in electrical potential between the two phases.[17] This drop can exert electrostatic forces on charged species present in the interfacial region, thus causing movement of ions to or from the electrode. The interplay between migration and electrochemical reactions can lead to a complicated physical transport process, and is thus difficult to control or interpret. This problem can be virtually eliminated using an electrochemically inert background electrolyte in high concentration.

2.5.2 Mass transport during an electrochemical reaction

Let us consider the following reaction in a cell containing bulk electrolyte solution:

$S\ (aq) \rightarrow S^{+}\ (aq) + e^{-}\ (m)$ (2)

This reaction involves the movement of *S* through the solution via diffusion, to a certain distance from the electrode surface. Once *S* is close enough to the electrode surface, the potential applied to the electrode drives Reaction (2), and as a result, S^{+} is produced. A diffusion layer is therefore created: the concentration of *S* is different in the diffusion layer to that in the bulk solution. The longer Reaction (2) proceeds, the thicker this diffusion layer grows, although, owing to natural convection and entropy, this layer eventually reaches a maximum thickness. For systems with convection in addition to diffusion, extra material can be brought to the electrode surface, resulting in larger currents.

2.5.3 The rotating disc electrode

The rotating disc electrode (RDE) is used to measure kinetic information on irreversible reactions which have very low exchange current densities, e.g. the oxygen reduction reaction (ORR). The RDE uses forced convection to dominate the transport of new reactants (oxygen) to the electrode surface. This method is designed to allow laminar flow, whereby the oxygen-saturated solution moves to the electrode along a constant direction. A schematic representation of an RDE is shown in Figure 2.6.

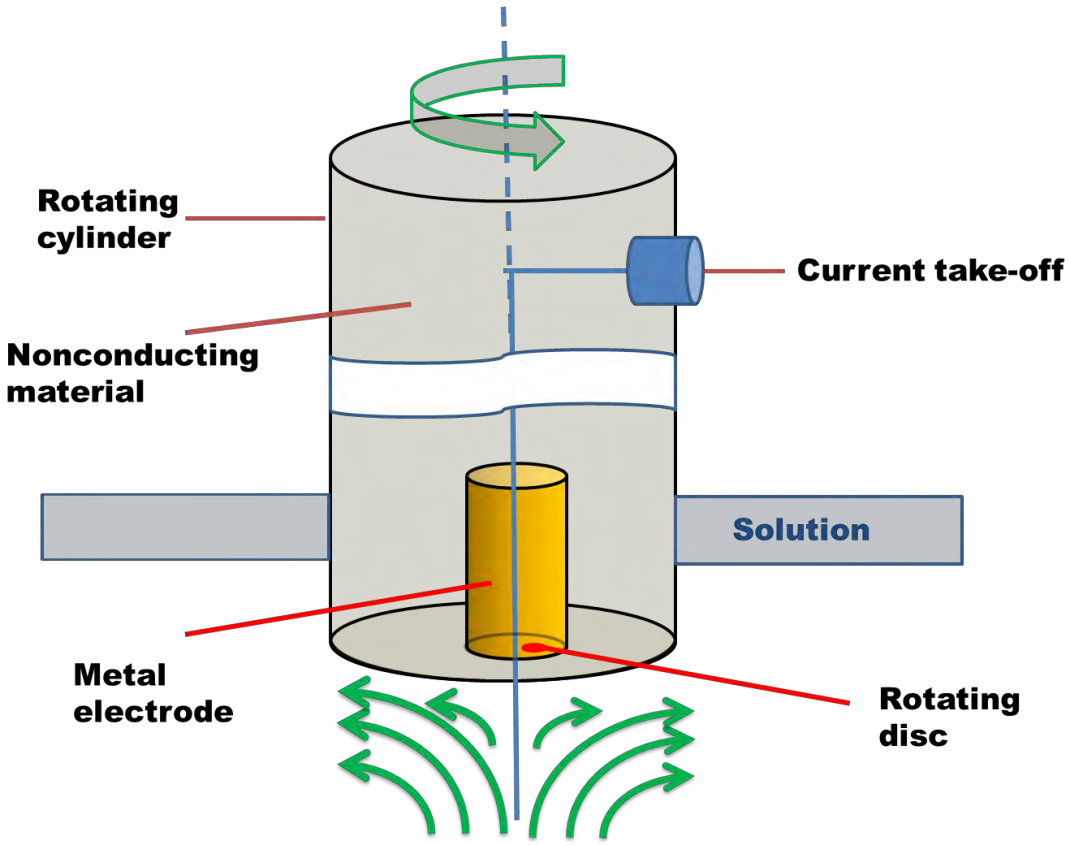

Figure 2.6. Schematic representation of a rotating disc electrode. The green arrows below the rotating disc show the radial flow of the solution while the disc rotates.

Adapted from Vielstich [2]

Figure 2.6 shows a small electrode disc embedded centrally within a large Teflon cylinder, which is rotated at a constant speed. The rotation spins the solution out from the cylinder surface in a radial direction and this movement causes fresh material to go towards the disc. Thus, in the case of the oxygen reduction reaction, there is a steady supply of oxygen to the electrode. Thanks to such forced convection, variations in surface concentration resulting from natural convection are minimised.

For the ORR at low overpotentials, the current follows the Butler-Volmer equation. Next, there is a transition region, in which both electron transfer kinetics and mass transport play a

role. Finally, there is the limiting current region, j_{lim} , where only mass transport is rate-determining.

The Levich equation is used to predict the variation in transfer limited current j_{lim} as a function of the rotation speed:

$$j_{lim} = 0.62nFD^{\frac{2}{3}}v^{-\frac{1}{6}}c^{o}\omega^{\frac{1}{2}} \qquad (13)$$

Here, j_{lim} is the limiting current density (the maximum current reached); v the kinematic viscosity measured in $cm^2\ s^{-1}$; ω represents the angular velocity and is the velocity at which the disc rotates is measured in s^{-1}; and c^o is the bulk concentration. A plot of j_{lim} versus the square root of the rotation speed, $\omega^{\frac{1}{2}}$, yields a straight line which passes through the origin. This linear relationship is due to the increase of the velocity of the solution towards the electrode as rotation speed increases. This leads to enhanced convective transport of O_2 and, at the same time, a decrease in the diffusion layer thickness.

2.6 Ultraviolet/visible spectroscopy

2.6.1 The electromagnetic spectrum

The absorption of visible light causes objects to be coloured. For example, blue paint appears blue because the light at the red end of the visible spectrum is absorbed, allowing for blue light to be transmitted. Figure 2.7 gives a diagram of the regions in the electromagnetic spectrum.

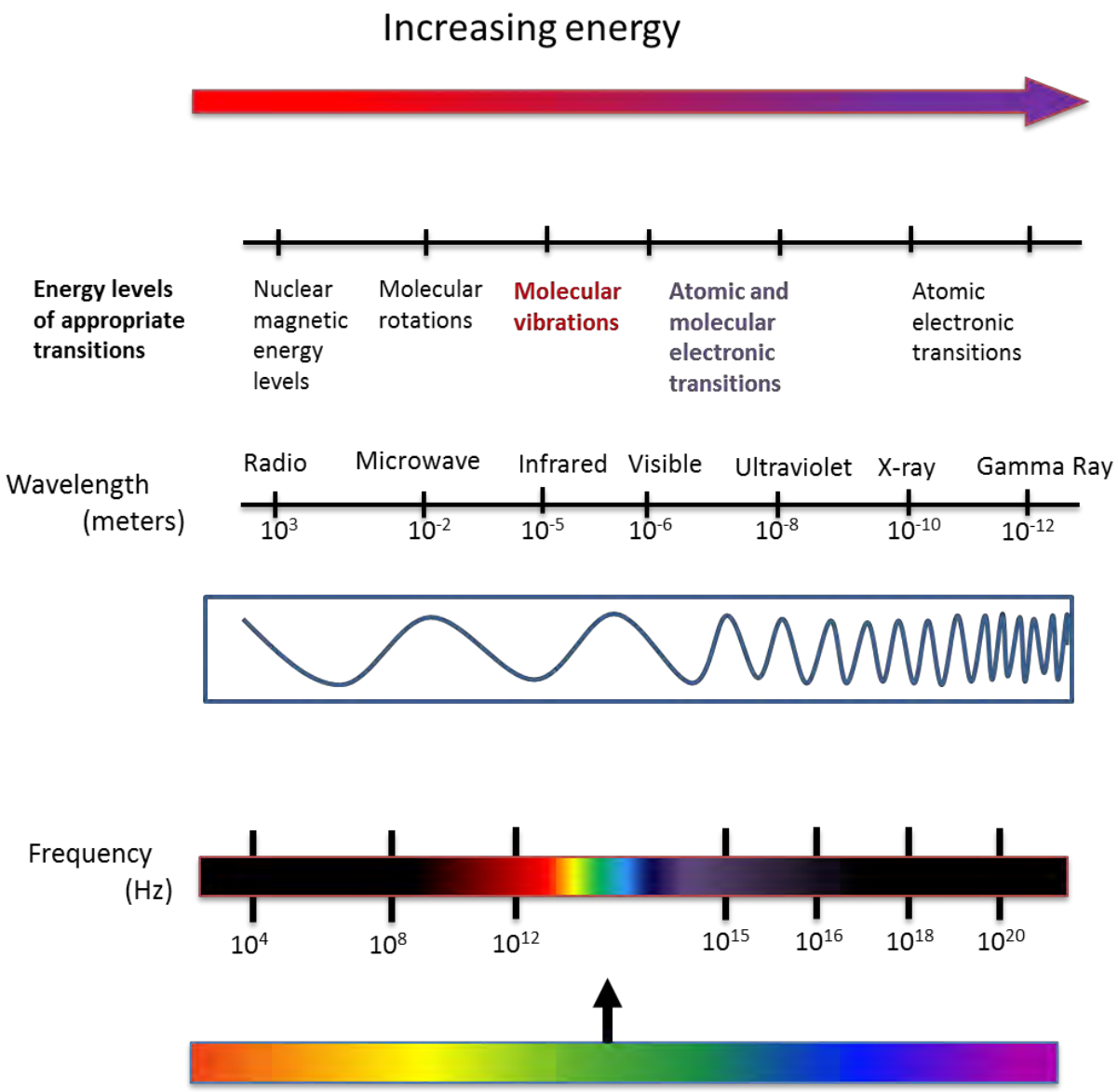

Figure 2.7 Regions of the electromagnetic spectrum

2.6.3 Surface plasmon resonance of Au NRs

An oscillating electromagnetic field of light applied to a colloidal suspension of metal nanoparticles results in the conduction band electrons of the metal nanoparticles to undergo a collective coherent oscillation in resonance with the frequency of light. This is called a surface

plasmon resonance (SPR);[18] it brings about a charge separation between the free electrons and the ionic metal core, which in turn restores Coulombic force, making the electrons oscillate on the particle. The SPR oscillation causes strong absorption bands. The location and intensity of these bands depend on the size, shape, structure and dielectric properties of the metal particles, as such factors affect the electron charge density on the particle surface.[19] Spherical gold, silver, and copper nanoparticles show strong surface plasmon resonance (SPR) bands in the visible region.[18]

For Au NRs, plasmon absorption splits into 2 bands. The two types of oscillation leading to these bands are schematically represented in Figure 2.8. They are the free electron oscillations perpendicular to and along the 'long axis' or length of the rod.[20] The excitation of the surface plasmon oscillation perpendicular to the short axis is referred to as the transverse mode; the excitation of the surface plasmon oscillation along the length of the rod is referred to as the longitudinal surface plasmon resonance (LSPR) mode.

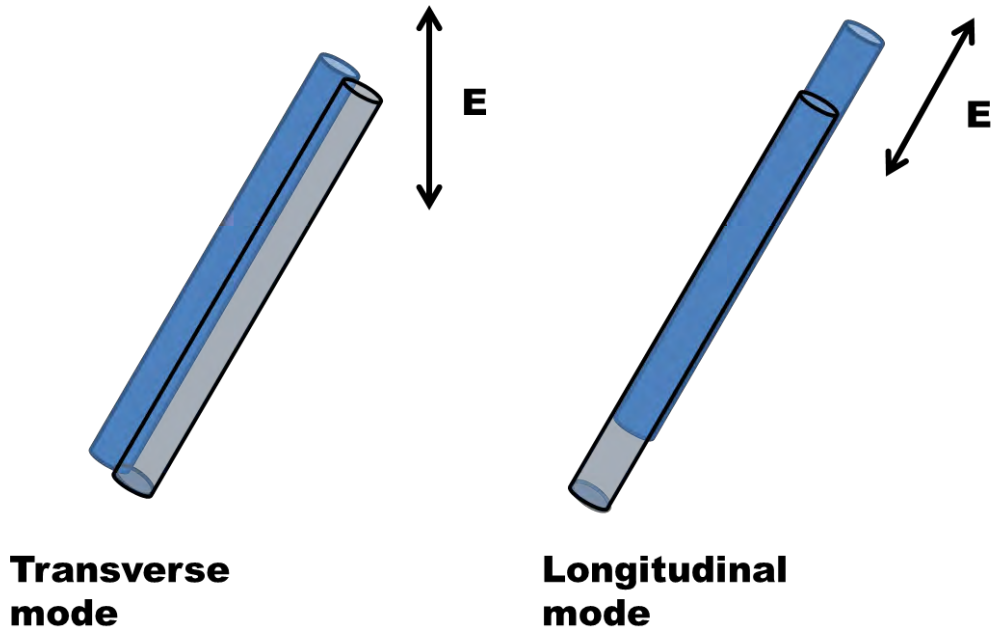

Figure 2.8 A schematic representation of plasmon resonance in rod-like particles.

Adapted from Huang et al [20]

The free electron oscillations in the longitudinal mode happen at a lower frequency than those in the transverse mode. Thus the longitudinal surface plasmon resonance (LSPR) has a longer wavelength. As the aspect ratio (length: width ratio) increases, the free electron oscillations in the longitudinal mode decrease in frequency. This is because, as the aspect ratio of the Au NR increases, the distance between the charges at opposite interfaces of the particle increases, thus causing a smaller restoring force and subsequently a smaller resonance frequency.[20] Thus the LSPR wavelength is an indication of the aspect ratio of the Au NR; a high wavelength indicates a high aspect ratio and a low wavelength indicates a low aspect ratio. The transverse mode is less affected by changes in aspect ratio. The free

electron oscillations increase in frequency slightly on the transverse mode with an increase in aspect ratio.[21]

A UV-visible spectrometer measures the absorbance against wavelength, with peaks in the absorbance indicating the transverse and longitudinal modes of the Au NRs.

2.6.3 The UV-visible spectrometer

As only few absorbing molecules are required in the UV-visible spectrometer, the sample is diluted in a solution (which does not absorb in the UV-visible region). Figure 2.9 gives a diagram of a UV-vis absorption experiment.

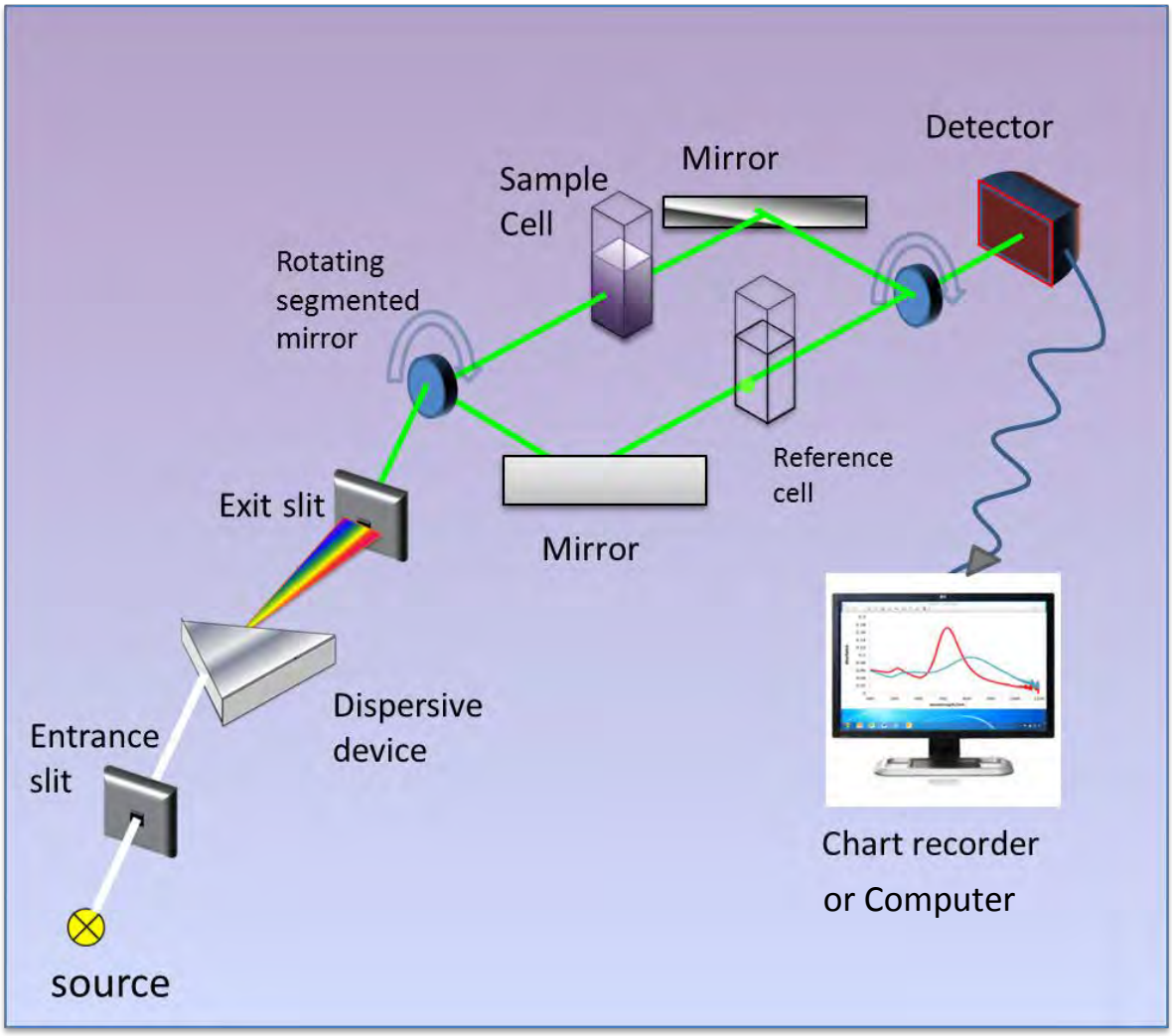

Figure 2.9 Diagram showing how a UV-vis spectrometer works. The rotating segmented mirrors allow the radiation to go through the sample cell and reference cell alternatively.

In a UV-vis spectrum, electromagnetic radiation passes through the sample, which is held in a small rectangular cell (known as a cuvette). Radiation across the entire ultraviolet/visible region is scanned over 30 seconds to 1 min. The same radiation is passed simultaneously through a reference cuvette containing only the solvent. Photocells subsequently detect the radiation transmitted and the spectrometer records the differences in intensity between the radiation passing though the sample and the reference cell.[22]

A single lamp cannot provide radiation across the entire UV-visible region: a hydrogen or deuterium lamp covers the UV-region, and a tungsten/halogen lamp covers the visible region. The source of light is directed to a dispersive device, giving rise to different wavelengths of light to be dispersed at different angles. This is done via a diffraction grating followed by a narrow slit, which squeezes the radiation to a narrow, monochromatic wave band. The radiation passing through the sample or reference cuvettes can be detected either by a photodiode or a photomultiplier, thus converting photons of radiation into a very small electric current followed by an electron multiplier. Comparing the currents produced by the sample cell with the blank reference cell provides the final spectrum.[22]

According to Beer's law, absorption is proportional to the number of absorbing molecules (which is related to the concentration of absorbing molecules in dilute solution). Lambert's law states that the fraction of radiation absorbed is independent of the intensity of radiation. The two laws combined give the Beer-Lambert law: [22]

$$log_{10} \frac{I_0}{I} = \varepsilon l c \qquad (14)$$

Here, I_0 is the intensity of the incident radiation; I is the transmitted radiation intensity; ε is the molar absorption coefficient (which is a constant for each absorbing material and is independent of the concentration and path length); l is the path length of the absorbing solution (in cm); and c is the concentration of the absorbing material. The $\log_{10} (I_0/I)$ value is known as the absorbance of the solution, or the optical density, and can be read directly from the spectrum. The units of this absorbance are known as absorbance units.

The energies of the orbitals involved in electronic transition have fixed values. Since this energy is quantised, the absorption peaks in the UV-vis spectrum ought in theory to be sharp. However, this is rarely the case, with broad absorption peaks often being observed instead, owing to a number of vibrational energy levels available at each electronic energy level. The transitions occurring to and from the different vibrational level results in the broadening of the peak.[22]

2.7 Electron microscopy

The resolution limit of any given microscope is defined by the formula:

$$D = 0.6\,\lambda\,/n\sin\alpha \qquad (15)$$

Here, D is the closest spacing of two points which can be seen to be two distinct entities. λ is the wavelength of the incident radiation, n is the refractive index and α is the half-angle subtended by the aperture. For a light microscope, the practical limit for $n\sin\alpha$ is 1.6; if green light (λ ~ 400 nm) is employed, it leads to a resolution limit of 150 nm.[23]

For transmission electron microscopy (TEM), the refractive index n is assumed to be unity (since the lenses used to focus the electron beam are magnetic fields in vacuum), and the angle through which the electrons are deflected is small (~ 0.1 rad). If the electrons are accelerated though 100 kV, they have an incident energy corresponding to a wavelength of around 0.0037 nm. A combination of these values, according to Equation (15), leads to a resolution, D, of approximately 0.02 Å. However, this is in practice limited to around 1.2 Å

because of imperfections in the magnetic lenses. Atomic resolution is therefore possible with TEM.[23]

Once the electron beam has passed through the sample, it is magnified and focused by an image-forming electromagnetic lens. It subsequently strikes a fluorescent screen, on which the energy of the electrons is converted to visible light, thus forming an image. Wherever the sample is less dense, more electrons get through, thus causing the image to be brighter. A darker image is produced in areas of the denser sample, thus allowing fewer electrons to pass though.[22]

In Scanning Transmission Electron Microscopy (STEM), an electron beam is focused into a narrow spot, which is scanned over the sample in a raster.

[1] Vielstich W. and Gerischer, H. (1955), *Z Phys Chem (N.F.)*, 4, p. 10.
[2] Vielstich, W. (2003), 'Methods in Electrocatalysis', *Handbook of Fuel Cells*, New York: Wiley
[3] Shchukin, E.D., Vidensky, I.V. and Petrova, I.V., (1995), *J Mater Science* 30 (12), p. 3111
[4] Hamann, C.H., Hamnett, A. and Vielstich, W. (1998), *Electrochemistry*, Weinheim: Wiley-VCH.
[5] Schmickler, W. (1996), *Chem Rev*, 96, p. 3177.
[6] Walters, M.J., Pettit, C.M., Bock, F.X., Biss, D.P. and Roy, D. (1999), *Surf Interface Anal*, 27, p. 1027.
[7] Bockris, J., Devanathan, M. and Müller, K. (1963), *Proc R Soc London A*, Vol. 274, pp. 55-79.
[8] Kolb, D.M. (1996), *Prog Surf Sci*, Vol. 51, N^{o} 2, p. 109.
[9] Schmickler, W. and Henderson, D. (1986), *Prog Surf Sci*, 22, p. 323.
[10] Nagy, G. and Roy, D. (1994), *Surf Sci*, 320, p. 7.
[11] Conway, B.E., Barber, J. and Morin, S. (1998), *Electrochim Acta*, 44, p. 1109.
[12] Pletcher, D., Greef, R., Peat, R., Peter, L.M and Robinson, J. (2001) *Instrumental Methods in Electrochemistry*, Chichester: Horwood Publishing.
[13] Scholtz. F. (2010), *Electroanalytical Methods*, New York: Springer.
[14] Richer, J. and Lipkowski, J. (1986), *J Electrochem Soc*, 133 p. 121.
[15] Lipkowski. J and Stolberg, L. (1992), *Adsorption of Molecules at Metal Electrodes,* Ch. 4, New York: VCH, p. 171.
[16] Bard, A.J. and Faulkner, L.R. (2001), *Electrochemical Methods: Fundamentals and Applications*, New York, John Wiley & Sons.
[17] Fisher, A. (1996), *Electrode Dynamics*, New York: Oxford University Press.
[18] Papavassiliou, G.C., (1980), *Prog Solid State Chem*, 12, p. 185.
[19] Link, S. and El-Sayed, M.A. (2000), *Int Rev Phys Chem*, 19, p. 409.
[20] Huang, X., Neretina, S. and El-Sayed, M.A. (2009), *Adv Mater*, 21, p 4910.
[21] Park, K. (2006), *Synthesis Characterization of Size Tunable Gold Nanorods*, published PhD thesis, School of Polymer, Textile and Fiber Engineering, Georgia Institute of Technology.
[22] Faust, B. (1997), *Modern Chemical Techniques*, Royal Society of Chemistry: Unilever.
[23] Rudenberg, G.H and Rudenberg P.G (2010). "Origin and Background of the Invention of the Electron Microscope: Commentary" in. *Advances in Imaging and Electron Physics:* Elsevier.

3. Experimental Methods

3.1 Preparation of glassware and solutions

All glassware was cleaned by heating in a 1:1 mixture of concentrated nitric and sulphuric acid for at least 1 hour followed by thorough rinsing in Milli-Q water. The water used throughout, including the solution preparation and rinsing, was purified by a Millipore™ system (resistivity > 18 MΩ cm, TOC< 5 ppb). Electrochemical experiments were carried out at acidic pH. Acidic electrolytes were prepared from H_2SO_4 (Aristar grade, BDH) at a concentration of 0.05 M.

3.2 Synthesis of CTAF and recrystallisation of all surfactants

3.2.1 Synthesis of CTAF

Cetyltrimethylammonium fluoride (CTAF) was prepared according to the reaction proposed by Binton et al.[1] First, 25 g of CTAB (Acros, 99+%) was dissolved in enough MeOH to give a clear solution. Then a 1.5-fold excess of Ag F (Aldrich, 99%) was added.

This solution was kept under a UV light for 2 weeks, after which, the excess Ag^+ ions reduced to Ag nanoparticles. These colloidal Ag particles were removed through filtration and by centrifuging (6000 rpm for 20 min). The resulting solution was put into a rotary evaporator for 15 mins at 50° C. A thick white slurry formed at the edge of the glass flask.

The remnants in the flask were mixed with di-ethyl ether. A white translucent liquid was formed and was later subsequently suction-filtered. The resultant filtrate of pure CTAF was a white waxy slurry. The dried CTAF was stored in an evacuated desiccator for several days.

3.2.2 Rectrystallisation of Surfactants

The surfactants, CTAF (as prepared in section 3.2.1) CTAB (Acros 99+ %), CTAC (Acros 98 %), CTAF and BDAC (97% Acros), were recrystallized before being used in experiments. First, the solutions of surfactants were rotary-evaporated at ca. 50°C and a white slurry remained. The remnants of the flask were mixed with diethyl ether. The surfactant was subsequently filtered using suction filtration. Any remaining diethyl ether was evaporated after the surfactant was stored in an evacuated desiccator for at least 24 h. Before each experiment, fresh solutions of surfactants were prepared, in order to minimise contamination.

3.3 Measurements of critical micelle concentration of surfactants

The critical micelle concentrations (CMCs) of cetyl trimethyl ammonium fluoride (CTAF), cetyl trimethyl ammonium chloride (CTAC), cetyl trimethyl ammonium bromide (CTAB) and cetyl dimethyl benzyenemethyl ammonium chloride (BDAC) was determined by measuring the surface pressure at the air/solution interface as a function of surfactant concentration in 0.1 M NaF (and in Milli-Q water for CTAB and CTAC). The Wilhelmy plate method was used to measure the surface pressure $\pi = (\gamma_0 - \gamma_c)$ at the gas/solution interface, where γ_c is the surface tension at the gas/solution interface in the presence of surfactant molecules,

and γ_0 is the surface tension in the absence of surfactant molecules.[2] The Wilhelmy plate was a rectangle of chromatography paper (supplied by NIMA) connected to a surface pressure sensor of a Langmuir trough (NIMA- ps4).

3.4 The electrochemical cell for surfactant electrochemistry

The electrolyte used in the cell was 0.1 mol dm^{-3} NaF (99.99 %, Suprapur, Merck), prepared in Milli-Q ultrapure water. The single-crystal working electrodes (WE) used were Au (111), a gold disc 0.25 cm in diameter (Mateck, Germany), and Au (100), obtained by means of an Au single-crystal bead with a diameter of 0.2 cm cut in the (100) orientation. The counter electrode (CE) was a gold coil. The WE and the CE were flame-annealed using a Bunsen burner and Milli-Q ultrapure water was used to that the surface was free from contamination. The reference electrode (RE) was an external saturated calomel electrode (SCE) connected to the cell with a salt bridge.

Before measurements were made, all solutions were de-aerated with argon and a constant flow of argon over the top of the solution was maintained during the experiments. All the measurements were conducted at room temperature (17$\pm$2 °C).

For all measurements, various salt concentrations were used. For measurements involving CTAB, CTAC and CTAF, 8 concentrations were used below the critical micelle concentration (CMC); for BDAC, 6 concentrations were below the CMC. In Addition, one experiment was performed at a surfactant concentration above the CMC. For NaCl and NaBr, the concentrations used were the same as those used for CTAC and CTAB respectively.

Generally, after each Addition of the surfactant or salt to the electrolyte, Ar was bubbled into the cell for 30 minutes to mix the solution well and to de-oxygenate the cell.

3.5 Electrochemical measurements of surfactants

For cyclic voltammetry (CV), the WE, CE and RE were connected to an AUTOLAB potentiostat (Eco chemie, model PGSTAT 10), running with GPES (general purpose electrochemical system). A sweep rate of 20 mV s^{-1} was used; the potential limits were between -0.7 V and 0.5 V (vs. SCE), and 3-4 cycles were recorded for each experiment.

The differential capacitance measurements were conducted using a potentiostat (HEKA PGStat 590, Germany) and a lock-in-amplifier (Signal recovery, 7265 DSP lock-in-amplifier, Ametek, Germany). A sweep rate of 5 mV s^{-1} was used with potential limits of between -1.0 V and 0.5 V (vs. SCE). Two forward and backward sweeps between these limits were recorded for each experiment. The a. c. signal had an amplitude of 5 mV and a frequency of 20 Hz.

The, HEKA PG 590, was also used for the chronocoulometric experiments. During chronocoulometry, the Au (111) or Au (100) single-crystal working electrode was maintained at a selected potential, E_{ads} for 3 mins, to establish adsorption equilibrium. The potential was then stepped to the desorption potential, E_{des} = -1000 mV, this potential was determined from the differential capacitance measurements. The current transient due to the desorption of the surfactant molecules and recharging the double layer was measured and subsequently integrated to determine the difference between the current density on the

electrode surface at potentials E_{ads} and E_{des}. This procedure was repeated by decreasing the potential from 500 mV to -1000 mV in 50 mV increments. The same procedure was carried out on the single-crystal working electrodes using 0.1 mol dm^{-3} NaF only. These resulting charge density vs electrode potential plots were used as baselines for the plots where various concentrations of the salt solution were used.

3.6 Preparation of nanorods

3.6.1 Synthesis of Gold nanorods

Gold nanorods (Au NRs) were prepared using the seed mediated growth method.[3] For the seed solution, 5.0 mL of cetyl trimethyl ammonium bromide (CTAB) (0.2 M) was mixed with 5.0 mL of $HAuCl_4$ (0.0005 M). 0.6 mL of 0.010 M ice-cold $NaBH_4$ was added to the stirred solution. This seed solution was stirred for another 2 minutes, and then kept at 25°C for 2 h, to allow the seeds to form. The solution gradually changed colour from yellow/orange to nutty brown in this process. For the growth solution, 5 mL of CTAB (0.2 M) was added to 5 mL of $HAuCl_4$ solution (0.001 M). 200 µL of $AgNO_3$ (0.004 M) was added to the solution at 25°C. After gentle mixing, 70 µL of 0.0778 M of ascorbic acid was added, which caused the solution to change colour from yellow/gold to colourless. 12 µL of the seed solution was then added, and left at 25°C for at least 12 h, during which time the solution changed from colourless to brown with a hint of purple. This colour change indicated the growth of gold nanorods. The synthesised gold nanorods were centrifuged twice at 6000 rpm for 20

minutes and re-dispersed in Milli-Q water after each time in order to remove excess CTAB from the AuNR surface.

3.6.2 Deposition of platinum on gold nanorods

Before Pt deposition, the Au NRs were centrifuged one more time at 6000 rpm for 20 minutes before being re-dispersed in 0.1 M CTAB solution. The CTAB solution allows reproducible Pt deposition on the Au NR surface to occur. The method of Pt deposition was adapted from Grzeczak et al. [4] Calculated amounts of the $PtCl_4^{2-}$ solution were mixed with 1 mL of Milli-Q water in to obtain a 2 mM $PtCl_4^{2-}$ solution. 1 mL of centrifuged Au NRs in CTAB solution were mixed for 30 minutes at 40°C with a calculated amounts of 2 mM K_2PtCl_4(aq), in order to achieve the desired Au:Pt molar ratio. This was followed by adding a known amount of ascorbic acid (AA). The solutions were kept at 40°C for 20 hours, during which time the colour changed from purple to black/grey, indicative of the formation of Pt coverage on the Au NRs.

For the second Addition of a Pt layer on the Pt coated Au NRs, the sample was divided into two parts. One half was for an Additional Pt layer, and the other half was for CO blocking followed by an Additional Pt layer. The Additional Pt layers were deposited using the same procedure as above.

3.6.3 CO blocking on Pt coated Au NRs

CO was bubbled gently through the Pt-coated Au NRs for 30 minutes. The CO-saturated nanorod solution was left to stand for 1 hour before it was bubbled with argon for 40

minutes, to remove the excess CO. A second layer of Pt was subsequently deposited on the CO-blocked surface.

3.7 Electrochemical cell

Cyclic voltammetry and rotating disc electrode measurements were conducted in a 3-electrode cell of 100 mL volume. The counter electrode was a polycrystalline Pt wire coil (99.999%, Metal crystals and oxides, Cambridge). This counter electrode wire was flame-annealed before each experiment and, after being quenched with Milli-Q water, was placed in the cell electrolyte. The reference electrode was a saturated calomel electrode (SCE) (Radiometer, Copenhagen). All potentials quoted in this text are with respect to SCE. The reference electrode was in a compartment connected to the main part of the solution with a Luggin capillary tip. The working electrodes used were polycrystalline Pt, polycrystalline Au, 2 mm in diameter sealed in Teflon and mounted on the shaft of the disc support, and gold nanorods (Au NRs) and Pt coated Au NRs supported by carbon powder, deposited on glassy carbon of 3 mm diameter sealed in Teflon and mounted on the shaft of the disc support.

3.8 Instrumentation

3.8.1 Cyclic voltammetry and rotating disc voltammetry.

For cyclic voltammetry, the 0.05 M electrolyte was purged of oxygen by bubbling argon through the cell for at least 25 minutes prior to measurements. The scan rate used was 100 mV s^{-1}.

For study of electrochemical reduction of oxygen, the electrolyte was saturated with oxygen for 30 minutes before starting measurements, and for 20 minutes between each measurement. During the oxygen reduction measurements, the electrode was rotated at speeds of 100-2500 rpm. The scan rate during the rotating disc electrode (RDE) measurements was 2 mV s^{-1}.

All experiments were carried out with an Autolab PGSTAT 12 using GPES software (ECO chemie, NL). The RDE controller was from Radiometer, Copenhagen, AUT 71130 CT101.

3.8.2 UV-visible absorption spectroscopy

Optical characterization was carried out by UV-visible spectroscopy with a Cary 50 spectrophotometer, using 10 mm path length quartz cuvettes.

3.8.3 Scanning Transition Electron microscopy (STEM)

STEM observations were carried out using a JEOL 2100F microscope equipped with a CEOS aberration corrector, operating at acceleration energy of 200 kV. High angle annular dark field (HAADF) images were recorded using a JEOL ADF detector. Dongsheng He carried out these experiments.

3.9 Immobilisation of nanoparticles on electrode

Prior to deposition of the catalyst ink, the glassy carbon electrode was polished to a mirror finish with aqueous slurries of successively finer grades of alumina powder (1 µm, 0.3 µm

and 0.05 μm, Buehler). The electrode was subsequently electrochemically cleaned through potential cycling. A 1 mL solution of centrifuged and re-dispersed Au NRs, or centrifuged and re-dispersed Pt-coated Au NRs, was sonicated with carbon powder (Vulcan XC-72 R) for 2.5 h to give an Au NRs loading where there is 30 % Au and 70 % carbon powder. 5 μL of the ink was pipetted onto the polished glassy carbon electrode, which was then dried in an oven, at about 70°C, for 5 min. This was repeated 4 times, to give an Au loading of 42 μg cm^{-2}.

After the catalyst ink had been dried, 3 μL of Nafion® solution (5% wt Aldrich) was pipetted onto the electrode surface; it was dried in an oven (approx. temp was 100°C) for a few minutes, and left to cool at room temperature for 30 minutes.

3.10 Electrode cleaning procedures

In order to remove impurities present on the nanoparticles, the surfaces were cleaned using the following procedures.

3.10.1 Cyclic voltammetry

The working electrode was electrochemically pre-treated in Ar-saturated H_2SO_4 solution by repeating potential scans in the potential range of -0.2 to 1.3 V (vs SCE) at 100 mV s^{-1} for 10 min, or until the CV characteristics of a clean surface of the working electrode were obtained.

3.10.2 Copper Under Potential Depostion (UPD)

The electrode was put into a cell containing a 1 mM $CuSO_4$ in 0.05 M H_2SO_4 electrolyte, which was then de-oxygenated for 30 min with argon. First, the electrode was held at 0.45 V (vs. SCE) for 20 seconds to ensure that there was no copper on the surface, and then the potential was swept at 400 mV s^{-1} to the desired UPD potential. After 10 min at this potential, the electrode was swept back to 0.65 V and kept there for 10 min, to ensure removal of the copper layer. The electrode was taken out of the copper electrolyte with potential control, washed in Milli-Q water and put into a cell containing argon-saturated 0.05 M H_2SO_4. Any remaining copper was removed using the cyclic voltammetry cleaning method described above.

3.10.3 CO-stripping voltammetry

A cell containing de-oxygenated 0.05 M H_2SO_4 electrolyte was saturated with carbon monoxide for 10 min. The working electrode was subsequently held at 0.055 V (vs SCE) for 10 min. The CO-saturated electrolyte was then replaced with new Ar-saturated 0.05 M H_2SO_4 electrolyte. The CO layer was oxidised by performing cyclic voltammetry to an upper limit of 1.3 V (vs SCE), to leave a clean nanoparticle surface. The CO layer usually was removed after 1 cycle. For Pt-coated Au NRs, the oxidation was seen as a sharp peak at 0.55 V (vs SCE). As well as for cleaning, this method was used for quantitative analysis of Pt on the AuNRs, by calculating the area under the CO oxidation wave.

[1] Bunton, C., Frankson, J. and Romsted, L. (1980), *J Phys Chem*, 84, p. 20.

[2]Shaw, D.J, (1992), *Colloid and Surface Chemistry,* 4th Ed., Oxford: Butterworth-Heinemann.
[3] Nikoobakht, B. and El-Sayed, M.A. (2003), *Chem Mater*, 15, p. 1957.
[4] Grzelczak, J., Perez-Juste, F., de Abajo, J. G. and Marzan, L.M. (2007), *J Phys Chem,* C111, p.6183.

4. The Electrochemistry of Halides and Cationic Surfactants on Au (111)

The cationic surfactants examined are amphiphilic molecules, which possess a hydrophobic hydrocarbon tail, a hydrophilic cationic head group and a halide counter ion. Figure 4.1 provides models of the four investigated in this study. In Figure 4.1, A. is Cetyltrimethylammonium-fluoride (CTAF), B. is Cetyltrimethylammonium-chloride (CTAC), C. is Cetyltrimethylammonium-bromide (CTAB) and D. Benzyldimethylhexadecylammonium-chloride (BDAC).

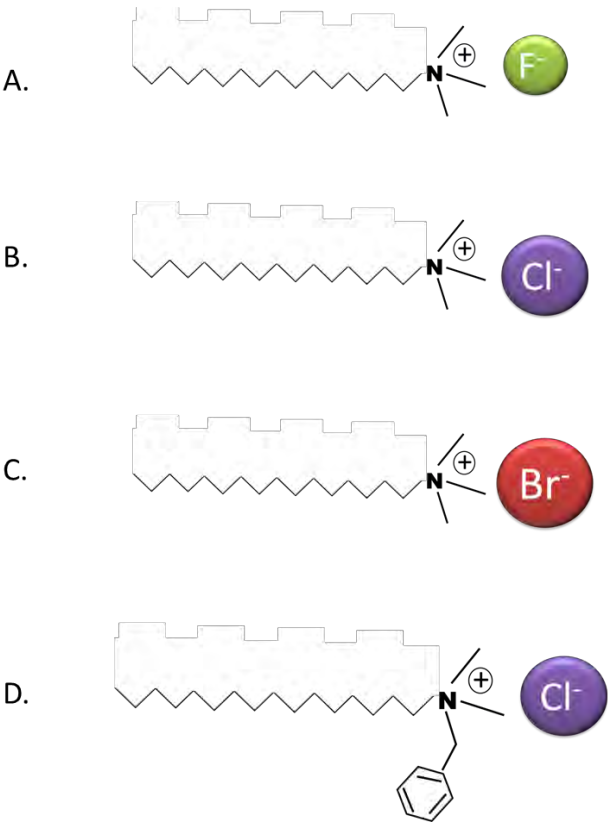

Figure 4.1 Structure of the cationic surfactants. A. Is cetyltrimethylammonium-fluoride (CTAF), B. is Cetyltrimethylammonium-chloride (CTAC), C. is cetyltrimethylammonium-bromide (CTAB) and D. cetyoldimethyl benzenemethyl ammonium chloride (BDAC).

4.1 Synthesis of CTAF

CTAF was synthesised according to the method proposed by Binton et al.[1] The mechanism for the synthesis of CTAF is given in Scheme 1.

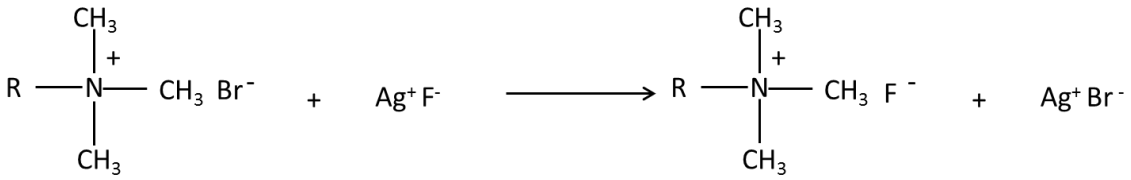

R = $(CH_2)_{15}CH_3$

Scheme 1 Mechanism for synthesis of cetyl trimethyl ammonium fluoride (CTAF). This involves adding an excess of AgF to CTAB in MeOH.

After AgF was added to CTAB, insoluble AgBr was produced and filtered off along with the excess AgF. However, excess Ag^+ ions were present in the final CTAF in MeOH solution. This solution was then irradiated with ultraviolet (UV) light. As a result, the electrons in the MeOH valence band were possibly excited to the conduction band and the excited electrons transferred to Ag^+, resulting in the formation of Ag nanoparticles. A similar mechanism has previously been proposed.[2] After the CTAF solution was exposed to UV light for several hours, it turned light brown, showing the formation of Ag nanoparticles. After several days, the sides of the beaker were coated with bulk silver, indicating that the Ag nanoparticles had grown into large clusters.

The CTAF produced was a cream-coloured waxy slurry and the melting point was determined as 158-165°C, lower than that of CTAC and CTAB, which had melting points of 178-200°C and 237-243°C, respectively. The mass spectrum of CTAF yielded one peak at 284.4 g mol^{-1}, which is the molar mass of CTA^{+}.

4.2 The Critical Micelle Concentration of CTAF, CTAB, CTAC, and BDAC in NaF Solution.

When the bulk concentration of surfactant molecules exceeds a critical value, the hydrophobic alkyl tail groups of the surfactants segregate from the aqueous solution and colloidal micelles are formed. The CMC of the surfactants in 0.1 M NaF was determined by measuring the surface pressure at the air/solution interface as a function of surfactant concentration, using the Wilhelmy plate method. Figure 4.2 gives plots of the surface pressure as a function of the natural logarithm of surfactant concentration of CTAB, CTAC, CTAF and BDAC in 0.1 M NaF solution.

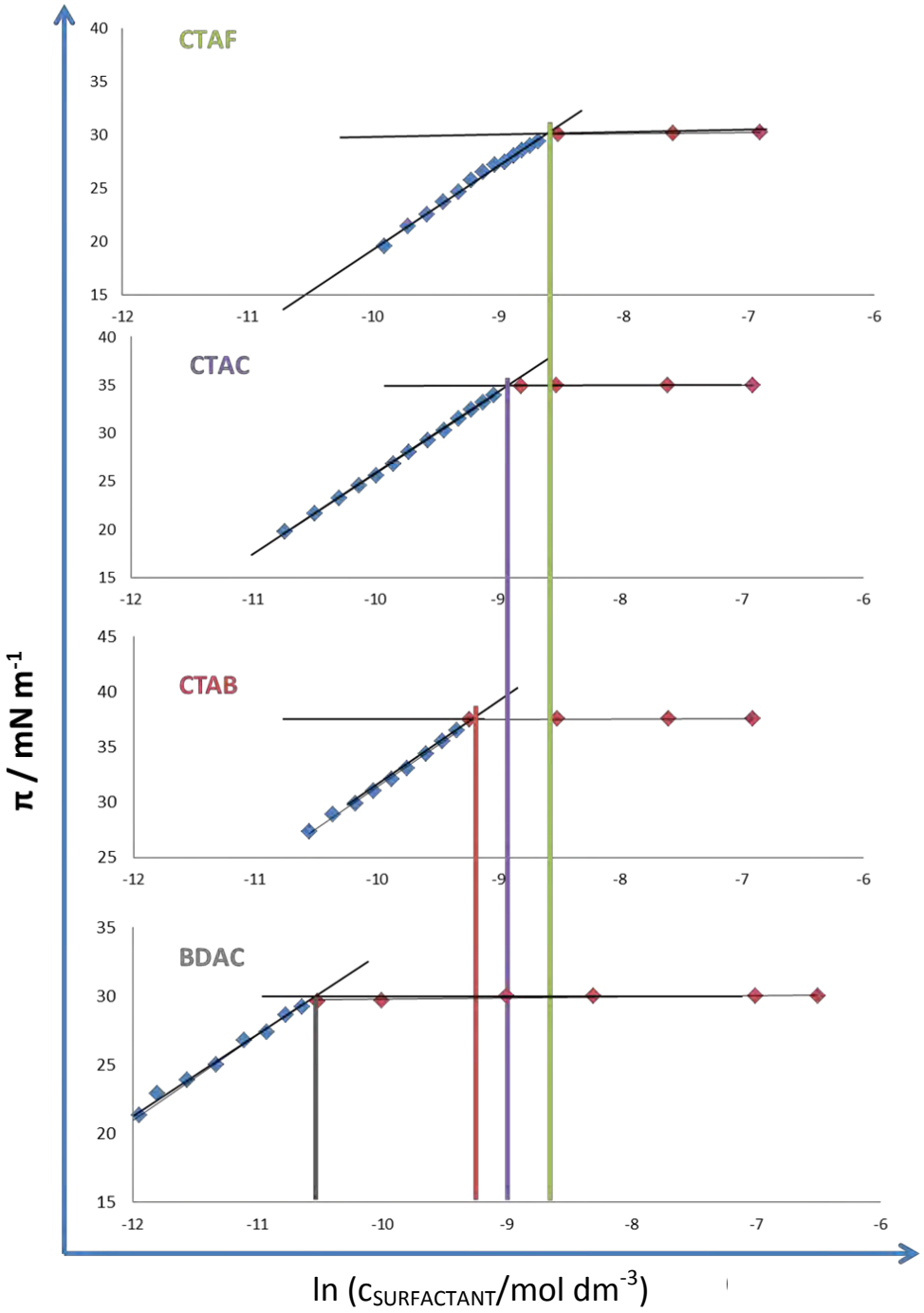

Figure 4.2 Calculating the critical micelle concentration of A. CTAB, B. CTAC, C. CTAF and D. BDAC, by plotting the surface pressure at the air/solution interface versus the logarithm of the bulk concentration of surfactant in 0.1 M NaF solution. The CMC is the concentration at which the surface pressure plateaus. R^2>0.99 for all straight line fits.

In Figure 4.2, the surface pressure initially rises but then levels off to a plateau, which corresponds to the surfactant concentration when the surfactant reaches the CMC. Above the CMC, the chemical potential becomes independent of the bulk surfactant concentration. The CMC is therefore obtained from the intersection of the straight line fitted to the measurements obtained below the plateau and the straight fitted line for the plateau. The CMC values for the four surfactants are presented in Table 4.1.

Table 4.1: The critical micelle concentrations of CTAB, CTAC, CTAF and BDAC in 0.1 M NaF solution, calculated from the surface pressure vs. natural logarithm of surfactant concentration plots given in Figure 4.1. The cmc is the concentration at which the two fitted straight lines (surface pressure vs ln [surfactant] before and after cmc) intercept.

Surfactant	Critical micelle concentration in 0.1 M NaF solution/mM
CTAB	0.104
CTAC	0.138
CTAF	0.177
BDAC	0.0255

The CMC of CTAB and CTAC were also measured in Milli-Q water. The calculated CMCs were 1 mM and 1.4 mM, respectively. These values are consistent with those found in literature.[3] The CMCs of the CTAB and CTAC in 0.1 M NaF solution in Table 1 are around 10 times lower than the values in water, owing to the interaction of the CTA^+ cation with the F^- anion (from the NaF salt) prior to the start of the normal CTA^+ self-aggregation.[4] These interactions help to screen the electrostatic repulsions between the cationic head groups, thus assisting micelle formation.

Table 4.1 and Figure 4.2 show that the CMC of the surfactants in 0.1 M NaF increases in the order CTAB < CTAC < CTAF. This is caused by the halide counter-ion interaction with the cationic head group. It has been reported that bromide ions have a 5-fold greater binding for the cationic CTA^+ surfactant micelles than chloride ions.[5] This has been attributed to Br^- ions having a higher ion exchange constant than Cl^- ions relative to hydroxyl ions found in water. It has also been reported that there is a higher degree of micellar counter-ion binding for CTAB (71%) than for CTAC (55%).[3] Cl^- ions would likewise have a greater binding affinity for CTA^+ than F^- ions in CTAF. The stronger the interactions and binding affinity between the cationic head groups and the halide counter-ions, the more screening there is for the electrostatic repulsions between the ionic headgroups. A decrease in the electrostatic repulsions of the headgroup allows micelles to form at lower concentrations.

The benzene ring present on BDAC is the most likely reason why BDAC has a considerably lower CMC than CTAC. As benzene rings are highly hydrophobic, BDAC is more hydrophobic than CTAC. Thus the aggregation of BDAC molecules in an aqueous solution would happen more readily than for CTAC. Another possibility is that the benzene ring in BDA^+ causes it to have a bulkier head group. The distance between the cationic head groups would therefore be larger on BDAC than on CTAB, CTAC and CTAF. Thus the electrostatic repulsive forces on the cationic head groups of BDAC are weaker than on the other molecules. These lower electrostatic repulsive forces would allow BDAC micelles to form at lower concentrations than CTAF, CTAC and CTAB.

The shape of the cationic surfactant micelles, according to mathematical modelling, is determined by the packing parameter, g,[6] defined by Equation (1):

$$g = \frac{v}{a_o\, l_c} \quad (1)$$

Here, v is the volume of the hydrocarbon tail, l_c is the fully extended length of the tail and a_o is the surface area per amphiphile at which the free energy per amphiphile in the micelle is a minimum. Spherical micelles are formed when $g \leq 0.33$; globular, sphero-cylindrical micelles for $0.33 < g < 0.5$, and vesicles for $g > 0.5$. [6] The packing parameter for cationic/zwitterionic surfactants such as CTAB, CTAC, and CTAF is around 0.3.[7] Thus these micelles would be expected to be spherical. However, owing to the benzene ring present in BDAC, the hydrocarbon tail in the surfactant would have a larger volume. Therefore the packing parameter would be bigger for BDAC than for CTAB, CTAC and CTAF, and hence the micelles formed by BDAC would be globular/sphero-cylindrical.

4.3 The Concentrations of CTAF, CTAC, CTAB and BDAC in 0.1 M NaF solution to be used in electrochemical measurements

In the electrochemical study of CTAF, CTAC, CTAB and BDAC on Au (111) and Au (100), various concentrations are used relative to the CMC of each surfactant in 0.1 M NaF. Seven concentrations of each surfactant below CMC, level with CMC and one above CMC are used. For example, after Addition 1 of the surfactant, the concentration of a surfactant in the cell is 1/128 of its CMC in 0.1 M NaF solution; after Addition 2, the concentration of surfactant is 1/64 of the CMC in 0.1 M NaF solution. The concentration of each surfactant after each addition and what fraction of the CMC each Addition of surfactant corresponds to are given in Table 4.2.

Table 4.2. The bulk concentrations of CTAF, CTAC, and CTAB in 0.1 M NaF solution after each Addition of surfactant. The concentrations used are all relative to the CMC of each surfactant; the fraction of CMC each surfactant concentration corresponds to is given in column 3.

Molecule	Addition number	Fraction of CMC	Concentration/mM
CTAF	1	$^1/_{128}$	0.0014
	2	$^1/_{64}$	0.0028
	3	$^1/_{32}$	0.0056
	4	$^1/_{16}$	0.0112
	5	$^1/_{8}$	0.0225
	6	$^1/_{4}$	0.0450
	7	$^1/_{2}$	0.0900
	8	1	0.1800
	9	2	0.3600
CTAC (NaCl experiments used exactly the same concentrations, in order to compare directly it with CTAC)	1	$^1/_{128}$	0.0011
	2	$^1/_{64}$	0.0022
	3	$^1/_{32}$	0.0044
	4	$^1/_{16}$	0.0088
	5	$^1/_{8}$	0.0175
	6	$^1/_{4}$	0.0350
	7	$^1/_{2}$	0.0700

	8	1	0.1400
	9	2	0.2800
CTAB (NaBr experiments used exactly the same concentrations, in order to compare directly it with CTAB)	1	$^1/_{128}$	0.0008
	2	$^1/_{64}$	0.0016
	3	$^1/_{32}$	0.0031
	4	$^1/_{16}$	0.0062
	5	$^1/_{8}$	0.0125
	6	$^1/_{4}$	0.0250
	7	$^1/_{2}$	0.0500
	8	1	0.1000
	9	2	0.2000
BDAC	2	$^1/_{64}$	0.00004
	3	$^1/_{32}$	0.00008
	4	$^1/_{16}$	0.00016
	5	$^1/_{8}$	0.00031
	6	$^1/_{4}$	0.00062
	7	$^1/_{2}$	0.0013
	8	1	0.00255
	9	2	0.00510

4.4 The Electrochemistry of Au (111) in 0.1 M NaF solution

NaF has been used as a baseline electrolyte in the study of cationic adsorption on Au single-crystals because the Na^+ and F^- ions have a solvation layer at the electrode interface. Neither of these ions, therefore, goes into the inner Helmholtz plane. Owing to their non-adsorbing nature, the double-layer region covers a large potential range compared with when acidic electrolytes such as H_2SO_4 or $HClO_4$ have been used.[8] Figure 4.3A gives a cyclic voltammogram and Figure 4.3B gives differential capacitance curves of an Au (111) single-crystal electrode in 0.1 M NaF solution. In Figure 4.1A, the potential range is -700 mV to 500 mV, with a sweep rate of 20 mV s^{-1}. Within this potential range, the Au (111) single-crystal electrode is ideally polarised, and the interface between the electrode and the solution behaves as an ideal capacitor. More negative potentials than -700 mV (vs. SCE) are not used in order to avoid hydrogen evolution. More positive potentials are not investigated because of the formation of the gold oxide layer at potentials more positive than 500 mV (vs. SCE). For the differential capacitance curve in Figure 4.3B, the positive potential limit is also 500 mV. The negative potential limit for the differential capacity curve is -1000 mV. In this potential range, the electrode can be treated as an ideally polarisable interface.

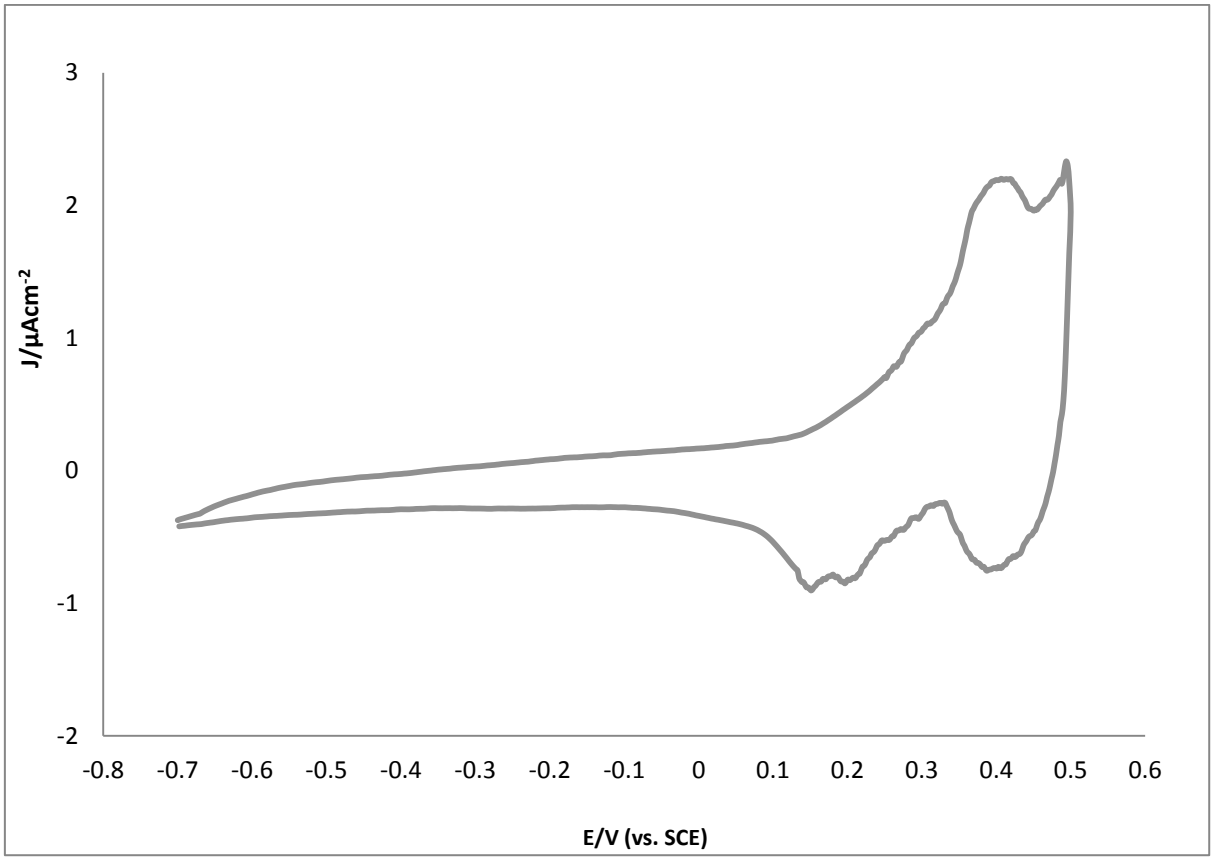

Figure 4.3A. Cyclic Voltammogram of Au (111) in 0.1 M NaF solution.
Sweep rate 20 mV s^{-1}

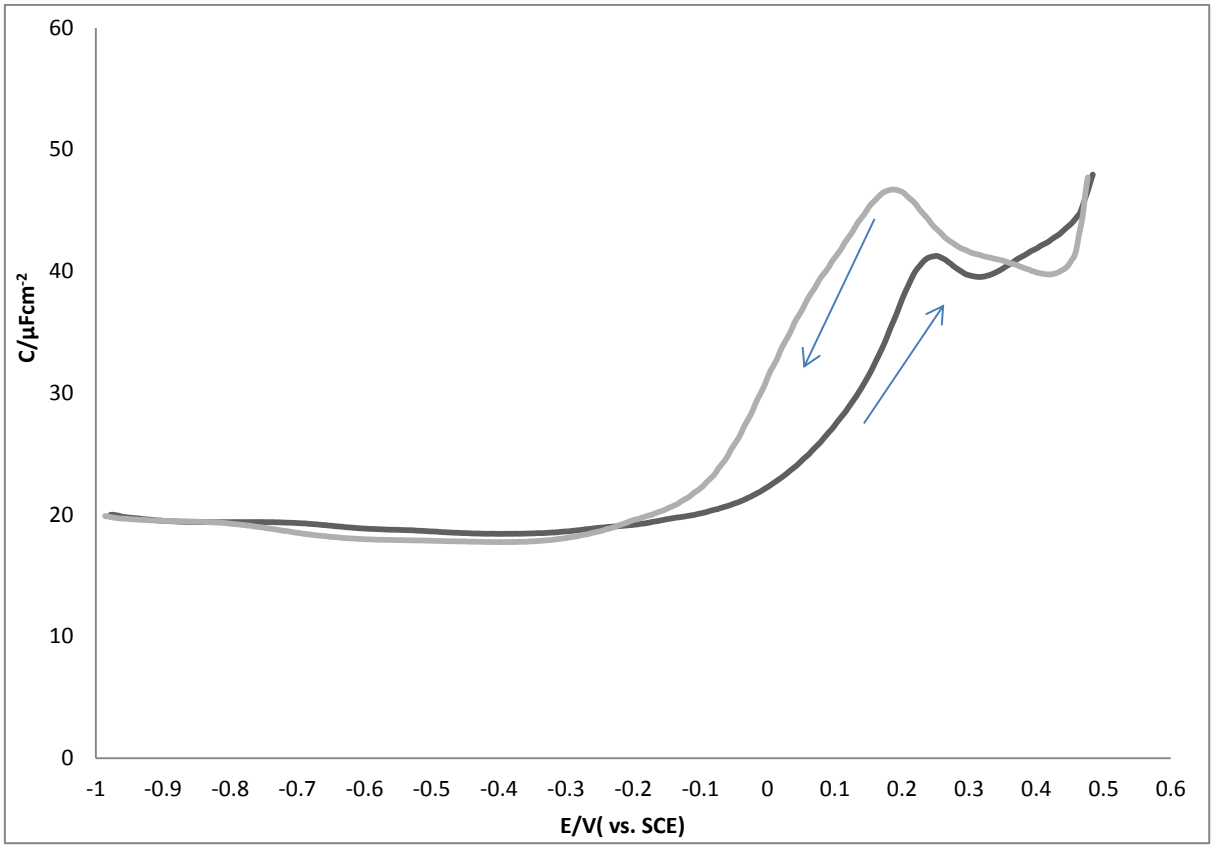

Figure 4.3B Differential Capacity curves of Au (111) in 0.1 M NaF solution. Here, the positive-going sweep is represented by the black line and the negative-going sweep by the grey line.
Sweep rate 5 mV s^{-1}

In Figures 4.3A and 4.3B, at the negative potential limit, there is maximum compression of the reconstructed (23 x $\sqrt{3}$) phase on the Au (111) surface.[9] According to XRD studies, when the Au (111) surface is negatively charged, the Na^+ ion plays a negligible role in the surface structure of the Au (111) surface. If Na^+ is replaced with Li^+ or Cs^+, no difference is observed in the diffraction patterns.[9] In a 0.1 M NaF solution, the potential at which the reconstructed phase of Au (111) is most ordered is found to be -0.2 V (vs. SCE).[9] This is known as the optimum potential (E_{OPT}). It arises because at this potential there is a balance between the driving force of the formation of the reconstructed phase, which is the increase in free energy of the reconstructed phase relative to the (1×1) phase (this increases as the potential

becomes more negative), and the driving force of the lifting of the surface reconstruction, which is the mobility of the surface gold atoms, which increases with increasing potential.[10] [11] At -0.05 V (vs. SCE), the $(23 \times \sqrt{3})$ reconstruction of the Au (111) surface starts to lift.[9] In Figures 4.3A and 4.3B, the current and the differential capacitance begin to increase at this potential in the positive sweep. It has been found through XRD studies that in 0.1 M NaF at 0.5 V (vs. SCE) the $(23 \times \sqrt{3})$ reconstruction is completely lifted.[9] In the anodic sweep, Figure 4.3B, there is a differential capacitance minimum at 290 mV, which represents the potential of zero charge (pzc) of the Au (111) electrode.[12] It is noteworthy that the pzc of an electrode is usually measured in more dilute NaF solution, nevertheless, this value is consistent with previously found pzc values of Au (111) in NaF solutions.[12] There is thus a negligible change in the pzc of Au (111) if the concentration of NaF changes. [9] This shows that no F^- is adsorbed on the Au (111) surface, as the double layer thickness, which is inversely proportional to the square root of the concentration[13] (according to the Grahame model), hardly affects the potential dependence of the Au (111) surface structure.

4.5 The Electrochemistry of Au (111) in NaCl and NaBr solution

Figures 4.4A and 4.4B present CV and DC curves of Au (111) in 0.1 mM NaBr in 0.1 M NaF solution (orange lines), 0.1 mM NaCl in 0.1 M NaF (blue lines) and 0.1 M NaF (black dotted lines).

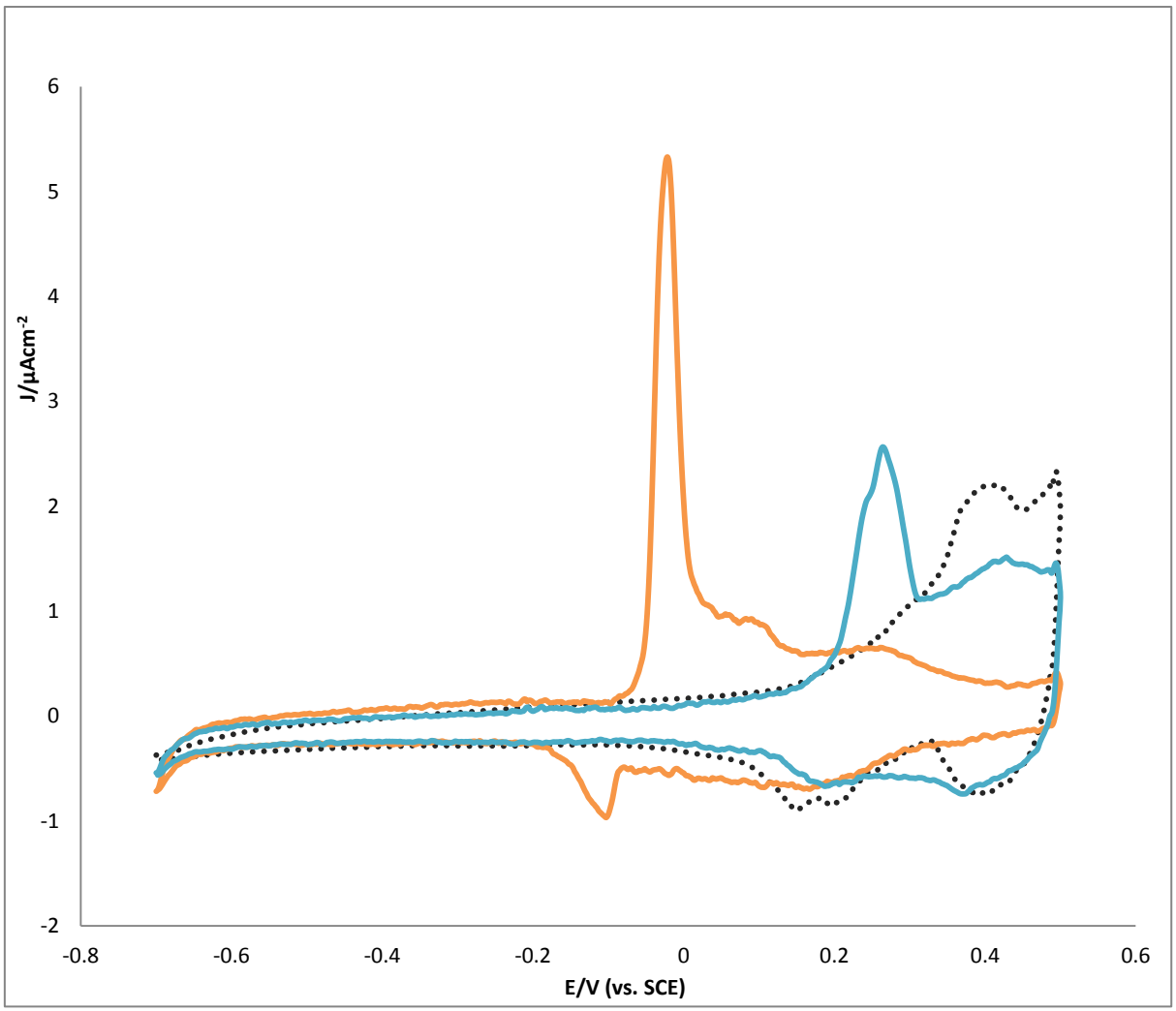

Figure 4.4A Cyclic Voltammogram of Au (111) in 0.1 M NaF solution (black dotted line), 0.1 mM NaCl in 100 mM NaF solution (blue line) and 0.1 mM NaBr in 100 mM NaF solution (orange line). Sweep rate 20 mV s^{-1}

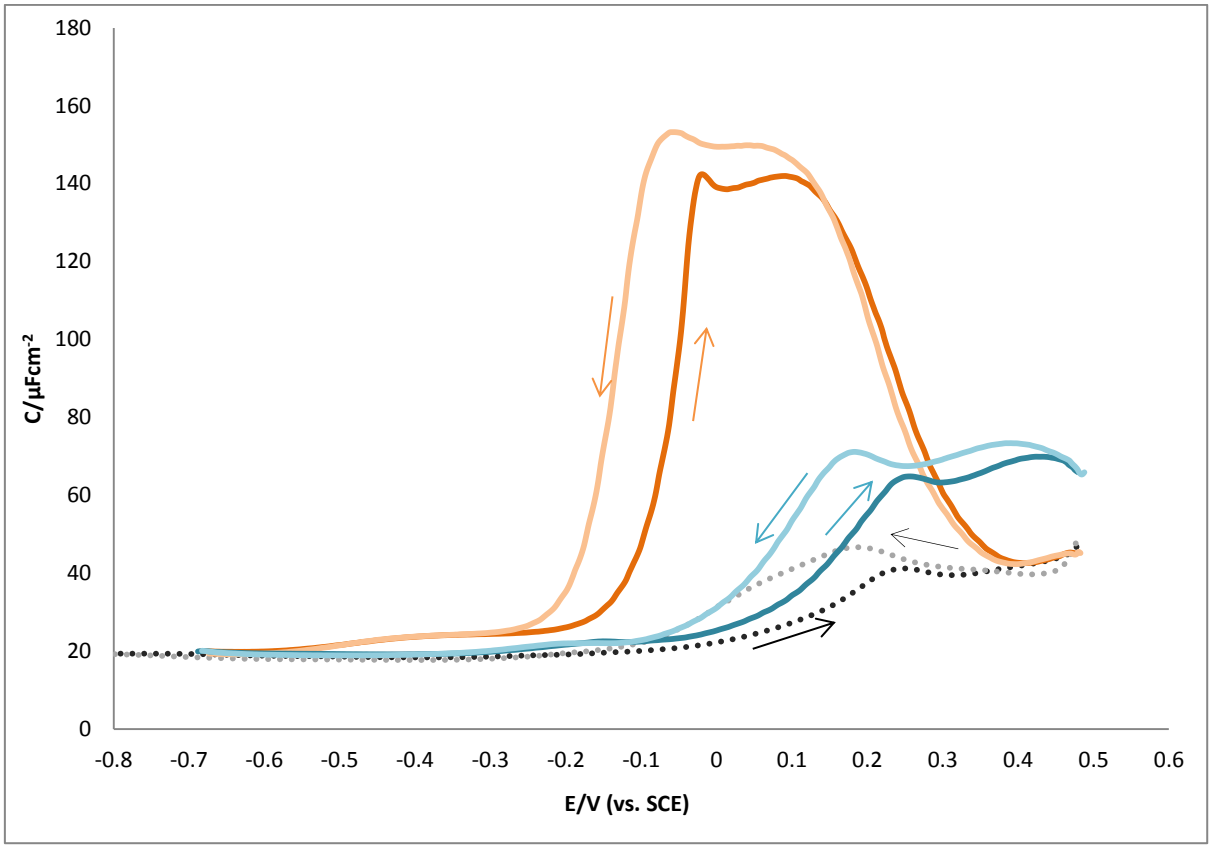

Figure 4.4B Differential Capacitance curves of Au (111) in 0.1 M NaF solution (black dotted lines), 0.1 mM NaCl in 100 mM NaF solution (blue lines) and 0.1 mM NaBr in 100 mM NaF solution (orange lines). The dark shaded lines represent the anodic sweep, and the light shaded lines represent the anodic sweep.
Sweep rate 5 mV s^{-1}

In Figures 4.4A and 4.4B, there are maxima at 250 mV and -25 mV in the CV and DC curves of NaCl and NaBr, respectively. These maxima are caused by the lifting of the reconstruction of the Au (111) surface as a result of Cl^- [14] and Br^- [15] being in the electrolyte solution.

Figures 4.5A and 4.5B show CVs of various concentrations of NaCl (blue lines) and NaBr (orange lines) between 0.001 and 0.2 mM. Both sets of curves acquire progressively lighter shades as the concentration of NaCl/NaBr in the 0.1 M NaF increases. The CV of Au (111) in 0.1 M NaF (black dotted line) is added for reference.

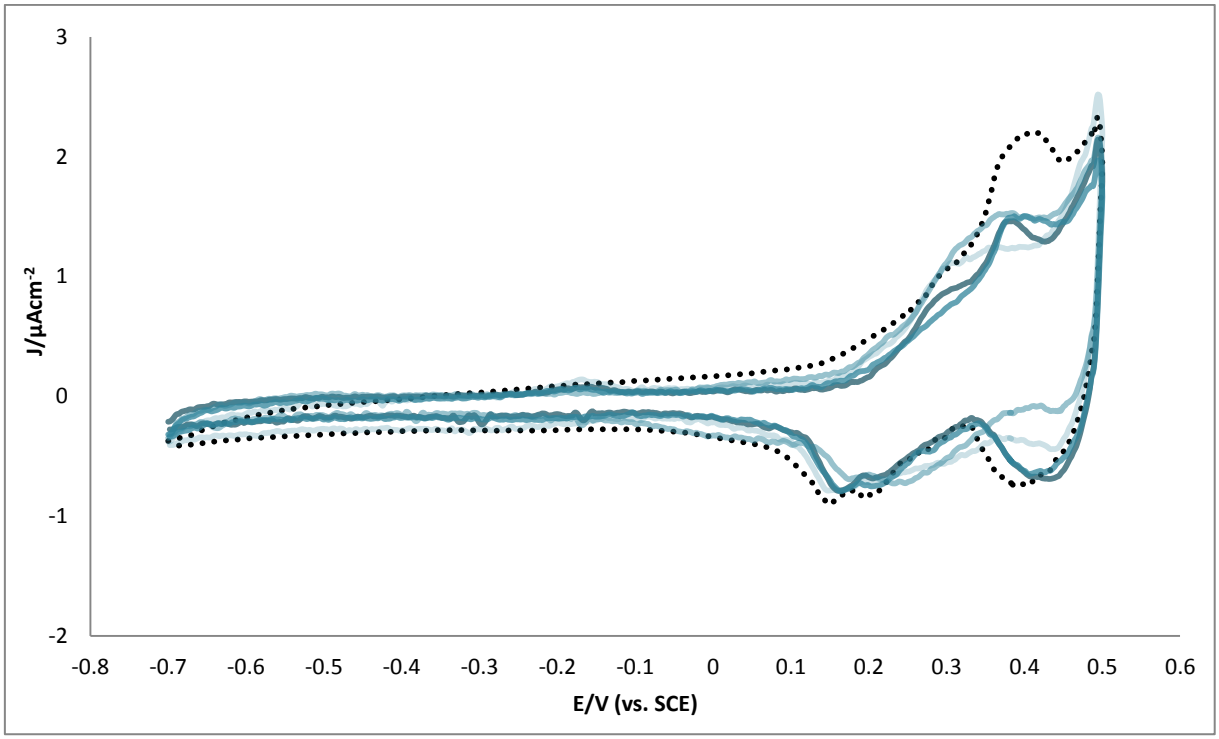

Figure 4.5A (i) Cyclic Voltammetry curves recorded for Au (111) in 100 mM NaF solution without NaCl (black dotted line), and with selected NaCl concentrations starting from 0.001 mM NaCl (darkest blue line) to 0.01 mM NaCl (lightest blue line).
Sweep rate 20 mV s^{-1}

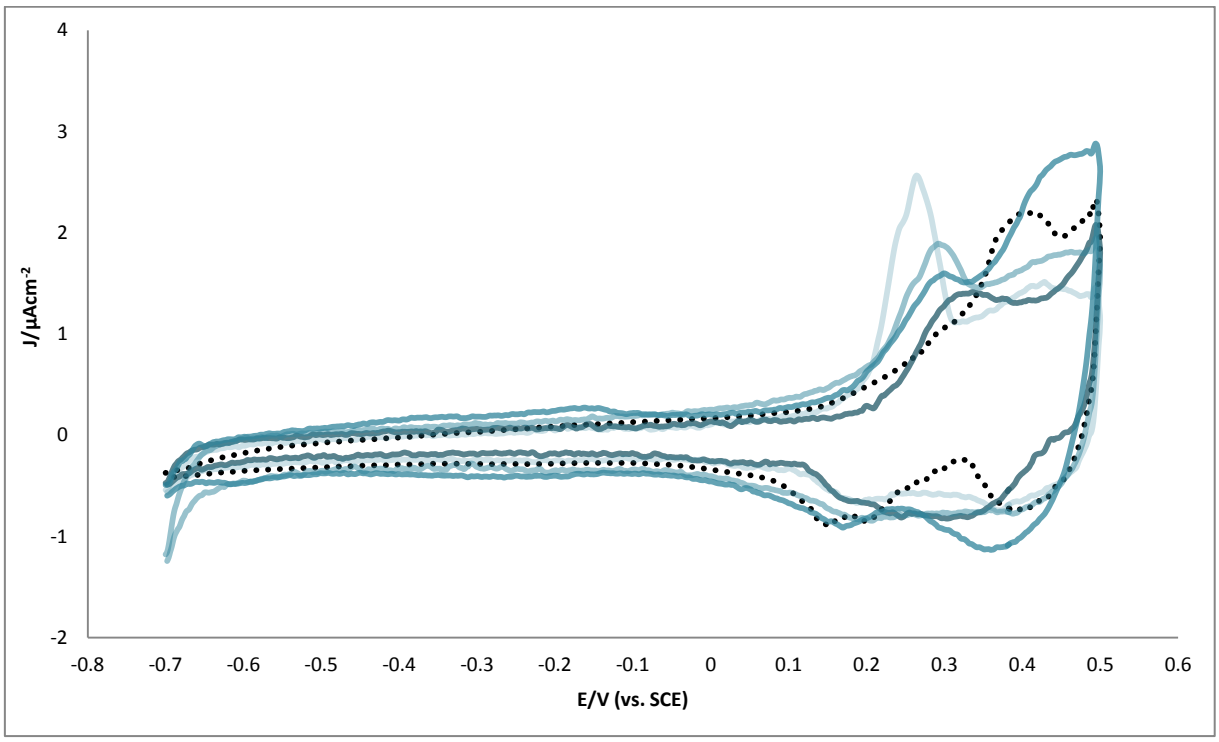

Figure 4.5A (ii) Cyclic Voltammetry curves recorded for Au (111) in 100 mM NaF solution without NaCl (black dotted line), and with selected NaCl concentrations starting from 0.025 mM NaCl (darkest blue line) to 0.2 mM NaCl (lightest blue line).
Sweep rate 20 mV s^{-1}

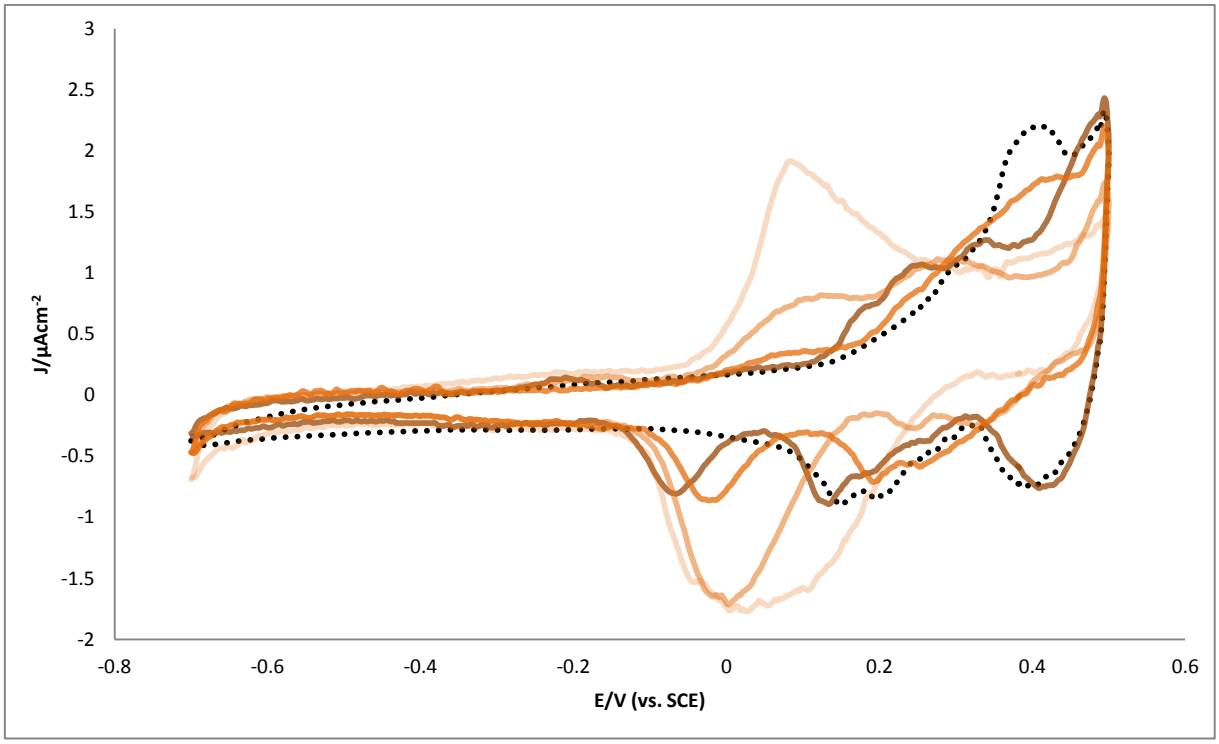

Figure 4.5B (i) Cyclic Voltammetry curves recorded for Au (111) in 0.1 M NaF solution without NaBr (black dotted line), and with selected NaBr concentrations starting from 0.001 M NaBr (darkest orange line) to 0.01 mM NaBr (lightest orange line).
Sweep rate 20 mV s^{-1}

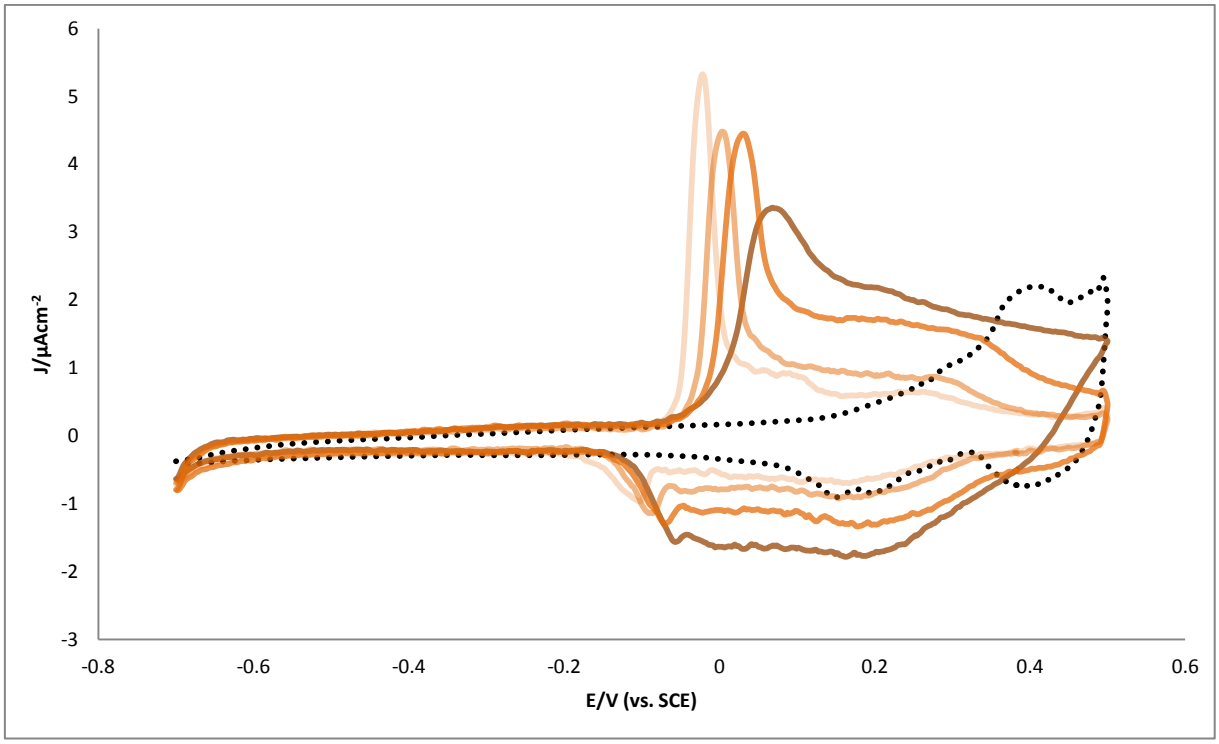

Figure 4.5B (ii) Cyclic Voltammetry curves recorded for Au (111) in 0.1 M NaF solution without NaBr (black dotted line), and with selected NaBr concentrations starting from 0.025 M NaBr (darkest orange line) to 0.2 mM NaBr (lightest orange line).
Sweep rate 20 mV s^{-1}

Figure 4.5A clearly shows that the peak potential of the phase transition becomes more negative as the concentration of NaCl increases. When the concentration of NaCl is 0.025 mM or less, a defined phase transition peak is not observed in the CV, possibly because the concentration of Cl^- ions in the solution is too low to influence the phase transition of the Au (111) surface.

For NaBr, Figure 4.5B, a defined phase transition or lifting of the $(23 \times \sqrt{3})$ reconstruction is observed when the concentration of NaBr is as low as 0.01 mM. This indicates that Br^- has a stronger interaction with the Au (111) surface than Cl^-. Br^- thus influences the single-crystal surface structure more.

Figures 4.6A and 4.6B give the cathodic sweeps of DC curves of Au (111) in a 0.1 M NaF solution containing concentrations of NaCl and NaBr at regular increments between 0.001 mM and 0.2 mM. As with the CV curves in Figure 4.3, the DC curves acquire progressively lighter shades of blue and orange as the concentrations of NaCl and NaBr increase. In Figures 4.6A and 4.6B, the baseline cathodic DC curve of Au (111) in 0.1 M NaF solution is represented by a black dotted line.

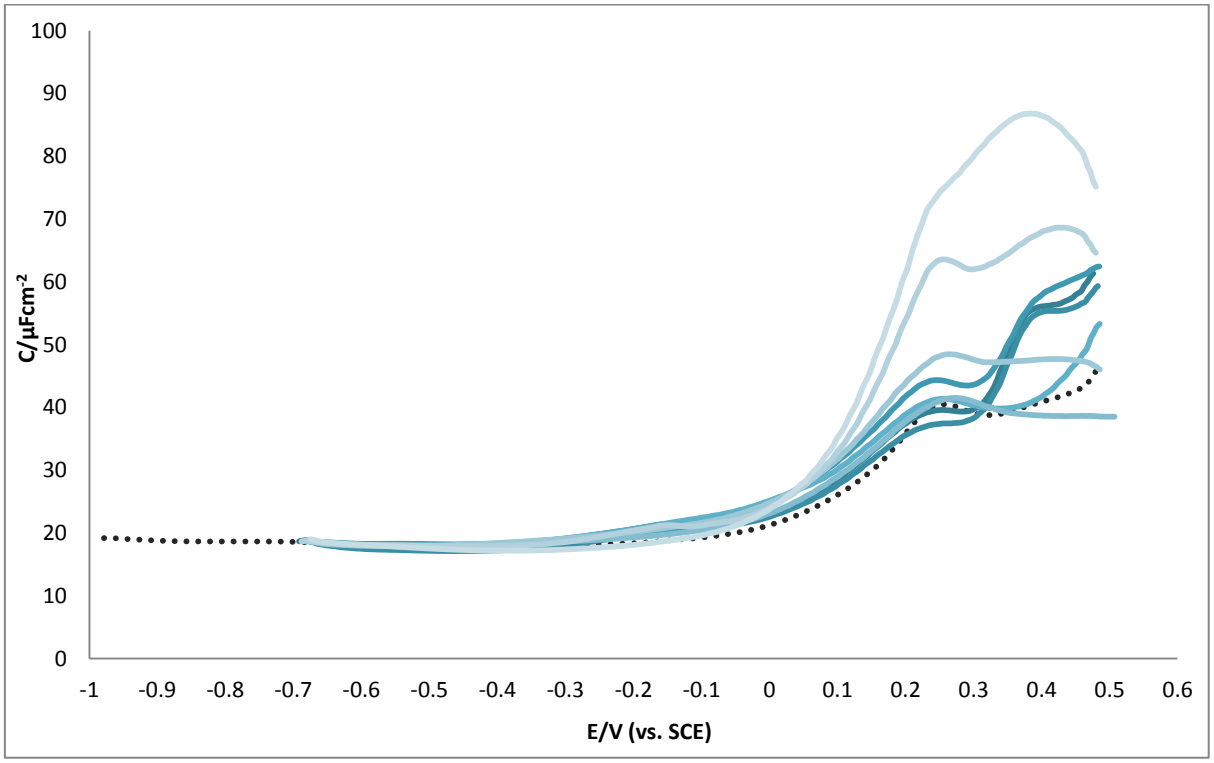

Figure 4.6A Differential Capacitance curves of the cathodic sweep recorded for Au (111) in 0.1 M NaF solution without NaCl (black dotted line); and with selected NaCl concentrations starting from 0.001 mM NaCl (darkest blue line) to 0.2 mM NaCl (lightest blue line).
Sweep rate 5 mVs^{-1}

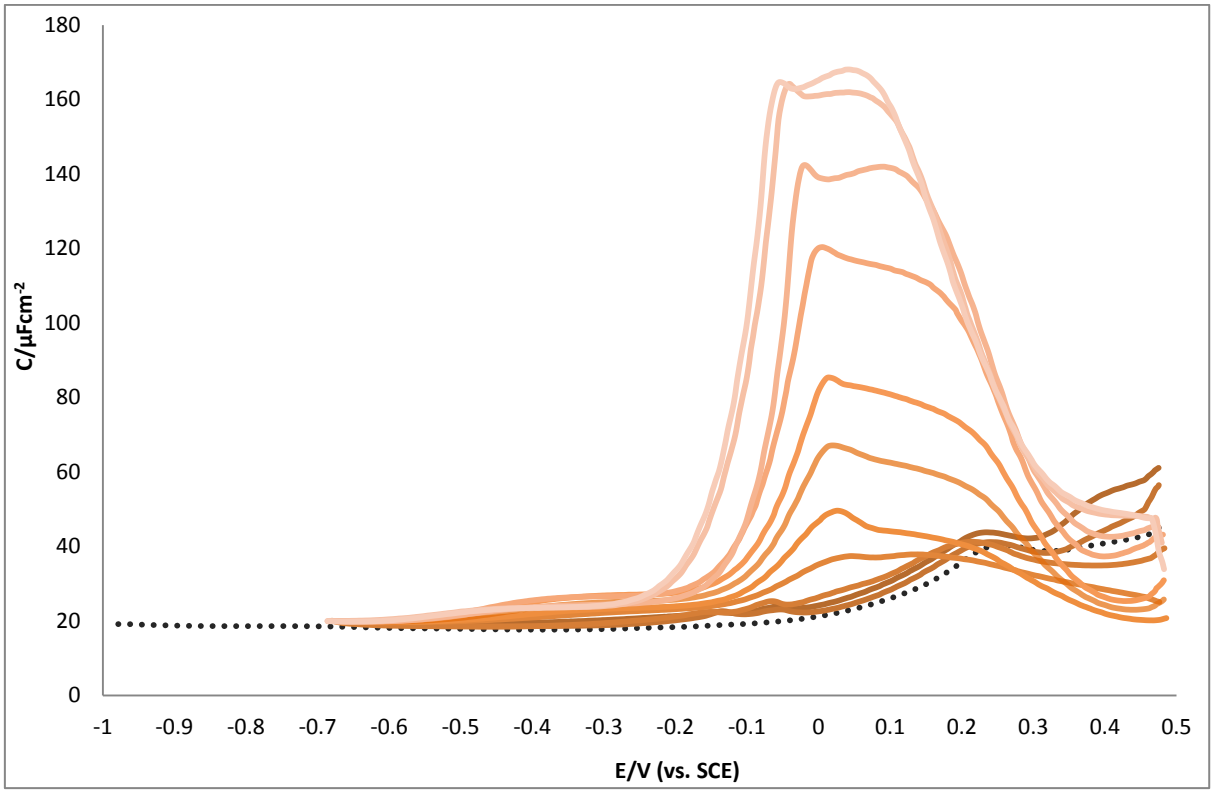

Figure 4.6B Differential Capacitance curves of the cathodic sweep recorded for Au (111) in 0.1 M NaF solution without NaBr (black dotted line), and with selected NaBr concentrations starting from 0.001 mM NaBr (darkest orange line) to 0.2 mM NaBr (orange line).
Sweep rate 5 mV s^{-1}

Figures 4.5 and 4.6 indicate that the adsorption of Cl^- and Br^- on the Au (111) causes the lifting of the $(23 \times \sqrt{3})$ surface reconstruction to occur at progressively more negative potentials as the concentration of the ions increases. Previous studies on single crystal surfaces under electrochemical conditions have suggested that the adsorption of anions is the reason for lifting of single-crystal surface reconstructions.[16] However, there has been no conclusive evidence of the role of anions in this process.

It is clear from the increase in differential capacitance, Figure 4.6, as the concentration of NaCl and NaBr increases, that Cl^- and Br^- ions are present on the Au (111) surface as the $(23 \times \sqrt{3})$ reconstruction lifts. However, as discussed in Section 4.4, when Au (111) is in

NaF solution, no fluoride anions are adsorbed on the Au (111) as the surface reconstruction lifts.

Anion adsorption is thus not the only cause of the lifting of the $(23 \times \sqrt{3})$ reconstruction on the Au (111) surface. The potential at which the Au (111) surface reconstruction lifts is due to the surface charge density, which is a function of both applied potential and anion adsorption. When the Au surface is negatively charged, there is a high sp-electron density between the Au surface atoms, thus bringing about increased attraction between these atoms and allowing for a $(23 \times \sqrt{3})$ reconstruction. When the Au surface is positively charged, the sp-electron density decreases and the $(23 \times \sqrt{3})$ lifts, with the (1×1) structure being more stable. Since Cl^- or Br^- anions are adsorbed at the electrode interface, the Au (111) becomes more positively charged.[9] There has been much evidence that surface charge, rather than simply ion adsorption, is the cause of changes in single-crystal electrode surface structure.[17 18 4 19]

Figures 4.7A and 4.7B show a family of charge curves for Au (111) in several concentrations of NaCl and NaBr, respectively, from 0.001 mM to 0.05 mM. The charge densities were measured by holding the Au (111) electrode in the solution containing NaCl or NaBr long enough for adsorption equilibrium to be reached (up to 3 minutes) and measuring the charge during desorption. The charge densities therefore represent the state of adsorption equilibrium.

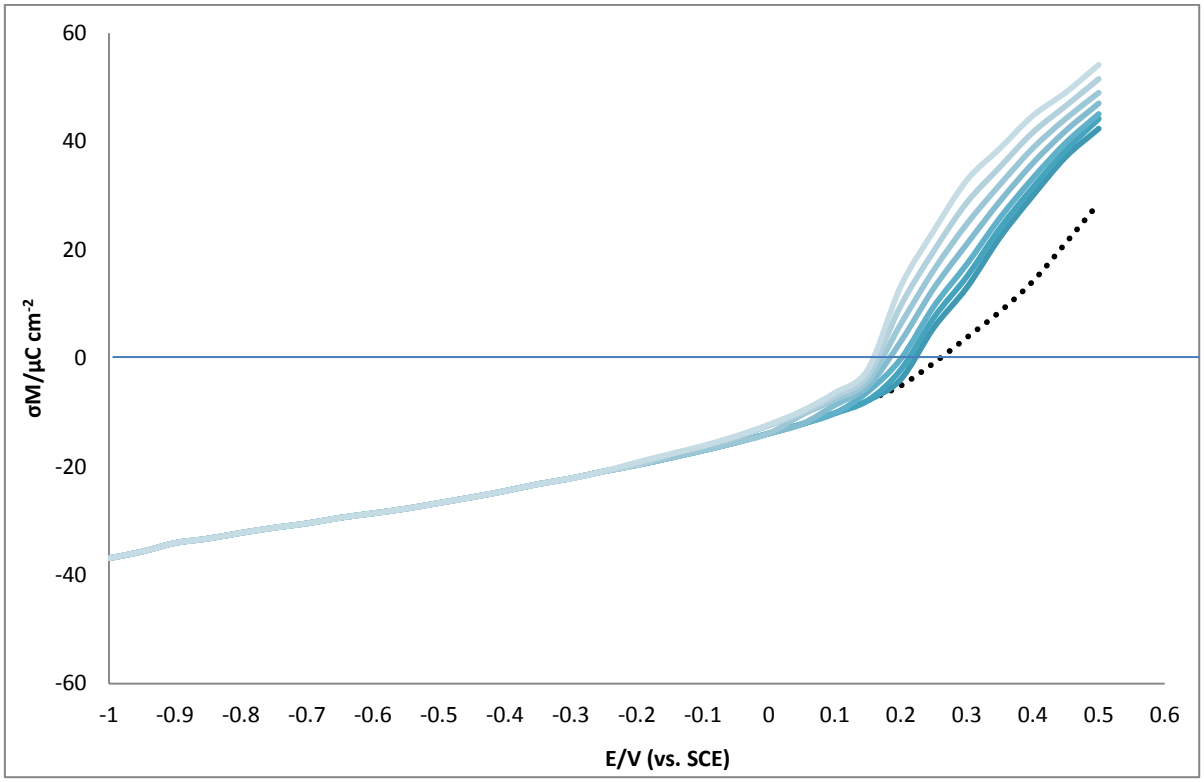

Figure 4.7A Charge density versus electrode potential curves for Au (111) in pure 0.1 M NaF solution (black dotted line), and with selected NaBr concentrations starting from 0.001 M NaBr (darkest blue line) to 0.05 mM NaBr (lightest blue line).

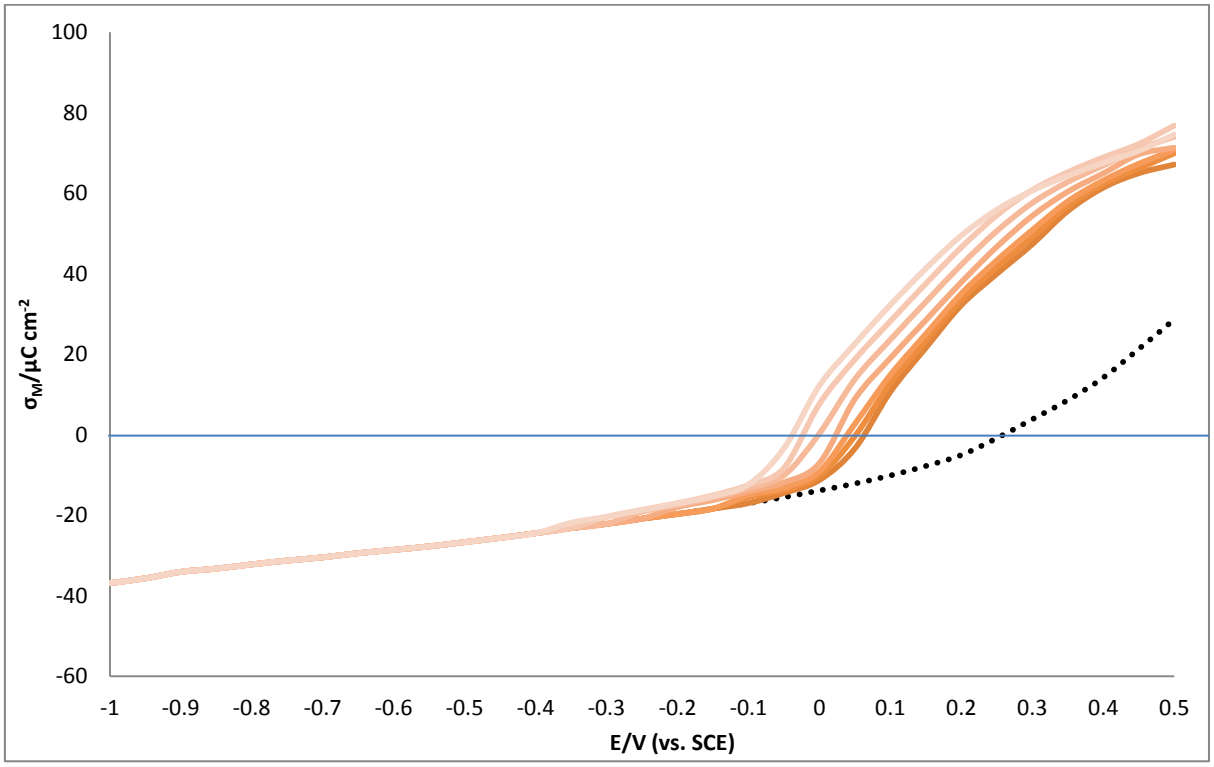

Figure 4.7B Charge density versus electrode potential curves for Au (111) in pure 0.1 M NaF solution (black dotted line), and with selected NaBr concentrations starting from 0.001 M NaBr (darkest orange line) to 0.05 mM NaBr (lightest orange line).

Figure 4.7 clearly shows that the presence of Cl^- and Br^- ions in the solution make the pzc of the electrode become more negative in potential. The pzc of the electrode surface can be seen on a charge versus potential curve when the lines cross the x-axis.

According to Figure 4.7A, the onset potential of the Cl^- adsorption (the potential at which the charge becomes more positive of the baseline charge curve) becomes more negative as the bulk concentration of NaCl increases. The shape of the charge curves in Figure 4.7A are consistent with charge curves previously recorded of Au (111) in a solution containing a base electrolyte of $HClO_4$ and various concentrations of KCl.[14] The steep increase in charge at 200

mV correlates with the sharp peak observed for the CV of Au (111) in NaCl in Figure 4.3A, which represents the lifting of the Au (111) surface reconstruction.

The charge curves of Au (111) in solutions containing various concentrations of NaBr in 0.1 M NaF solution, Figure 4.5B, are consistent with the charge curves of Au (111) in a solution containing a base electrolyte of $HClO_4$ and various concentrations of KBr.[15] As with Figure 4.7A, the onset of the increase in charge as a result of Br^- adsorption becomes more negative as the bulk concentration of NaBr increases. The onset potential decreases from -100 mV, when the bulk concentration of NaBr is 0.001 M, to -500 mV, when the bulk concentration of NaBr is 0.05 mM. In the potential range between -500 mV and -100 mV, the charge density is only slightly greater than the base electrolyte charge. This area corresponds to a low coverage of adsorbed Br^- ions, which are disordered. The sharp increase in current from around -100 mV is caused by the lifting of the Au (111) surface reconstruction. Surface X-ray scattering (SXS) studies have shown that from the potential at which the rapid rise in the current occurs in Figure 4.5B, a much denser layer of bromide is formed on the electrode surface.[20] However, although there is a densely packed Br^- layer in this potential region, studies have shown that the bromide adlayer structure remains largely disordered.[21]

When $E \geq 300$ mV, the decrease of the charge slopes in Figure 4.7B, especially at higher Br^- concentrations, signifies the ordering of the Br^- adlayer to form a hexagonal overlayer. The ordering of the Br^- layer in this potential region has been shown with SXS[20] and STM.[22] The ordering of the Cl^- overlayer on an Au (111) surface has been found to occur at 750 mV (vs. SCE);[23] this is far too positive a potential of the double-layer potential region used in this study.

Figures 4.8A and 4.8B give plots of the Gibbs excess of Cl^-, and Br^- versus the electrode potential for bulk concentrations of NaCl and NaBr between 0.002 and 0.05 mM. Details on how the Gibbs excess is calculated are given in Section 1.3. As with all the previous Figures, the lines acquire progressively lighter shades of blue and orange as the bulk concentrations increase.

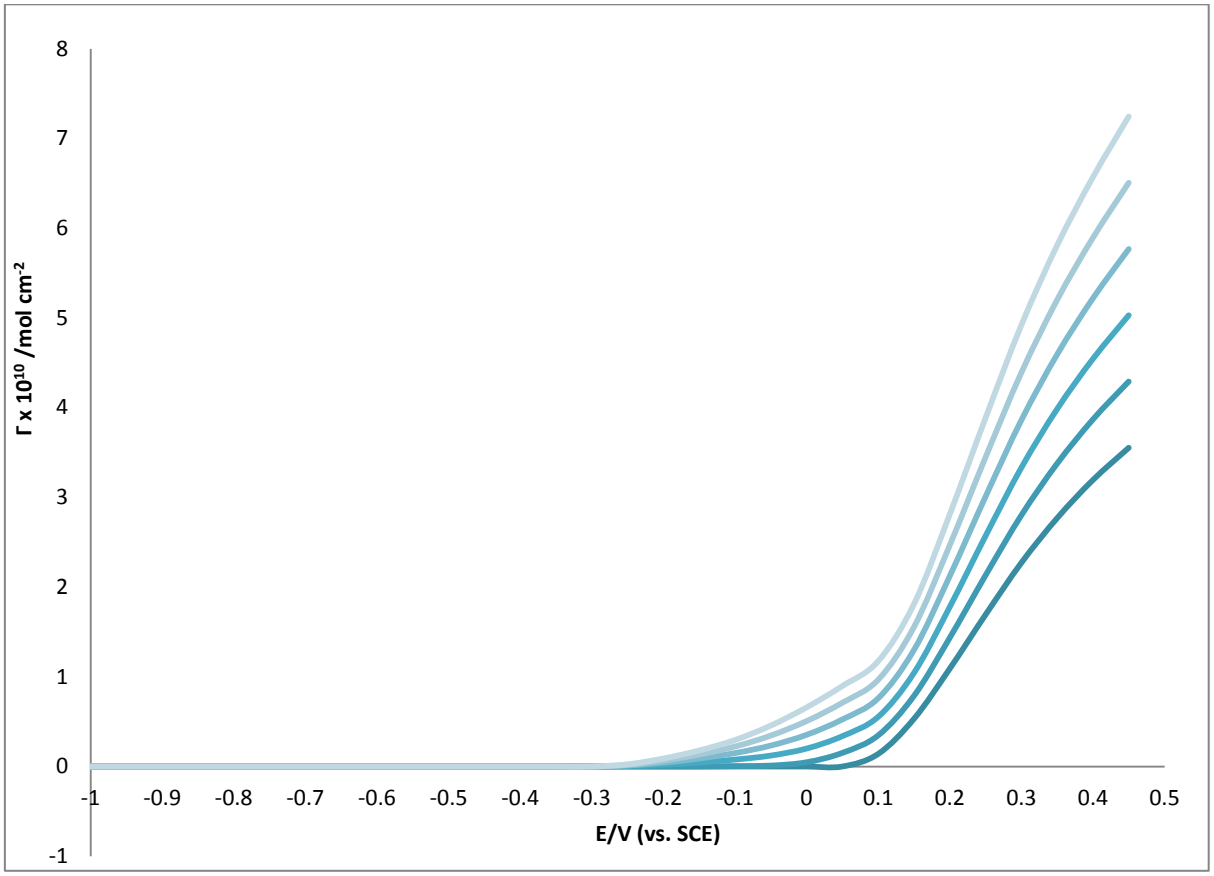

Figure 4.8A Plot of the Gibbs excess of NaCl versus the electrode potential for various bulk NaCl concentrations between 0.002 mM (darkest blue line) and 0.05 mM (lightest blue line).

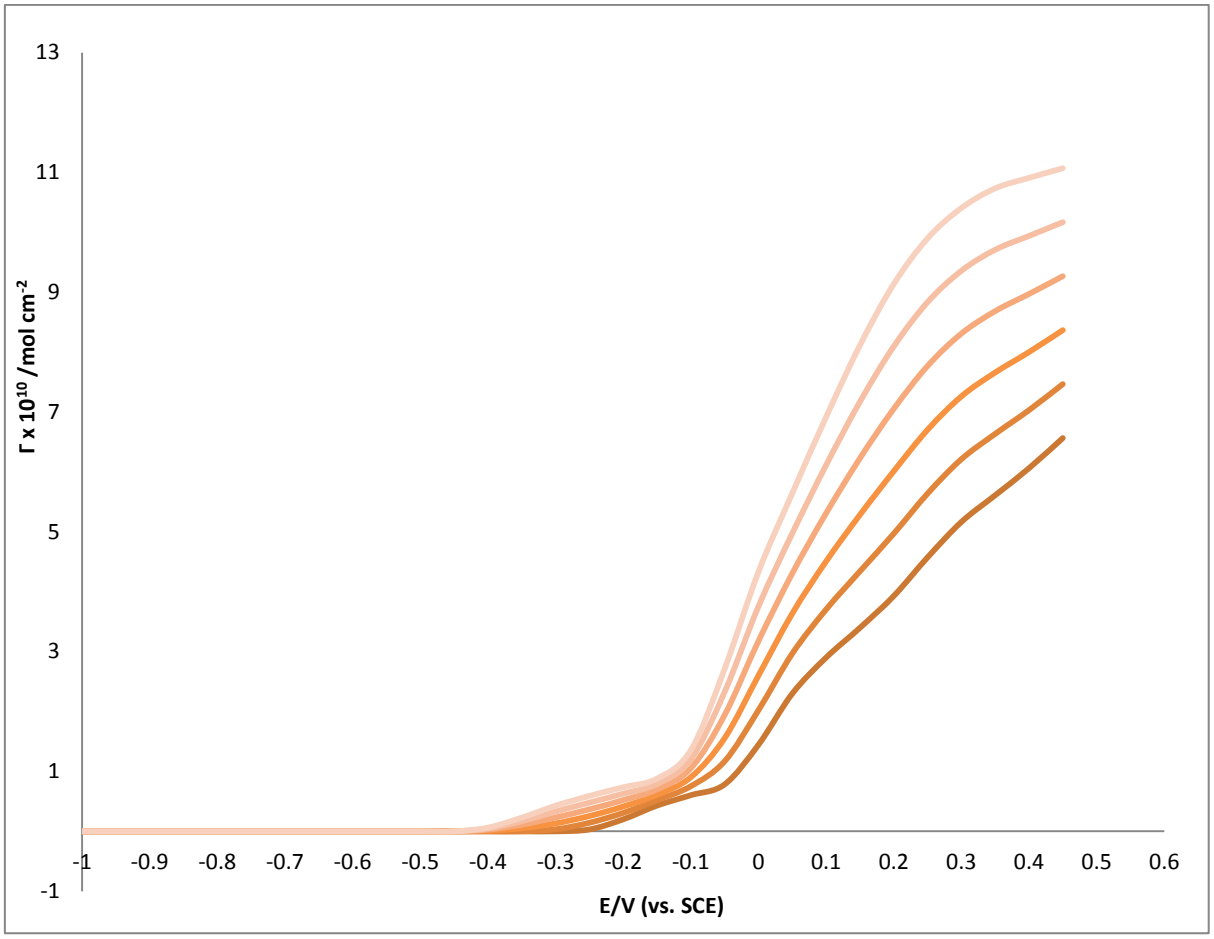

Figure 4.8B Plot of the Gibbs excess of NaBr versus the electrode potential for various bulk NaBr concentrations between 0.002 mM (darkest orange line), and 0.05 mM (lightest orange line).

The Gibbs excess data in Figures 4.8A and 4.8B show the characteristic sections mentioned for the charge changes with potential, observed in Figures 4.7A and 4.7B. In Figure 4.8A, the dependence of the Gibbs excess values on the bulk concentration reflects the disorder of the Cl^- layer on the Au (111) surface. In Figure 4.8B, for the highest concentration (0.05 mM), when $E \geq 300$ mV, the Gibbs excess plateaus, indicating that a maximum Br^- coverage has been reached. This results in the hexagonal close packed adlayer structure of Br^- anions on the Au (111) surface being formed.

4.6 The Electrochemistry of Au (111) in CTAF solution

A better idea of the structure of CTA^+ layers on an Au (111) surface can be obtained by studying the adsorption of CTAF rather than CTAC or CTAB because the F^- counter-ion does not specifically adsorb on the electrode surface.

The DC and CV curves in this section and the rest of Chapter 4 are split into four sections: Section I is at $E \leq$ -400 mV, Section II between -400 mV and 50 mV, Section III between 50 mV and 400 mV and Section IV between 400 mV and 500 mV.

Figures 4.9A and 4.9B give CVs and DCs of the Au (111) electrode when CTAF is in 0.1 M NaF solution after Addition 7 (1/2 CMC of CTAF in NaF solution, 0.09 mM). The CV and DC curves of the Au (111) electrode are also added for reference; these are represented by black/grey dotted lines.

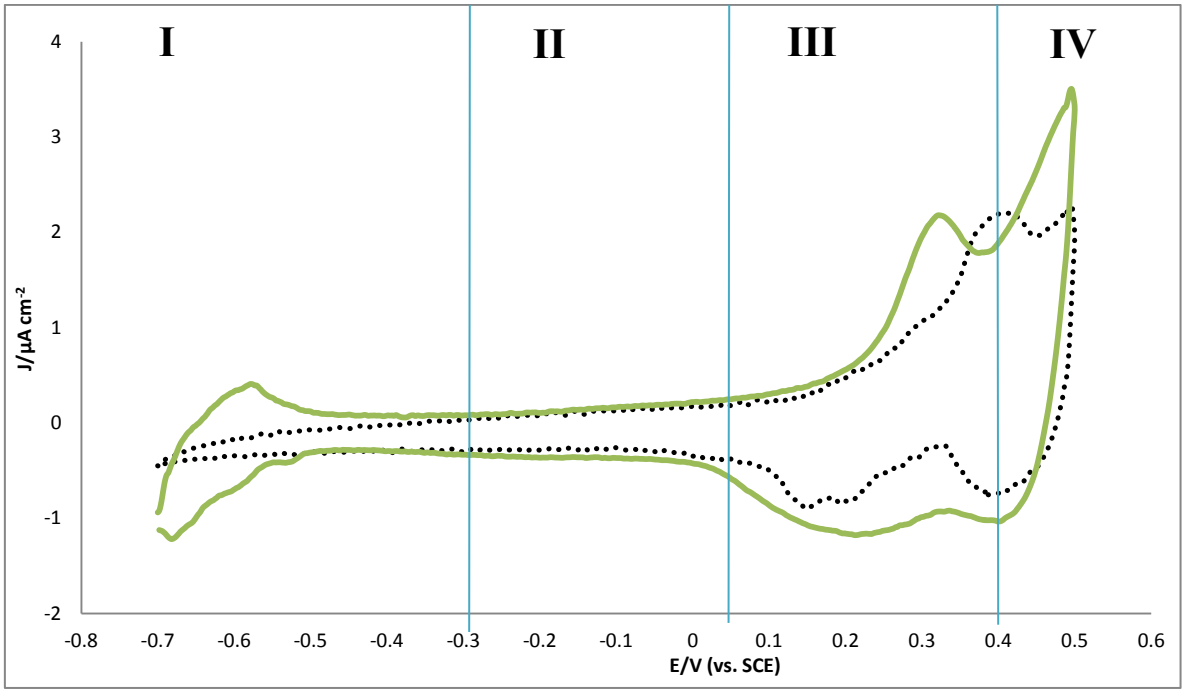

Figure 4.9A A cyclic voltammogram of Au (111) in 0.1 M NaF with CTAF after Addition 7 (1/2 CMC of CTAF in 0.1 M NaF solution; 0.09 M). A CV of Au (111) in 0.1 M NaF solution (black dotted line) is also included as a reference.
Sweep rate 20 mV s^{-1}

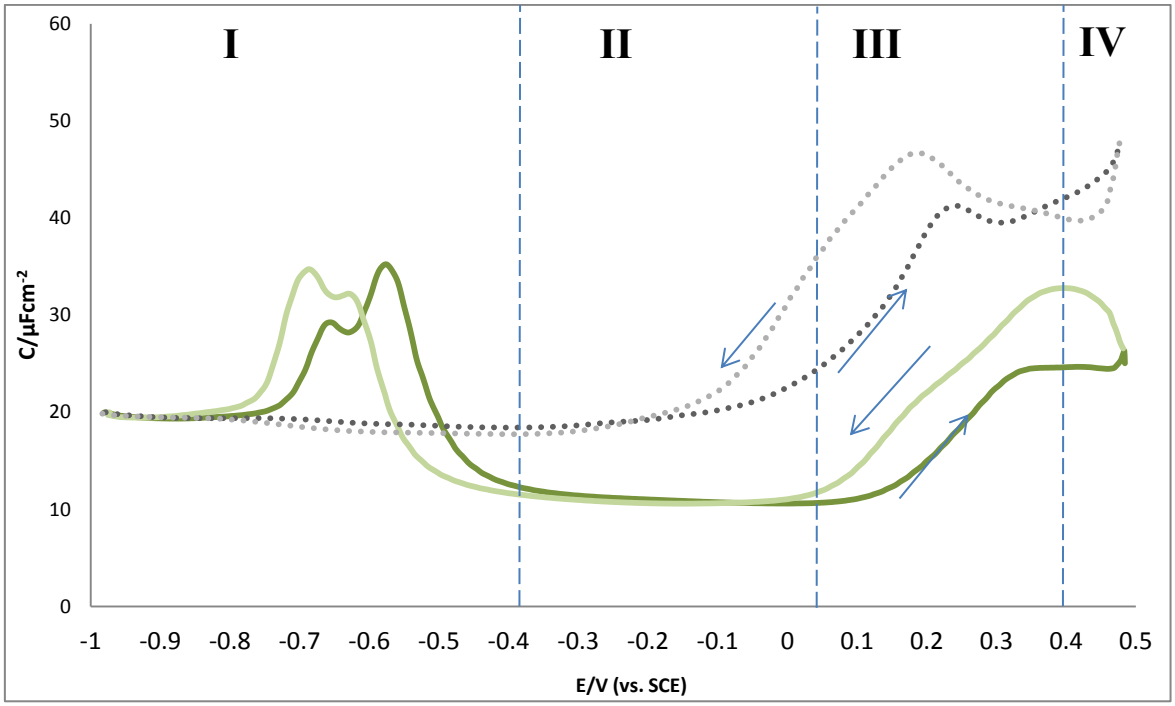

Figure 4.9B Differential capacitance curves of Au (111) in 0.1 M NaF with CTAF after Addition 7 (1/2 CMC of CTAF in 0.1 M NaF solution; 0.09 M). The positive-going sweep is represented by the dark green line; the negative-going sweep, by the light green line. A CV of Au (111) in 0.1 M NaF solution (black dotted line) is also included for reference.
Sweep rate 5 mV s^{-1}

In Region I, Figure 4.9A, a peak in the current is observed on the anodic and cathodic sweeps. The current peak in the anodic sweep is due to the adsorption of the surfactant on the Au (111) surface; the peak in the current in the anodic sweep is due to the desorption of the surfactant from the Au (111) surface. In Region III, there is a steep increase in current in the cathodic sweep at 150 mV, culminating in a peak in the current, probably caused by a phase change in the surfactant film.[24] In Region IV, there is a sharp increase in the current density caused by the onset of the hydroxide adsorption and pre-oxidation of the gold surface.

CVs have previously been carried out on the cationic surfactant DeTATf in 0.1 M NaF solution.[24] DeTATf is similar to CTAF; it too has a trimethyl ammonium cationic head group,

but in this case its alkyl tail group consists of ten carbon atoms, rather than the 16 present in the tail group of CTAF. It also has a significantly larger counter-ion; trifluromethane sulphonate, as opposed to fluoride, (though it is also non-adsorbing). The noticeable difference between both CVs, are the current peaks in Region I caused by the adsorption and desorption of the surfactant. For DeTATf, the adsorption and desorption peaks are at the same potentials and hence more reversible than the corresponding peaks on CTAF. The other difference is that the DeTATf surfactant adsorption and desorption peaks are at more positive potentials -550 mV (vs. SCE), as opposed to CTAF, which has adsorption and desorption peaks at -600 mV and -670 mV (vs. SCE), respectively.

The more negative position of the adsorption/desorption peaks for CTAF could indicate that CTA^+ couples less with its F^- counter-ion than decyltrimethylammonium ($DeTA^+$) couples with its trifluoromethanesulphonate (Tf^-) counter-ion. Surfactant adsorption and desorption peaks for the zwitterionic surfactant DDAPS has been found to be at around -500 mV (vs. SCE).[25]

In Region I of the DC curves, Figure 4.9B, two peaks can be observed representing adsorption and desorption of the surfactant. The peaks representing surfactant adsorption are at -590 and -670 mV; those corresponding to desorption peaks are at -620 and -690 mV. The double peaks observed for the adsorption and desorption of the surfactants could indicate two different types of adsorption on the Au (111) surface. Another possibility is that the more negative absorption and desorption peaks at -670 and -690 mV, respectively, represent the CTA^+ molecules adsorbed on the Au (111) surface. The peaks at the more

positive potentials of -590 and -620 mV could correspond to adsoption/desorption of CTA^+ ions coupled with F^- counter ions.

In Region II, a capacitance minimum of 10.3 µF cm^{-2} can be observed between -380 and 90 mV. The most likely cause of this extended region of minimum capacitance is the compact surfactant layer on the Au (111) surface. This capacitance minimum could indicate that in potential Region II, the CTAF surfactant molecules on the Au (111) surface are in one phase or state. A DC plot has previously been reported for Au (111) in NaF solution containing the cationic surfactant DeTATf, [24] also with a bulk concentration equivalent to that of Addition 7 (around ½ CMC of DeTATf in 0.1 M NaF solution). In Region II of that plot, the differential capacitance is not at a minimum over a larger potential range, as it is when CTAF is in the solution. A minimum is reached; then the DC curve gradually increases. STM images of DeTATf on Au (111) show that there is no ordered surfactant layer in potential Region II. There is a mobile surfactant film followed by a disordered layer.[26] CTA^+ having less coupling with its F^- counter-ion, than $DeTA^+$ with its triflate counter-ion could be the reason why there is a more stable surfactant layer at negative potentials when CTAF is in the solution. The negatively charged Au (111) surface in this potential region could shield the repulsive forces between the positively charged trimethyl ammonium headgroups, thus allowing a stable surfactant layer to form and providing an attraction which would encourage this layer to form.

In Region III of Figure 4.9B, it is unclear whether the increase in capacitance is due to the lifting of the $(23 \times \sqrt{3})$ surface reconstruction or to the phase change of the surfactant film. It is most likely to be a combination of both, as both these chemical changes happen at

a similar potential. It is clear that a phase change occurs at this potential because of the phase change peak of the CV of CTAF in Figure 4.9A, and also by analogy with DeTATf.

Figures 4.10A and 4.10B give CVs and DC curves for Au (111) in 0.1 M NaF solution with CTAF after Additions 1-8 (1/128 CMC to the CMC of CTAF in 0.1 M NaF solution: 0.0014-0.18 mM). The lines become progressively lighter shades of green as the concentration of CTAF in the NaF solution increases. The baseline CVs and DCs of Au (111) in 0.1 M NaF are represented by a black dotted line.

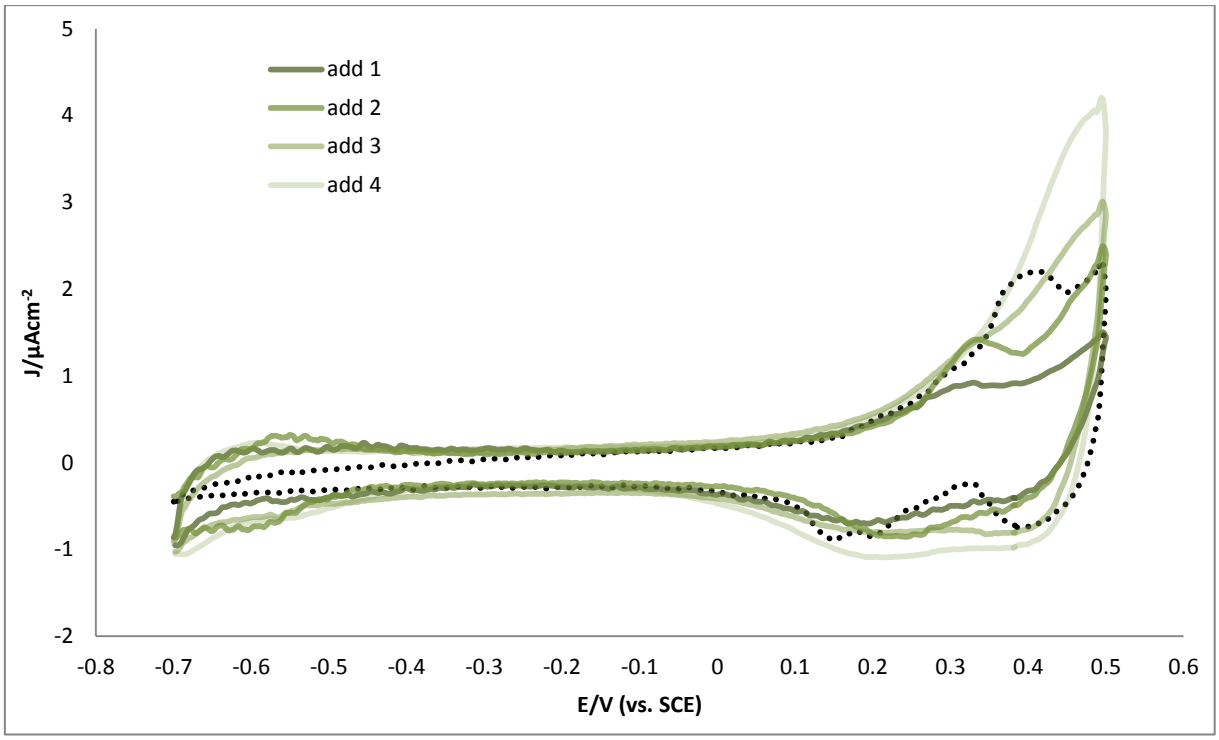

Figure 4.10A (i) Cyclic voltammetry curves recorded for Au (111) in 0.1 M NaF solution without CTAF (black dotted line), with CTAF concentrations after Additions 1-4 (1/128 CMC to 1/16 CMC of CTAF in 0.1 M NaF solution: 0.0014-0.0112 mM). The CV curves acquire progressively lighter shades of green as the bulk concentration of CTAF increases.
Sweep rate 20 mV s^{-1}

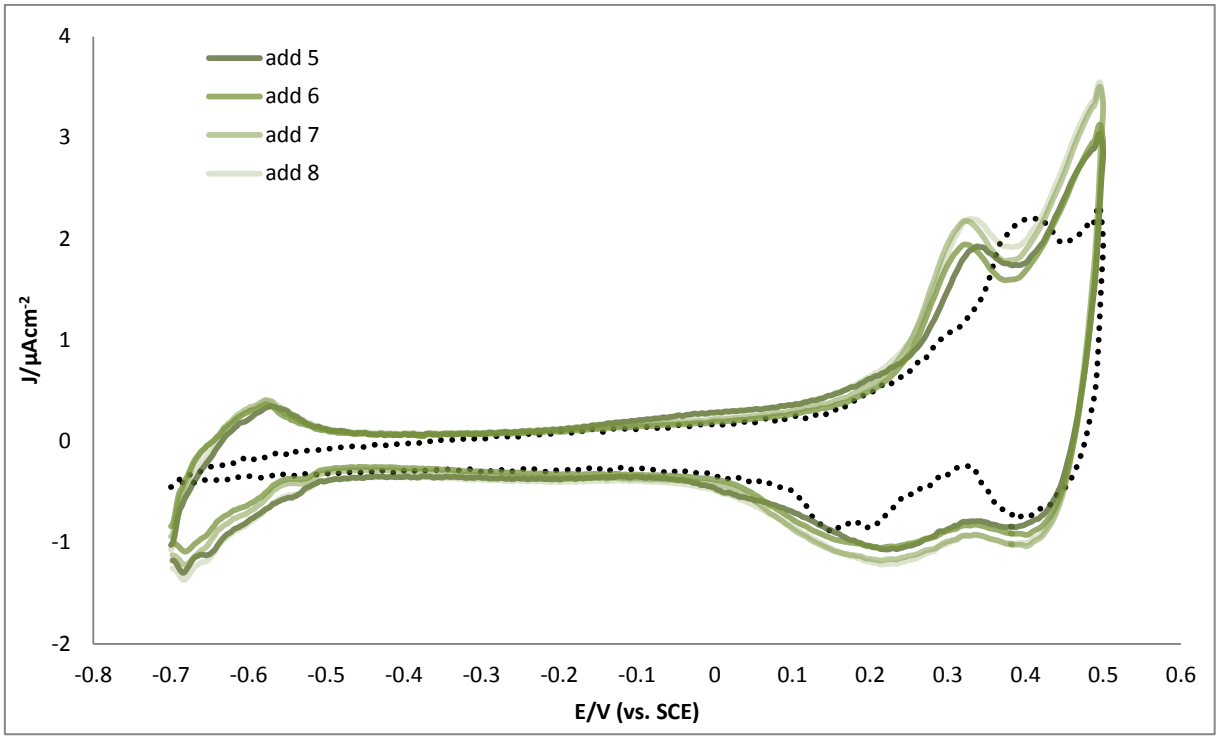

Figure 4.10A (ii) Cyclic voltammetry curves recorded for Au (111) in 0.1 M NaF solution without CTAF (black dotted line), with CTAF concentrations after Additions 5-8 (1/8 CMC to the CMC of CTAF in 0.1 M NaF solution: 0.0225-0.18 mM). The CV curves acquire progressively lighter shades of green as the bulk concentration of CTAF increases.
Sweep rate 20 mV s^{-1}

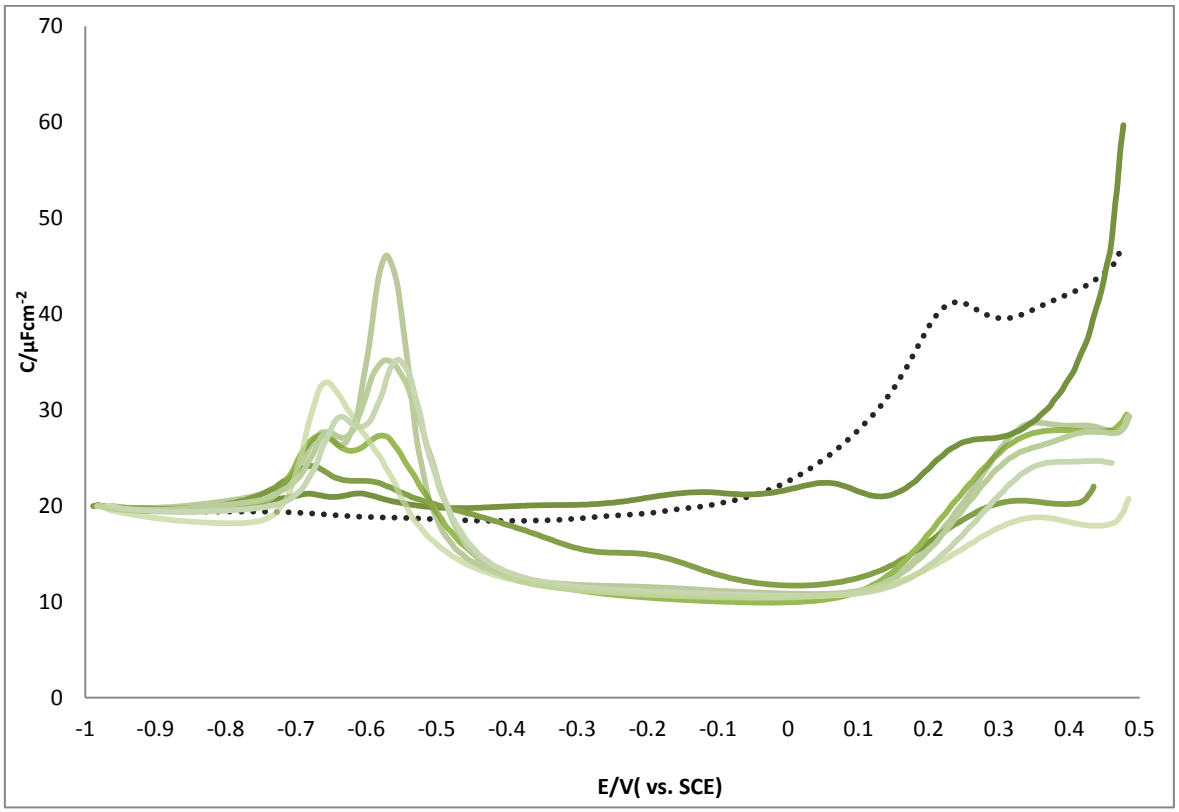

Figure 4.10B Differential capacity curves of the positive going sweep recorded for Au (111) in 0.1 M NaF solution without CTAF (black dotted line), with CTAF concentrations after Additions 1-8 (1/128 CMC to the CMC of CTAF in 0.1 M NaF solution: 0.0014-0.18 mM). The DC curves acquire progressively lighter shades of green as the bulk concentration of CTAF increases.
Sweep rate 5 mV s^{-1}

In Figure 4.10A, the peaks in Region I do not change greatly with potential, staying at around -0.6 V (vs. SCE). In Figure 4.10 B, for Additions 3-8 (1/32 CMC to the CMC of CTAF in 0.1M NaF solution: 0.0056-0.18 mM), there is a nearly identical capacitance minimum with a differential capacitance of between 10-11 µF cm^{-2}. This indicates that the stable surfactant layer formed in this potential region (Region II) does not change as the bulk concentration changes. Thus only a two-dimensional adlayer structure is likely to be formed. A 3D aggregation at higher bulk concentrations might not be possible because of the negligible

stabilisation effect of the F^- counter-ion. This is surprising because the CTAF molecules aggregate to form micelles in bulk solution at the CMC, but seemingly do not aggregate on the electrode surface. This is probably due to different kinetics for surfactant aggregation at an electrode interface and in-bulk solution. It also might be because the curvature of a CTAF micelle produces different headgroup-headgroup distances (larger than for a planar layer).

The charge density curves of Au (111) 0.1 M NaF supporting the electrolyte after Additions 1-7 or CTAF (from 1/128 to ½ of the CMC of CTAF in 0.1M NaF solution, see Section 4.3) are plotted in Figure 4.11. The lines acquire a progressively lighter shade of green as the bulk concentration of CTAF increases.

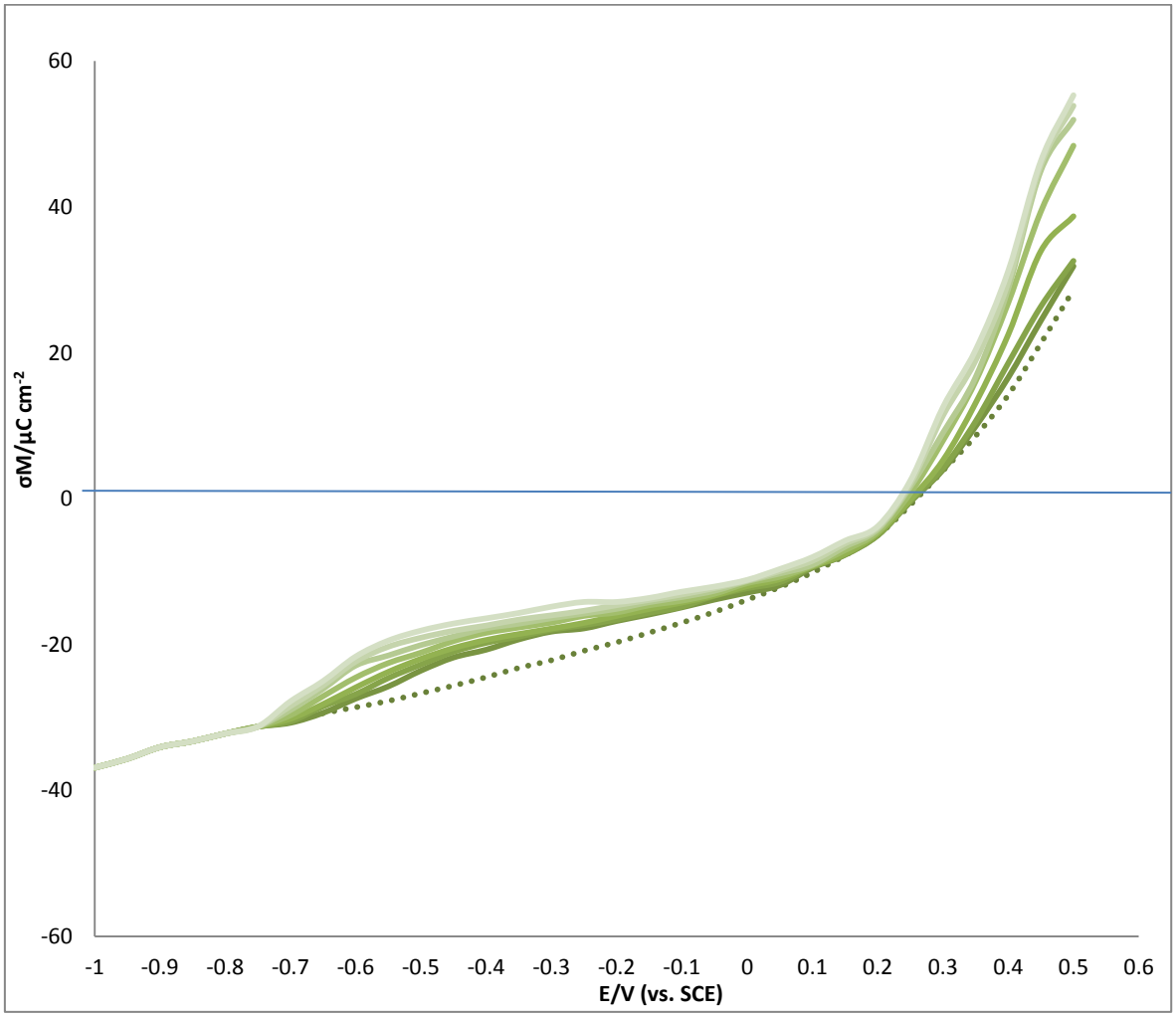

Figure 4.11 Charge density versus electrode potential curves for Au (111) in pure 0.1 M NaF solution (black dotted line), and with selected CTAF concentrations starting from Addition 1 of CTAF (darkest green line) to Addition 7 (of CTAF (lightest green line).

From -750 mV, the curves exhibit a sigmoidal inflection indicative of the adsorption of the surfactant molecules, before gradually merging with the baseline electrolyte charge curve. The CTAF charge curves are approximately merged with the baseline charge curves at the potential of zero charge. This shows that that the adsorbed surfactant molecules in the positive potential region do not charge the surface, possibly because in the positive potential

region, no cationic head group is adsorbed onto the Au surface, and the only interactions of the surfactant with the surface come from the alkyl tail group. This could be due to the positively charged electrode surface repelling the positively charged head groups, although, owing perhaps to the van der Waals interactions of the alkyl tail groups with the gold surface, a surfactant layer remains. The phase transition shown by the increase in differential capacitance, Figure 4.10B, when the potential is greater than 150 mV, might represent the process of the cationic head groups desorbing from the Au (111) surface.

Figure 4.12 gives the Gibbs excess as a function of the electrode potential for the CTAF concentrations used in the charge density-potential curves of Figure 4.11. The Gibbs excess values have a positive potential limit of 400 mV. Beyond this potential limit, owing to the base electrolyte solution having a pH > 7, hydroxide adsorption and peroxidation of the gold surface starts.[27] It is therefore impossible to separate these processes from any structural processes taking place in the adsorbed CTAF layer.

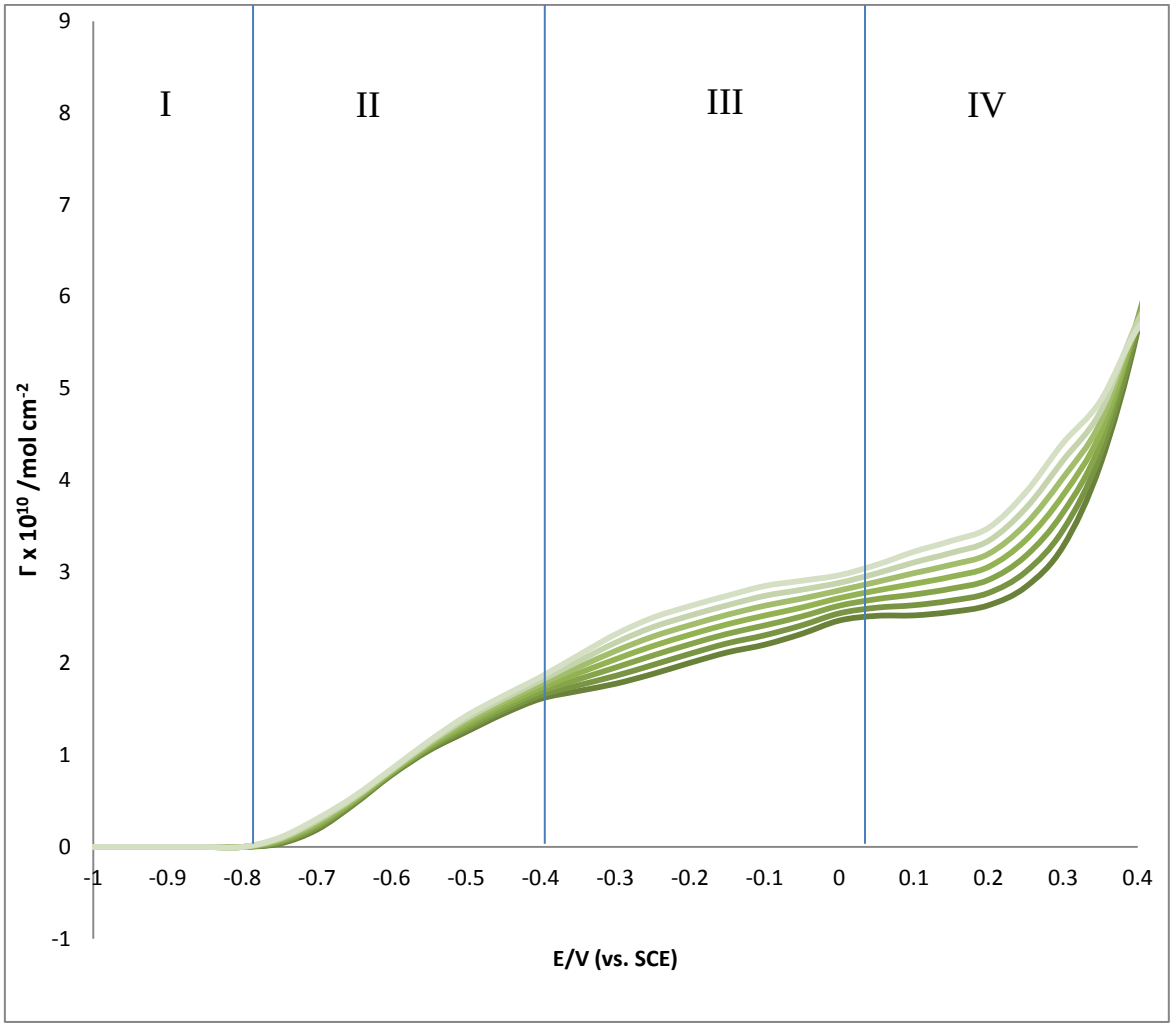

Figure 4.12 Plot of the Gibbs excess of CTAF versus the electrode potential for bulk concentrations of CTAF after Additions 1-7 (where the concentrations of CTAF are 1/128 to ½ of its CMC in 0.1 M NaF solution see Section 4.3). The lines acquire progressively lighter shades of green as the bulk concentration of CTAF increases. In Region I, there are no molecules on the Au (111) surface, in Region II surfactants adsorb on the Au (111) surface, in Region III the surfactants form a stable layer on the electrode surface, in Region IV a phase change in the surfactant layer occurs.

In Region II of Figure 4.12 (where surfactant adsorption occurs) there is a linear increase from 0 mol cm^{-2} at -750 mV to around 1.7×10^{-10} mol cm^{-2} at -400 mV. The coverage of the surfactant on the Au surface does not greatly change as the bulk concentration of CTAF increases. This infers that the rate of surfactant adsorption on the Au (111) surface in Region II is not strongly dependent on the bulk concentration of CTAF. In Region III, the sloped

plateau representing the stable surfactant layer increases slightly in Gibbs excess as the bulk concentration of CTAF increases. The ordered layer of surfactant molecules on the Au (111) surface is thus not saturated.

In potential Region IV the Gibbs excess plateaus between 50 and 200 mV showing that no more surfactant molecules are adsorbed in this potential range. This possibly confirms that the increase in capacitance observed in Figure 4.10B is caused by the surface molecules changing their adsorption state on the Au (111) surface from head group interactions to tail group interactions. It is not clear what causes the steep increase in Gibbs excess for E>200 mV. It may be as a result of the onset of OH adsorption. A possibility is that the van der Waals interactions of the surfactant tail groups with the positively charged electrode causes the surfactant molecules to aggregate on the surface.

The Gibbs excess at 0 V in Figure 4.13 is at around 3.1×10^{-10} mol cm^{-2}. For DeTATf [24,] which has a similar shaped plateau in a potential region equivalent to Region III, the Gibbs excess at 0 V (vs. SCE) is at 1.7×10^{-10} mol cm^{-2}. These lower Gibbs excess values would be due to the bulky co-adsorbed triflate counter ion decreasing the density of surfactant molecules on the Au surface. For the anionic surfactant SDS, at 0 V,[28] the Gibbs excess is around 4×10^{-10} mol cm^{-2}, which is slightly higher than that of CTAF. This could be because SDS has a higher packing parameter than CTAF or because microscopy images have shown that a 3D aggregate structure can be formed in the potential region above the critical aggregation potential. The zwitterionic surfactant DDAPS has a considerably higher Gibbs excess value of 8×10^{-10} mol cm^{-2} at 0 V (vs. SCE),[29] owing to the multi-layer nature of its adsorptive states on Au (111).

4.7 The Electrochemistry of Au (111) in CTAC solution

Figure 4.13A and 4.13B give a CV and a DC curve for an Au (111) in 0.1 M NaF solution after Addition 7 of CTAC (purple line) (1/2 CMC of CTAC in 0.1 M NaF solution: 0.07 mM). CVs and DC curves for Au (111) in 0.1 M NaF solution with NaCl after Addition 7 (blue line) (0.07 mM) and 0.1 M NaF (black dotted line) are also included.

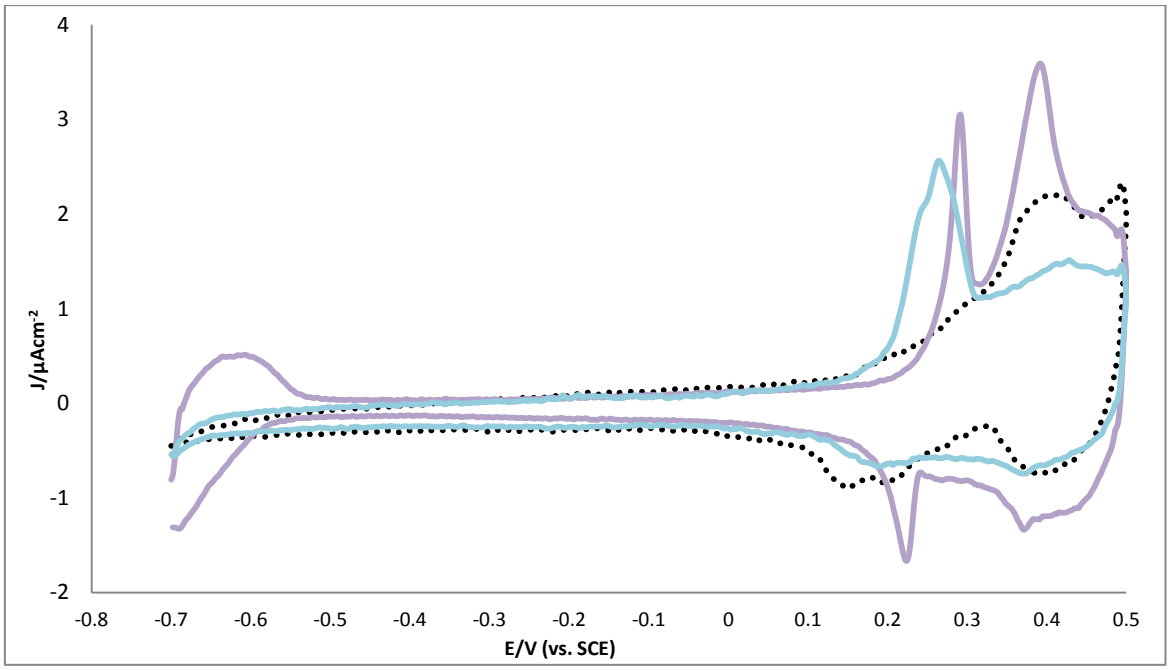

Figure 4.13A Cyclic voltammogram of Au (111) in 0.1 M NaF solution with CTAC after Addition 7 (1/2 CMC of CTAC in 0.1 M NaF solution: 0.07 mM) (purple line). A CVs of Au (111) in 0.1 M NaF with 0.07 mM NaCl (blue line) (0.07 mM), and Au (111) in 0.1 M NaF solution (black dotted line) are also included.

Sweep rate 20 mV s^{-1}.

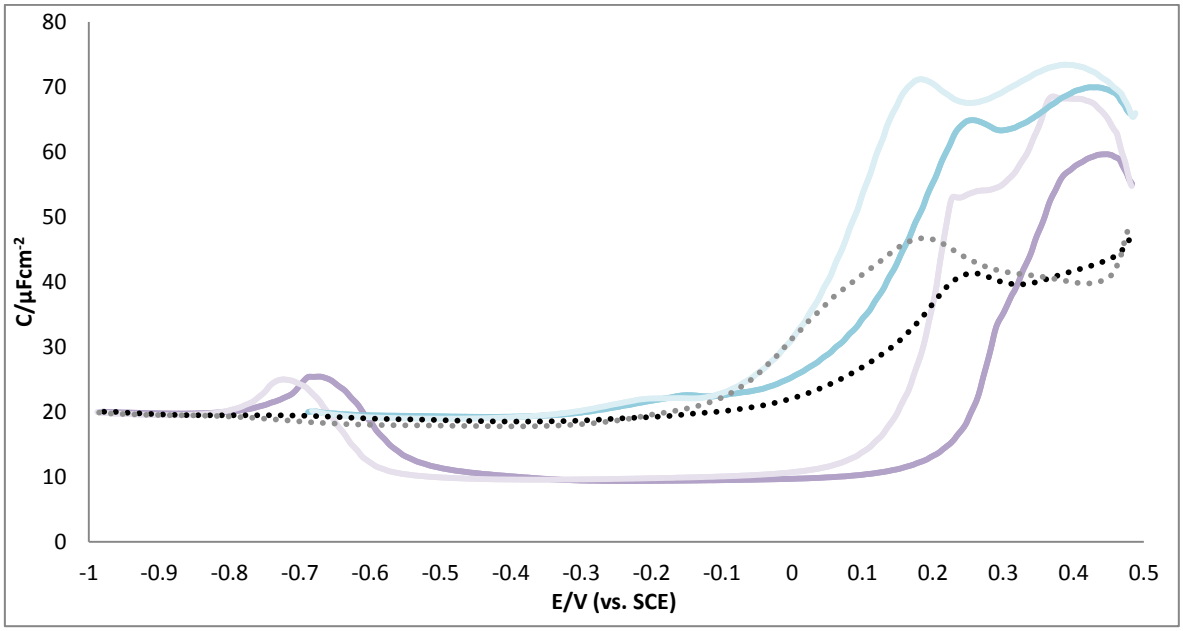

Figure 4.13B Differential capacitance curves of of Au (111) in 0.1 M NaF solution with CTAC after Addition 7 ((1/2 CMC of CTAC in 0.1 M NaF solution: 0.07 mM (purple line). A CVs of Au (111) in 0.1 M NaF with 0.07 mM NaCl (blue line), and Au (111) in 0.1 M NaF solution (black dotted line) are also included. In all three sets of DC curves, the dark shaded lines represent the positive sweep, and the light shaded lines represent the negative sweeps.

Sweep rate 5 mV s^{-1}.

For the CV of Au (111) in CTAC solution, Figure 4.13A, an adsorption peak is observed at -640 mV and a desorption peak at -680 mV. In potential Region III, Figure 4.13A, two peaks are observed at 230 and 380 mV. The most likely cause of the peak at 230 mV is the lifting of the surface reconstruction, as this is in a similar potential region to the lifting of the reconstruction peak of Au (111) in NaCl solution. The position of this peak shows that the reconstruction of the Au (111) surface lifts at a more positive potential than when NaCl is in the solution. This could be due to the cationic surfactant film stabilising the negative charge on the Au (111) surface. The peak at 380 mV is likely to be caused by a phase transition in the surfactant film.

For the DC curve acquired for CTAC in Figure 4.13B, a single surfactant adsorption peak is observed at -690 mV and a single surfactant desorption peak is at -700. These peaks are followed by a capacitance minimum between -460 mV and 120 mV, indicating (as in Figure 4.8B when CTAF is in NaF solution), a layer of surfactant molecules on the Au (111) surface. In the anodic sweep, at 150 mV, there is a noticeable increase in the differential capacitance, and this increase culminates in a differential capacitance maximum at 380 mV, which is at the same potential as the peak in the CV in Figure 4.13A that corresponds to a phase change.

Figures 4.14A and 4.14B give CV and DC curves of Au (111) in 0.1 M NaF solution with CTAC after Addition 1-8 (1/128 CMC to the CMC of CTAC in 0.1 M NaF solution: 0.0011-0.14 mM). The lines acquire progressively lighter shades of purple as the concentration of CTAC in NaF solution increases. The baseline CV and DC curves of Au (111) in 0.1 M NaF solution are represented by a black dotted line.

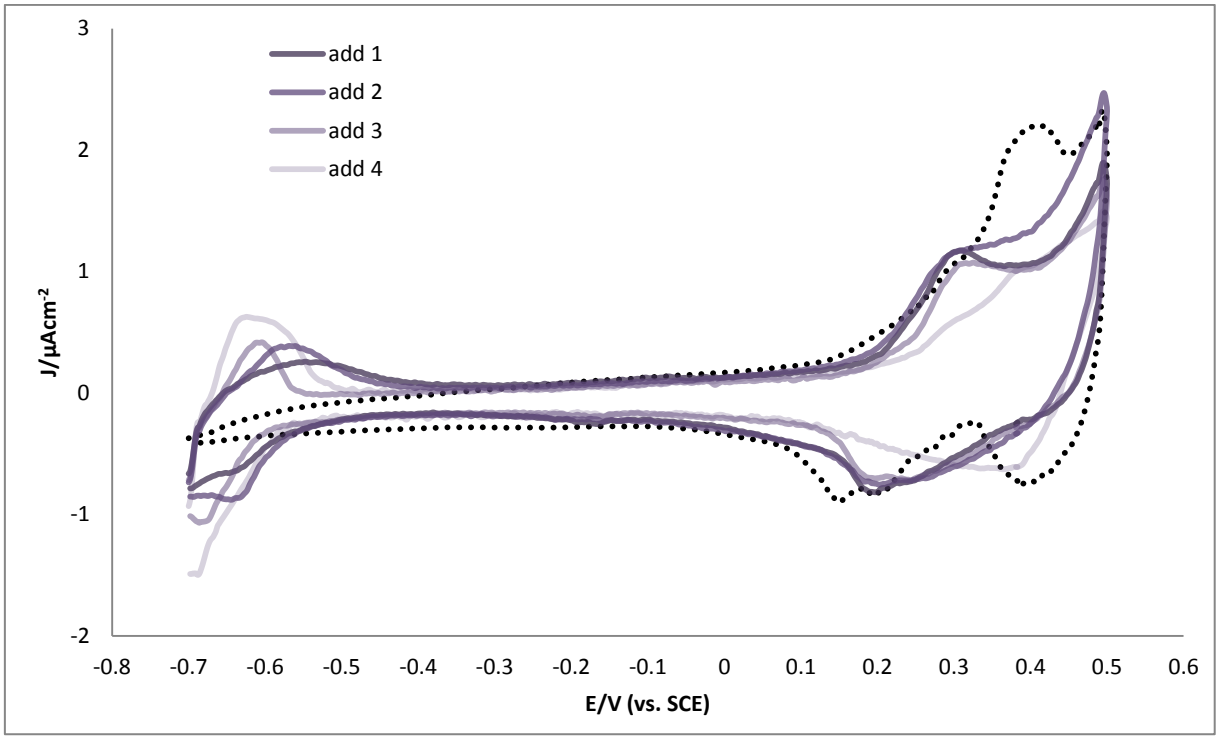

Figure 4.14A (i) Cyclic voltammetry curves recorded for Au (111) in 0.1 M NaF solution without CTAC (black dotted line) and with CTAC after Additions 1-4 (1/128 CMC to 1/16 CMC of CTAC in 0.1 M NaF solution; 0.0011- 0.0088 mM) the CV curves become progressively lighter shades of purple as the bulk concentration of CTAF increases.

Sweep rate 20 mV s^{-1}

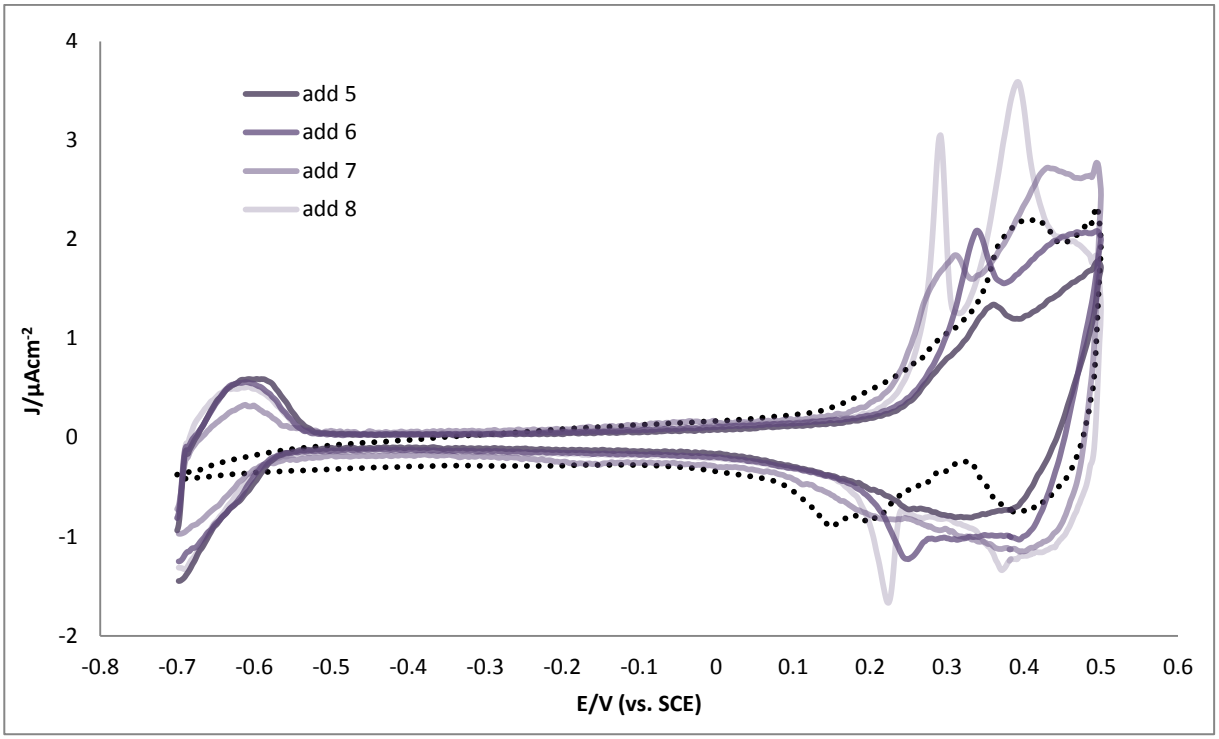

Figure 4.14A (ii) Cyclic voltammetry curves recorded for Au (111) in 0.1 M NaF solution without CTAC (black dotted line) and with CTAC after Additions 5-8 (1/8 CMC to the CMC of CTAC in 0.1 M NaF solution; 0.0175- 0.14 mM) the CV curves become progressively lighter shades of purple as the bulk concentration of CTAF increases.

Sweep rate 20 mV s^{-1}

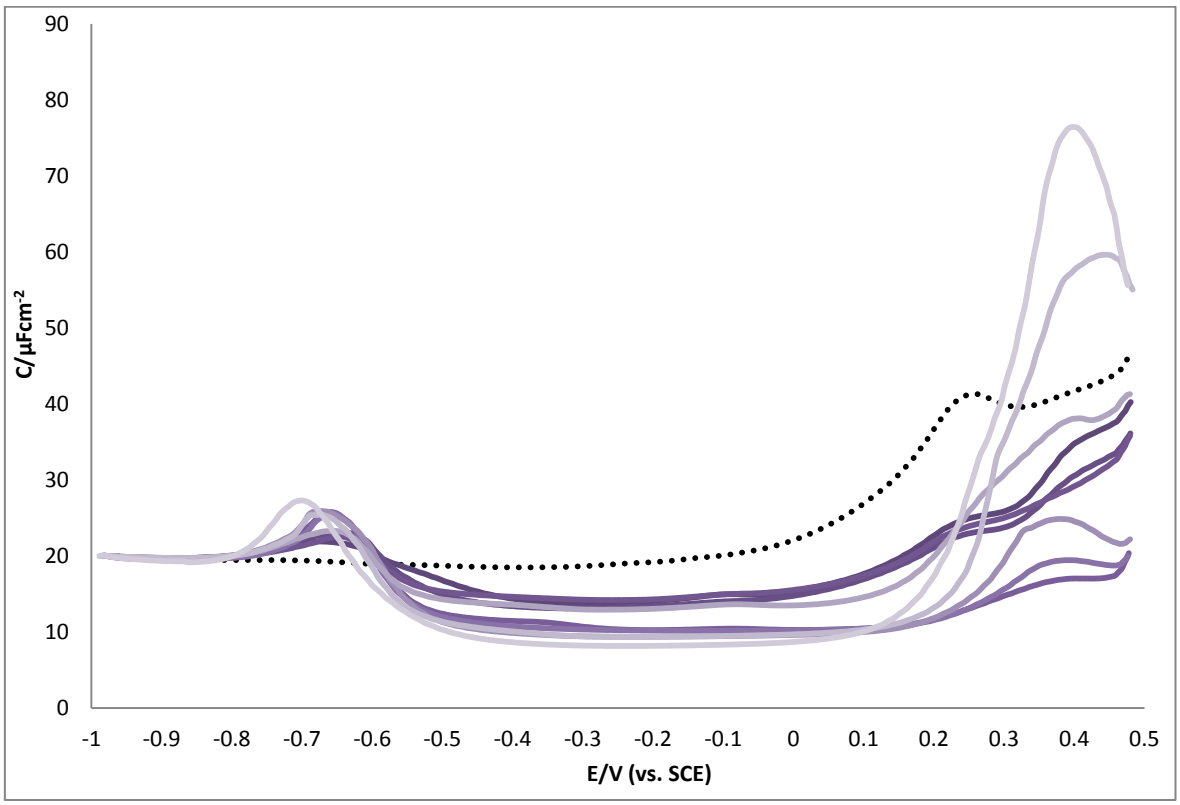

Figure 4.14B Differential capacity curves of the anodic sweep, recorded for Au (111) in 0.1 M NaF solution without CTAC (black dotted line) and with CTAC after Additions 1-8 (1/128 CMC to the CMC of CTAC in 0.1 M NaF solution; 0.0011- 0.14 mM) the DC curves become progressively lighter shades of purple as the bulk concentration of CTAF increases.

Sweep rate 5 mV s^{-1}

In Figure 4.14A, the peaks corresponding to surfactant adsorption shift to more negative potentials as the CTAC concentration increases. Indicating that surfactant adsorption becomes thermodynamically more stable as the bulk concentration of CTAC increases. The same trend is observed in Figure 4.14B, with the most visible negative shift in the differential capacitance peak representing surfactant adsorption when the CTAC concentration reaches the CMC (Addition 8).

In Region II of Figure 4.14B, for Additions 1-3 (1/128- 1/32 CMC of CTAC in 0.1 M NaF: 0.0011- 0.0044 mM), the capacitance minimum is at -13 µF cm^{-2}. For Addition 4- 8 (1/16 CMC to the CMC of CTAC in 0.1 M NaF), the minimum has a lower capacitance of 10 µF cm^{-2}. This could mean that at these higher bulk concentrations of CTAC, Cl^- stabilises the surfactant layer on the Au (111) surface and therefore allows a more densely packed layer. However, for Additions 4-8, no great change in the DC curves in this potential region can be observed, possibly because the surfactant layer in potential Region II changes little with increasing bulk CTAC concentration. This could indicate that, as with CTAF (Figure 4.10B), only a 2D adlayer surfactant structure is formed in this potential region, with further aggregation of surfactant molecules, and a formation of micellar structures on the Au (111) at higher bulk CTAC concentrations being unlikely.

The differential capacitance of peak in region III increases greatly when the concentration of CTAC is at half its CMC, and at its CMC. The likely cause of these maxima are looked at with chronocoulometry measurements.

The charge density curves for Au (111) 0.1 M NaF supporting electrolyte after Additions 1-7 of CTAC (1/128- 1/2 CMC of CTAC in 0.1 M NaF; 0.011- 0.07 mM) are plotted in Figure 4.15, in which the lines acquire a progressively lighter shade of purple as the bulk concentration of CTAC increases.

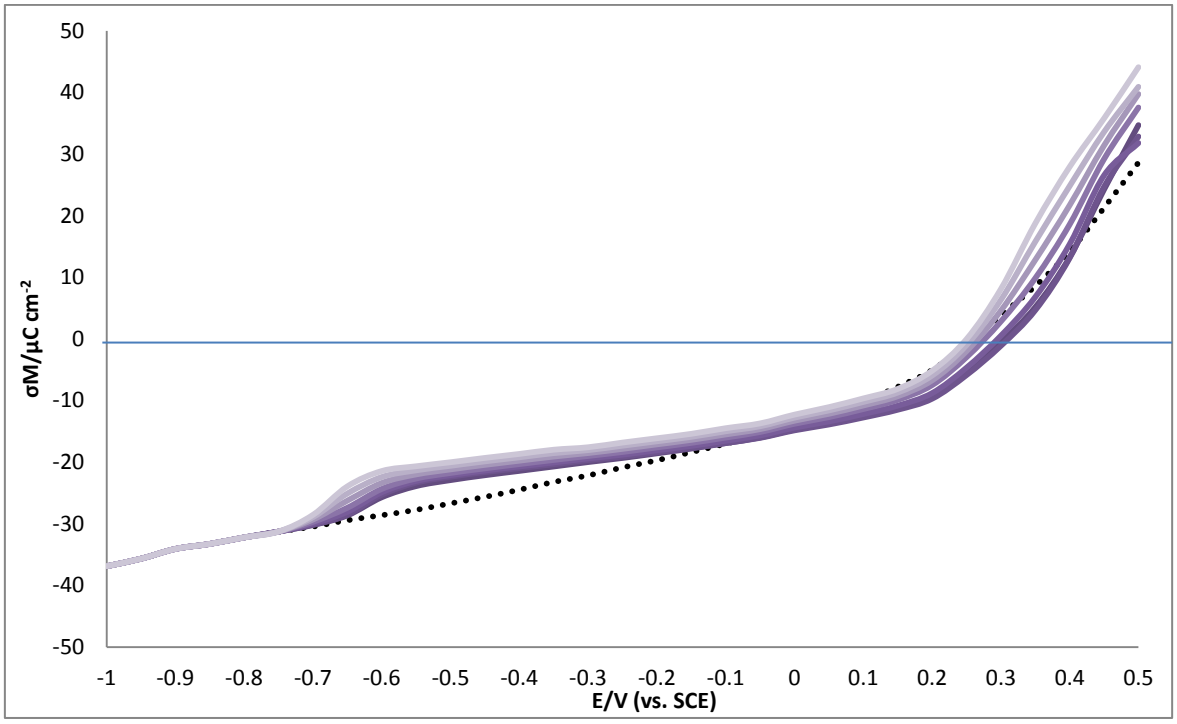

Figure 4.15 Plot of the Gibbs excess of CTAC versus the electrode potential for bulk concentrations of CTAC after Additions 1-7 (1/128- 1/2 CMC of CTAC in 0.1 M NaF; 0.011- 0.07 mM). The lines acquire progressively lighter shades of purple as the bulk concentration of CTAC increases.

In Figure 4.15, the charge-potential curves cross the x-axis at different values, showing that the pzc of the Au (111) electrode changes as the bulk concentrations of CTAC increase. After The pzc of Au (111) after Addition 1 (1/128 CMC of CTAC in 0.1 M NaF; 0.0011 mM) is 100 mV positive of the pzc of Au (111) in bulk 0.1 M NaF solution, showing perhaps that there is a nett positive charge on the Au (111) surface due to cationic head group adsorption on the electrode surface. When CTAF is in the solution, the cationic head groups desorb from the Au (111) electrode surface. However, in the case of CTAC, the less strongly bonded solvation shell of its Cl^- counter-ion would stabilise the cationic head groups on the Au (111) surface, by either being co-adsorbed on the surface or, near the electrode interface. The pzc becomes progressively more negative as the bulk concentration of CTAC increases and the

pzc of Au (111) after Addition 7 (1/2 CMC of CTAC in 0.1 M NaF: 0.07 mM) of CTAC is slightly negative of the pzc of Au (111) in NaF solution, implying that there is a slightly nett negative charge on the Au (111) surface, probably as a result of specific chloride adsorption.

Figure 4.16A gives the Gibbs excess as a function of the electrode potential for the CTAC concentrations used in the charge density-potential curves of Figure 4.15.

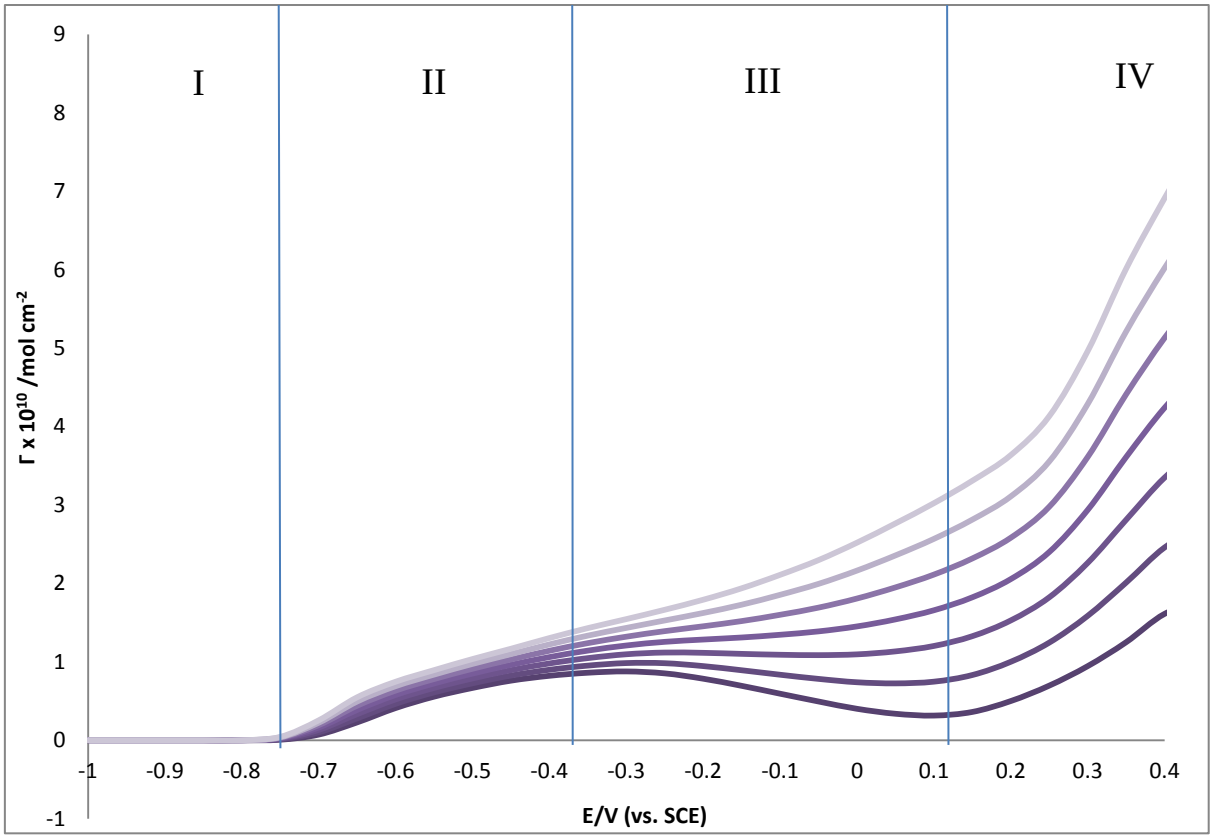

Figure 4.16A Plot of the Gibbs excess of CTAC versus the electrode potential for bulk concentrations of CTAC after Additions 1-7 (where the concentrations of CTAC are 1/128 to ½ of its CMC in 0.1 M NaF solution; 0.011- 0.07 mM: see Section 4.3). The lines acquire progressively lighter shades of purple as the bulk concentration of CTAC increases. In Region I, there are no molecules on the Au (111) surface, in Region II surfactants adsorb on the Au (111) surface, in Region III the surfactants form a stable layer on the electrode surface, in Region IV a phase change in the surfactant layer occurs.

For the CTAC concentrations after Additions 1-3 (1/128- 1/32 CMC of CTAC in 0.1 M NaF: 0.0011- 0.0044 mM), the Gibbs excess values reach a maximum at -300 mV before

decreasing. The Gibbs excess value decrease even though it is clear from Figure 4.10B that there is a stable surfactant layer on the Au (111) surface in this potential region. This could be because in this potential region, the CTAC molecules form a flat lying 2D $\sqrt{3}$ x $\sqrt{3}$ structure, as schematically represented in Figure 1.16 of Section 1. This structure means that the co-adsorption of Cl^- causes there to be less available Au (111) surface for the adsorption of surfactant molecules. Moreover, the flat-lying configuration of the CTAC alkyl tail groups in this suggested structure would mean that each surfactant molecules takes up more room. The Gibbs excess increases in this potential region for CTAC concentrations 4-7 probably because of an increase in density of this 2D $\sqrt{3}$ x $\sqrt{3}$ structure as a result of more Cl^- being co-adsorbed on the Au (111) surface and increasing the stability of this adlayer structure. Another possibility is that at higher concentrations of CTAC, 3D hemi cylindrical aggregates form, with the stable 2D $\sqrt{3}$ x $\sqrt{3}$ structure being used as a template.

In Region IV, the Gibbs excess curves for every concentration of CTAC linearly increase. For a better idea of the phase change process taking part in region IV, the Gibbs excess curves of CTAC in Figure 4.16A are compared with the Gibbs excess curves of NaCl at the same concentrations. This comparison is given in Figure 4.16B.

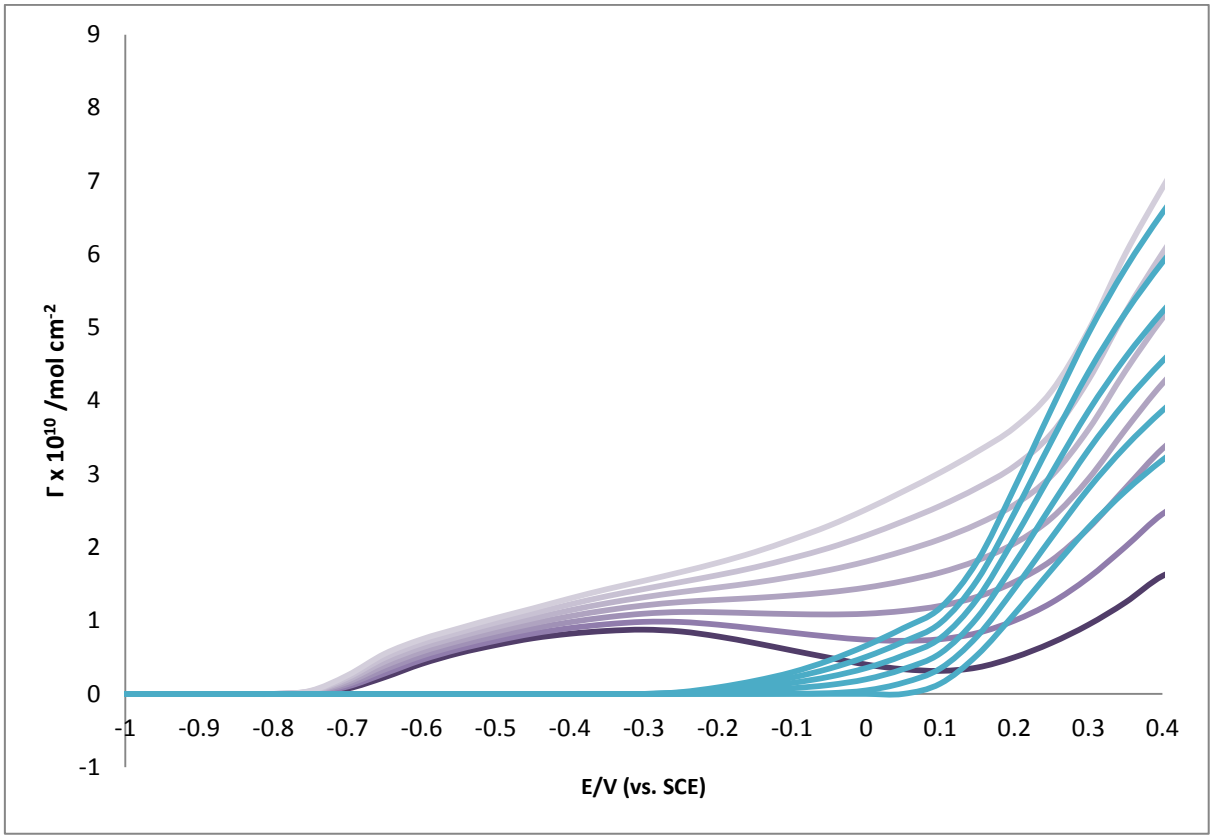

Figure 4.16B Plot of the Gibbs excess of CTAC (purple lines) and NaCl (blue lines) versus the electrode potential for bulk concentrations of CTAC and NaCL after Additions 1-7 (0.011- 0.07 mM, see Section 4.3).

Figure 4.16B clearly shows that the increase in Gibbs excess in Region IV is a result of specific Cl^- adsorption on the Au (111), surface as the Gibbs excess values of CTAC and NaCl start steeply to rise at the same potential of around 100 mV. Additions 6 and 7 or CTAC (1/4 and 1/2 CMC of CTAC in 0.1 M NaF; 0.035 and 0.07 mM) superimpose over Additions 6 and 7 of the Gibbs excess plots of NaCl (0.035 and 0.07 mM) between 300 and 400 mV. This indicates that at such concentrations there is nearly an identical coverage of molecules on the Au (111) surface, when NaCl is in the solution, as when CTAC is in the solution. This could show that the Cl^- adlayer structure on the Au (111) surface at these concentrations and in this potential region is very similar when CTAC and NaCl are in the solution. The charge curves in Figure 4.16 clearly show that the layer of Cl^- anions at higher concentrations in the positive

potential region, when CTAC is in the solution, are co-adsorbed with the CTA^+ surfactants: the charge curves show that the pzc of Au (111) after Additions 6 and 7 of CTAC is similar to the pzc of Au (111) in NaF solution. This indicates that the Cl^- adlayer does not positively charge the electrode surface, as Cl^- anions do. In CTAC Additions 1 and 2 (0.0011 mM and 0.0022 mM), Figure 4.17B, the Gibbs excess is considerably lower than that in Additions 1 and 2 of NaCl (0.0011 mM and 0.0022 mM). This is because the surfactant molecules present on the Au surface would block the Cl^- adsorption.

The surfactant phase in Region IV, Figure 4.17A, is most likely to be a bilayer-type structure. The packing parameter of CTAC molecules would be around 0.3, according to equation (4.1) (see section 4.2); this value is the suggested packing parameter value for cationic surfactants.[7] The structure of the top layer of this bilayer, according to a mathematical model proposed by Retter,[30] would therefore be semi-cylindrical.

4.8 The Electrochemistry of Au (111) in CTAB Solution

Figures 4.17A and 4.17B give CV and DC curves for an Au (111) surface in 0.1 M NaF solution after Addition 7 of CTAB (red line) (1/2 CMC of CTAB in 0.1 M NaF; 0.05 mM). CVs and DC curves for Au (111) 0.1 M NaF with NaBr after Addition 7 (orange line) (0.05 mM) and 0.1 M NaF (black dotted line) are also included.

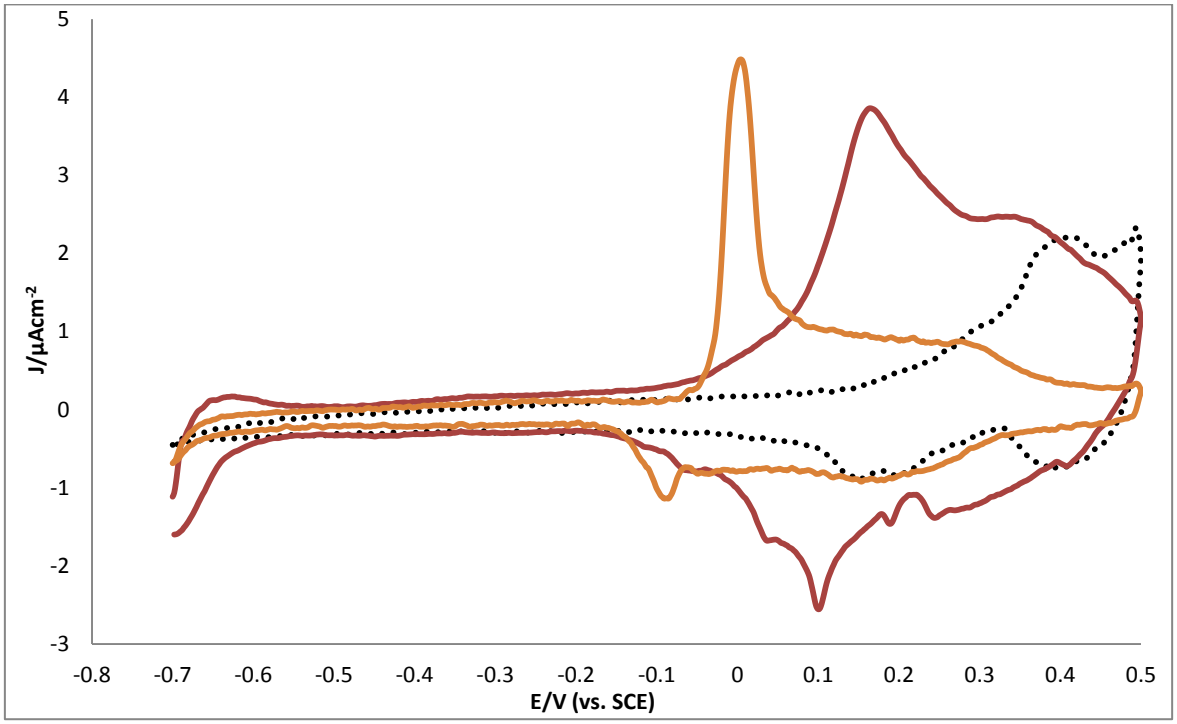

Figure 4.17A Cyclic voltammogram of Au (111) in 0.1 M NaF solution with CTAB after Addition 7 (1/2 CMC of CTAB in 0.1 M NaF; 0.05 mM) (red line). A CVs of Au (111) in 0.1 M NaF with 0.05 mM NaCl (orange line), and Au (111) in 0.1 M NaF solution (black dotted line) are also included.
Sweep rate 20 mV s^{-1}.

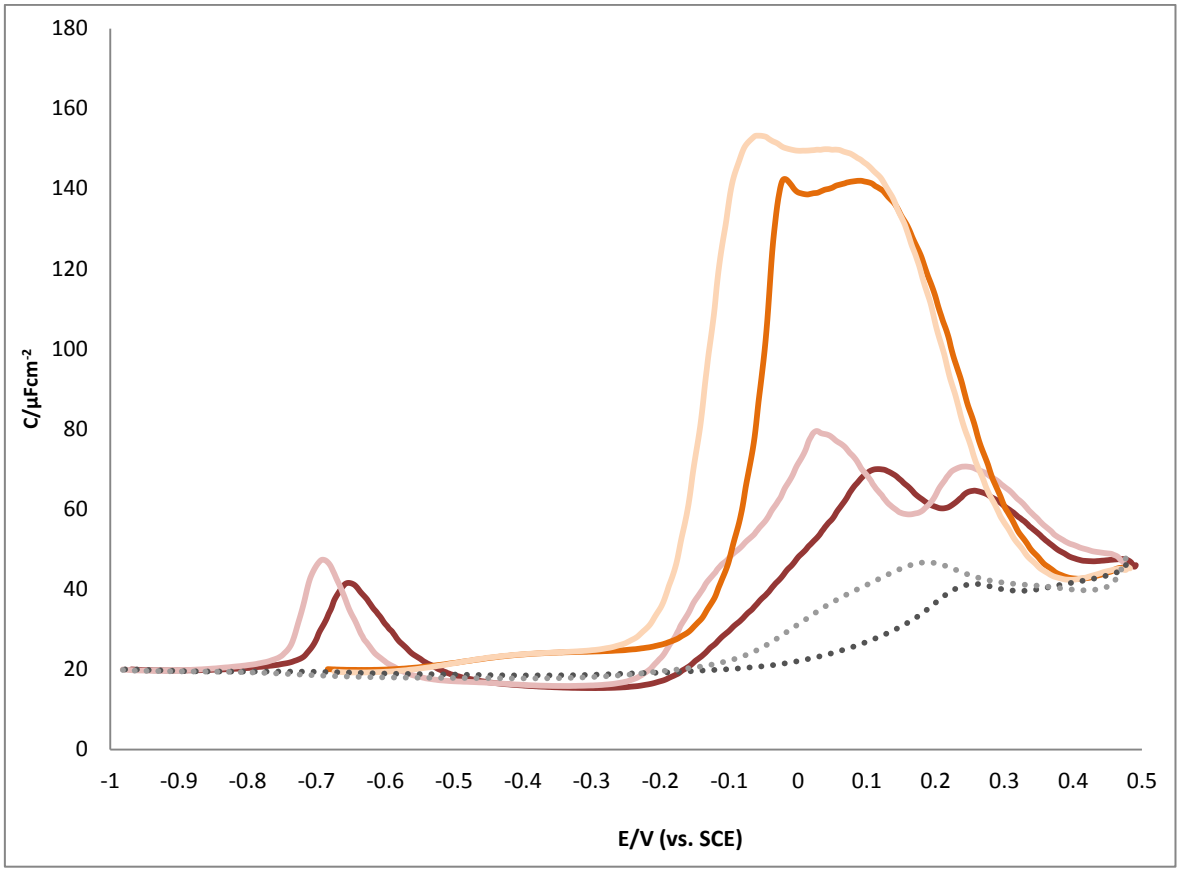

Figure 4.17B Differential capacitance curves of Au (111) in 0.1 M NaF solution with CTAB after Addition 7 (1/2 CMC of CTAB in 0.1 M NaF: 0.05 mM) (red line), of Au (111) in 0.1 M NaF with 0.05 mM NaCl (orange line), and Au (111) in 0.1 M NaF solution (black dotted line).In all three sets of DC curves, the dark shaded lines represent the anodic sweep, and the light shaded lines represent the cathodic sweeps.
Sweep rate 5 mV s^{-1}.

In Figure 4.17A, peaks corresponding to surfactant adsorption and desorption are observed at -650 V and -680 V, respectively. In Region III, there is a sharp peak at 150 mV in the anodic sweep. The most likely cause of these peaks is the lifting of the Au (111) surface reconstruction as a result of the adsorption of bromide. The lifting of the reconstruction when Au (111) NaBr is in solution peaks at a more negative potential of 0 mV. However, the onset of the increase in current for CTAB and NaBr is at the same potential of around -100 mV. Whereas with NaBr the current rises very sharply as the potential is swept cathodically, the current for CTAB initially rises at a comparatively much slower rate. It is possible that

bromide adsorbs on the Au (111) surface at a similar potential as when CTAB is in the solution, as it does when NaBr is in the solution. However, that the surfactant layer present on the Au (111) surface would inhibit the lifting of the surface reconstruction and reduce the kinetics compared with when NaBr is in the solution. Following this peak in the CV of Au (111) in CTAB solution, there is a second current maximum at 320 mV. The most likely cause of this is a surfactant phase transition on the Au (111) surface. These peaks are also observed in Figure 4.17B.

In Figure 4.17B, Region II, there is a differential capacitance minimum between -500 mV and -200 mV at a differential capacitance of 16 μF cm^{-2}, which is at a higher value than the DC minima of CTAC and CTAF. This shows that the Br^- counter-ion causes the surfactant adlayer structure to form a different phase to the stable flat-lying 2D structures that are likely to be present with CTAF and CTAC molecules.

Figures 4.18A and 4.18B give CV and DC curves of Au (111) in 0.1 M NaF solution with CTAB after Additions 1-8 (1/128 CMC to the CMC of CTAB in 0.1 M NaF solution: 0.0008- 0.1 mM). The lines become progressively lighter shades of red as the concentration of CTAB in NaF solution increases. The baseline CV and DC curves of Au (111) in 0.1 M NaF solution are represented by a black dotted line.

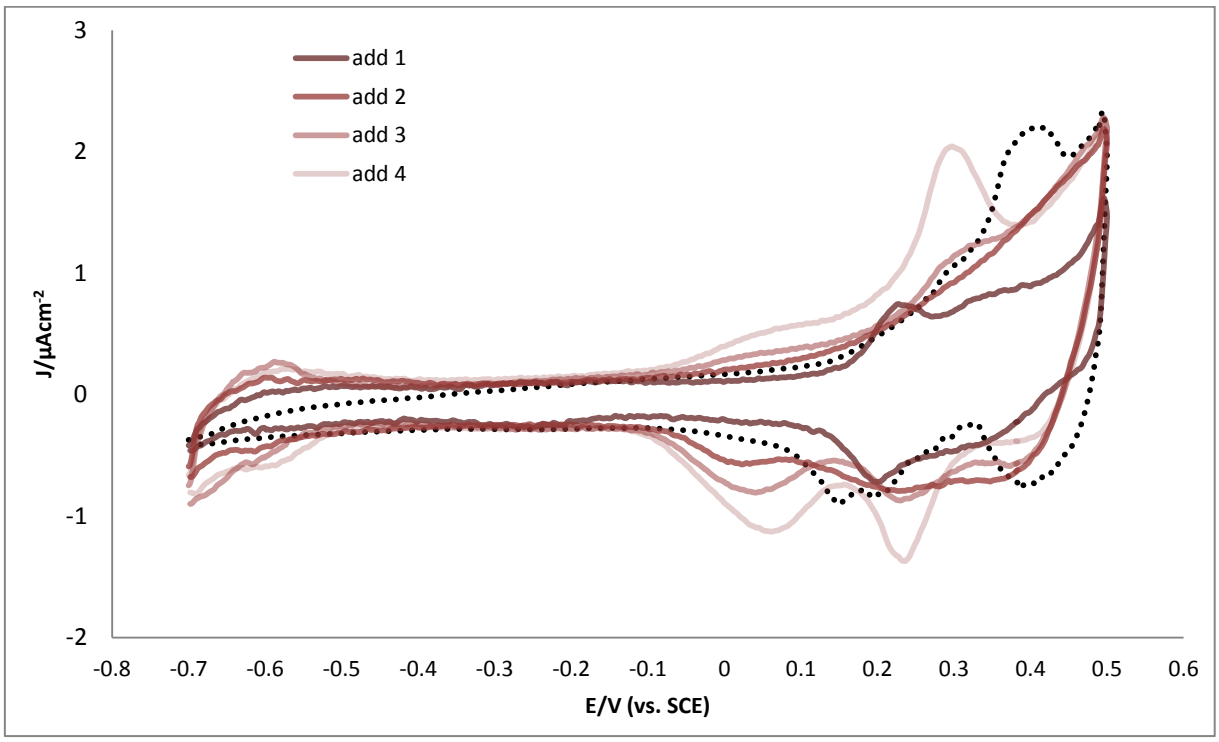

Figure 4.18A (i) Cyclic voltammetry curves recorded for Au (111) in 0.1 M NaF solution without CTAB (black dotted line) and with CTAC after Additions 1-4 (1/128 CMC to 1/16 CMC of CTAB in 0.1 M NaF solution; 0.0008- 0.062 mM) the CV curves become progressively lighter shades of red as the bulk concentration of CTAB increases.
Sweep rate 20 mV s^{-1}

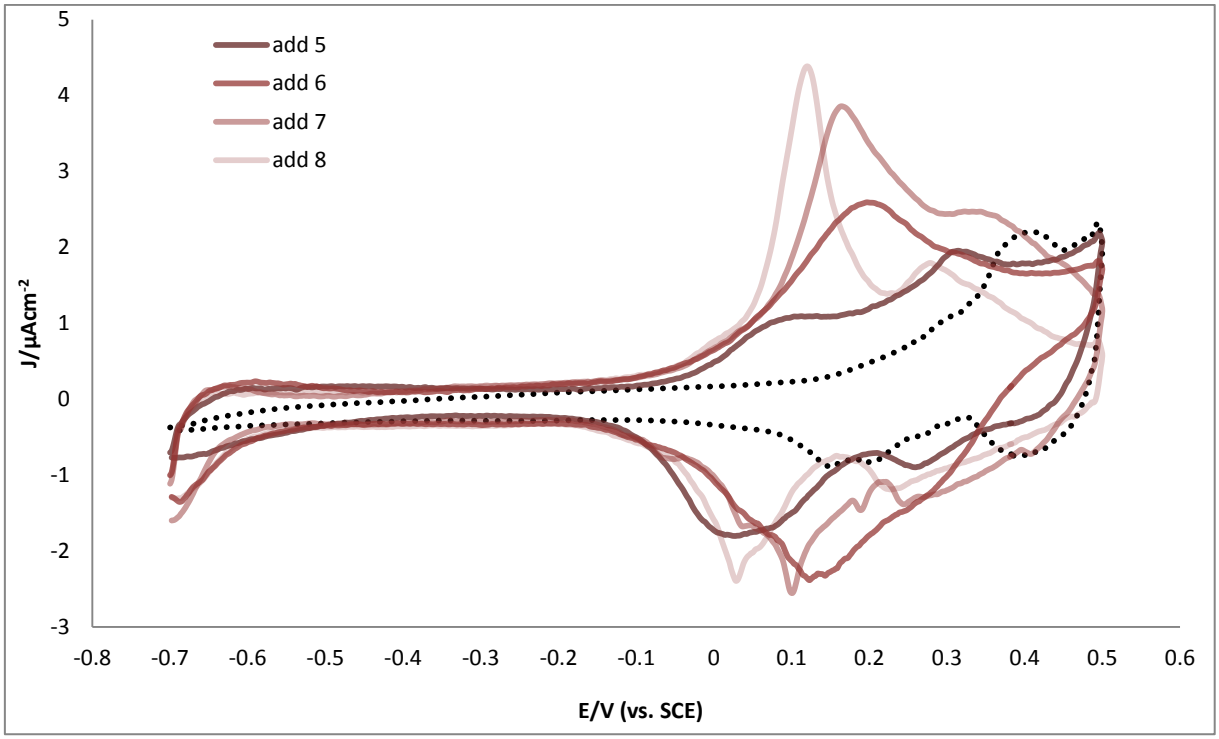

Figure 4.18A (ii) Cyclic voltammetry curves recorded for Au (111) in 0.1 M NaF solution without CTAB (black dotted line) and with CTAC after Additions 5-8 (1/8 CMC to the CMC of CTAB in 0.1 M NaF solution; 0.0125-0.1 mM) the CV curves become progressively lighter shades of red as the bulk concentration of CTAB increases.
Sweep rate 20 mV s^{-1}

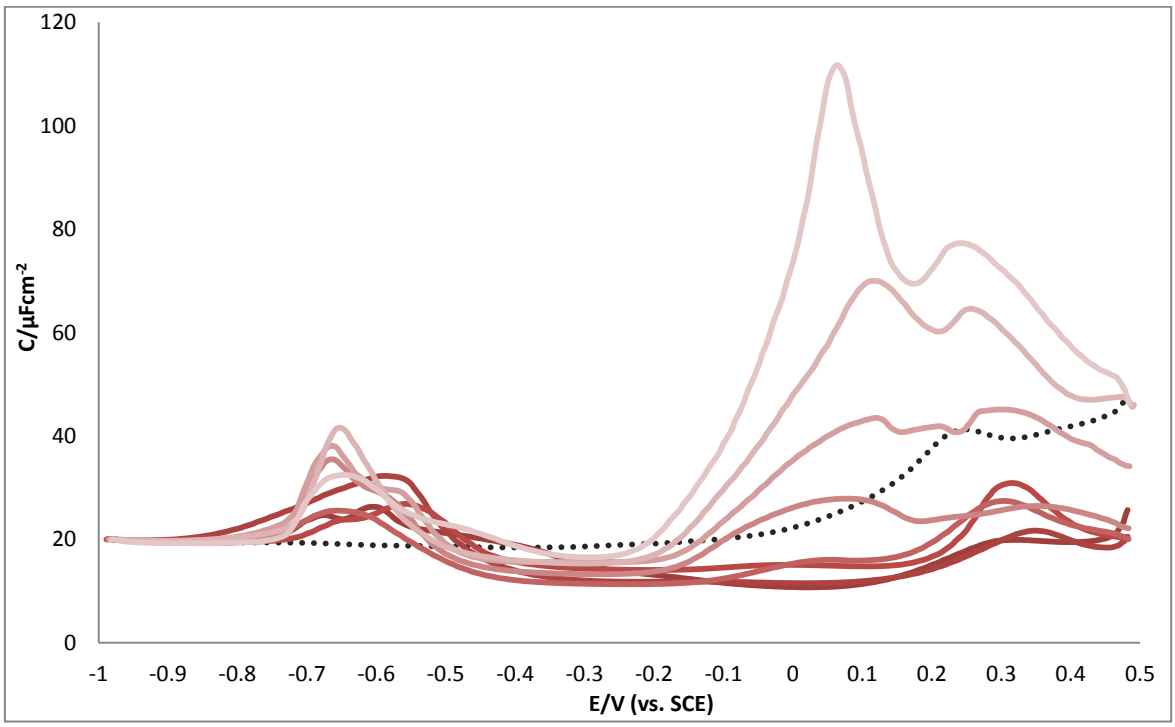

Figure 4.18 B Differential capacity curves of the anodic sweep, recorded for Au (111) in 0.1 M NaF solution without CTAB (black dotted line) and with CTAB after Additions 1-8 (1/128 CMC to the CMC of CTAB in 0.1 M NaF solution; 0.0008- 0.1 mM). The CV curves become progressively lighter shades of red as the bulk concentration of CTAB increases.
Sweep rate 5 mV s^{-1}

For the CV and DC curves in Figures 4.18 A and 4.18B, the peaks related to surfactant adsorption slightly shift towards negative potentials as the concentrations of CTAB in the solution increases, showing that the adsorption becomes thermodynamically more favourable as the bulk concentration of CTAB increases.

In Figure 4.16A, for low concentrations of CTAB, after Additions 1-3 (1/128 to 1/32 CMC of CTAB in 0.1 M NaF: 0.0008 mM to 0.003 mM), only a very small increase in current in Region III can be observed, representing the lifting of the$(23 \times \sqrt{3})$ reconstruction on the Au (111) surface. However in the CVs of Au (111) in various concentrations of NaBr solution,

Figure 4.5B, there is a small peak arising from the lifting of the surface reconstruction when the concentration of NaBr is equivalent to Addition 1 of CTAB (0.008 mM). This suggests that after Additions 1-3, CTAB molecules adsorb onto the Au (111) surface, but the concentration of Br^- is too low for enough co-adsorption to occur to change the surface structure of the Au (111) electrode.

In Region II, Figure 4.16B, the minimum increases in differential capacitance as the bulk concentration of CTAB increases. This trend is not observed for CTAF and CTAC, thus showing the influence Br^- has on the surfactant adlayer in this potential region.

The charge density curves of Au (111) 0.1 M NaF supporting electrolyte after Additions 1-7 or CTAB (1/128 to 1/2 CMC of CTAB in 0.1 M NaF: 0.0008- 0.05 mM), are plotted in Figure 4.19. Here, the lines acquire a progressively lighter shade of red as the bulk concentration of CTAB increases.

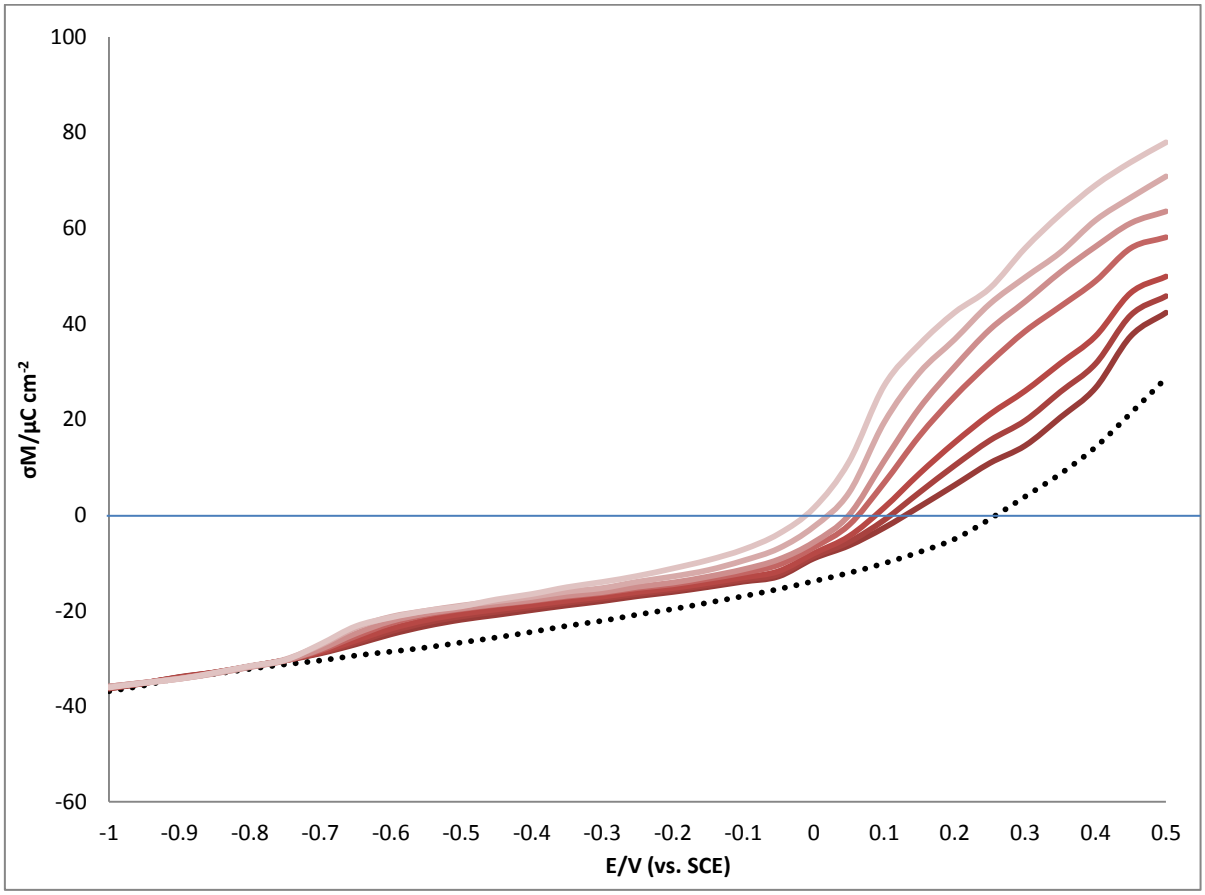

Figure 4.19 Charge density versus electrode potential curves for Au (111) in pure 0.1 M NaF solution (black dotted line), and with CTAB concentrations starting from Addition 1 of CTAB (1/128 CMC of CTAB in 0.1 M NaF 0.0008 mM) (darkest red line) to Addition 7 of CTAB (1/2 CMC of CTAB in 0.1 M NaF; 0.05 mM) (lightest red line).

In Figure 4.19, after the sigmoidal inflection at -750 mV indicating surfactant adsorption, the charge curves of Au (111) in CTAB solution plateau. At -200 mV, the charge curves begin to rise as a result of specific Br^- adsorption. This is at the same potential in which the onset of the increase in differential capacitance in Figure 4.19 is observed. The charge curves crossing the x-axis at progressively more negative potentials, as the surfactant concentration

increases, clearly show the influence of CTAB on the pzc on the Au (111) surface, by applying a nett negative charge to the surface.

Figure 4.20A gives the Gibbs excess as a function of the electrode potential for the CTAB concentrations used in the charge density-potential curves of Figure 4.19.

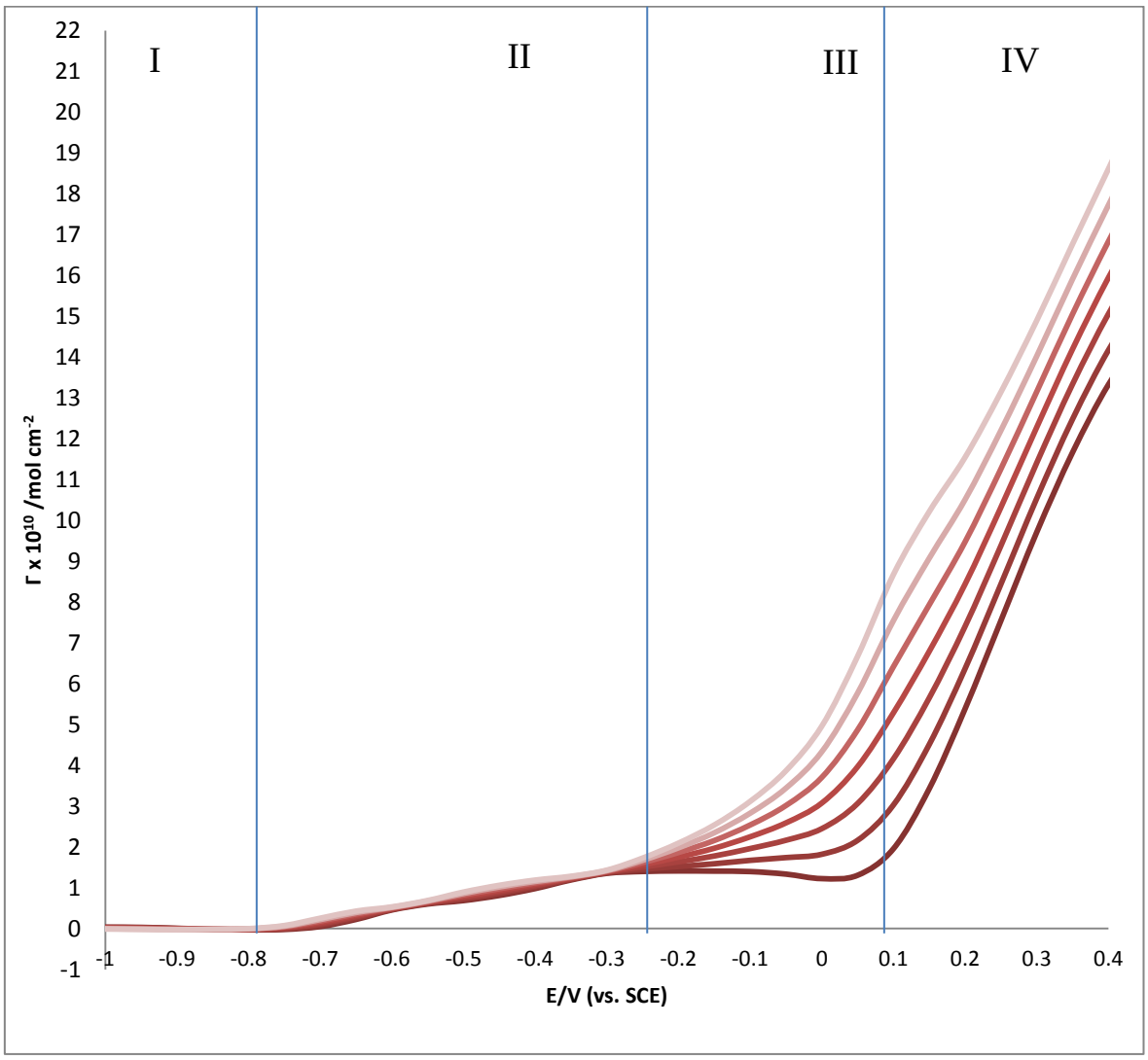

Figure 4.20A Plot of the Gibbs excess of CTAB versus the electrode potential for bulk concentrations of CTAB after Additions 1-7 (1/128- 1/2 CMC of CTAB in 0.1 M NaF; 0.0008- 0.05 mM). The lines become progressively lighter shades of red as the bulk concentration of CTAB increases.

Figure 4.20A is divided into four sections represented by Roman numerals. In Section I, no molecules are adsorbed on the gold surface. Section II shows that in the potential region between -500 mV and -200 mV there is no change in the Gibbs excess as the bulk concentration of CTAB increases. This potential region corresponds to the differential capacitance minimum observed in the DC curves of Au (111) in CTAB solution, Figure 4.18. The increase in differential capacitance of this minimum as the bulk concentration of CTAB increases is therefore probably caused not by the co-adsorption of Br^-, but by increased concentrations of non-adsorbed Br^- at the Au (111) interface. Br^- counter ions at the interface would greatly stabilise the surfactant layer because the repulsive interactions between the cationic head groups would decrease.

In Section III of Figure 4.20A, the onset of the increase in the Gibbs excess is highly dependent on the bulk CTAB concentration. For Addition 7 (1/2 CMC of CTAB; 0.05 mM), the onset of the increase of the Gibbs excess is at -200 mV, whereas, for Addition 1 (1/128 CMC of CTAB: 0.0008 mM), the Gibbs excess begins to increase at a potential that is 250 mV more positive, at 50 mV. This implies that the phase transition is dependent on the specific adsorption of Br^- on the Au (111) surface. In other words, such a phase transition cannot occur without the adsorption of Br^- on the gold surface. After this phase transition, the Gibbs excess rises very steeply, showing that this new phase has a far denser layer of molecules.

Figure 4.20B gives Gibbs excess versus potential curves of Au (111), in Additions 1-7 (0.0008-0.05 mM) of CTAB (red lines) and NaBr (orange lines).

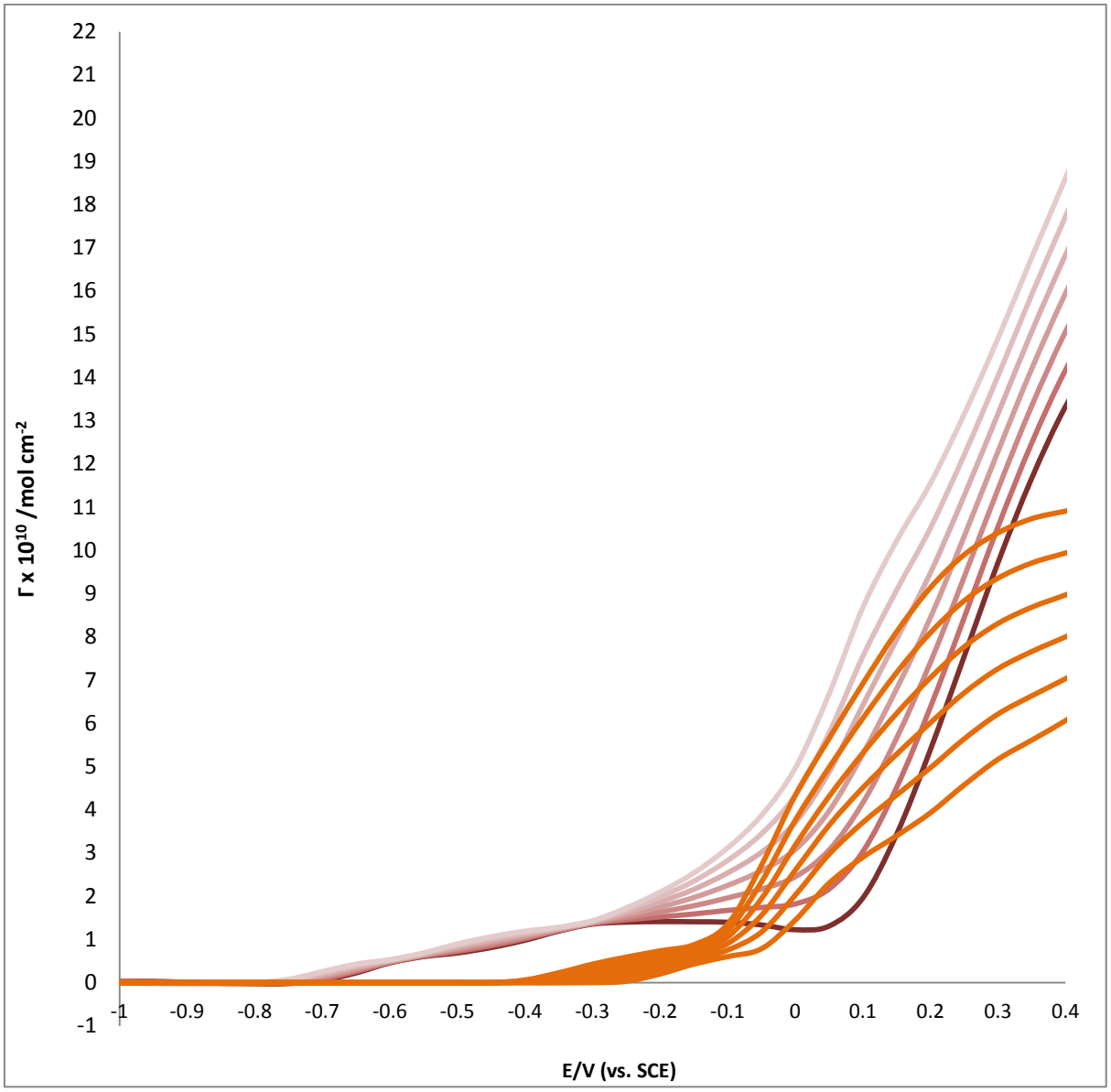

Figure 4.20B Plot of the Gibbs excess of CTAB (red lines) and NaBr (orange lines) versus the electrode potential for bulk concentrations of CTAB after Additions 1-7 (0.0008- 0.05 mM, see section 4.3).

According to Figure 4.20B, the molecules/ions form a more densely packed layer on the Au (111) surface when CTAB is in the solution than when NaBr ions are in the solution. Moreover, the shape of the Gibbs excess curves is different. Whereas for the NaBr plots, the Gibbs excess increases linearly before plateauing as a result of the formation of an ordered

Br^- adlayer, no such plateau is observed in the CTAB Gibbs excess curves and the Gibbs excess curves increase linearly up to the positive potential limit. Therefore an ordered hexagonal Br^- adlayer phase transition clearly does not occur when CTAB molecules are in the solution. The most likely reason why an ordered hexagonal Br^- structure does not occur on the Au (111) surface is that the positively charged cationic CTA^+ surfactant greatly decreases the electrostatic repulsive forces between the Br^- anions. It is therefore almost certain that CTA^+ bonds onto the Br^- layer, resulting in the formation of a bilayer structure. The packing parameter of CTAB molecules would be greater than 0.3, owing therefore to Br^- counters' ion decreasing the electrostatic repulsions between the positively charged head groups. The structure of the top layer of this bilayer, according to a mathematical model proposed by Retter, would therefore be semi-cylindrical or a layer.[30]

4.9. Comparison of Chronocoulometry measurements of Au(111) in CTAF, CTAC and CTAB Solutions

A comparison of the Gibbs excess plots Au (111) in NaF Solution after Additions 1, 3, 5 and 7 or CTAF (green line), CTAB (red line), and CTAC (purple), are given in Figure 4.22.

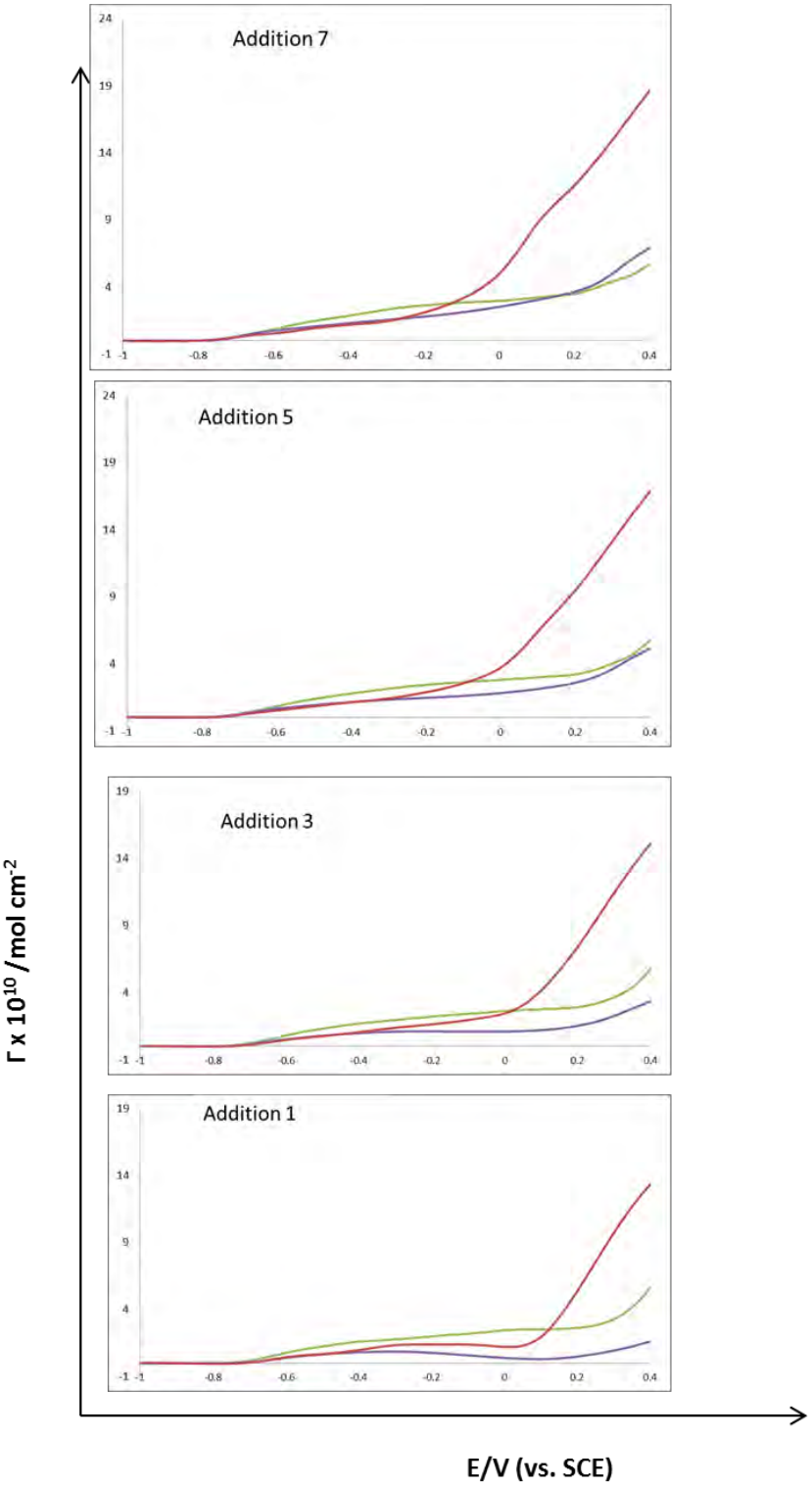

Figure 4.22 Gibbs excess plots of Au (111) in 0.1 M NaF solution after Additions 1 (1/128 CMC), 3 (1/32 CMC), 5 (1/8 CMC) and 7 (1/2 CMC) of CTAF (green lines), CTAC (purple lines), and CTAB (red lines).

In Figure 4.22, the onset of the increase in Gibbs excess is the same for all the surfactants. This shows that the CTA^+ molecule adsorbs at exactly the same potential, when it has F^-, Cl^- and Br^- as a counter-ion. At $E \leq$ -400 mV, for all the concentrations (1/128, 1/32, 1/8 and ½ CMC), the Gibbs excess plots of CTAB and CTAC superimpose. This indicates that in this potential region, there is a similar coverage of CTAC and CTAB surfactant molecules. Implying that, the type of bonding of CTAB and CTAC on the Au (111) surface is the same. For Additions 1 and 3 (1/128 and 1/32 CMC), between -400 mV and 0 mV, the CTAB Gibbs excess values are higher than the Gibbs excess values for CTAC. This is because the Gibbs excess of CTAC decreases owing to the possible formation of the $\sqrt{2}$ x $\sqrt{2}$ adlayer structure. For all the concentrations at $E \geq 0$ mV, the Gibbs excess values of CTAB are considerably higher than those of CTAC as a result of the higher coverage of Br^- anions on the Au (111) surface than Cl^- anions.

At potentials between -600 mV and -200 mV, CTAF has a greater Gibbs excess than CTAB and CTAC. This possibly because there are more positively charged cationic surfactant CTAF molecules at the electrode interface than CTAC and CTAB molecules. This would be owing to the fact that in bulk solution, CTA^+ would couple less readily with the heavily solvated F^- counter-ion than it would with the less solvated Cl^- or Br^- counter ions.

4.10 The Electrochemistry of Au (111) in BDAC solution

The difference between the cationic surfactants BDAC and CTAC is that the head group of BDAC has one benzyl group and two methyl groups, whereas that of CTAC has three methyl groups. A schematic representation of both these cationic surfactants is given in Figures 4.1B and 4.1D.

Figures 4.22A and 4.22B give a CV and a DC curve of Au (111) in 0.1 M NaF solution after Addition 7 (1/2 CMC of BDAC in 0.1 M NaCl solution: 0.013 mM) of BDAC (black solid line). CVs and DC curves Au (111) in 0.1 M NaF (black dotted line) NaF after Addition 7 (1/2 CMC of CTAC in 0.1 M NaF solution: 0.07 mM) of CTAC (purple line) and after 0.013 mM of NaCl (blue line) are also included for reference.

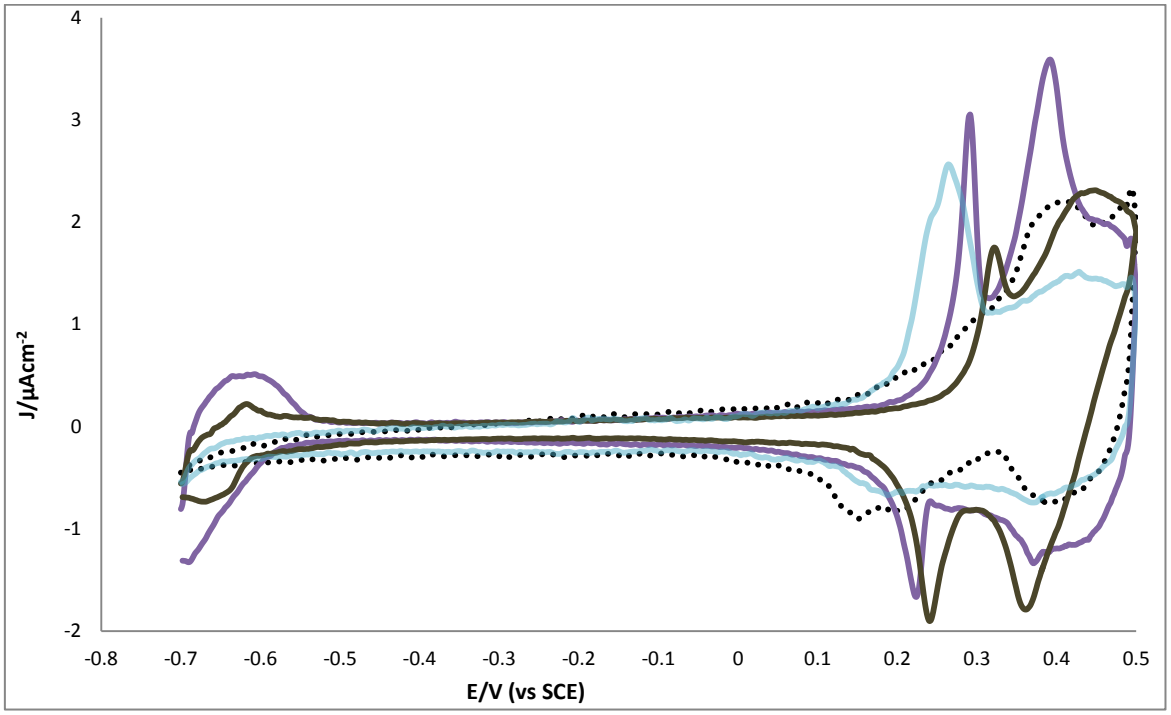

Figure 4.22A Cyclic voltammogram of Au (111) in 0.1 M NaF solution after Addition 7 (1/2 CMC of BDAC in 0.1 M NaCl solution: 0.013 mM) of BDAC (black solid line). CVs Au (111) in 0.1 M NaF (black dotted line), and NaF after Addition 7 (1/2 CMC of CTAC in 0.1 M NaF solution; 0.07 mM) of CTAC (purple line), and after 0.013 mM of NaCl (blue line) are also included for reference.

Sweep rate 20 mV s^{-1}.

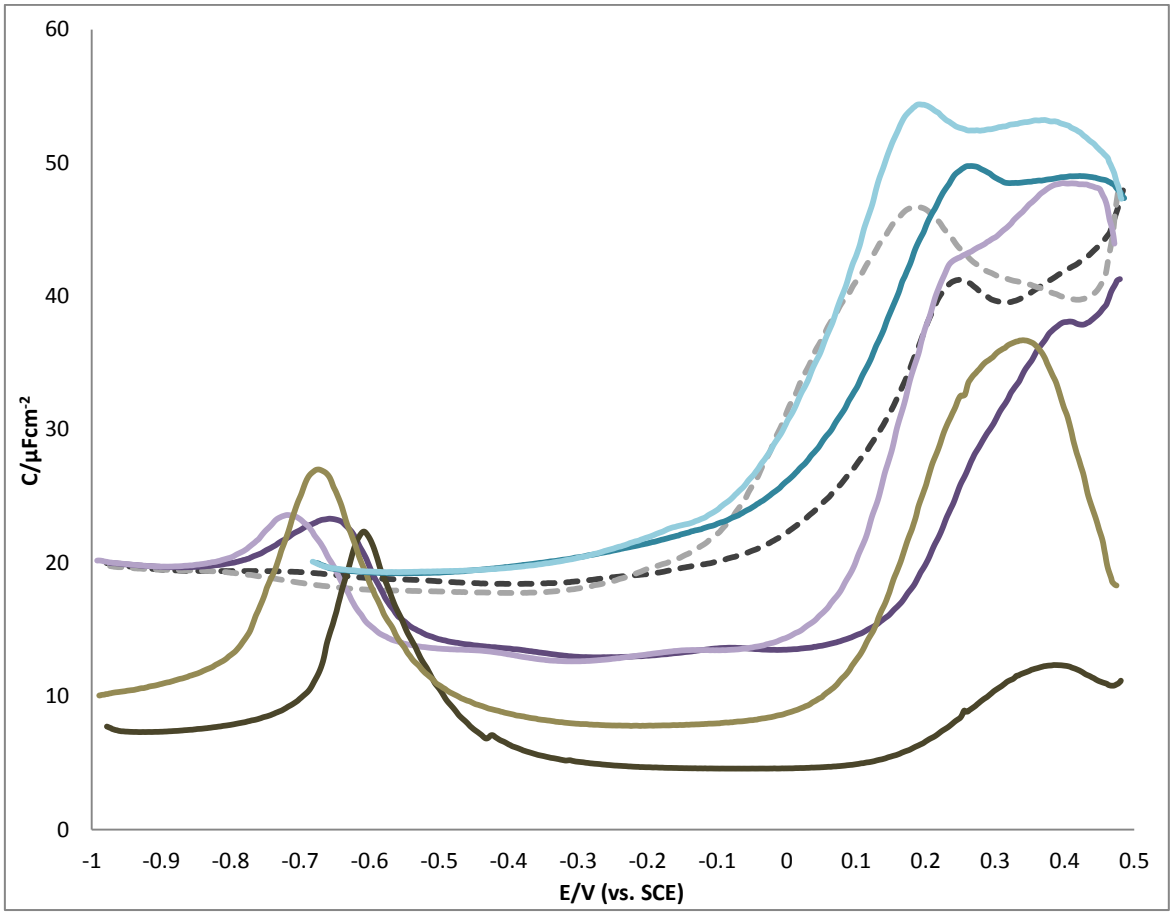

Figure 5.14B Differential capacitance curves of Au (111) in 0.1 M NaF solution after Addition 7 (1/2 CMC of BDAC in 0.1 M NaCl solution; 0.013 mM) of BDAC (dark brown line). DC curves Au (111) in 0.1 M NaF (black dotted line), and NaF after Addition 7 (1/2 CMC of CTAC in 0.1 M NaF solution; 0.07 mM) of CTAC (purple line), and after 0.013 mM of NaCl (blue line) are also included for reference. The anodic sweeps are the darker shaded lines, and the cathodic sweeps are the lighter shaded lines.
Sweep rate 5 mV s^{-1}.

In Figure 4.22A the peaks in the CV of BDAC are assigned analogously with the peaks in the CV of CTAC. It is noticeable that the separation in current between the lines in the positive-going and negative-going sweeps is slightly smaller for the CV of BDAC than for that of CTAC. Hence, although the interactions of BDAC molecules with the Au (111) surface are not necessarily more stable than the interactions of CTAC, the BDAC adlayer structure could be more stable, and thus more densely packed than the adlayer structure of CTAC molecules. This is probably due to the van der Waals interactions between the benzene rings of the

BDAC head groups. The CV of BDAC has a peak at 320 mV, corresponding to the lifting of the reconstruction, which is at a more positive potential than the corresonding peak in the CV of CTAC (290 mV); this indicates that the dimethylammonium cationic head group of BDAC stabilises the negative charge of the Au (111) surface more than the trimethylammonium head group of CTAC, or that the surfactant layer of BDAC is less permeable than the surfactant layer of CTAC. The extra stability of the BDAC layer would be as a result of the benzyl group. The electron-rich π system above and below the benzene ring hosts a partially negative charge, and a counterbalancing positive charge is associated with the plane of benzene ring atoms, causing an electric quadrupole.[31] The negative charge region of the quadrupole can interact with positively charged species. Moreover, the interaction between a quaternary ammonium cation and a benzene ring has been found to be strong.[32] This means that there is a possibility of intermolecular binding in the BDAC surfactant layer.

A peak corresponding to a phase change is observed for BDAC as a broad current maximum at 430 mV in the positive-going sweep, and a sharper current maximum at 370 mV in the negative-going sweep. The difference in potential and shape of these phase change maxima highlights the irreversibility of the phase change process.

In Figure 4.22B, at the negative potential limit of -1000 mV, the differential capacitance of the BDAC DC curve is less than 10 μF cm^{-2}; unlike for CTAC, it does not merge with the baseline differential capacitance at 20 μF cm^{-2}. This must be because, unlike with CTAC, there is a layer of surfactant molecules at this potential. BDAC is still present on the Au (111) surface at the negative potential limit because the benzene ring in the BDAC cationic head group adsorbs on the Au (111) surface. Clearly, a negative potential applied to the electrode

does not cause the benzene to desorb from the surface. In general, benzene adsorbs on transition metal surfaces with the plane of the ring parallel to the surface, bonding to the substrate predominantly though π-orbitals.[33 34 35] This interaction is evidently independent of the Au (111) surface applied potential.

As it is evident that BDAC molecules are on the Au (111) surface at the negative potential limit, the differential capacitance maxima at -600 mV for the anodic sweep, and -660 mV for the cathodic sweep are most likely to be as a result of a rearrangement of BDAC molecules on the Au (111) surface. This could be as a result of the N^+ part of the surfactant head group adsorbing and desorbing from the Au (111) surface while the benzyl group is continually adsorbed.

In both the positive- and negative-going sweeps, there is an extended differential capacitance minimum, which spans over a potential range similar to that of CTAC, of around 400 mV. However, unlike with CTAC, the differential capacitance minimum is at a higher differential capacitance in the negative-going potential sweep than in the positive-going potential sweep. This trend is consistently observed for the positive- and negative-going sweeps for all concentrations of BDAC. The BDAC surfactant layer is thus different in the positive-going and the negative-going sweeps. The most likely cause of this would be slow kinetics of surfactant film rearrangement.

Figures 4.23A and 4.23B give CV and DC curves of Au (111) in 0.1 M NaF solution with BDAC after Addition 3-8 (1/32 of the CMC to the CMC of BDAC in 0.1 M NaF solution: 0.0008-0.013 mM). The lines acquire progressively lighter shades of grey as the concentration of

BDAC in NaF solution increases. The baseline CV and DC curves of Au (111) in 0.1 M NaF solution are represented by a black dotted line.

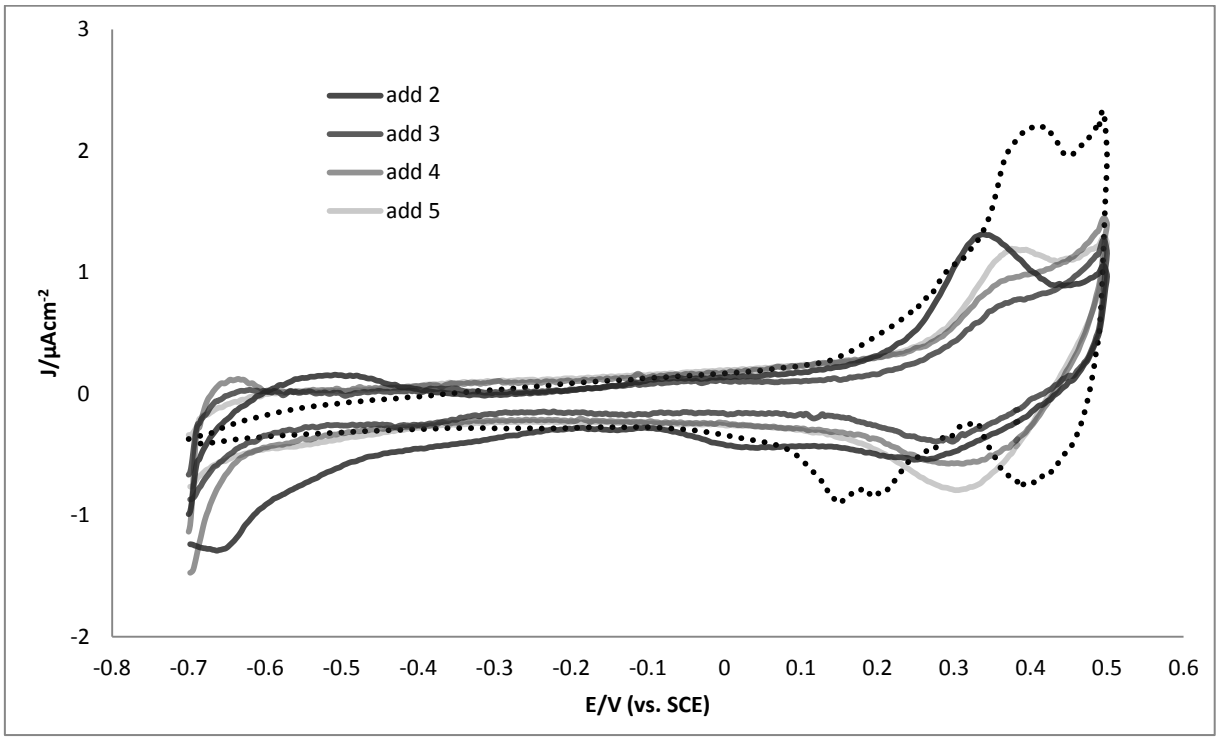

Figure 4.23A (i) . Cyclic voltammetry curves recorded for Au (111) in 0.1 M NaF solution without BDAC (black dotted line) and with BDAC (grey lines) after Additions 2-5 (1/64 of the CMC to 1/8 CMC of BDAC in 0.1 M NaF solution: 0.00004-0.00031 mM), the CV curves acquire progressively lighter shades of grey as the bulk concentration of BDAC increases.

Sweep rate 20 mV s^{-1}

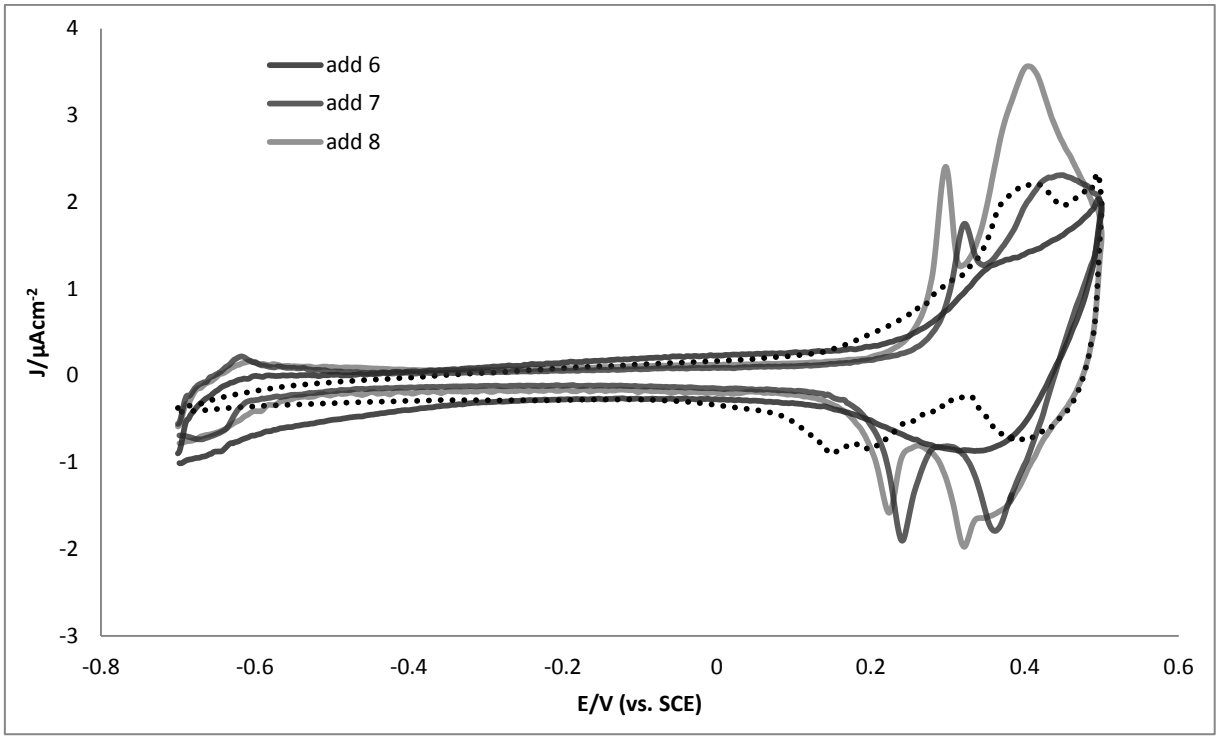

Figure 4.23A (ii). Cyclic voltammetry curves recorded for Au (111) in 0.1 M NaF solution withoutBDAC (black dotted line) and with BDAC (grey lines) after Additions 6-8 (1/4 of the CMC to the CMC of BDAC in 0.1 M NaF solution: 0.00062-0.0255 mM), the CV curves acquire progressively lighter shades of grey as the bulk concentration of BDAC increases.

Sweep rate 20 mV s^{-1}

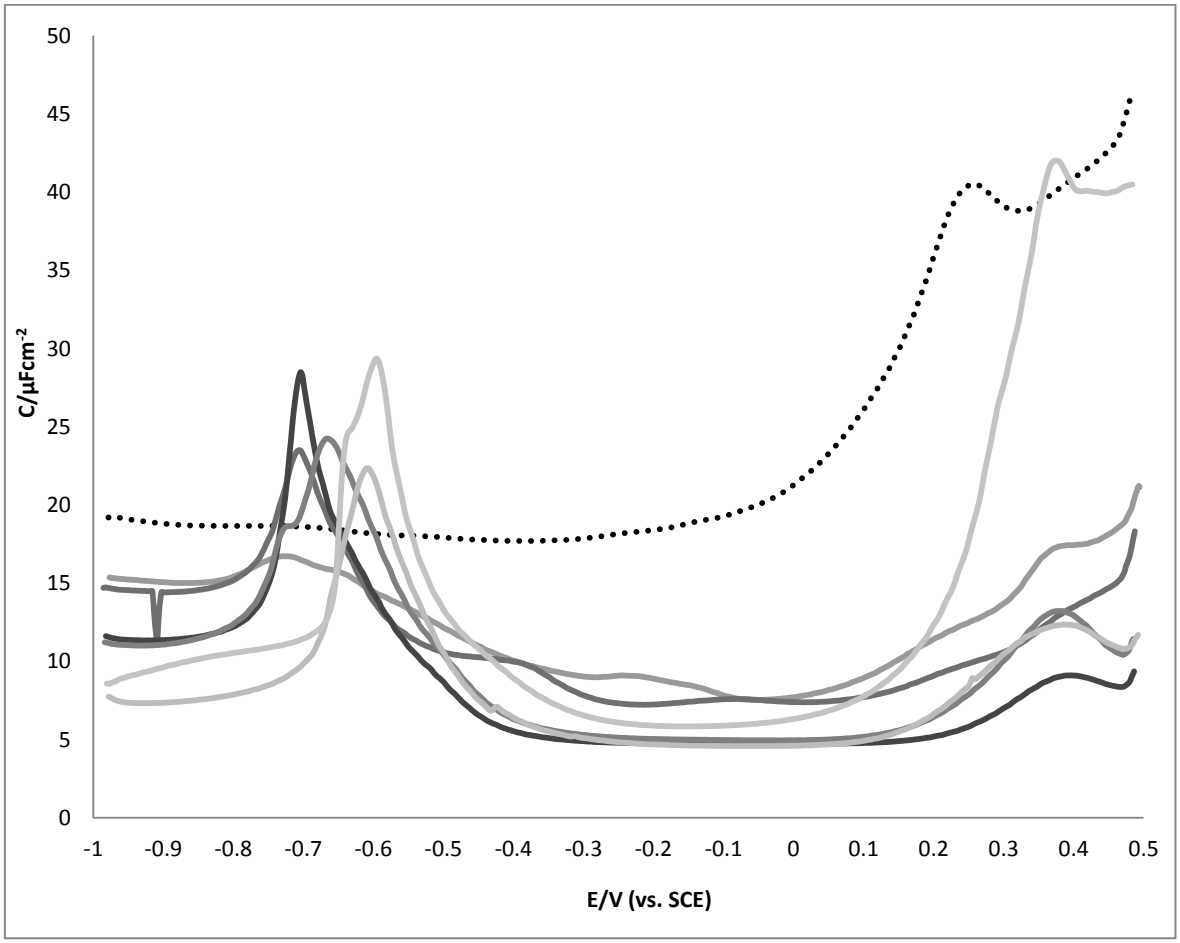

Figure 4.23 B. Differential capacity curves of the positive-going sweep, recorded for Au (111) in 0.1 M NaF solution without BDAC (black dotted line) and with BDAC (grey lines) after Additions 2-8 (1/64 of the CMC to the CMC of BDAC in 0.1 M NaF solution: 0.00004-0.00255 mM), the CV curves acquire progressively lighter shades of grey as the bulk concentration of BDAC increases.

Sweep rate 5 mV s^{-1}

In Figure 4.23A, the peak indicating the lifting of the (23 x $\sqrt{3}$) reconstruction appears only after Addition 7 of BDAC (at a concentration equivalent to 1/2 of the CMC of BDAC in 0.1 M NaF solution). Thus at lower bulk concentrations, the Cl^- counter ion cannot permeate easily the intermolecular bonded surfactant layer. It is difficult from Figures 4.22 and 4.23 to tell the influence the Cl^- counter-ion has, as the negatively charged quadrupole from the

benzene rings could also exert a negative charge on the Au (111) surface. Though the increase in charge under the peak at 400 mV, which is likely to be related to a phase change, as well as the negative shift in the reconstruction peak when the concentration of BDAC is at the CMC is could be a result of specific chloride adsorption.

Figure 4.23B shows that the peak in the negative potential region positively shifts from -700 mV to -600 mV as the bulk concentration of BDAC increases. The reason for this could be that the surfactant phase at potentials positive of -600 mV becomes less stable, or the phase at potentials negative of -600 mV becomes more stable as the bulk concentration of BDAC increases. It is noteworthy also that at -1000 mV, the differential capacitance of the DC curves decreases as the bulk concentration of BDAC increases. This shows that as the bulk concentration of BDAC increases, the coverage of benzyl groups on the Au (111) surface increases.

The differential capacitance minimum is at exactly the same differential capacitance (4.63 µF cm^{-2}) for concentrations of BDAC after Additions 5, 6 and 7 (1/8, 1/4 and 1/2 of the CMC of BDAC in 0.1 M NaF solution); hence in this concentration range and the surfactant film in this potential region varies only slightly. However, when the concentration of BDAC is at the CMC, the differential capacitance minimum has the slightly higher value of 6 µF cm^{-2}.

In order to carry out chronocoulometry measurements there must be a potential at which the Au surface is clean of all adsorbate molecules. This is not the case for experiments with BDAC and so chronocoulometric measurements were not performed for this surfactant.

4.11 Summary and Conclusion

When the substrate is negatively charged or uncharged, it is likely that CTAF and CTAC form ordered 2D over-layers on the Au (111) surface, which may consist of a film of flat-lying molecules packed side-to-side and tail-to-tail. The driving force for the formation of this 2D overlayer arrangement would be the striped nature of the Au (111) surface's atomic arrangement. CTAB possibly does not form this type of 2D adlayer structure when the substrate is uncharged because the Br^- counter-ions adsorb on the sites with which the alkyl tail groups interact via van der Waals forces.

As the Au (111) surface becomes more positively charged, the CTA^+ headgroup of the CTAF molecule is possibly repelled from the Au surface, resulting in a rise in capacitance, although some molecules may still interact with the surface through alkyl tail group van der Waals interactions. CTAC and CTAB form a bilayer structure on the positively charged Au (111) surface. The CTAB bilayer is more densely packed and more strongly bonded than the CTAC bilayer, owing to the stronger bonding/higher coverage of Br^- ions. It is noteworthy that, according to the Gibbs excess plots, CTAB has a higher coverage at positive potentials than Br^- anions for equivalent concentrations of NaBr. This shows that the CTA^+ molecules bonded on top of the adsorbed Br^- ions reduce the Br-Br repulsive interactions. Moreover, there could be energy gain from chain-chain interactions. These two factors would mean that there is a more densely packed adlayer.

[1] Bunton, C., Frankson, J. and Romsted, L. (1980), *J Phys Chem*, 84, p. 20.
[2] Tatsuma T. and Matsubara K. (2008), 'Photocatalytic Deposition and Plasmon-Induced Dissolution of Metal Nanoparticles on TiO_2', *Metal Nanoclusters in Catalysis and Materials Science*, Amsterdam: Elsevier.
[3] Velegol, S.B., Fleming, B.D., Biggs, S., Wanless E.J. and Tilton, R.D. (2000), *Langmuir*, Vol. 16, p. 6.
[4] Naskar, B., Dan, A., Ghosh, S., Aswal, V.K. and Moulik, S.P. (2012), *J Mol Liq*, 170, p. 1.
[5] Bartet, D., Gamboa, C. and Sepulveda, L. *(*1980), *J Phys Chem*, 84, p. 272.
[6] Israelachvili, J.N., Mitchell, D.J. and Ninham, B.W. (1976), *J Phys Chem Soc*, Faraday Trans, II, 72, p.1525.
[7] Chen, M.A., Burgess I. and Lipkowski, J. (2009), *Surf Sci*, 603, p. 1878.
[8] Angerstein-Kolzlowska, H., Conway, B.E., Hamelin, A. and Stoicoviciu, L. (1986), *Electrochim Acta,* Vol. 31, p. 1051.
[9] Wang J., Ocko, M., Davenport, A.J. and Isaacs, H.S. (1992), *Phys Rev B,* 46, p. 10321.
[10] Wiechers, J., Twomey, T., Kolb, D.M. and Behm, B.J. (1988), *J Electroanal Chem*, 248, p. 451.
[11] Alonso, C., Salvarezza, R.C., Vara, J.M. and Arvia, A.J. (1990), *Electrochim Acta*, 35, p. 1331.
[12] Lecoeur J. and Hamelin, A. (1974), *CR Acad Sci Ser*, C279, p. 1081.
[13] Bard A.J. and Faulkner, L.R. (1980), *Electrochemical Methods*, New York: Wiley.
[14] Shi, Z. and Lipkowski, J. (1996), *J Electroanal Chem*, 403, p. 225.
[15] Shi, Z., Lipkowski, J., Mirwald, S., Pettinger, B.J. (1996), *Chem Soc, Faraday Trans*, 92 (20), p. 3737.
[16] Kolb, D.M., Lehmpfuhl, G. and Zei, M.S. (1984), *J Electroanal Chem*, 179, p. 289.
[17] Fu C.L. and Ho, K.M. (1989), *Phys Rev Lett,* 63, p. 1617.
[18] Chan, C.N., Cunningham, S.L., Luke, K.L., Weinberg, W.H. and Witherow, S.P. (1978), *Surf Sci*, 78, p.15.
[19] Sette, F., Hashizume, T., Comin, F., MacDowell, A.A. and Citrin, P.H. (1988), *Phys Rev Lett*, 61, p.1384.
[20] Ocko, B. M., Magnussen, O. M., Wang, J. X., Adzic, R. R. and Wandlowski T. (1996), *Phys B: Cond Mat*, 221 (1−4), p. 238.
[21] Magnussen, O.M. (2002), *Chem Rev*, 102 (3), p. 679.
[22] Gao, X., Edens, G. J. and Weaver, M.J. (1994), *J Electroanal Chem*, 376, p. 21.
[23] Shi. Z, Lipkowski. J, (1996), *J Electroanal Chem*, 403, p. 225.
[24] Brosseau, C.L., Sheepwash, E., Burgess, I.J., Cholewa, E., Roscoe, S.G. and Lipkowski, J. (2007), *Langmuir*, 23*,* p. 1784.
[25] Cholewa, E., Burgess, I., Kunze, J. and Lipkowski, J. (2004), *J Sol St Electrochem*, 8, p. 693.
[26] Sek, S., Chen, M., Brosseau, C.L. and Likowski, J. (2007), *Langmuir*, 23, p. 12529.
[27] Chen, A. and Lipkowski, J. (1999), *J Phys Chem*, *103*, p. 682.
[28] Burgess, I., Zamlynny, V., Szymanski, G., Lipkowski, J., Majewski, J., Smith, G., Satija, S. and Ivkov, R. (2001), *Langmuir*, 17, p. 3355.
[29] Xu, S., Chen, M., Cholewa, E., Szymanski, G. and Lipkowski, J. (2007), *Langmuir*, 23, p. 6937.
[30] Retter, U. (2000), *Langmuir*, 16, p. 7752.
[31] Ma, J.C. and Dougherty, D.A. (1997), *Chem Rev*, 97, p. 1303.
[32] Zhong, W., Gallivan, JP., Zhang, Y., Li, L., Lester, H.A. and Dougherty, D.A. (1998), *Proc Nat Acad Sci USA*,95,(21), p. 12088.
[33] Netzer, F.P. (1991), *Langmuir*, 7, p. 2544.
[34] Weiss, K., Gebert, S., Wuhn, M., Wadephol, H. and Woll, C. (1998), *J Vac Sci Tech*, A16, p. 1017.
[35] Steinruck, H.P. (1996), *J Phys Condens Mat*, 8, p. 6465.

5. The Electrochemistry of Halides and Cationic Surfactants on Au (100)

5.1 The Electrochemistry of Au (100) in 0.1 M NaF solution

As discussed in section 1.4, a flame-annealed Au (100) surface reconstructs to a more densely packed (hex) configuration because this represents the most energetically favourable configuration. The aim is to lift the reconstruction by submerging the electrode in an NaCl solution because Cl^- adsorption increases the mobility of the surface atoms and causes the reconstruction to lift. After the electrode is removed from the adsorbate solution and rinsed at RTP, the (1×1) structure should remain because the activation barrier hinders spontaneous reconstruction. The activation barrier is large because reconstruction involves bond breaking and transporting atoms along the surface, rather than atom displacement, as is the case with reconstruction of the Au (111) surface. The Au (100) electrode used in this study is thus expected to have a fully unreconstructed (1×1) structure when placed into the cell. Figure 5.1A and 5.1B give a CV and a DC curve of Au (100) in 0.1 M NaF solution.

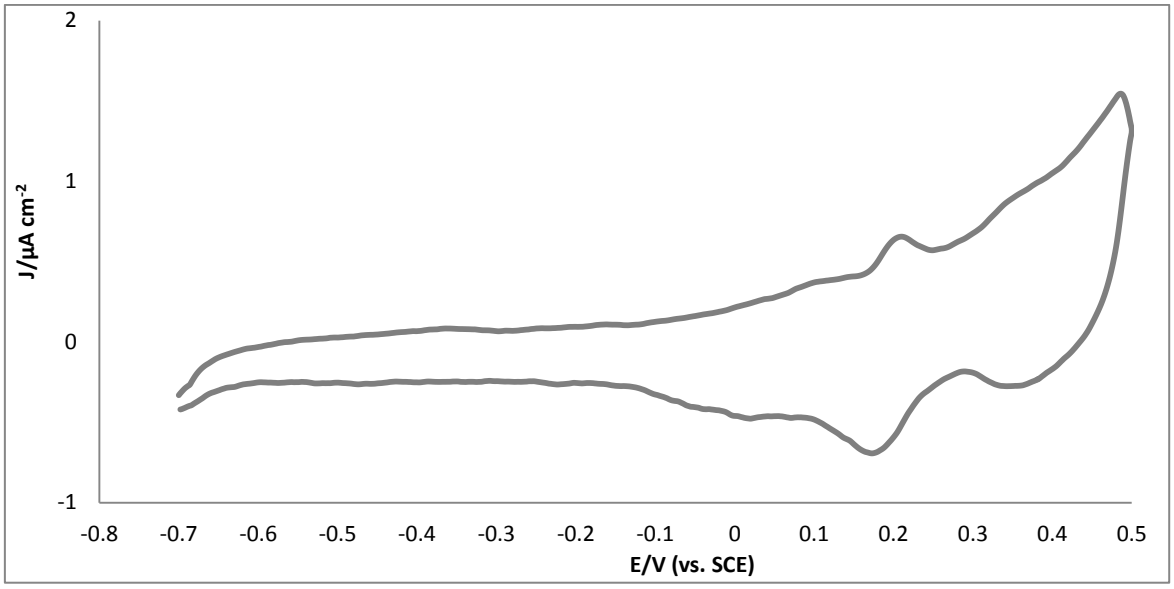

Figure 1A Cyclic Voltammogram of Au (100) in 0.1 M NaF solution.

Sweep rate 20 mV s^{-1}

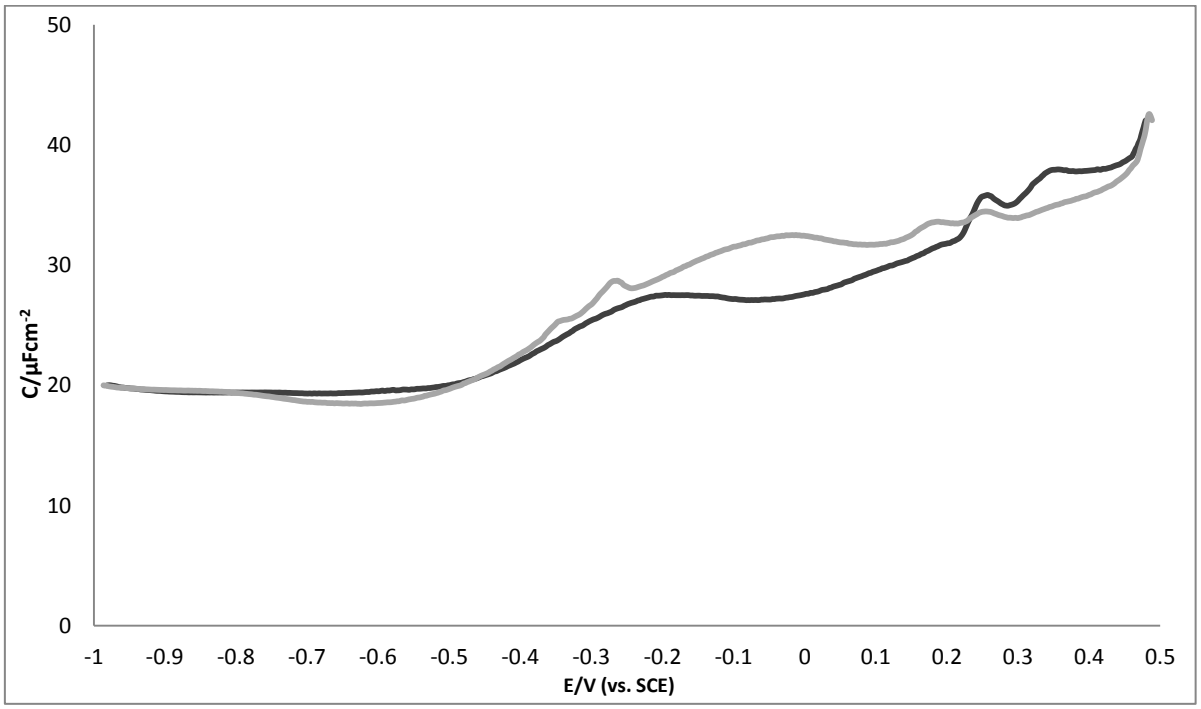

Figure 1B Differential Capacity curves of Au (100) in 0.1 M NaF solution. Here the anodic sweep is represented by the black line and the cathodic sweep by the grey line.

Sweep rate 5 mV s^{-1}

When a negative potential is applied to a clean, unreconstructed Au (100) surface, the reconstructed (hex) structure is said to reappear.[1] This can be seen in the CV of Figure 1A where a peak at 200 mV is evident, which represents the transition between the reconstructed (hex) and unreconstructed (1 × 1) phases. The reconstruction of an Au (100)-(1 × 1) surface at a negative potential has also previously been observed in electroreflectance spectra[2] and LEED studies,[3] as well as surface x-ray scattering (SXS)[4] and STM.[5]

Potential-induced excess electron density lowers the activation barrier for reconstruction. Moreover, at negative potentials, F^- is not present at the electrode interface, so the mobility of the surface Au atoms decreases. Potential-induced reconstruction is purely a kinetic phenomenon, as studies with in situ STM [6] have shown that potential induced reconstruction occurs even with no monoatomic ad-islands on the gold surface, which energetically drive the reconstruction of the Au (100) during processes such as flame annealing. The potential-induced reconstruction follows a two-step mechanism.[2]. The fast step has been related to the monoatomic islands as a source of the extra gold atoms. The second, slower step, less dependent on potential, has been attributed to the rearrangement of the surface atoms. The disintegration of the monoatomic islands is driven by the charging of the surface and the breaking of Au-Au bonds.

According to a study by Kolb and Schneider,[2] the length of time the electrode is held at a negative potential determines how much of the surface reconstructs. When the potential was held at -700 mV for 3 minutes, 90 % of the Au (100)-(1 × 1) surface reconstructed. For the CV in Figure 1A, the electrode is swept from -0.7 V and not held at this potential for any

amount of time. Therefore less of the surface would be expected to be reconstructed. This can be seen by the peak representing the lifting of the reconstruction in Figure 1A; it is considerably smaller than the large and sharp peaks representing the lifting of the reconstruction previously observed in the literature for CVs of clean reconstructed Au (100) surfaces.[1]

It should be noted that in Section 4, Figure 4.4A, a peak is not observed for the CV of Au (111) in 0.1 M NaF solution because the unreconstructed Au (111)-(1 × 1) surface has a similar structure to the reconstructed Au (111)-(23 × $\sqrt{3}$) surface. Both surfaces thus have similar work functions and, consequently, similar pzcs. However, as the (hex)→(1 × 1) transition occurs, the pzc of the surface decreases by around 220 mV.[7] This is because the packing density decreases as the reconstruction lifts, resulting in a decrease of the work function. The sudden shift in pzc with the lifting of the reconstruction therefore means that Additional charging of the electrode surface is required in order to maintain the applied potential during the structural transition, which causes a peak in the current. The greater the current peak, the greater the difference in pzcs of the two surfaces and the greater the peak current density.

In the DC curve of Au (100), the peak at E > 200 mV also represents the lifting of the Au (100)-(hex) reconstruction. The charge under this peak on a DC curve is said to depend on the anion in the solution.[1] The small charge of the peak in Figure 5.1B could reflect the weak adsorptive nature of the F^- anion on the Au (100) surface. It is clear from Figure 4.1B that the double-layer capacities of Au (100)-(hex) and Au (100)-(1 × 1) are different because the DC curves in the positive and negative-going sweeps are a different shape.

The negative-going sweep has several small peaks, which consistently appeared after the DC sweeps were repeated many times with the Au (100) electrode, and flame-annealed and dipped in NaCl solution before each instance. The most probable cause of these peaks is the stepped monoatomic sites on the Au (100) surface after the (hex) reconstruction has been lifted. These step sites have previously been observed in STM images after the Au (100)-(hex) reconstruction has been lifted.[8]

In the negative-going sweep, a DC minimum is observed at 100 mV (vs. SCE), which is the pzc of unreconstructed Au (100).[9] This confirms that in the negative-going sweep, the surface has a (1×1) structure and the surface transition would happen at more negative potentials than the surface transition in the positive-going sweep.

5.2 The Electrochemistry of Au (100) in NaCl and NaBr solution

Figures 5.2A and 5.2B represent CV and DC curves of Au (100) in 0.1 mM NaBr in 0.1 M NaF solution (orange lines), 0.1 mM NaCl in 0.1 M NaF (blue lines) and 0.1 M NaF (black dotted lines).

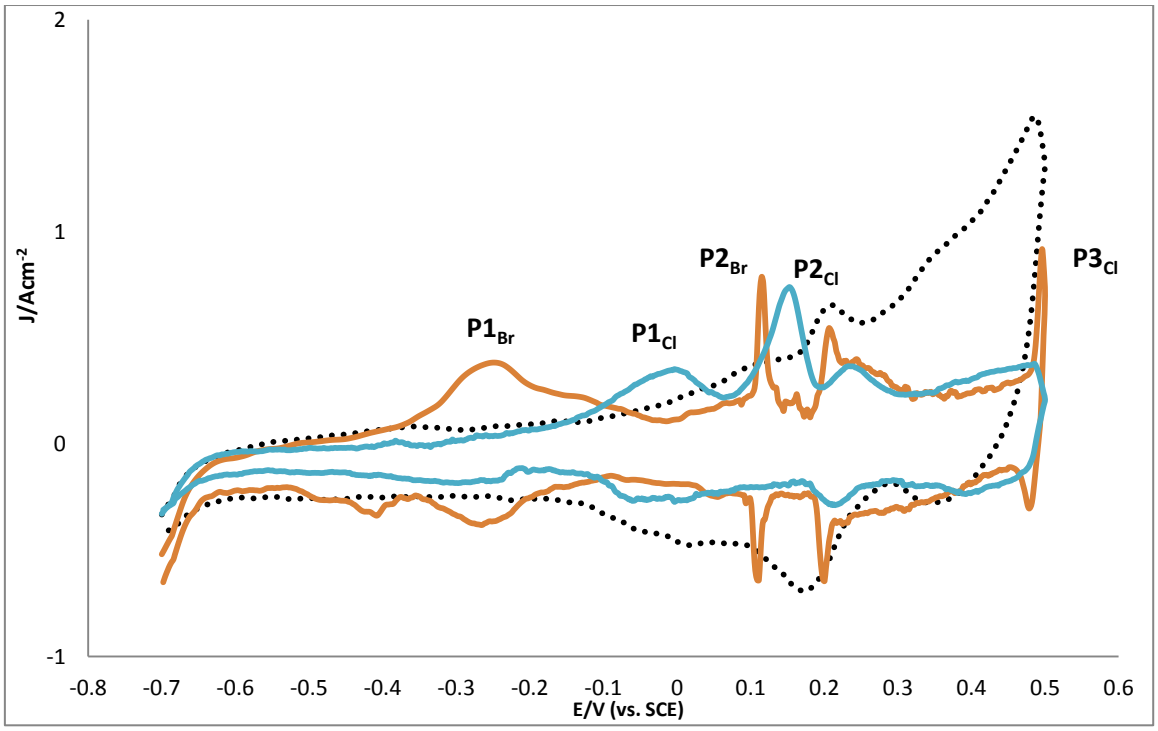

Figure 5.2A Cyclic Voltammogram of Au (100) in 100 mM NaF solution (black dotted line), 0.1 mM NaCl in 100 mM NaF solution (blue line) and 0.1 mM NaBr in 100 mM NaF solution (orange line).

Sweep rate 20 mV s^{-1}

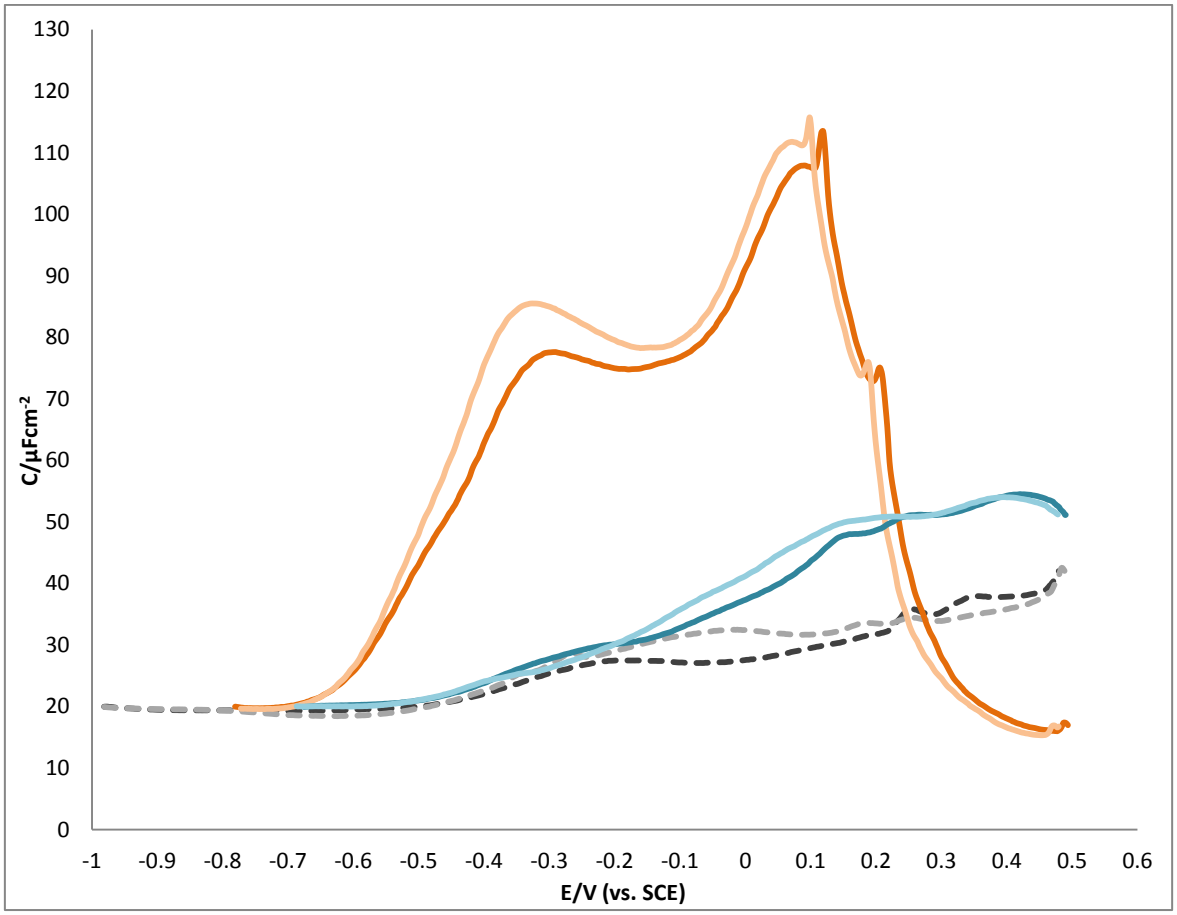

Figure 5.2B Differential Capacitance curves of Au (100) in 100 mM NaF solution (black dotted lines), 0.2 mM NaCl in 100 mM NaF solution (blue lines) and 0.2 mM NaBr in 100 mM NaF solution (orange lines). The dark shaded lines represent the anodic sweep, and the light shaded lines represent the cathodic sweep.

Sweep rate 5 mV s^{-1}

The current peaks of the CVs in Figure 5.2A have been labelled P1, P2 and P3. Peak $P1_{Br}$ and $P1_{Cl}$ at -270 mV and -37 mV, respectively, signal the lifting of the Au (100)-(hex) reconstruction due to Br^- [10] and Cl^- [11] specific adsorption on the substrate. The coverage of Br^- and Cl^- on the electrode surface increases as the electrode potential becomes more positive. Thus at the negative potentials of $P1_{Br}$ and $P1_{Cl}$, the coverage of the halide anions on the electrode surface would be very low. This shows that only a very low coverage of Br^- and Cl^- lifts the reconstruction of the Au (100) surface.

At positive potentials of P1, the surface should have the unreconstructed (1 × 1) configuration. After P1, the concentrations of Br^- and Cl^- increase with increasing potential. $P2_{Br}$ and $P2_{Cl}$ are at potentials of 113 and 142 mV, respectively, and are likely to be caused by the disorder/order phase transition involving specifically adsorbed anions.[10] The ordered phase would have a c($\sqrt{2} \times 2\sqrt{2}$)R45° structure. [12 13] It is noteworthy that $P2_{Br}$ and $P2_{Cl}$ are considerably closer together in potential than $P1_{Br}$ and $P1_{Cl}$, indicating that the lifting of the Au (100)-(hex) reconstruction has much to do with the strength of the anion-surface interaction, as well as with the surface coverage.[12] The beginning of a phase transition involving the compression of the c($\sqrt{2} \times 2\sqrt{2}$)R45° is probably the cause of $P3_{Br}$.[12]

In Figures 5.2B, P1 and P2 are represented by maxima in the differential capacitance, although the maxima for the NaBr DC curve are more pronounced, owing to the stronger adsorptive nature of the Br^- ions.

Figures 5.3A and 5.3B show CVs and DC curves of of various concentrations of NaCl (blue lines) between 0.001 and 0.2 mM. The curves acquire lighter shades of blue as the concentration of NaBr in the 0.1 M NaF increases. The CV and DC curve of Au (100) in 0.1 M NaF (black dotted line) is added as a reference.

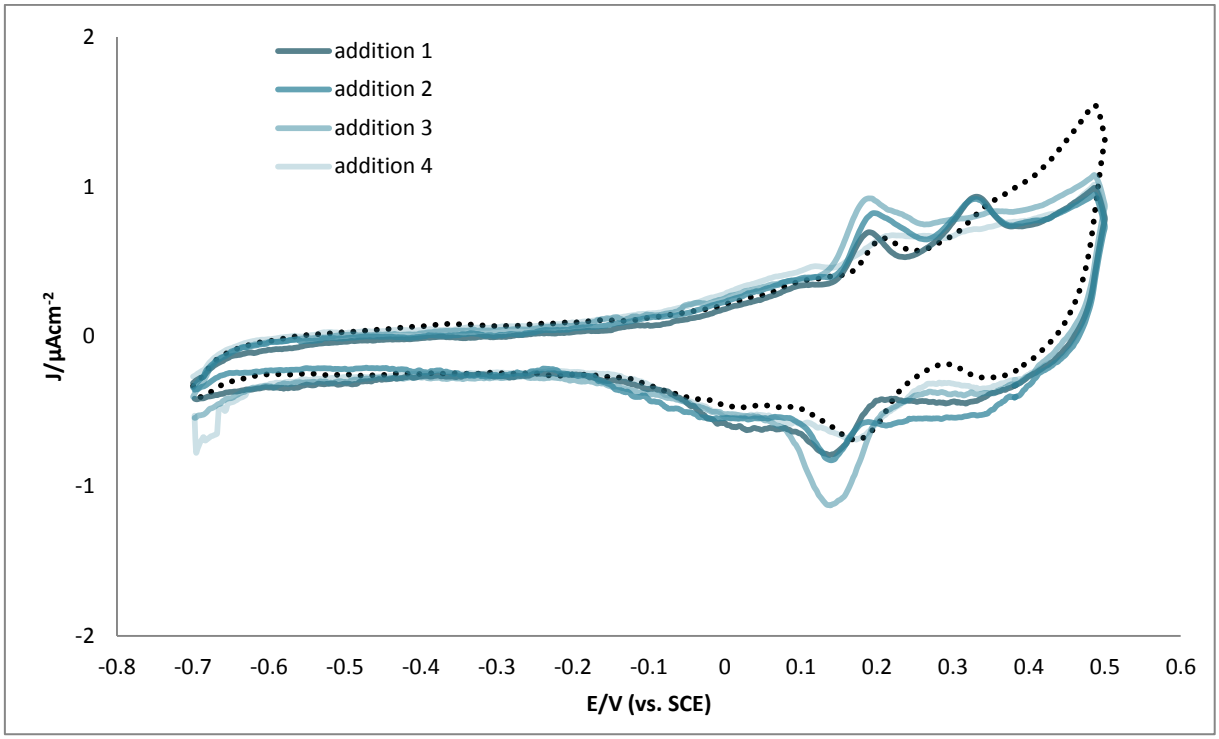

Figure 5.3A (i) Cyclic Voltammetry curves recorded for Au (111) in 100 mM NaF solution without NaCl (black dotted line), and with selected NaCl concentrations starting from 0.001 mM NaCl (darkest blue line) to 0.01 mM NaCl (lightest blue line).
Sweep rate 20 mV s^{-1}

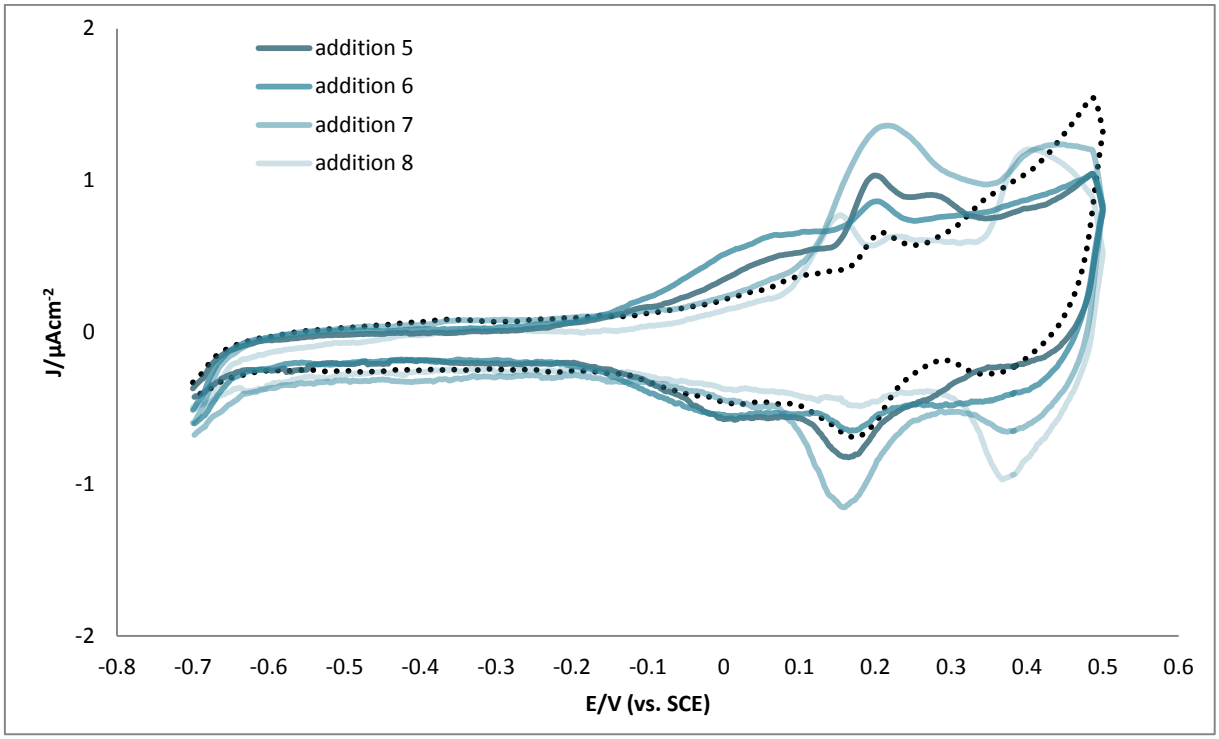

Figure 5.3A (ii) Cyclic Voltammetry curves recorded for Au (111) in 100 mM NaF solution without NaCl (black dotted line), and with selected NaCl concentrations starting from 0.025 mM NaCl (darkest blue line) to 0.2 mM NaCl (lightest blue line).
Sweep rate 20 mV s^{-1}

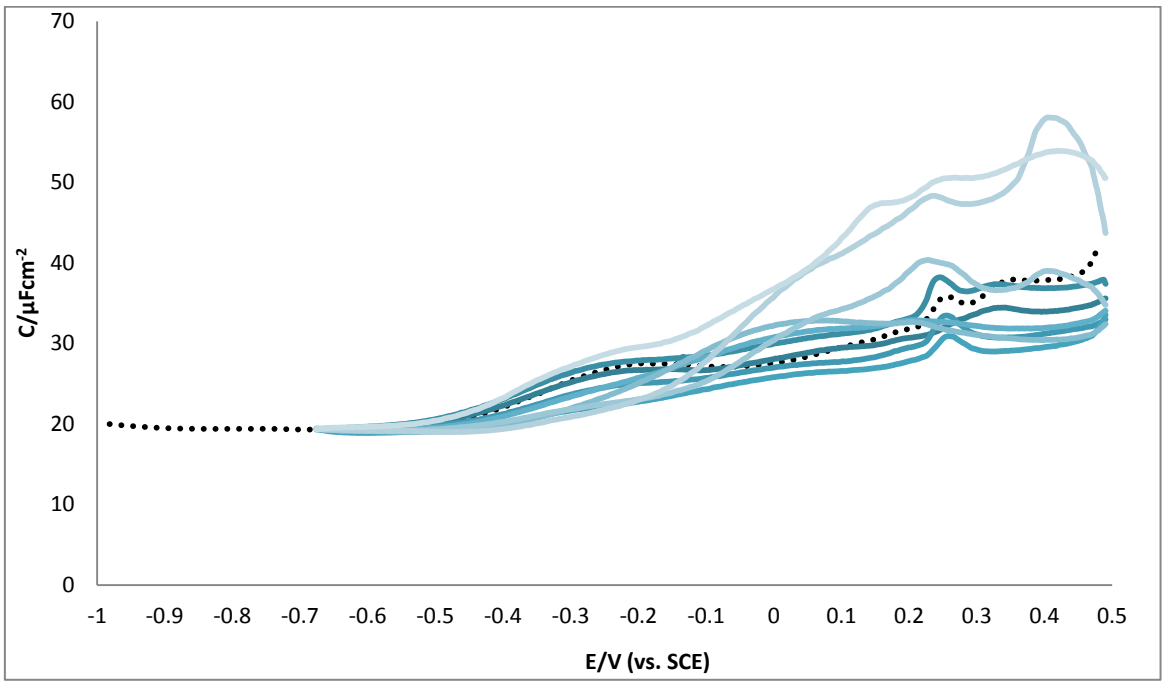

Figure 5.3B Differential Capacitance curves of the cathodic sweep recorded for Au (100) in 0.1 M NaF solution without NaCl (black dotted line) and with selected NaCl concentrations starting from 0.001 M NaCl (darkest blue line) to 0.2 mM NaCl (lightest blue line).

Sweep rate 5 mV s^{-1}

In Figure 5.3A, the current between -200 and 200 mV increases gradually as the concentration of NaCl in the solution increases from 0.01 to 0.1 mM, showing the increasing influence of the Cl^- ions on the lifting of the reconstruction. Crucially, however, in this concentration range, no peak in this potential region can be observed. There is only a peak once the concentration of NaCl reaches 0.2 mM. This could be because the coverage of Cl^- is not sufficient, at concentrations at or below 0.1 mM of NaCl, fully to influence the lifting of the reconstruction.

For the CVs of Au (100) between concentrations of 0.001 to 0.1 mM NaCl, there is a peak at around 200 mV representing the lifting of the reconstructed Au (100)-(hex) structure. In Fiugre 5.3B, these peaks have exactly the same shape as the lifting of the Au corresponding peak found for the DC curve of Au (100) in 0.1 M NaF solution. When the concentration of NaCl is below 0.2 mM, it is likely that there is a partial Cl^- layer on the Au (100) surface. The reconstruction of the Au (100) would therefore partially lift because of the specifically adsorbed Cl^- and partially lift owing to the F^- ions present in the bulk solution.

When the concentration of NaCl is between 0.001 and 0.005 mM, the peak at around 300 mV representing a phase transition of the Cl^- becomes more negative in potential as the concentration of NaCl increases. For higher concentrations of NaCl; between 0.02 mM and 0.1 mM, the peak representing a phase change seems to merge into the peak representing the lifting of the reconstruction, so both these structural phenomena probably occur at similar potentials.

When the concentration of NaCl reaches 0.2 mM, the area, or charge, under the cyclic voltammogram is significantly reduced. This is probably due to a more densely packed Cl^- layer.

Figures 5.4A and 5.4B show CVs and DC curves of various concentrations of NaBr in 0.1 M NaF solution, between 0.001 and 0.2 mM. The curves acquire lighter shades of orange as the concentration of NaBr in the 0.1 M NaF increases. The CV and DC curve of Au (100) in 0.1 M NaF (black dotted line) is added as a reference.

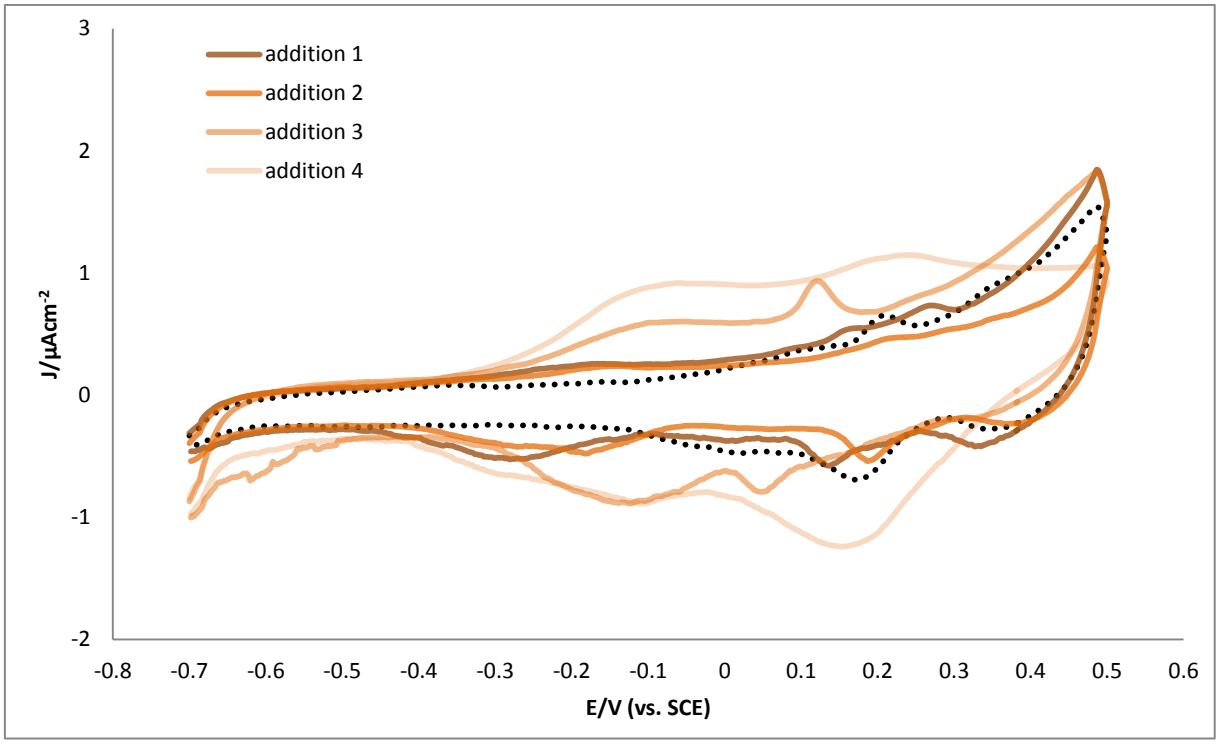

Figure 5.4B (i) Cyclic Voltammetry curves recorded for Au (111) in 0.1 M NaF solution without NaBr (black dotted line), and with selected NaBr concentrations starting from 0.001 M NaBr (darkest orange line) to 0.01 mM NaBr (lightest orange line).
Sweep rate 20 mV s^{-1}

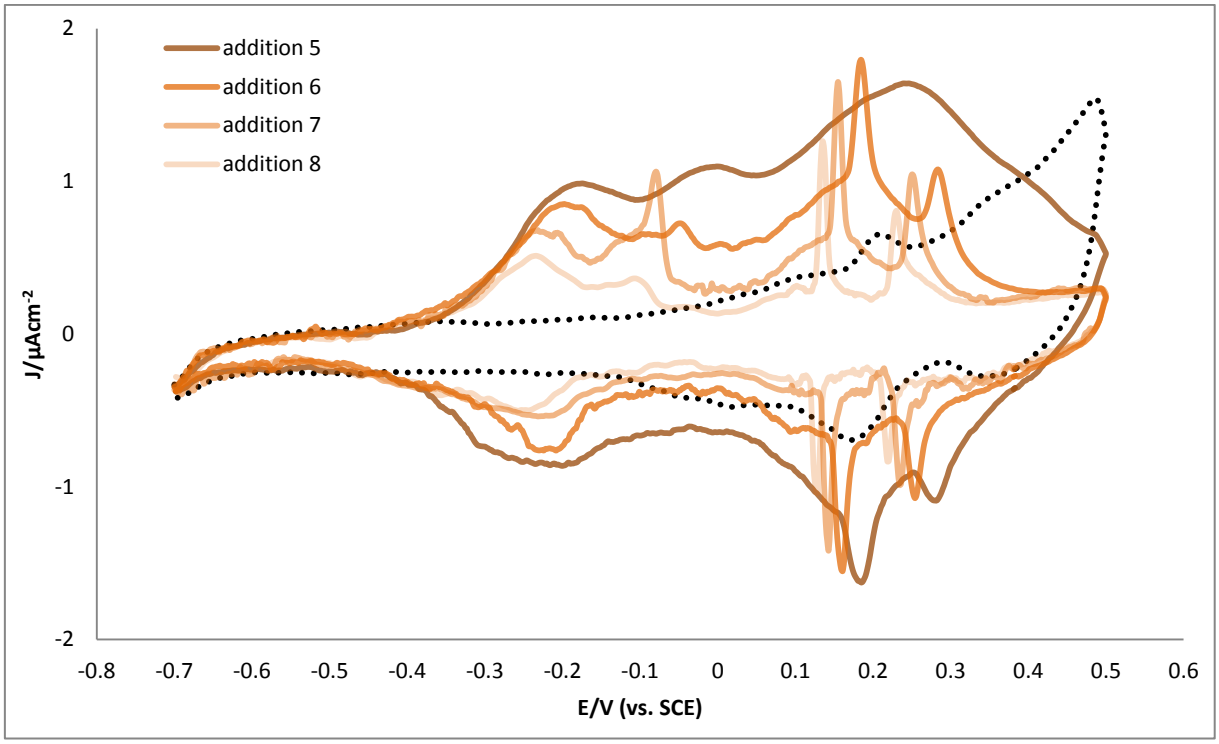

Figure 5.4B (ii) Cyclic Voltammetry curves recorded for Au (111) in 0.1 M NaF solution without NaBr (black dotted line), and with selected NaBr concentrations starting from 0.025 M NaBr (darkest orange line) to 0.2 mM NaBr (lightest orange line).
Sweep rate 20 mV s^{-1}

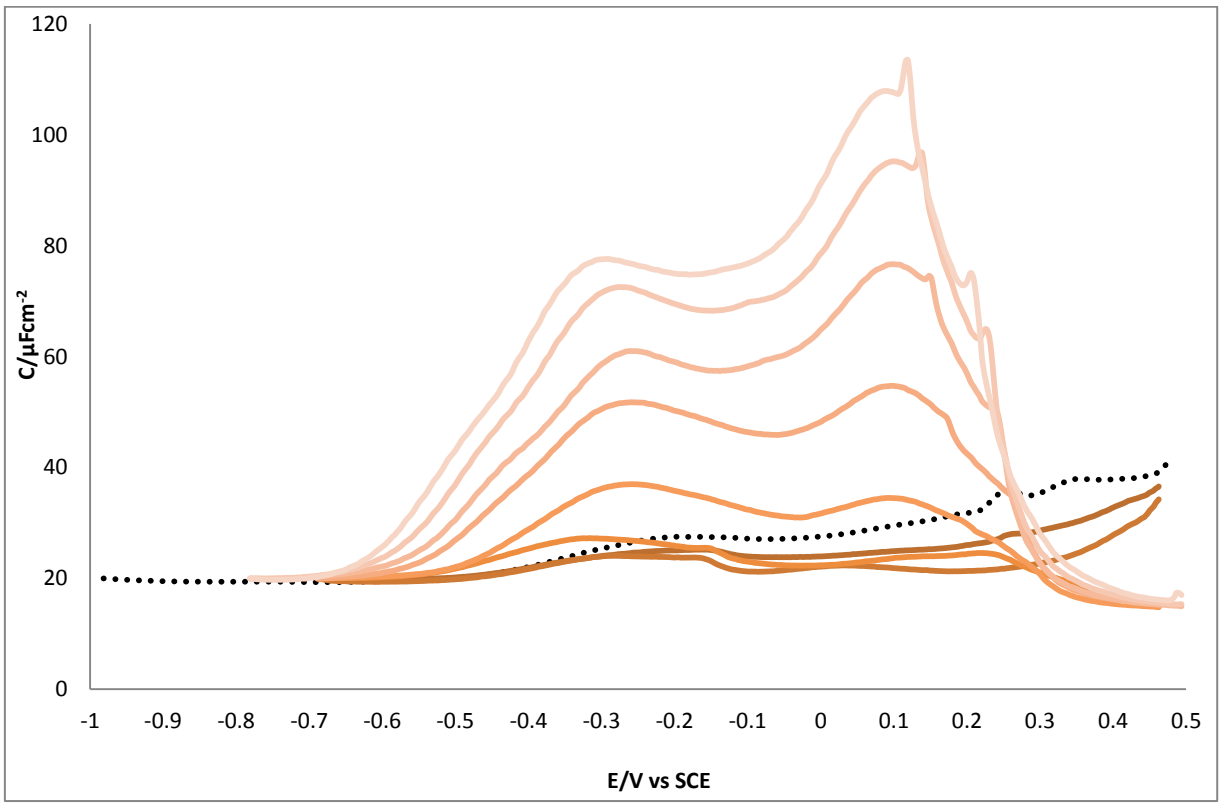

Figure 5.4B. Differential Capacitance curves of the cathodic sweep recorded for Au (100) in 0.1 M NaF solution without NaBr (black dotted line) and with selected NaBr concentrations starting from 0.0005 mM NaBr (darkest orange line) to 0.2 mM NaBr (lightest orange line).

Sweep rate 5 mV s^{-1}

In Figure 5.4A, the very broad peak in the current represent the specific adsorption of bromide, culminating in the lifting of the Au (100) reconstruction stays at -200 mV, at concentrations of NaBr between 0.001 and 0.005 mM. As the concentration of NaBr increases from 0.01 to 0.2 mM, the peak arising from lifting of the reconstruction shifts from -200 mM to -300 mM. The maxima representing this process in Figure 4B greatly increase in differential capacitance as the bulk NaBr in this concentration range. These features in

Figure 5.4B show that increased coverage of Br^-, as well as the strong Br-Au surface interactions, help to lift the Au (100) reconstruction. For concentrations of NaBr higher than 0.02 mM, there are spiked maxima in the potential region between 110 and 200 mV, representing the disordered to ordered phase transition of the Br^- adlayer. For concentrations lower than 0.02 mM, there is only a broad peak in this potential region. This shows that the coverage of Br^- ions is not high enough for there to be an ordered adlayer structure. These broad peaks could represent the compression of the Br^- layer.

5.3 The Electrochemistry of Au (100) in CTAF solution

Figures 5.5A and 5.5B give CV and DC curves of the Au (100) electrode when CTAF is in 0.1 M NaF solution after Addition 7 (when the concentration is half of the CMC of CTAF in NaF solution). The CV and DC curves of the Au (100) electrode are also added as a reference; these are represented by black/grey dotted lines.

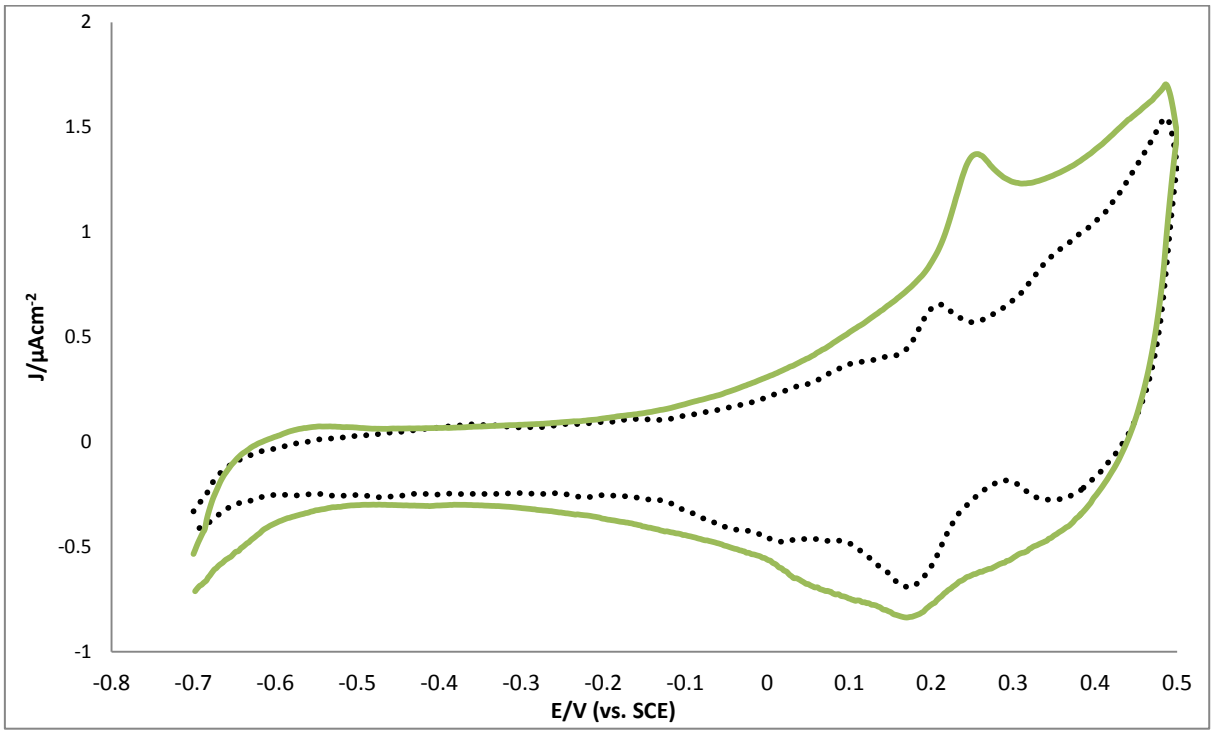

Figure 5.5A A cyclic voltammogram of Au (100) in 0.1 M NaF with CTAF after Addition 7 (9×10^{-5} mol dm^{-3}). A CV of Au (100) in 0.1 M NaF solution (black dotted line) is also included as a reference.

Sweep rate 20 mV s^{-1}

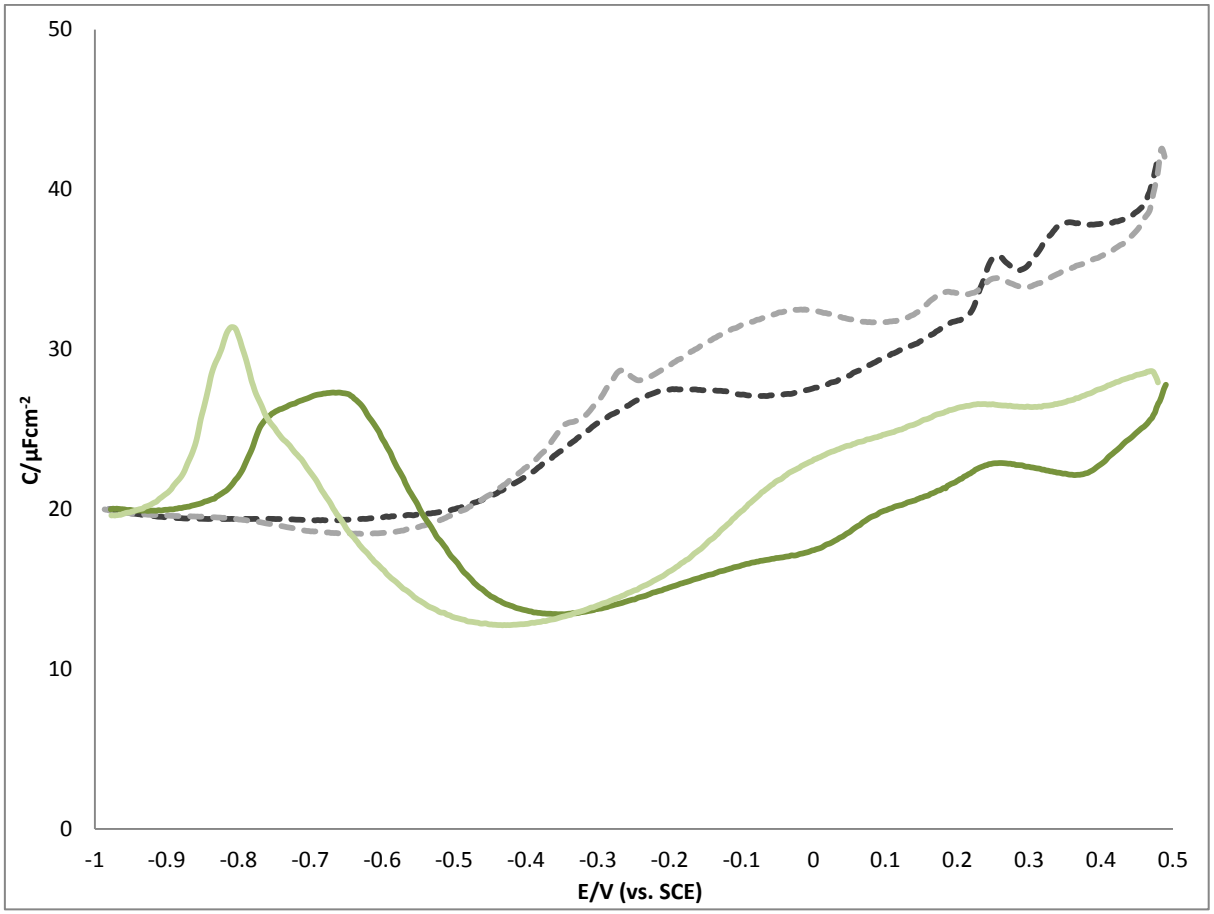

Figure 5.5B Differential capacitance curves of Au (111) in 0.1 M NaF with CTAF after Addition 7 (9 x 10^{-5} mol dm^{-3}). The cathodic sweep is represented by the dark green line; the anodic sweep, by the light green line. A CV of Au (111) in 0.1 M NaF solution (black dotted line) is also included as a reference.

Sweep rate 5 mV s^{-1}

In Figure 5.5A, the peak representing the lifting of the reconstruction Au (100)-(hex) reconstruction is at 240 mV and is at a more positive potential than that the corresponding peak of Au (100) in in NaF solution. This shows that CTAF suppresses the lifting of the reconstruction. A reason for this could be that the adsorbed organic tail group of CTAF hinders the interaction of F^- with the Au (100) surface: the mobility of the Au (100) surface atoms thus decreases, rendering the Au (100)-(hex) structure more stable. Similar theories

for the reason why organic molecules hinder the lifting of the reconstruction of Au (100) surfaces have previously been proposed by Kolb[14] and Skoluda.[15] The cationic surfactant OTATf has also been found to hinder the lifting of the Au (100) reconstruction,[16] though making a direct comparison with these data is difficult because the concentrations of OTATf in NaF solution are around twenty times higher (relative to the CMC) than those of CTAF used in this study.

In Figure 5.5B, there is a broad differential capacitance maximum at -670 mV that can be ascribed to the adsorption of the surfactant. In the negative-going sweep, however, there is a sharp peak representing the surfactant desorption at a considerably more negative potential of -800 mV. This could indicate that the Au (100) surface has more (1×1) unreconstructed sites in the negative-going sweep. The surface packing and work functions are thus different; as a result, pzcs of the surface in the positive and negative sweeps would cause the different potentials of the adsorption and desorption maxima. The broadness of the surfactant adsorption peak is most likely because the Au (100) surface is not fully reconstructed, and hence as a result of (hex) and (1×1) sites on the Au (100) surface.

In Figure 5.5B, there is a minimum at -340 mV with a differential capacitance of around 13 μF cm^{-2}. A minimum is also observed in the DC curve of Au (111) containing the same concentration of CTAF (see Fig 4.9B), though in Figure 5.5B, the DC minimum is not present over an appreciable potential range. This is likely to be because the buckled nature of the Au (100)-(hex) surface[17] means that the CTAF molecules do not form an ordered adlayer structure on the substrate surface as they do on Au (111). However the atomic arrangement of Au (100)-(hex) is similar to Au (111) so it is possible that some CTAF molecules do adsorb

side-on in a similar configuration to that proposed in Figure 1.14, the van der Waals interactions of the alkyl tail groups of the CTAF molecules with the compressed Au surface atoms could stabilise the Au (100)-(hex) reconstructed structure. This could be another reason why the adsorption of CTAF molecules on the Au (100) surface hinders the lifting of the surface reconstruction.

The increase in differential capacitance after the differential capacitance minimum in Figure 5.5B is likely caused by the transition of the CTAF film on the Au (100) surface, desorption of CTAF molecules and lifting of the Au (100)-(hex) reconstruction, culminating in a maximum at 240 mV.

Figure 5.6A and 5.6B give CVs and DC curves of Au (111) in 0.1 M NaF solution with concentration of CTAF between 1/128 of its CMC and its CMC. The lines acquire progressively lighter shades of green as the concentration of CTAF in the NaF solution increases. The baseline CVs and DCs of Au (111) in 0.1 M NaF are represented by a black dotted line.

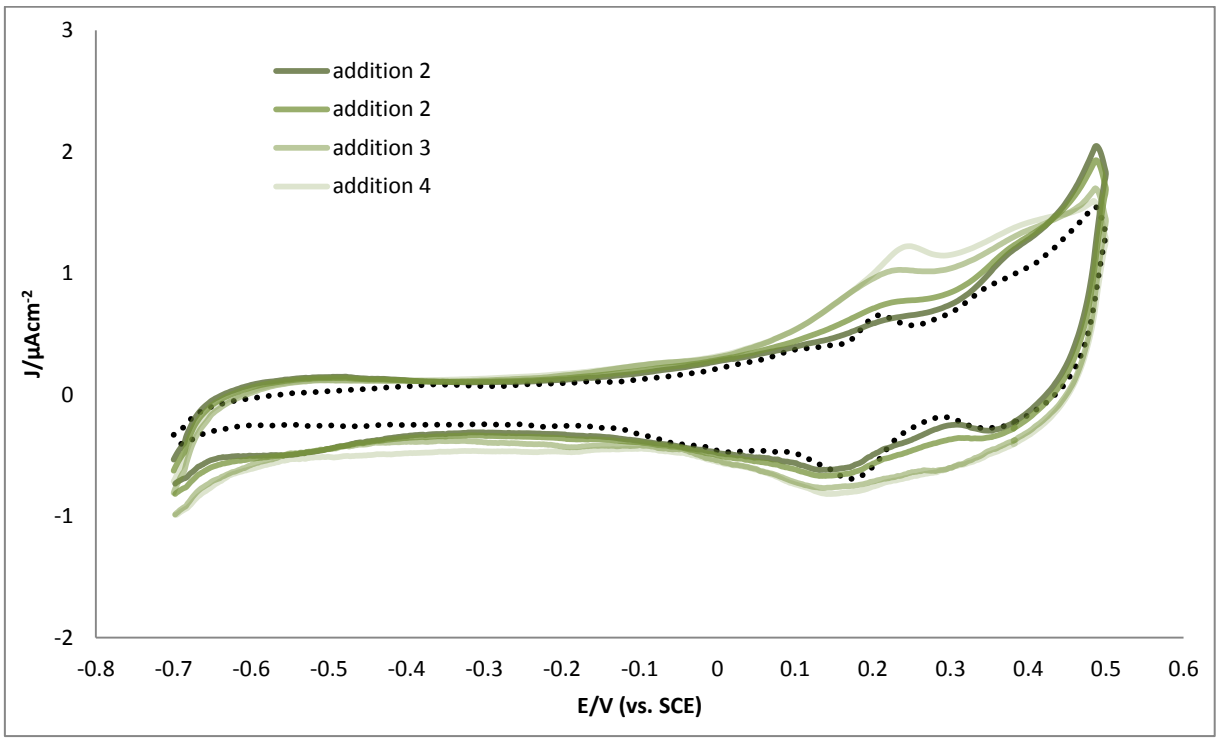

Figure 5.6A (i) Cyclic voltammetry curves recorded for Au (111) in 0.1 M NaF solution without CTAF (black dotted line), with CTAF concentrations after Additions 1-4 (1/128 CMC to 1/16 CMC of CTAF in 0.1 M NaF solution: 0.0014-0.0112 mM). The CV curves acquire progressively lighter shades of green as the bulk concentration of CTAF increases.
Sweep rate 20 mV s^{-1}

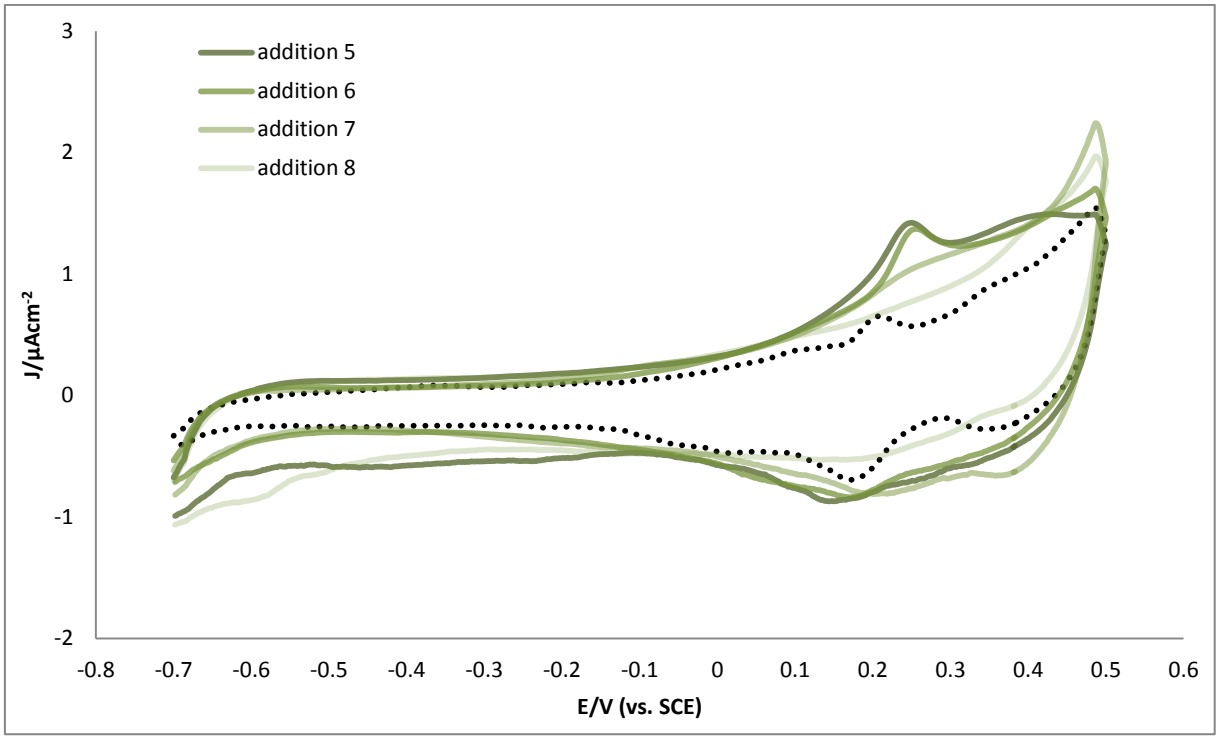

Figure 5.6A (ii) Cyclic voltammetry curves recorded for Au (111) in 0.1 M NaF solution without CTAF (black dotted line), with CTAF concentrations after Additions 5-8 (1/8 CMC to the CMC of CTAF in 0.1 M NaF solution: 0.0225-0.18 mM). The CV curves acquire progressively lighter shades of green as the bulk concentration of CTAF increases.
Sweep rate 20 mV s^{-1}

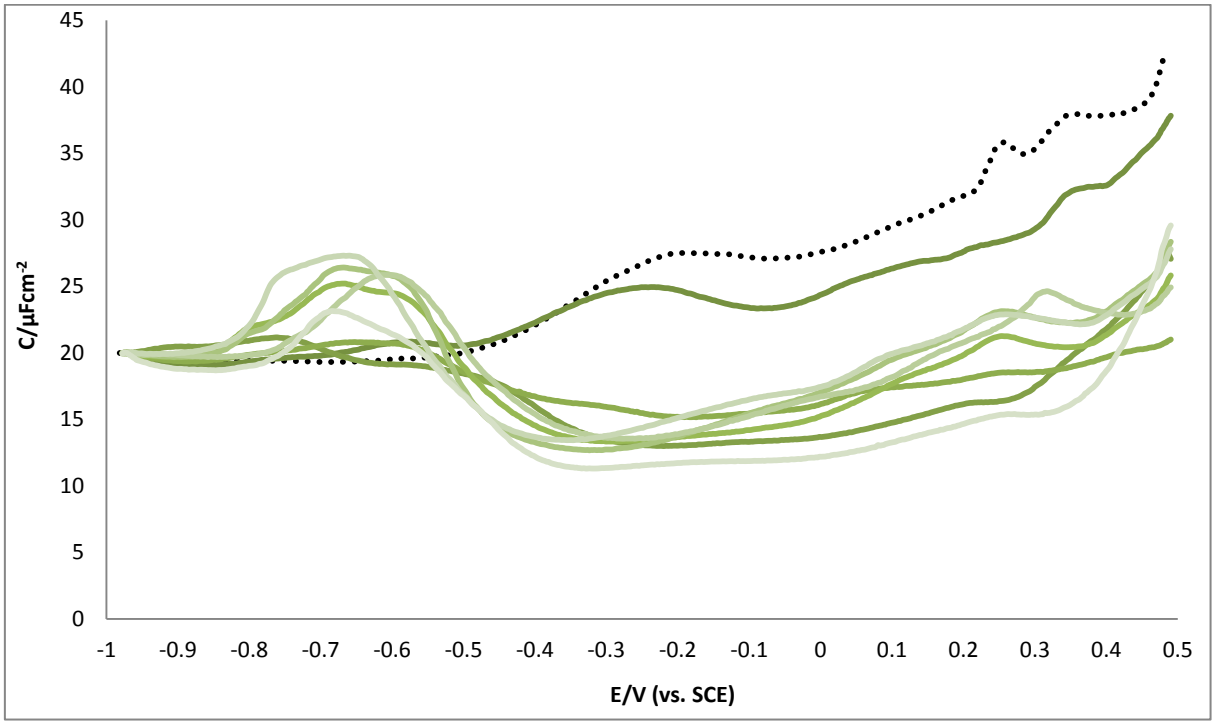

Figure 5.6B Differential capacity curves of the positive going sweep recorded for Au (100) in 0.1 M NaF solution without CTAF (black dotted line), with CTAF concentrations after Additions 1-8 (1/128 CMC to the CMC of CTAF in 0.1 M NaF solution: 0.0014-0.18 mM). The DC curves acquire progressively lighter shades of green as the bulk concentration of CTAF increases.
Sweep rate 5 mV s^{-1}

In Figures 5.6A and 5.6B, no big changes in the CV or DC curves are observed, showing that the adlayer structure of CTAF molecules on the electrode surface does not greatly vary with bulk concentration. This is because the heavily solvated F^- counter-ion does not stabilise the surfactant molecules. The disordered nature of the surfactant adlayer structure can be seen by the CV and DC curves not superimposing over each other, as they do for the CV and DC curves of CTAF on Au (111).

It is possible that when the concentration of CTAF is at the CMC, the van der Waals interactions of the surfactant tail groups with the substrate cause the CTAF molecules to form hemi-micellar aggregates. This enhanced coverage would be the reason why the DC minimum when the concentration of CTAF is at the CMC has a lower value and is flatter than the DC curves for the lower concentrations of CTAF. No peak for lifting of reconstruction is observed in Figure 5.6B for the CV curve when the concentration of CTAF is at the CMC. The enhanced coverage of CTAF molecules at the CMC could suppress potentially induced reconstruction by inhibiting the rearrangement of surface atoms. Alternatively, if potentially induced reconstruction does occur, the CTAF molecules could stabilise Au (100)-(hex) structure, by blocking the F^- interactions with the surface, or decreasing the mobility of the surface atoms.

5.4 The Electrochemistry of Au (100) in CTAC solution

Figure 5.7A and 5.7B give a CV and a DC curve for an Au (100) in 0.1 M NaF solution after Addition 7 of CTAC (purple line) (1/2 CMC of CTAC in 0.1 M NaF solution: 0.07 mM). CVs and DC curves for Au (111) in 0.1 M NaF solution with NaCl after Addition 7 (blue line) (0.07 mM) and 0.1 M NaF (black dotted line) are also included

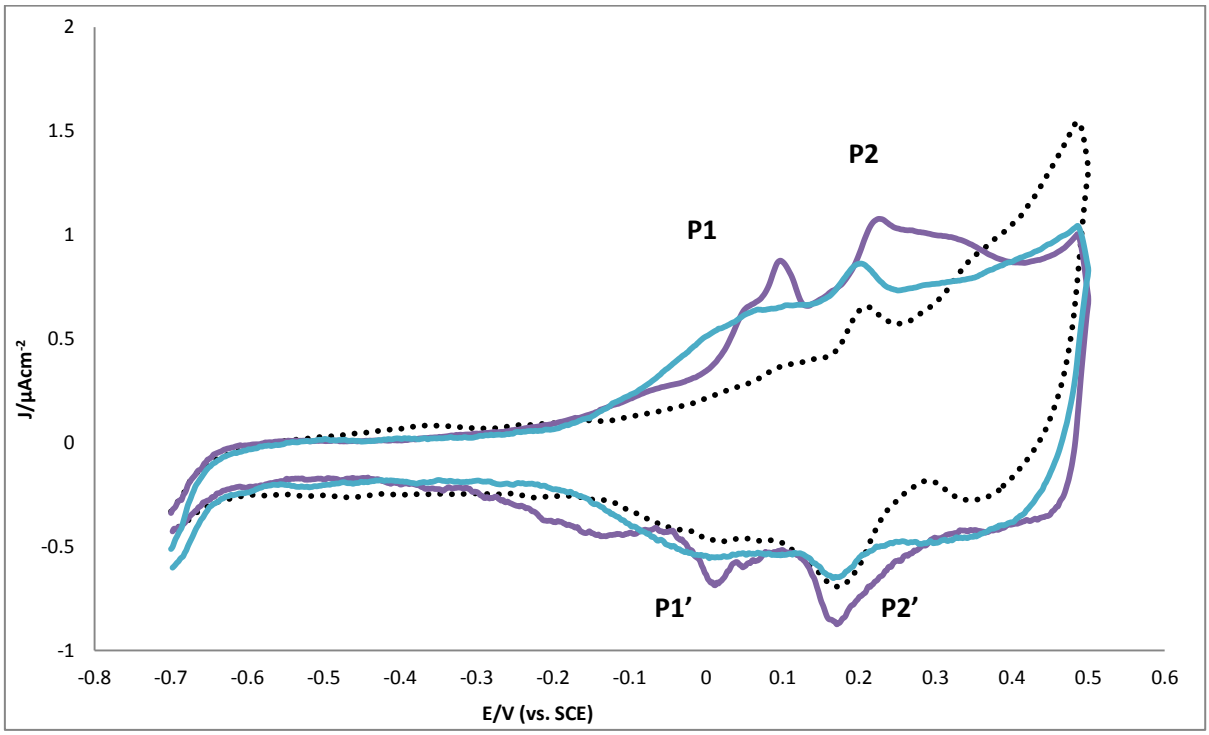

Figure 5.7A Cyclic voltammogram of Au (100) in 0.1 M NaF solution with CTAC after Addition 7 (0.5 CMC of CTAC in 0.1 M NaF solution or 0.07 mM) (purple line). CVs of Au (100) in 0.1 M NaF with 0.07 mM NaCl (blue line) and Au (100) in 0.1 M NaF solution (black dotted line) are also included.

Sweep rate 20 mV s^{-1}.

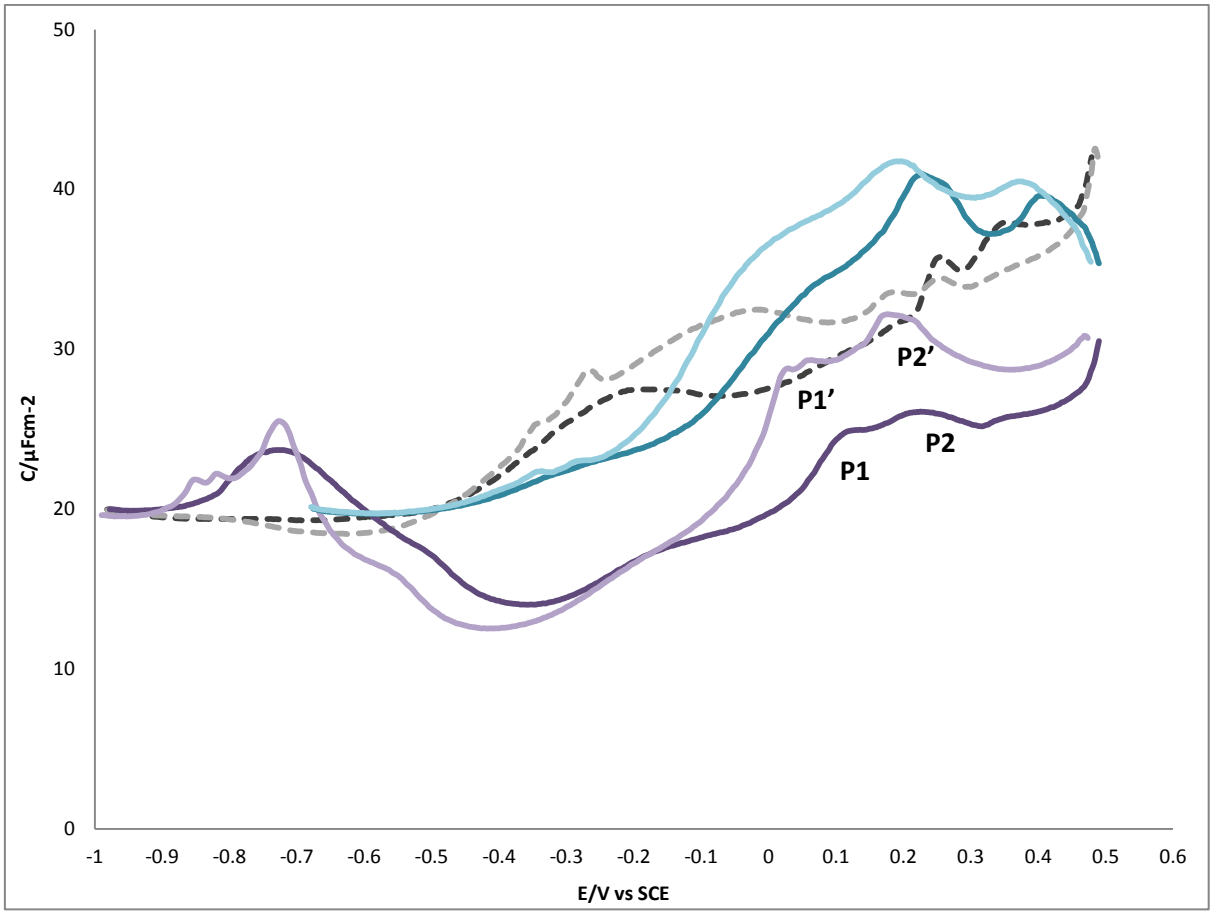

Figure 7B Differential capacitance curves of Au (100) in 0.1 M NaF solution with CTAC after Addition 7 (half of CMC of CTAC in 0.1 M NaF solution or 0.07 mM) (purple line). CVs of Au (100) in 0.1 M NaF with 0.07 mM NaCl (blue line) and Au (100) in 0.1 M NaF solution (black dotted line) are also included. In all three sets of DC curves, the dark shaded lines represent the anodic sweep; the light shaded lines, the anodic sweeps.

Sweep rate 5 mV s^{-1}.

Figure 7A shows two clear maxima at 90 mV and 212 mV, labelled P1 and P2 respectively. P1 and P2 have corresponding peaks in the negative-going sweep and are labelled P1' and P2'.

The most likely cause of P1 is a phase change in the surfactant film. A shoulder at 45 mV precedes the maximum of P1. In the cathodic sweep, P1' has a similar shape to P1. The reversible nature of these sets of peaks indicates a surface process of fast kinetics.

P2 is most likely caused as a result of the lifting of the Au (100)-(hex) reconstruction. It is at a more positive potential than the corresponding peaks in of the CVs of Au (100) in 0.1 M NaF only and NaCl (also at 0.07 mM) in 0.1 M NaF. However, P2 is at a more negative potential than the equivalent peak for CTAF at the same concentration relative to the CMC. This shows that, while CTAC clearly suppresses the lifting of the Au (100) reconstruction, the effect Cl^- anions have on enhancing the mobility of the Au (100) surface atoms slightly counterbalances the stability the CTA^+ molecules have on the Au (100)-(hex) structure. Unlike the case of CTAF, as P2 has a corresponding peak in the negative-going sweep at 178 mV, the transition between the Au (100)-(hex) and (1x1) states is a relatively reversible process.

In Figure 5.7B, peaks P1 (and P1'), and P2 (and P2') are at the same potentials as P1 and P2 in Figure 5.7A, and thus correspond to the same processes. In Figure 5.7B, there is a minimum at -360 mV. Subsequently, as with CTAF, the differential capacitance increases with potential; indicating the disordered nature of the CTAC molecule film on the Au (100) surface. The gradual increase in the differential capacitance culminates in the peak P1, resulting from the phase transition in the overlayers.

Figures 4.14A and 4.14B give CV and DC curves of Au (100) in 0.1 M NaF solution with CTAC after Addition 1-8 (1/128 CMC to the CMC of CTAC in 0.1 M NaF solution: 0.0011-0.14 mM). The lines acquire progressively lighter shades of purple as the concentration of CTAC in NaF solution increases. The baseline CV and DC curves of Au (100) in 0.1 M NaF solution are represented by a black dotted line.

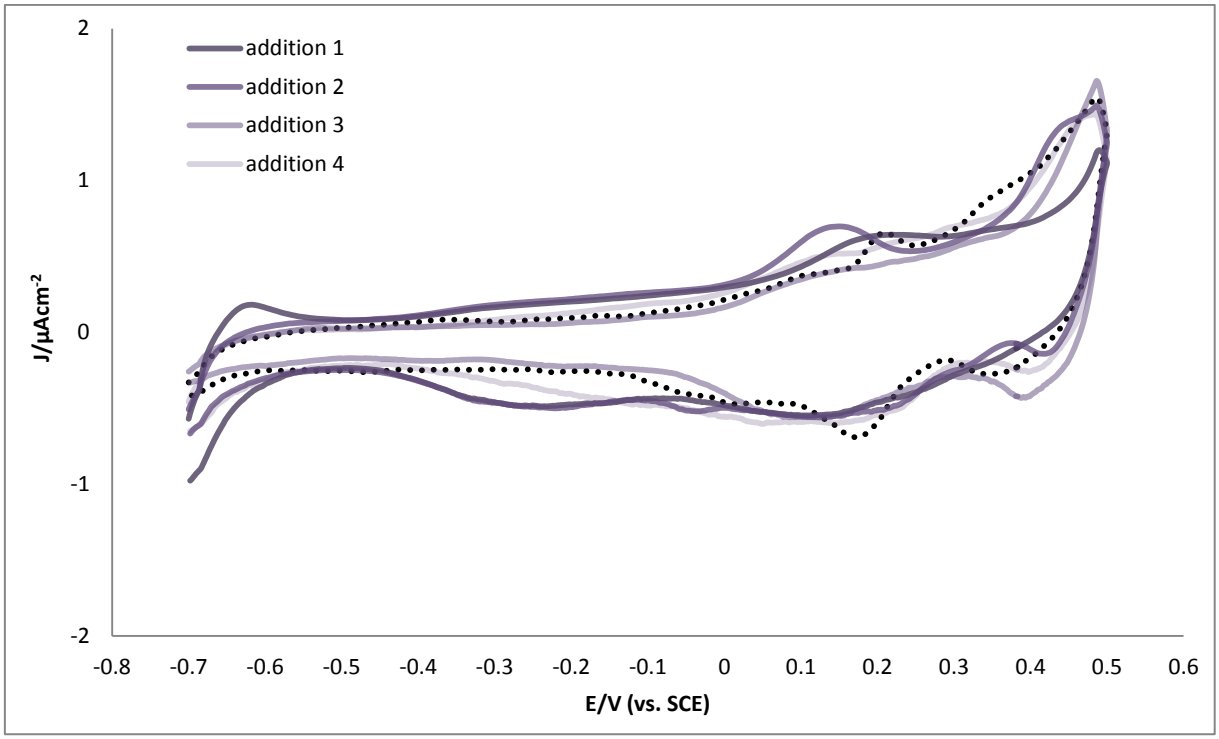

Figure 5.8A (i) Cyclic voltammetry curves recorded for Au (111) in 0.1 M NaF solution without CTAC (black dotted line) and with CTAC after Additions 1-4 (1/128 CMC to 1/16 CMC of CTAC in 0.1 M NaF solution; 0.0011- 0.0088 mM) the CV curves become progressively lighter shades of purple as the bulk concentration of CTAF increases.

Sweep rate 20 mV s^{-1}

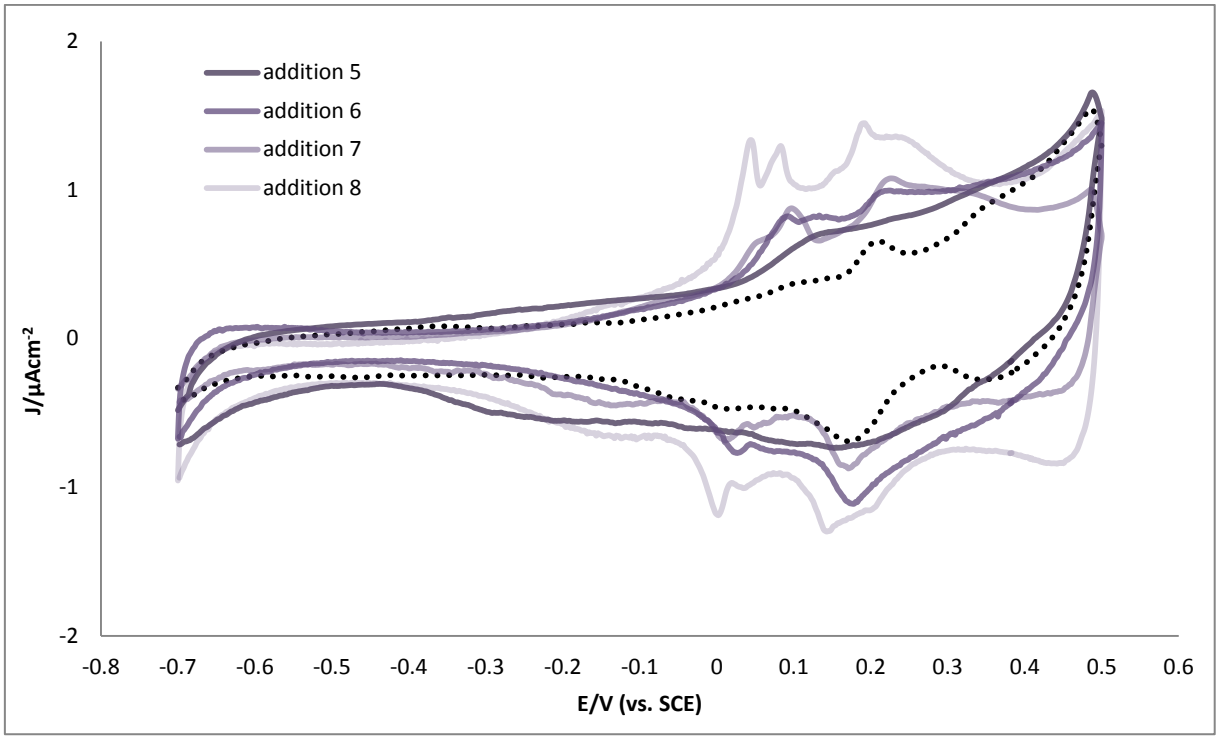

Figure 5.8A (ii) Cyclic voltammetry curves recorded for Au (111) in 0.1 M NaF solution without CTAC (black dotted line) and with CTAC after Additions 5-8 (1/8 CMC to the CMC of CTAC in 0.1 M NaF solution; 0.0175- 0.14 mM) the CV curves become progressively lighter shades of purple as the bulk concentration of CTAF increases.

Sweep rate 20 mV s^{-1}

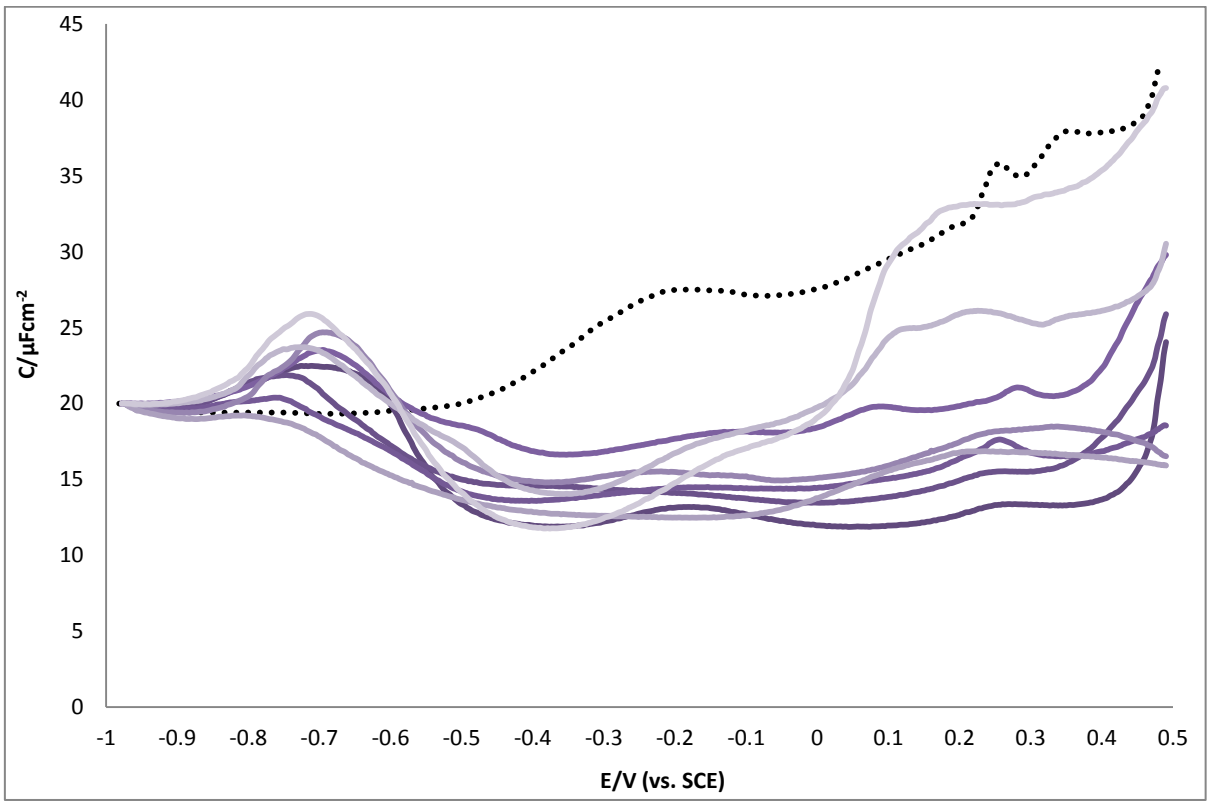

Figure 5.8B Differential capacity curves of the anodic sweep, recorded for Au (100) in 0.1 M NaF solution without CTAC (black dotted line) and with CTAC after Additions 1-8 (1/128 CMC to the CMC of CTAC in 0.1 M NaF solution; 0.0011- 0.18 mM) the DC curves become progressively lighter shades of purple as the bulk concentration of CTAF increases.

Sweep rate 5 mV s^{-1}

In Figure 5.8A, the peak corresponding to the transition of the surfactant film appears only when the concentration of CTAC is at ¼ CMC. Thus below this concentration, there is insufficient CTA^+ or Cl^- at the electrode interface for phase transition in the surfactant film to occur. The phase transition maxima become more negative in potential and greatly increase in current as the CTAC concentration increases from ¼ CMC through to the CMC of CTAC. At the CMC of CTAC, there are two spiked maxima (rather than one) representing phase transitions of the surfactant film. This indicates that a phase forms once this concentration is

reached, this phase probably involving specifically adsorbed or co-adsorbed Cl^- anions. There is an evident negative shift in the peak representing the lifting of the reconstruction for the CV of CTAC at CMC, confirming the presence of a possible Cl^- adlayer on the Au (100) substrate at this concentration.

In Figure 5.8B, when the concentration of CTAC is between 1/128 and ¼ of its CMC (0.0011-0.035 mM), the differential capacitance does not increase by more than 5 µF cm^{-2} from the differential capacitance minima at ca. -500 mV. This also shows that no phase transition of the surfactant film occurs at low bulk concentrations of CTAC. Since the DC curves are a similar shape and at a similar differential capacitance value in this concentration range, the surfactant adsorption layer does not greatly vary. The differential capacitance does not stay flat for these concentrations in this potential range, indicating the multi-phase disordered state of the surfactant layer on the Au (100) surface. When the concentration of CTAC is at ½ of CMC and at its CMC, the differential capacitance increases between 0 and 500 mV, culminating in a DC maximum, thus confirming that specifically adsorbed Cl^- leads to a surfactant adlayer structure. This structure is likely to be a bilayer, such as the one proposed for CTAC molecules on Au (111) at higher concentrations and at positive potentials, where CTA^+ molecules absorb onto the formed Cl^- adlayer.

5.5 The Electrochemistry of CTAB on Au (100)

Figures 5.9A and 5.9B give CV and DC curves for an Au (100) surface in 0.1 M NaF solution after Addition 7 of CTAB (red line) (1/2 CMC of CTAB in 0.1 M NaF: 0.05 mM). CVs and DC curves for Au (100) 0.1 M NaF with NaBr after Addition 7 (orange line) (0.05 mM) and 0.1 M NaF (black dotted line) are also included.

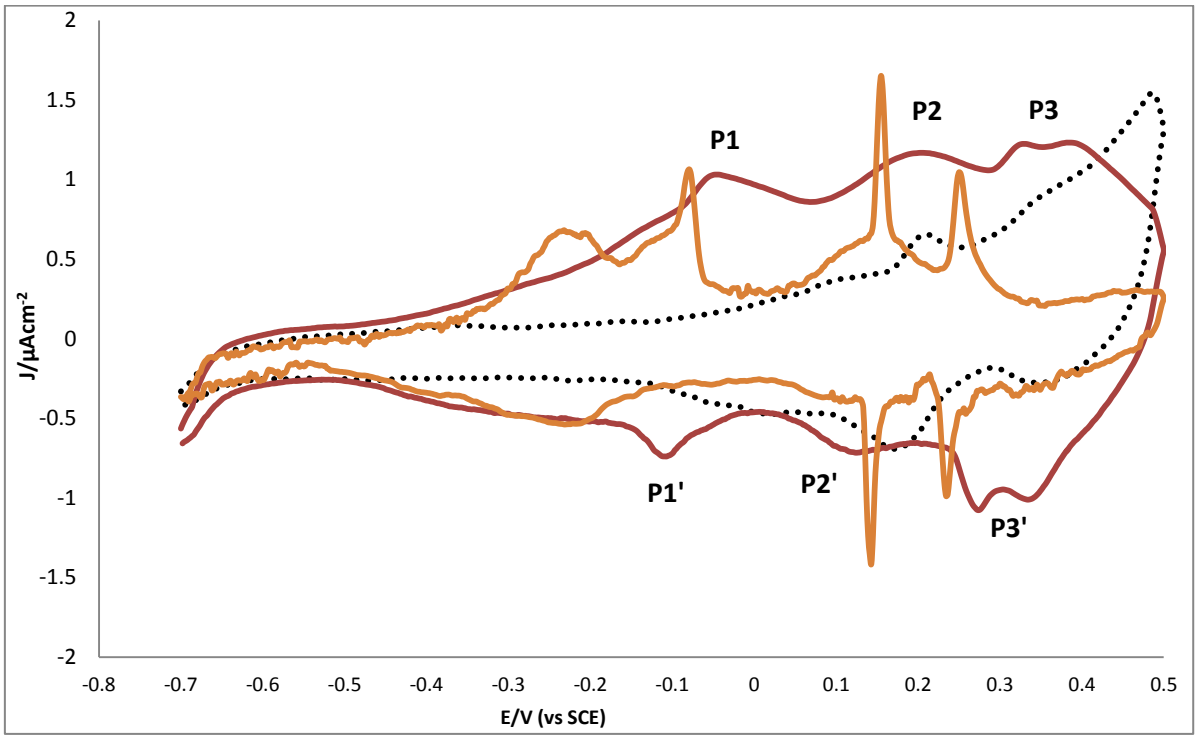

Figure 5.9A Cyclic voltammogram of Au (100) in 0.1 M NaF solution with CTAB after Addition 7 (1/2 CMC of CTAB in 0.1 M NaF: 0.05 mM) (red line). A CVs of Au (100) in 0.1 M NaF with 0.05 mM NaCl (orange line), and Au (100) in 0.1 M NaF solution (black dotted line) are also included.
Sweep rate 20 mVs^{-1}.

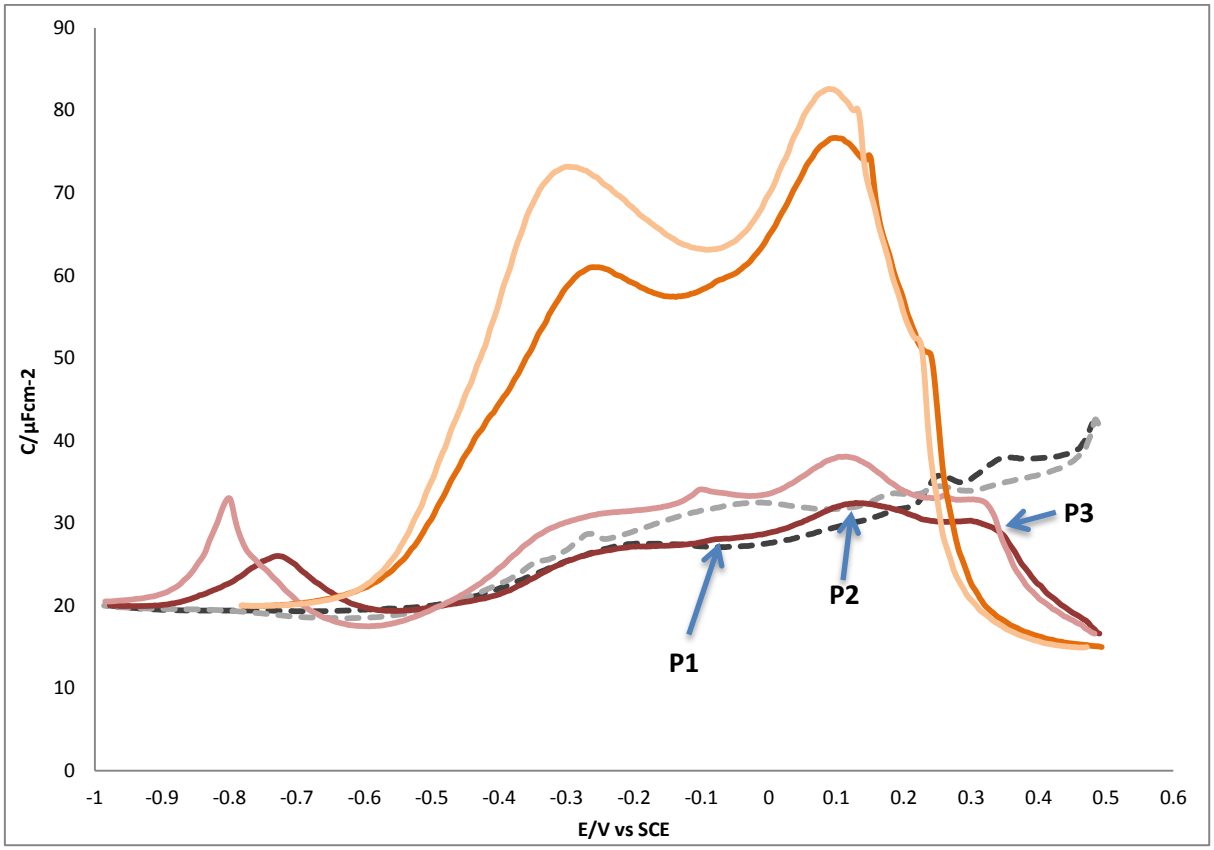

Figure 5.9B Differential capacitance curves of Au (111) in 0.1 M NaF solution with CTAB after Addition 7 (1/2 CMC of CTAB in 0.1 M NaF; 0.05 mM) (red line), of Au (111) in 0.1 M NaF with 0.05 mM NaCl (orange line), and Au (111) in 0.1 M NaF solution (black dotted line).In all three sets of DC curves, the dark shaded lines represent the anodic sweep, and the light shaded lines represent the cathodic sweeps.
Sweep rate 5 mVs^{-1}.

In Figure 5.9A and 5.9B, P1 is caused the by the lifting of the Au (100)-(hex) reconstruction. The current and DC maxima of P1 are at -60 mV. This is considerably more negative than corresponding peaks at equivalent concentrations of CTAC. This shows that more Br^- anion molecules are specifically adsorbed on the Au (100) surface than Cl^- anions, and the binding is stronger. P2 is a similar shape and at a similar potential to peaks observed in the CV and DC curves of Au (100) in lower concentrations of NaBr solution (around 0.01 mM); these peaks arise from the compression of the Br^- adlayer. Therefore P2 probably also represents the compression of the Br^- counter-ion adlayer structure. P3, which is particularly noticeable

in the CV, Figure 5.9A, is very likely to be caused by a specifically adsorbed Br^- induced phase change in the surfactant adlayer structure.

Figures 5.10A and 5.10B give CV and DC curves of Au (100) in 0.1 M NaF solution with CTAB after Additions 1-8 (1/128 CMC to the CMC of CTAB in 0.1 M NaF solution; 0.0008- 0.1 mM). The lines become progressively lighter shades of red as the concentration of CTAB in NaF solution increases. The baseline CV and DC curves of Au (100) in 0.1 M NaF solution are represented by a black dotted line.

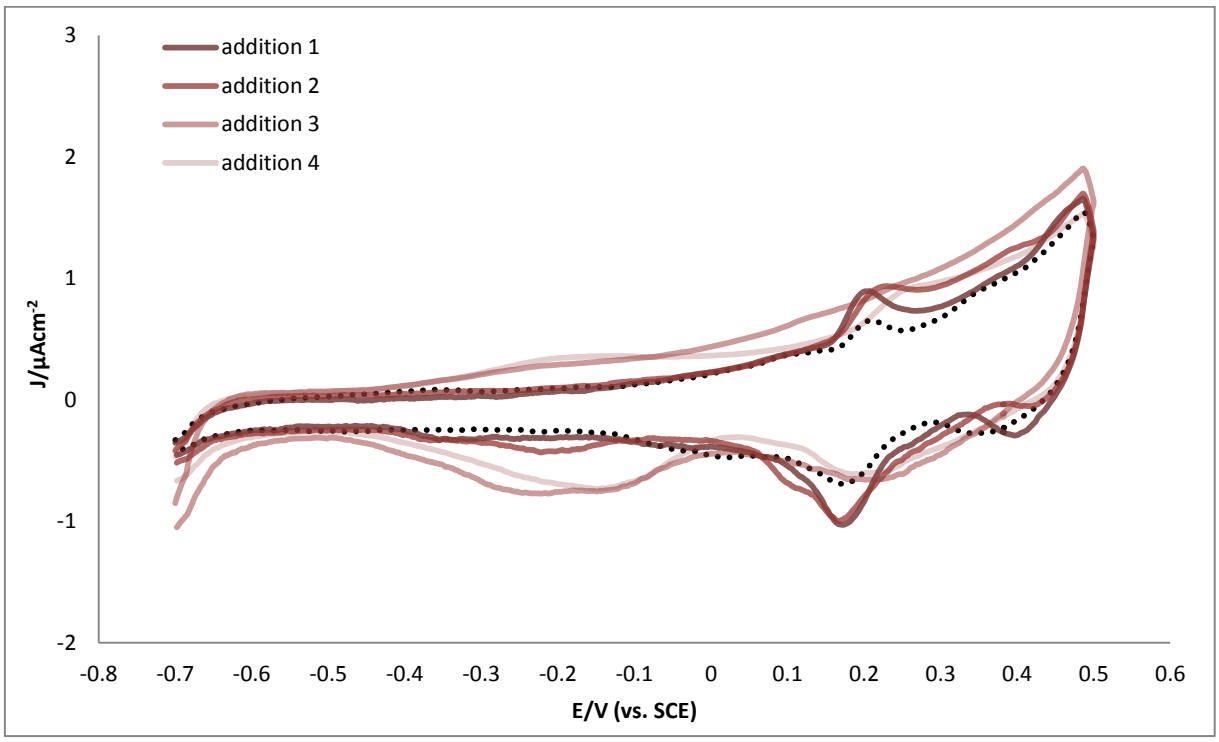

Figure 5.10A (i) Cyclic voltammetry curves recorded for Au (111) in 0.1 M NaF solution without CTAB (black dotted line) and with CTAC after Additions 1-4 (1/128 CMC to 1/16 CMC of CTAB in 0.1 M NaF solution; 0.0008- 0.062 mM) the CV curves become progressively lighter shades of red as the bulk concentration of CTAB increases.
Sweep rate 20 mV s^{-1}

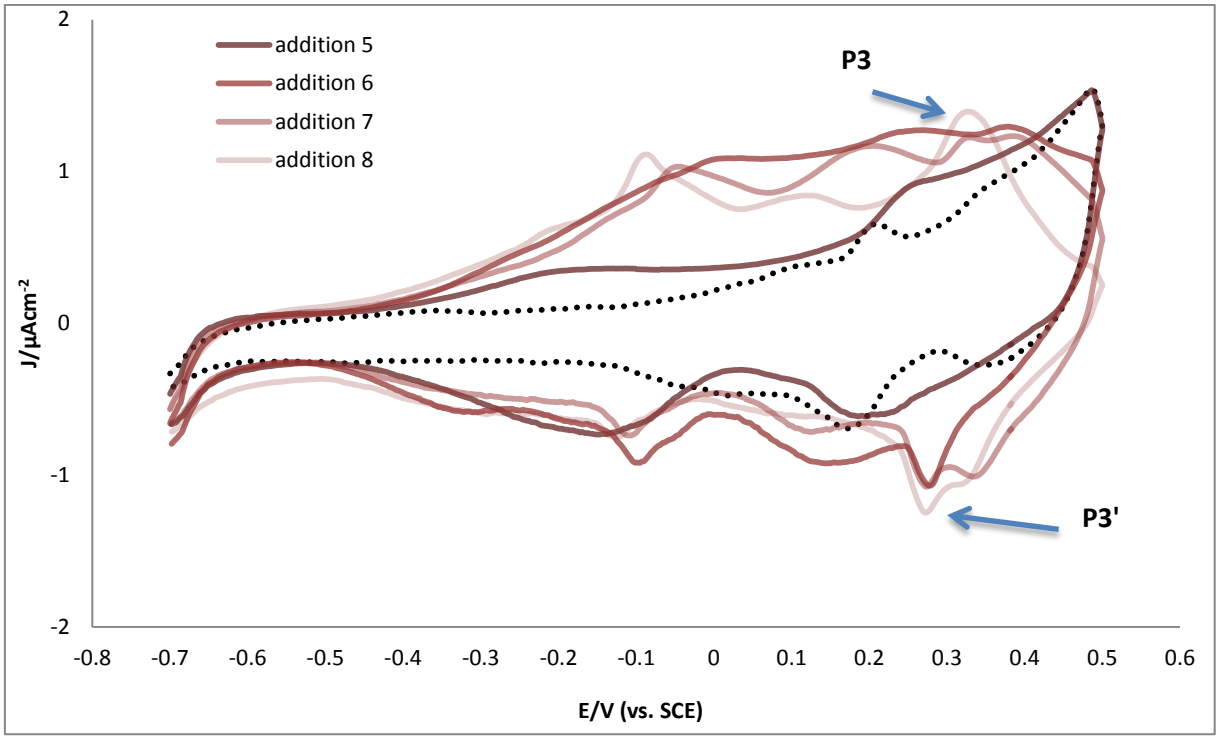

Figure 5.10A (ii) Cyclic voltammetry curves recorded for Au (111) in 0.1 M NaF solution without CTAB (black dotted line) and with CTAC after Additions 5-8 (1/8 CMC to the CMC of CTAB in 0.1 M NaF solution; 0.0125- 0.1 mM) the CV curves become progressively lighter shades of red as the bulk concentration of CTAB increases.
Sweep rate 20 mV s^{-1}

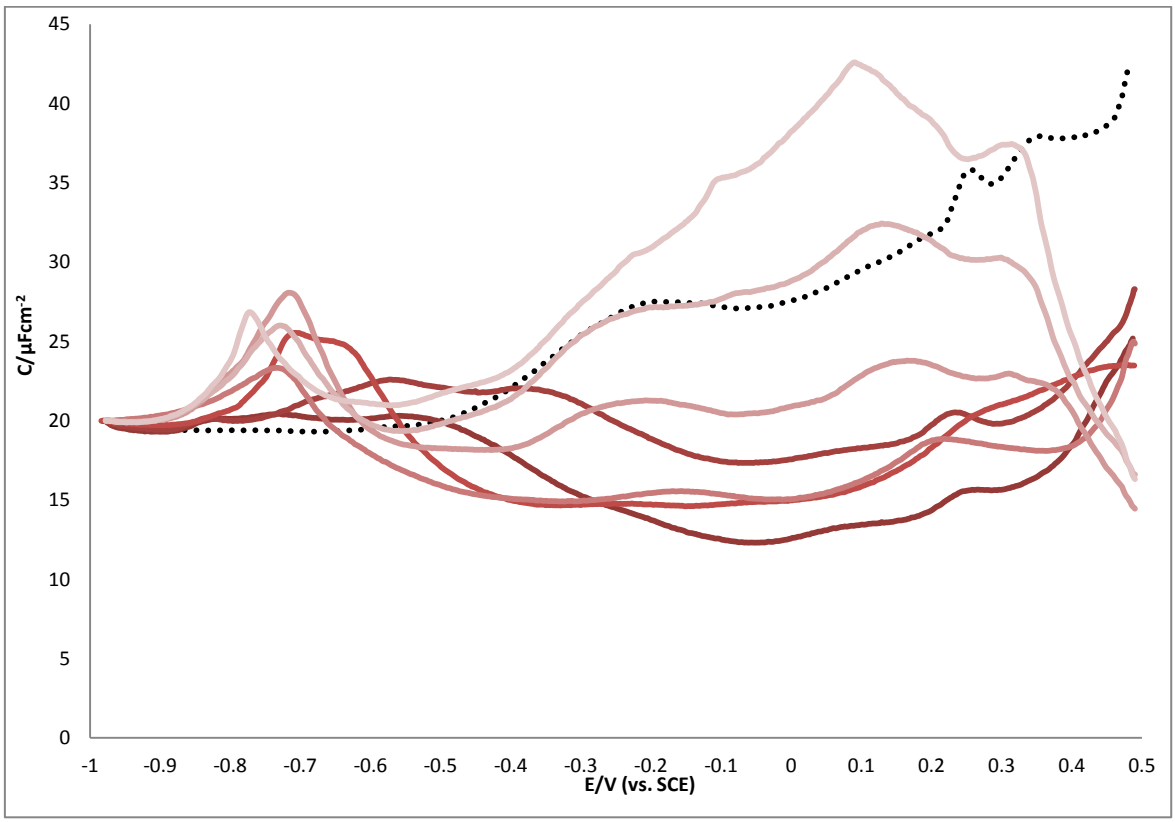

Figure 5.10B Differential capacity curves of the anodic sweep, recorded for Au (111) in 0.1 M NaF solution without CTAB (black dotted line) and with CTAB after Additions 1-8 (1/128 CMC to the CMC of CTAB in 0.1 M NaF solution; 0.0008- 0.1 mM). The CV curves become progressively lighter shades of red as the bulk concentration of CTAB increases.
Sweep rate 5 mV s^{-1}

In Figure 5.10A, P3 can only be observed when the concentration of CTAB is between ¼ of its CMC and its CMC. This confirms that the phase change is Br^- adlayer-induced. The phase change that results in this peak is most likely to be a densely packed bilayer structure with the CTA^+ molecules adsorbing on top of the Br^- adlayer. At low concentrations of CTAB (≤ 1/8 CMC of CTAB), the CVs in Figure 5.10B are a similar shape to the CVs of Au (100) in CTAF solution, thus showing that the influence of the Br^- ions to the surfactant adlayer is negligible. This is because little Br^- is adsorbed on the surface at these concentrations, not

enough is adsorbed to change the surfactant layer structure. This pattern can also be observed in the DC curves in Figure 5.10B. When the bulk CTAB concentrations are $\leq$ 1/8 of the CMC, the DC curves have a shape similar to that of the DC curves of CTAF and CTAC. However, when the concentration of CTAB is between ¼ of its CMC and its CMC, the DC curves have a shape that is more similar to the DC curves of Au (100) in NaBr solution between -400 and 500 mV. This shows that the Br^- adlayer on the Au (100) surface at these bulk concentrations of CTAB determines the structure of the surfactant layer.

For the higher concentrations of CTAB, (1/4 of CMC to CMC) the negative shift of the lifting of the reconstruction peaks in Figure 5.10A and the increasing capacitance of the DC curves in Figure 10B as the bulk concentration increases shows the increasing Br^- on the Au (100) substrate.

5.6 Chronocoulometry analysis of CTAF, CTAC and CTAB on Au (100)-(hex)

Chronocoulometry procedures requires the electrode potential to be stepped from a potential at which molecules are adsorbed; for long enough to reach adsorption equilibrium, E_{ADS}, to a potential at which the molecules are completely desorbed, E_{DES}. The integration of the resulting current transient gives a change in electrode charge density between both potentials.[18 19 20] However, transitions occurring between the reconstructed (hex) phase and the unreconstructed (1×1) phase on the Au (100) surface during this potential step contribute to this measured charge, rendering the chronocoulometry data invalid. In chronocoulometry measurements of surfactant adsorption on the Au (100) surface, the adsorption potential is limited to $E_{ADS} \leq 0$ mV in order to ensure that a transition between reconstructed and unreconstructed states does not occur. Thus all the chronocoulometry and the resulting the Gibbs excess plots in this section, measure the adsorption of surfactants on the reconstructed (hex) surface. As is evident in the previous section, an unreconstructed surface is only stable at potentials positive of 0 V. A modified potential step routine has previously been employed to minimise reconstruction of the Au (100) surface.[21] These experiments involve the use of an intermediate potential of -200 mV (vs. SCE) and the enhancement of mass transport by stirring the solution during measurements, thus allowing shorter times for adsorption equilibrium at negative potentials. It is questionable, however, whether or not this technique completely eliminates potential-induced reconstruction because desorption potentials cannot be avoided. The negative potential value at which the surfactant completely desorbs off the Au surface, -1000 mV, according to Schneider and Kolb, is the optimal potential for potential-induced reconstruction.[2] If, therefore,

chronocoulometry measurements were to be made for surfactant adsorption on unreconstructed Au (100), it would be difficult to tell whether an increase in current is caused by adsorption of molecules or by surface reconstruction / lifting of reconstruction. Chronocoulometry measurements of Au (100) in NaCl and NaBr solutions were not made because, according to the CV and DC curves in section 5.2, the Au (100) reconstruction lifts at potentials more negative of 0 mV when the electrode is in these solutions.

The charge density curves of Au (100) 0.1 M NaF supporting the electrolyte in concentrations of 1/128 of the CMC to ½ of the CMC of **A.** CTAF (green lines), **B.** CTAC (purple lines) and **C.** CTAB (red lines) are given in Figure 5.11. The lines acquire progressively lighter shades of the surfactant increases.

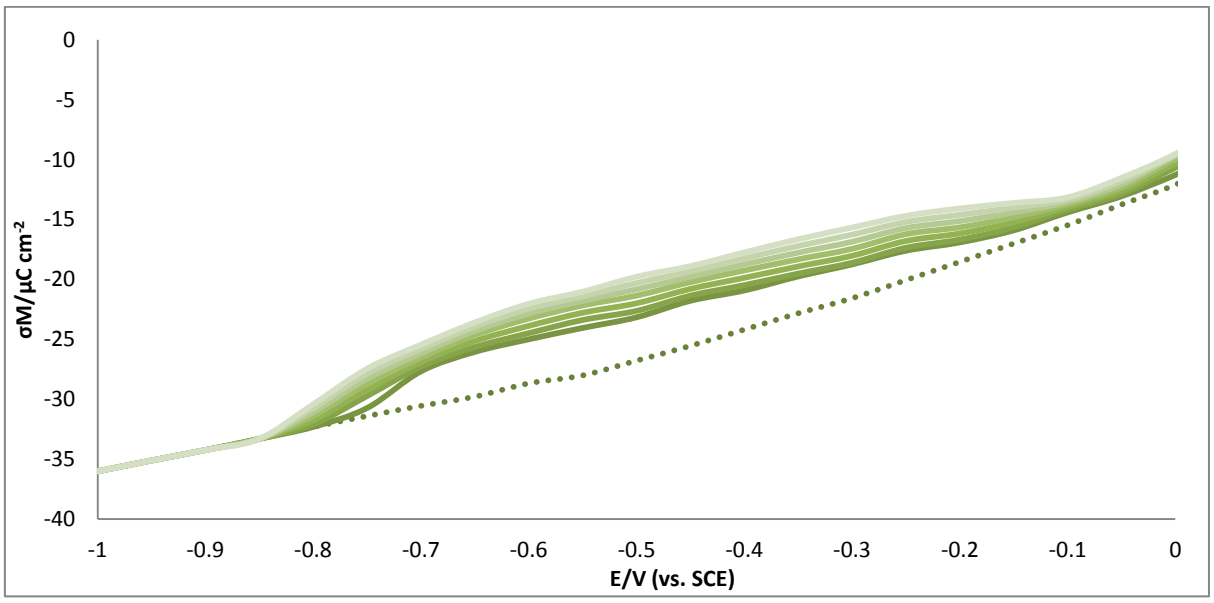

Figure 5.11A Charge density versus electrode potential curves for Au (100) in pure 0.1 M NaF solution (black dotted line), and with selected CTAF concentrations starting from Addition 1/128 of the CMC of CTAF of CTAF (darkest green line) to ½ CMC of CTAF (lightest green line).

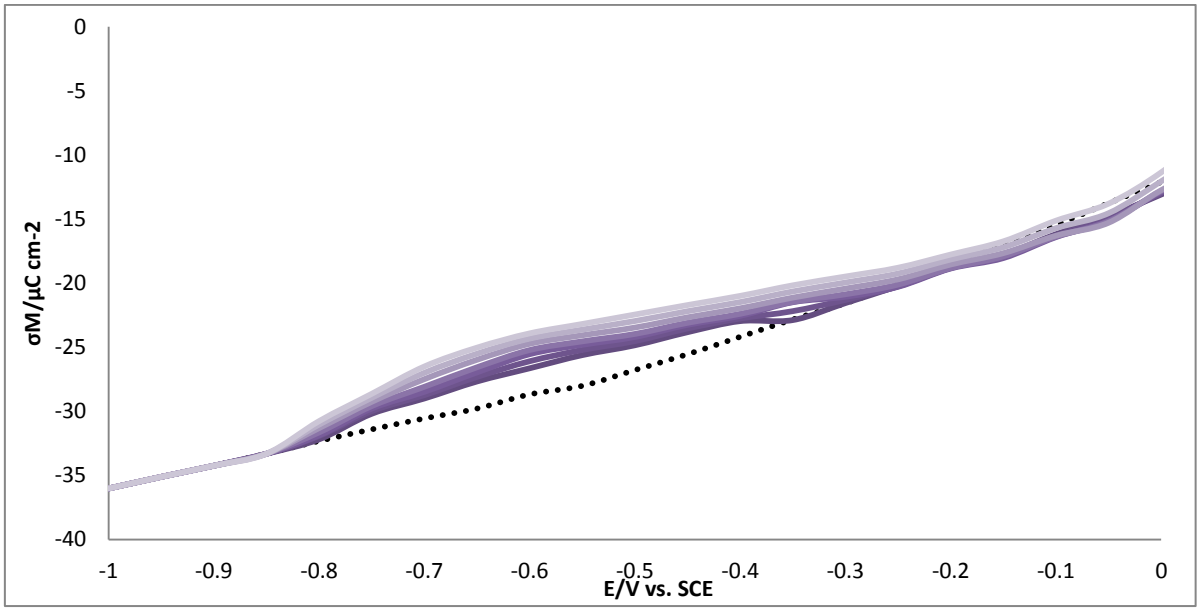

Figure 5.11A Charge density versus electrode potential curves for Au (100) in pure 0.1 M NaF solution (black dotted line), and with selected CTAF concentrations starting from Addition 1/128 of the CMC of CTAF of CTAF (darkest green line) to ½ CMC of CTAF (lightest green line).

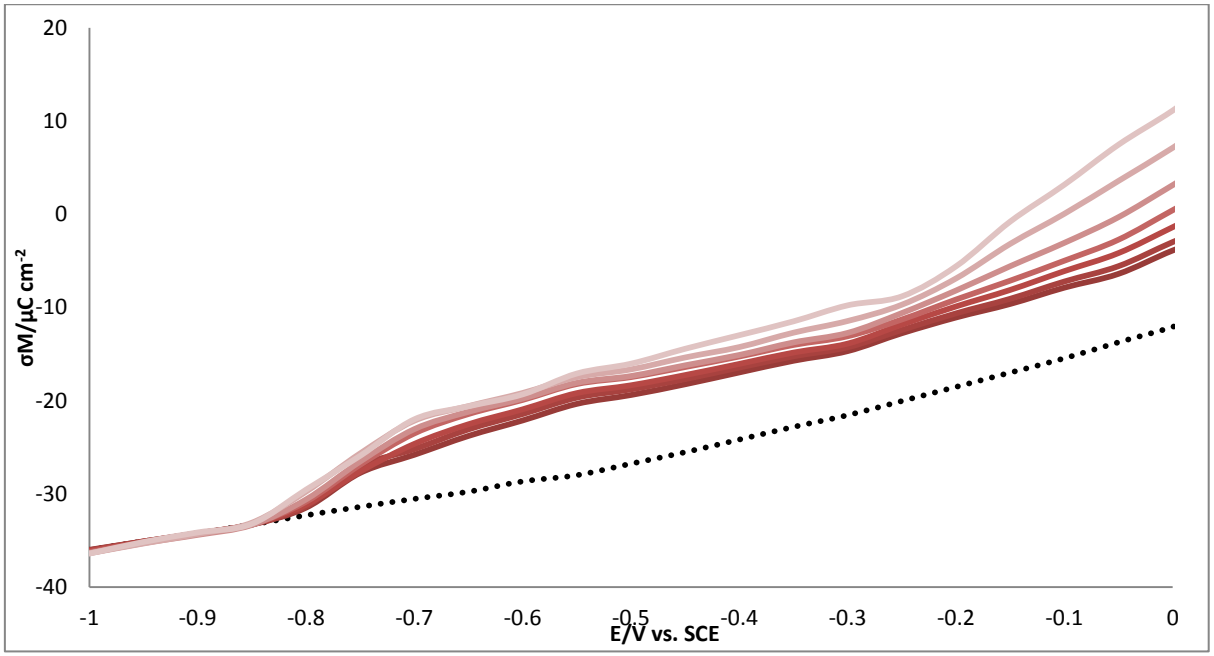

Figure 5.11A Charge density versus electrode potential curves for Au (111) in pure 0.1 M NaF solution (black dotted line), and with selected CTAF concentrations starting from Addition 1/128 of the CMC of CTAF of CTAF (darkest green line) to ½ CMC of CTAF (lightest green line).

In Figures 5.11A, 5.11B, and 5.11C, there is a sigmoidal inflection at -850 mV to -900 mV, indicating surfactant adsorption. In Figure 5.11B, the charge curves of CTAC merge with the baseline electrolyte charge curve from E > -300 mV. Interestingly, for the charge curves of CTAF in Figure 5.11A, this pattern is not observed, with the slopes of the curves decreasing and having values similar to that of the baseline at E > -150 mV, but not merging with it. The CTAC charge curves merging with the baseline at E> -300 mV therefore is caused by the Cl^- counter counter-ions. Cl^- counter ions being present in the interface region could attract the cationic head groups of the surfactant molecules as the potential becomes more positive, thus causing the head groups to desorb from the surface, resulting in the Au (100) electrode having a neutral charge. Alternatively, the co-adsorption of Cl could counter-balance the positive charge of the cationic surfactants on the substrate surface. The CTAC charge curves merging with the baseline electrolyte could also be a combination of both these factors.

In Figure 5.11C, showing the charge curves vs. potential curves of CTAB, the charge plateaus between -650 mV and -250 mV, indicating a surfactant adlayer structure. This plateau continues from -250 mV to 0 mV for CTAB concentrations between 1/128.CMC and 1/16 CMC. For CTAB concentrations between 1/8 and ½ of the CMC, the charge linearly increases from -250 mV to 0 mV, as a result of specific bromide adsorption or co-adsorption.

Figure 5.12 gives the Gibbs excess curves as a function of the electrode potential for **A.** CTAF, **B.** CTAC, and **C.** CTAB; the same concentrations are used as for the charge density plots in Figure 5.11

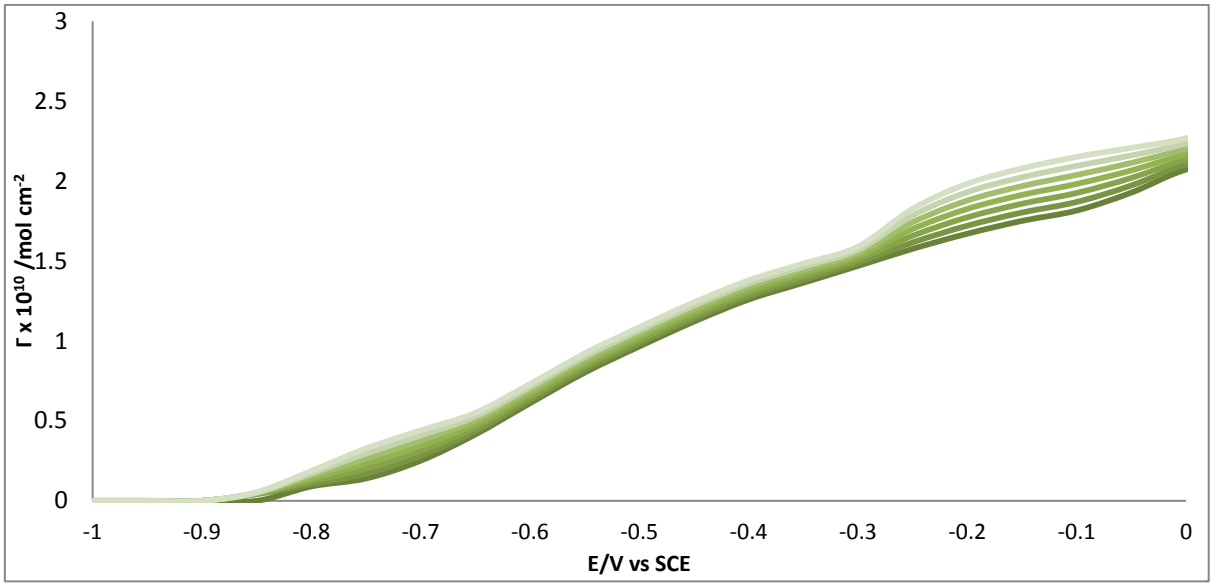

Figure 5.12A Plot of the Gibbs excess of CTAF versus the electrode potential for bulk concentrations of CTAF with concentrations between 1/128 and ½ of its CMC in 0.1 M NaF solution. The lines acquire progressively lighter shades of green as the bulk concentration of CTAF increases. Calculated from CTAF charge curves in Figure 5.11A

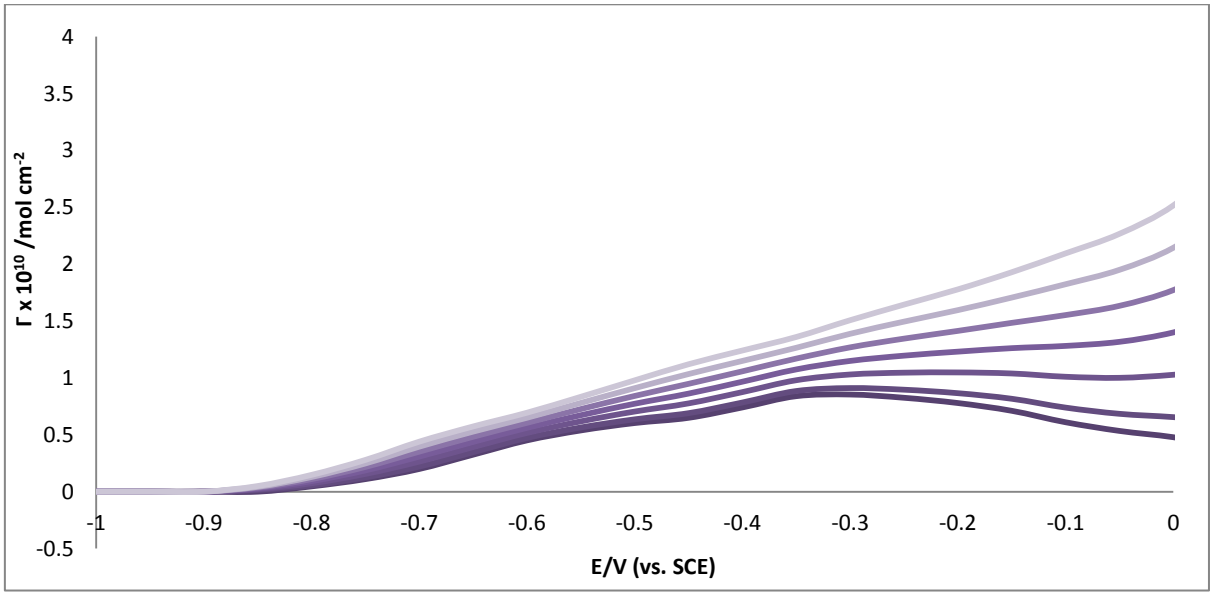

Figure 5.12B Plot of the Gibbs excess of CTAC versus the electrode potential for bulk concentrations of CTAF with concentrations between 1/128 and ½ of its CMC in 0.1 M NaF solution. The lines acquire progressively lighter shades of purple as the bulk concentration of CTAC increases. Calculated from CTAC charge curves in Figure 5.11B.

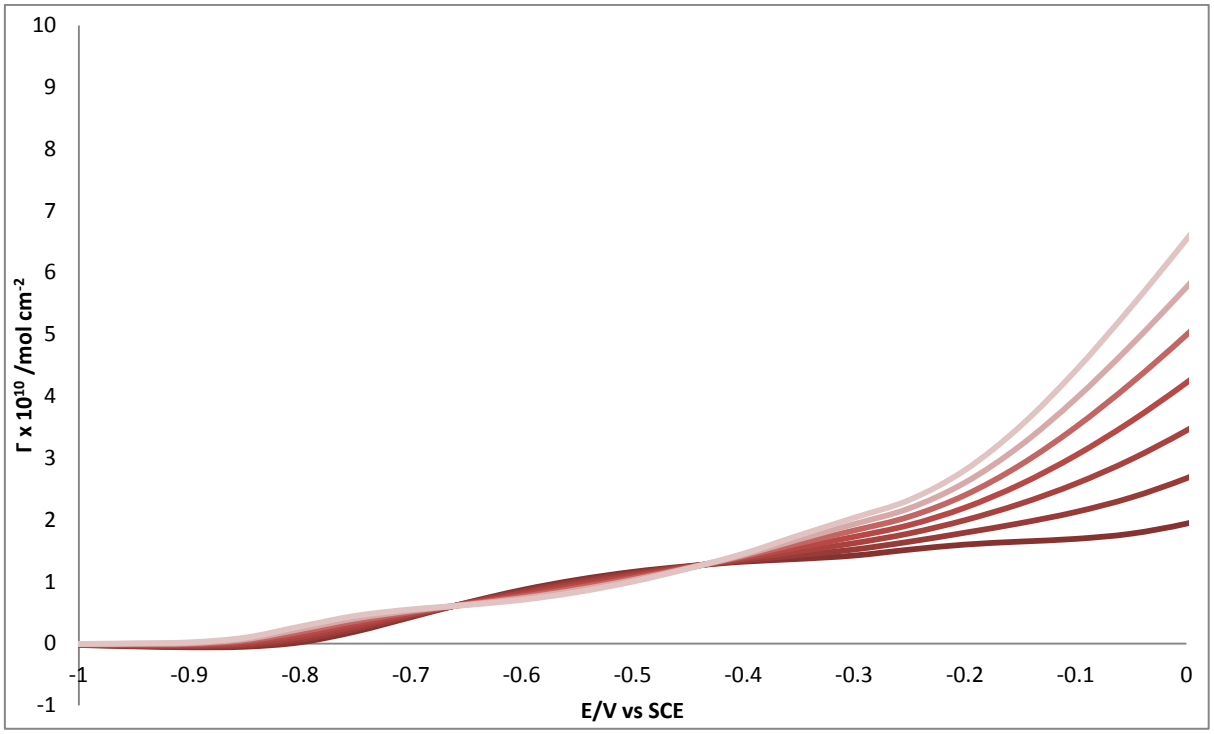

Figure 5.12C Plot of the Gibbs excess of CTAB versus the electrode potential for bulk concentrations of CTAF with concentrations between 1/128 and ½ of its CMC in 0.1 M NaF solution. The lines acquire progressively lighter shades of red as the bulk concentration of CTAB increases. Calculated from CTAB charge curves in Figure 5.11C.

The Gibbs excess vs. potential curves for each surfactant in Figure 5.12 are a very similar shape to the charge curves of the same surfactants on Au (111) when the potential is less than 0 mV (see Figures 4.12, 4.16A and 4.20A). This is because the similarity between the atomic arrangements of Au (111) and Au (100)–(hex), would mean there is a similar coverage of surfactants on both surfaces.

A comparison of Gibbs excess plots of Au (100)-(hex) and Au (111) in NaF solution containing concentrations equivalent to, 1/32 and 1/64 of the CMC of **A.** CTAF, **B.** CTAC and **C.** CTAB are given in Figure 5.13. The Gibbs excess is plotted as a function of the rational potential scale ($E - E_{pzc}$). The Gibbs excess plots of the Au (100)-(hex), and Au (111) surface are represented by solid lines and dashed lines, respectively.

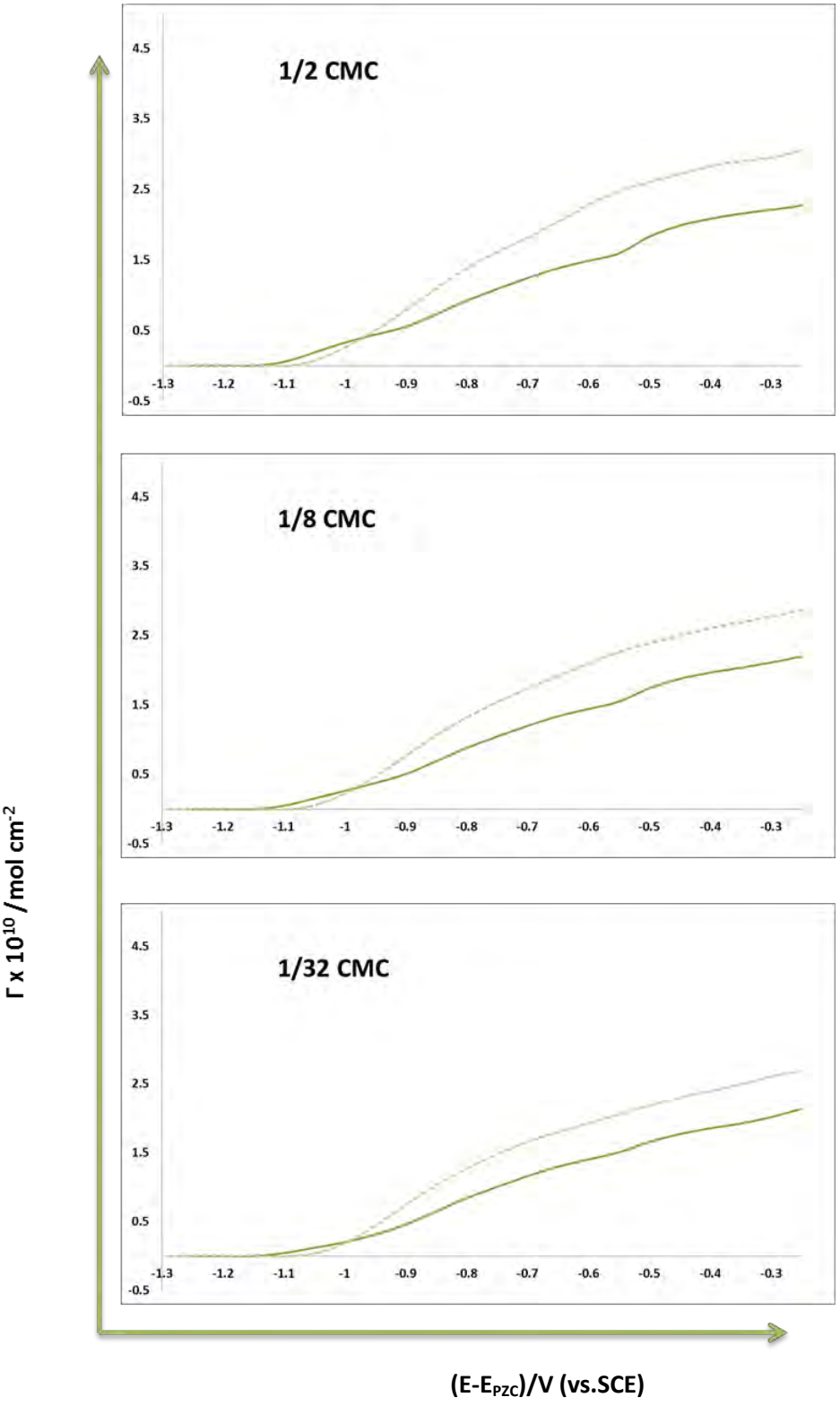

Figure 5.13A Gibbs excess plots of Au (100)-(hex) (green solid lines), and Au (111) (green dashed lines) in CTAF solution when the concentration is 1/32, 1/8 and ½ of its CMC

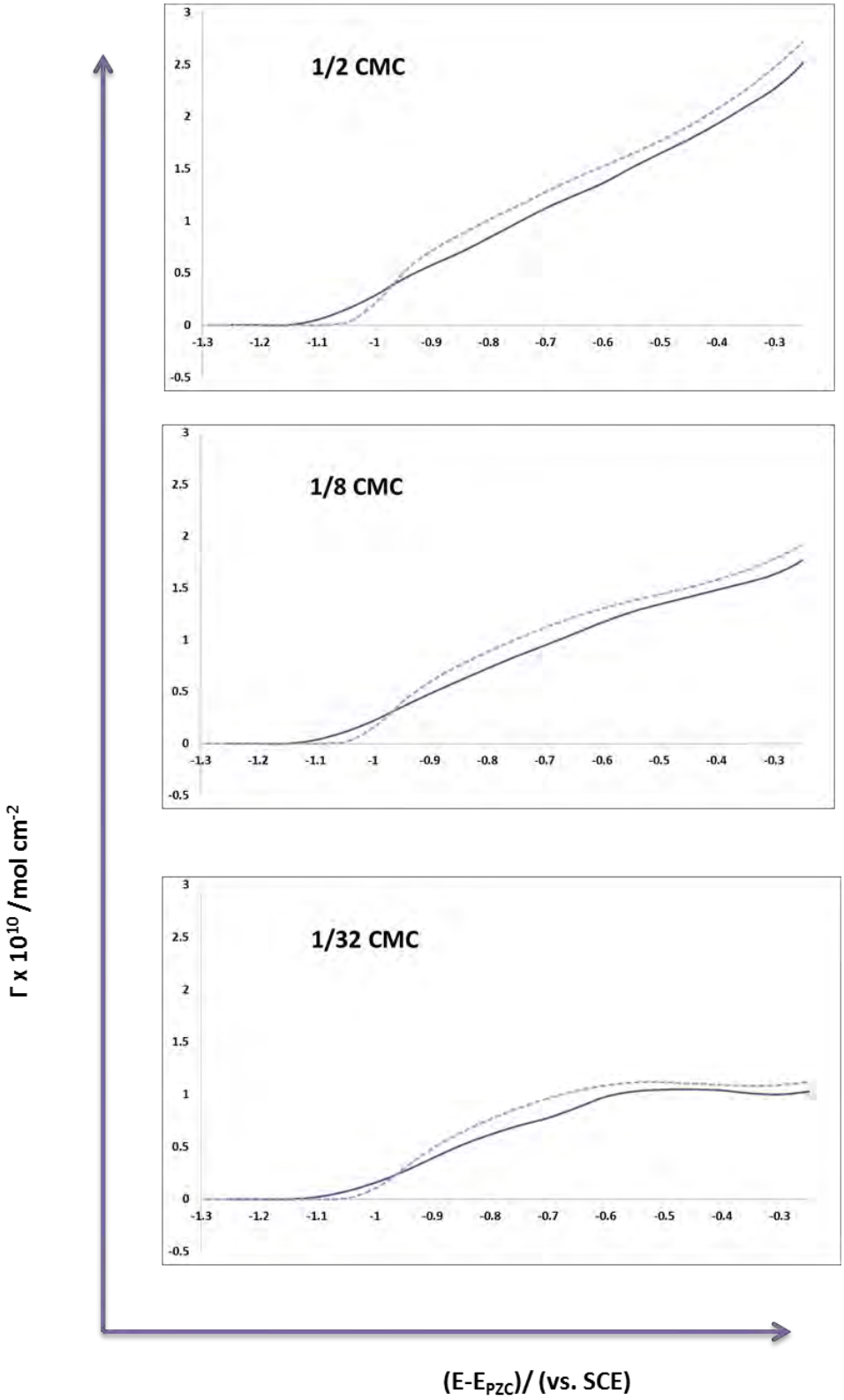

Figure 5.13B Gibbs excess plots of Au (100)-(hex) (purple solid lines), and Au (111) (purple dashed lines) in CTAC solution when the concentration is 1/32, 1/8 and ½ of its CMC.

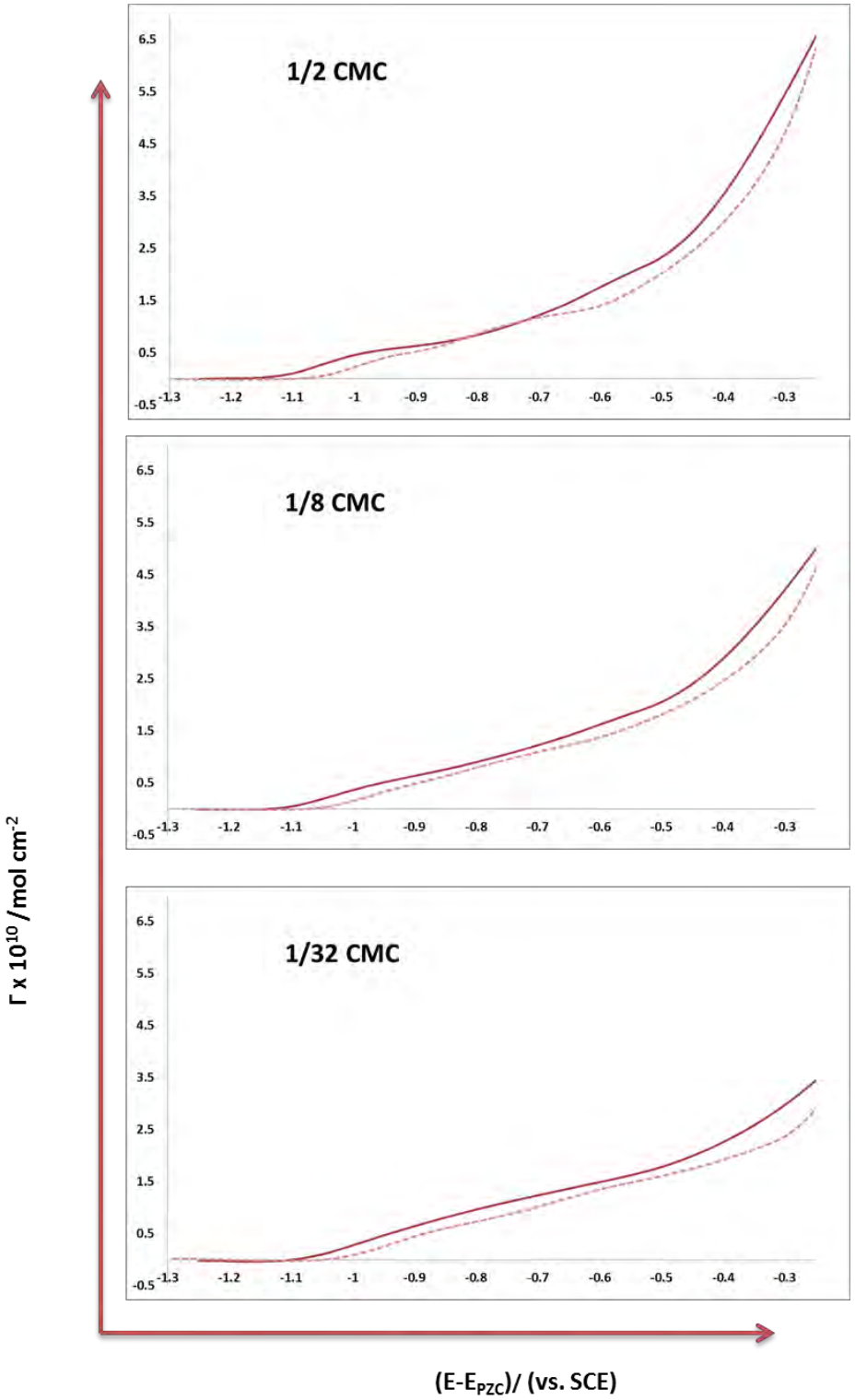

Figure 5.13C Gibbs excess plots of Au (100)-(hex) (red solid lines), and Au (111) (red dashed lines) in CTAB solution when the concentration is 1/32, 1/8 and ½ of its CMC.

In Figures 5.13A, B and C, the initial onset of the increase of the Gibbs excess is at a slightly more negative potential for the Au (100)-(hex) surface than the Au (111) surface. This indicates that the adsorption is slightly more energetically favourable on Au (100)-(hex). A likely reason for this is that the buckled corrugated nature of Au (100)-(hex) means that surfactant molecules will have more contact with its surface atoms.

In Figure 5.13A, there is a higher coverage of CTAF molecules on the Au (111) surface at more positive potentials. This could be due to the arrangement of the surface atoms on this surface; the Au (100)-(hex) have a less flat surface. Van der Waals interactions of the alkyl tail group with the surface are therefore more problematic. Another reason could be that the more ordered surfactant layer on Au (111), as a result of the crystallographic structure of this surface, could allow for a higher density of surfactant molecules.

In Figure 5.13B, the coverage of CTAC molecules is also higher on the Au (111) surface is than on the Au (100)-(hex) surface; however the Gibbs excess values are closer together. This would be due to the stabilising effects of the Cl^- counter-ion on the surfactant molecules on the Au (100)-(hex) surface at the interface, meaning there can be a similarly densely packed surfactant layer even though there are fewer van der Waals interactions between the alkyl tail groups and the substrate.

In Figure 5.13C, the coverage of CTAB molecules is higher on the (100) surface for all the concentrations and over the entire potential range. This is probably because the Br^- provides such enhanced stability to the surfactant molecules' cationic head groups that more molecules will bond on the slightly energetically more favourable Au (100)-(hex) adsorption sites (the buckled nature of the Au (100)-(hex) surface means that adsorbed molecules are in

more contact with the surface atoms), regardless of there being few van der Waals interactions between the alkyl tail groups of the surfactants with this substrate surface on this surface.

5.7 The Electrochemistry of Au (100) in BDAC solution

Figures 5.14A and 5.14B give a CV and a DC curve of Au (100) in 0.1 M NaF solution after Addition 7 (1/2 CMC of BDAC in 0.1 M NaCl solution: 0.013 mM) of BDAC (black solid line). CVs and DC curves Au (111) in 0.1 M NaF (black dotted line), NaF after Addition 7 (1/2 CMC of CTAC in 0.1 M NaF solution; 0.07 mM) of CTAC (purple line) and after 0.013 mM of NaCl (blue line) are also included for reference.

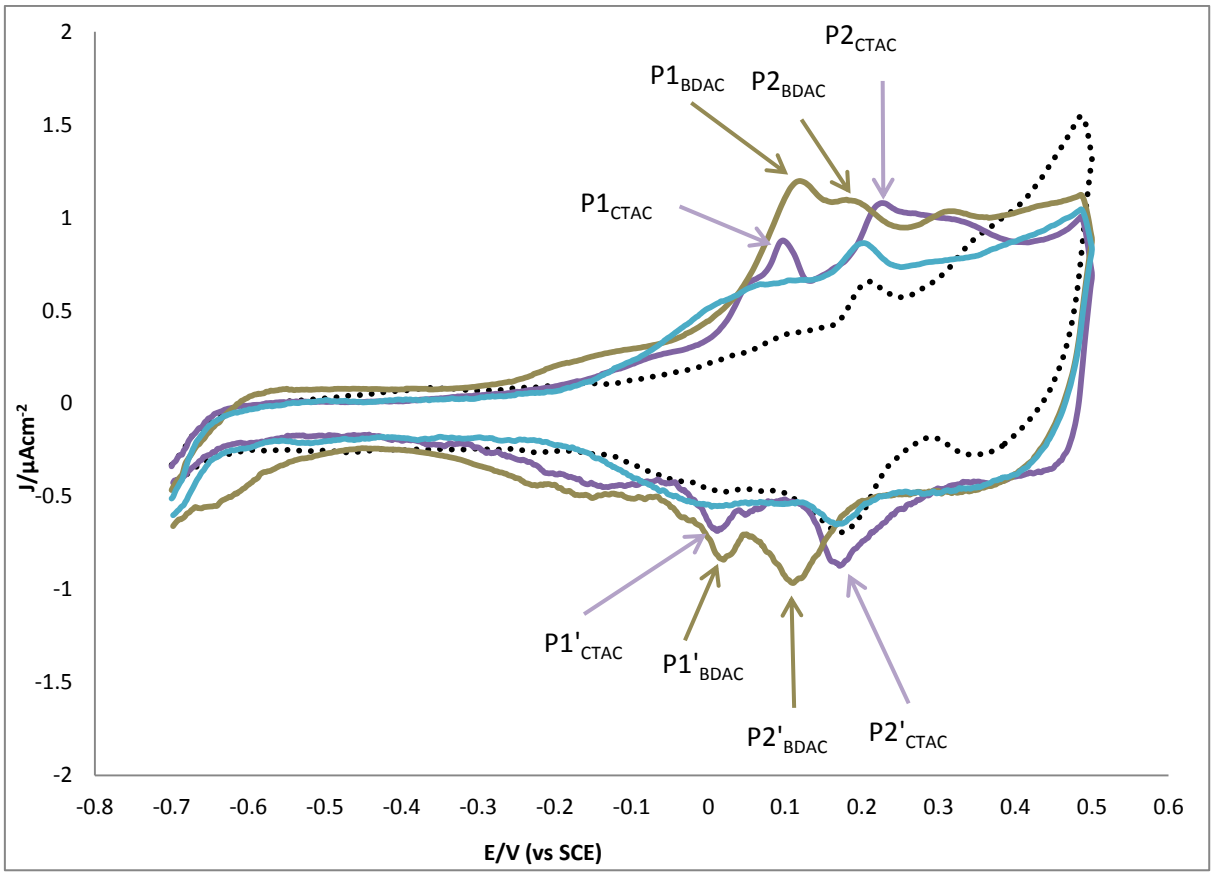

Figure 5.14A Cyclic voltammogram of Au (100) in 0.1 M NaF solution after Addition 7 (1/2 CMC of BDAC in 0.1 M NaCl solution; 0.013 mM) of BDAC (black solid line). DC curves Au (111) in 0.1 M NaF (black dotted line), and NaF after Addition 7 (1/2 CMC of CTAC in 0.1 M NaF solution: 0.07 mM) of CTAC (purple line), and after 0.013 mM of NaCl (blue line) are also included for reference. In all four sets of DC curves, the dark shaded lines represent the anodic sweep, and the light shaded lines represent the cathodic sweeps.

Sweep rate 20 mV s^{-1}.

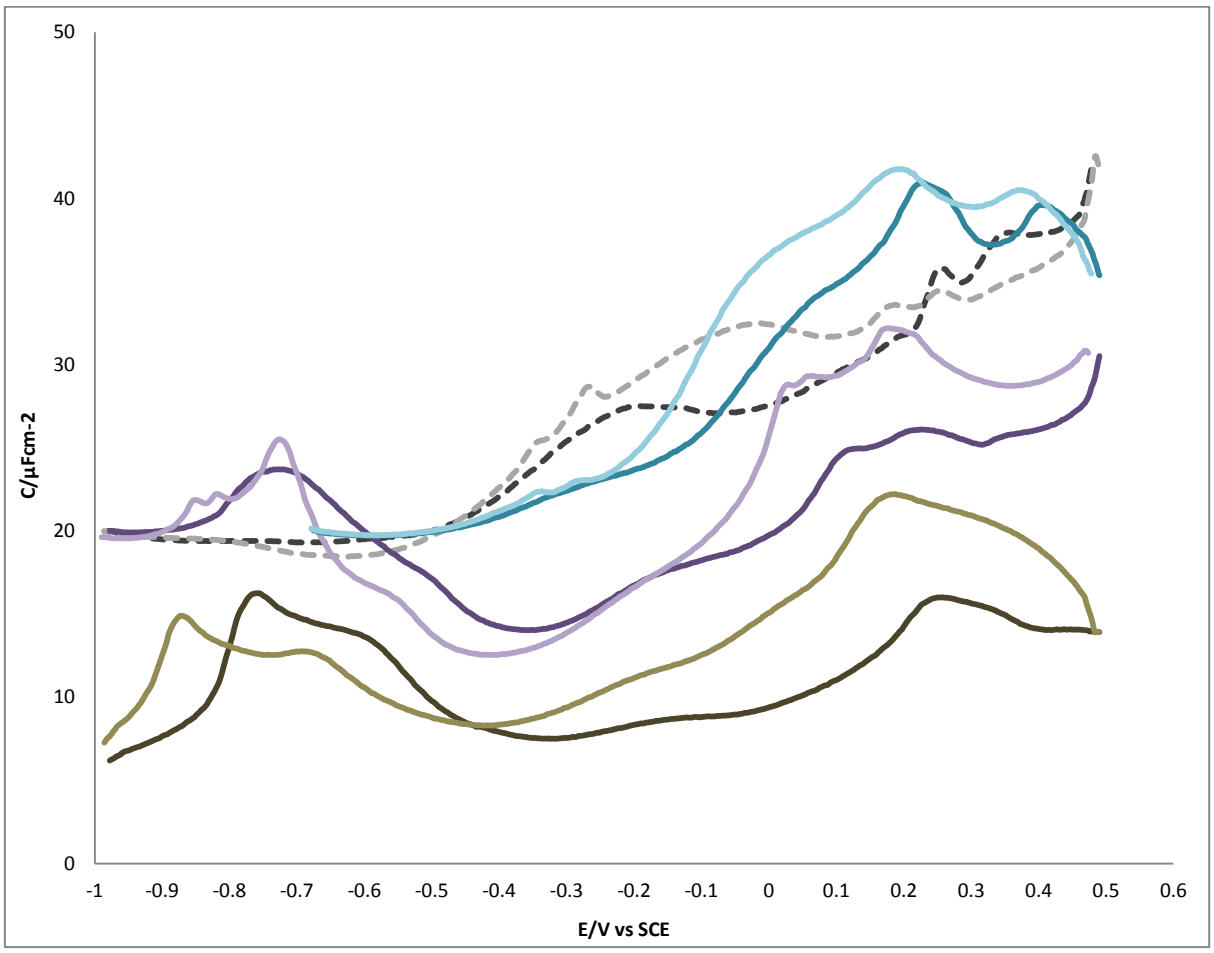

Figure 5.14B Differential capacitance curves of Au (100) in 0.1 M NaF solution after Addition 7 (1/2 CMC of BDAC in 0.1 M NaCl solution: 0.013 mM) of BDAC (dark brown line). DC curves Au (100) in 0.1 M NaF (black dotted line), and NaF after Addition 7 (1/2 CMC of CTAC in 0.1 M NaF solution: 0.07 mM) of CTAC (purple line), and after 0.013 mM of NaCl (blue line) are also included for reference. The anodic sweeps are the darker shaded lines, and the cathodic sweeps are the lighter shaded lines.

Sweep rate 5 mV s^{-1}.

In Figure 5.14A, the current maxima on the CV of BDAC are labelled $P1_{BDAC}$ and $P2_{BDAC}$, with corresponding peaks in the negative-going sweeps labelled $P1'_{BDAC}$ and $P2'_{BDAC}$. The equivalent peaks of CTAC ($P1_{CTAC}$ and $P2_{CTAC}$), labelled as in Figure 7, are also included for reference. As with CTAC, $P1_{BDAC}$ probably corresponds to a phase change of the surfactant layer, and P2 is caused by the lifting of the Au (100)-(hex) reconstruction.

$P1_{BDAC}$ is at a more positive potential than $P1_{CTAC}$. While $P1_{CTAC}$ and $P1'_{CTAC}$ are the same shape and are at similar potentials, $P1_{BDAC}$ and $P1'_{BDAC}$ are completely different shapes, and $P1'_{BDAC}$ is at a more negative potential than $P1_{BDAC}$. This shows the slight irreversibility of such a phase change process of BDAC compared with CTAC. The current maximum representing the lifting of the Au (100)-(hex) reconstruction, $P2_{BDAC}$, is at a more negative potential than $P2_{CTAC}$; it is also at around the same potential as the corresponding peak when Au (100) is in NaCl solution. Previous literature describes how organic molecules destabilise the Au (100)-(hex) reconstruction and cause this reconstruction to lift at more negative potentials. For example, pyridazine, phthalazine,[14] pyridine[20] and adenine[21] specifically adsorb on the Au (100)-(hex) surface and thus increase the mobility of the surface atoms. It is therefore likely that the specific adsorption of the benzene ring in the BDAC head group slightly destabilises the Au (100)-(hex) structure and causes an increase in the mobility of the Au surface atoms. In the CV of BDAC, Figure 5.14A, the lifting of the Au (100)-(hex) reconstruction brings about the broad shoulder in the current between -200 mV and 0 mV. Indeed, the potential (vs. SCE) at which the Au (100)-(hex) reconstruction lifts when phthalazine and pyridine are in the solution occurs in this potential region.[14]

In Figure 5.14B, at -1000 mV, the differential capacitance is less than 10 μF cm^{-2} for both the positive- and negative-going sweeps of the BDAC DC curves. This is also observed for Au (111) in BDAC solution; it indicates that by the adsorbed head group of the BDAC head group does not desorb from the Au surface at this potential. In the positive-going sweep, there is a peak at -780 mV followed by a shoulder at -630 mV. The shoulder at -630 mV is at a similar potential on the rational scale ($E-E_{pzc}$) as that of the peak observed for the differential capacitance curve of Au (111) in BDAC solution (at the same concentration of 0.013 mV) (see

Figure 4.22B), which indicates a phase transition of the surfactant film. The peak at -780 mV in Figure 5.14A probably represents a more stable phase. This phase is surface specific, and could be as a result of the benzyl groups having a strong interaction with the four fold hollow sites on the Au (100) substrate.

In the anodic sweep of Figure 5.14B, in the potential region of -400 mV to 100 mV, the differential capacitance of the BDAC DC curve changes less with potential and is flatter than the DC curve of CTAC in the same potential region. The surfactant layer of BDAC is thus more stable in the positive-going sweep than surfactant layer of CTAC. The shape of the DC curve is different in this potential region for the negative-going sweep. This further shows the difference in phases of the surfactant adlayer in the anodic and cathodic scans.

Figures 5.15A and 5.15B give CV and DC curves of Au (111) in 0.1 M NaF solution with BDAC after Addition 3-8 (1/32 of the CMC to the CMC of BDAC in 0.1 M NaF solution; 0.0008-0.013 mM). The lines acquire progressively lighter shades of grey as the concentration of BDAC in NaF solution increases. The baseline CV and DC curves of Au (111) in 0.1 M NaF solution are represented by a black dotted line.

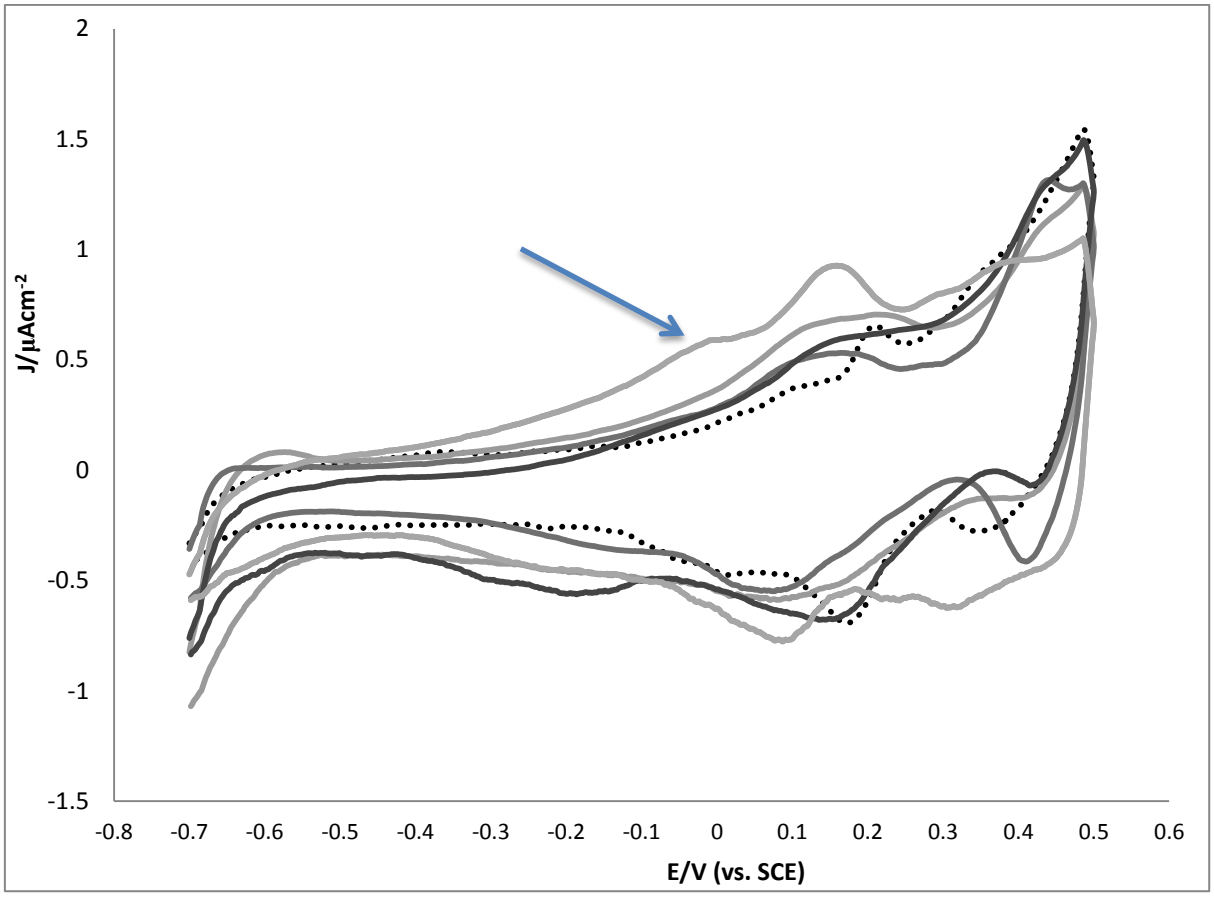

Figure 5.15A (i) . Cyclic voltammetry curves recorded for Au (111) in 0.1 M NaF solution without BDAC (black dotted line) and with BDAC (grey lines) after Additions 2-5 (1/64 of the CMC to 1/8 CMC of BDAC in 0.1 M NaF solution: 0.00004-0.00031 mM), the CV curves acquire progressively lighter shades of grey as the bulk concentration of BDAC increases.

Sweep rate 20 mV s^{-1}

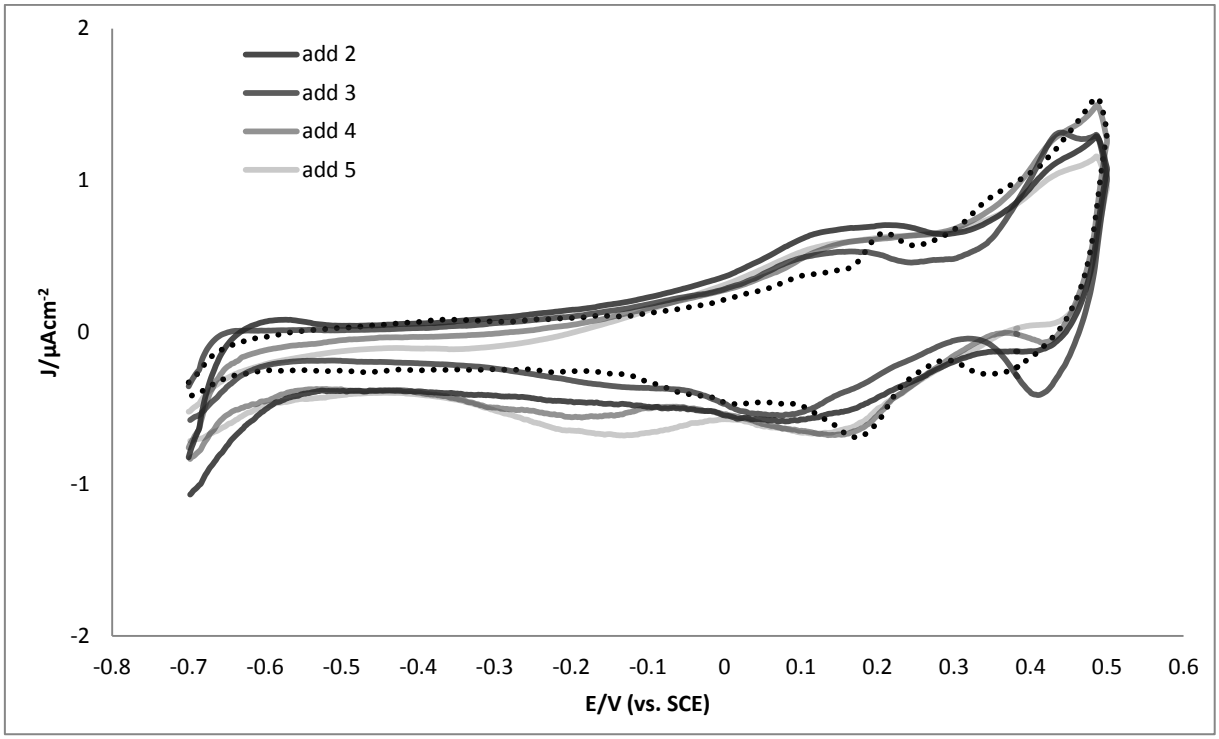

Figure 5.15A (ii). Cyclic voltammetry curves recorded for Au (111) in 0.1 M NaF solution withoutBDAC (black dotted line) and with BDAC (grey lines) after Additions 6-8 (1/4 of the CMC to the CMC of BDAC in 0.1 M NaF solution: 0.00062-0.00255 mM), the CV curves acquire progressively lighter shades of grey as the bulk concentration of BDAC increases.

Sweep rate 20 mV s^{-1}

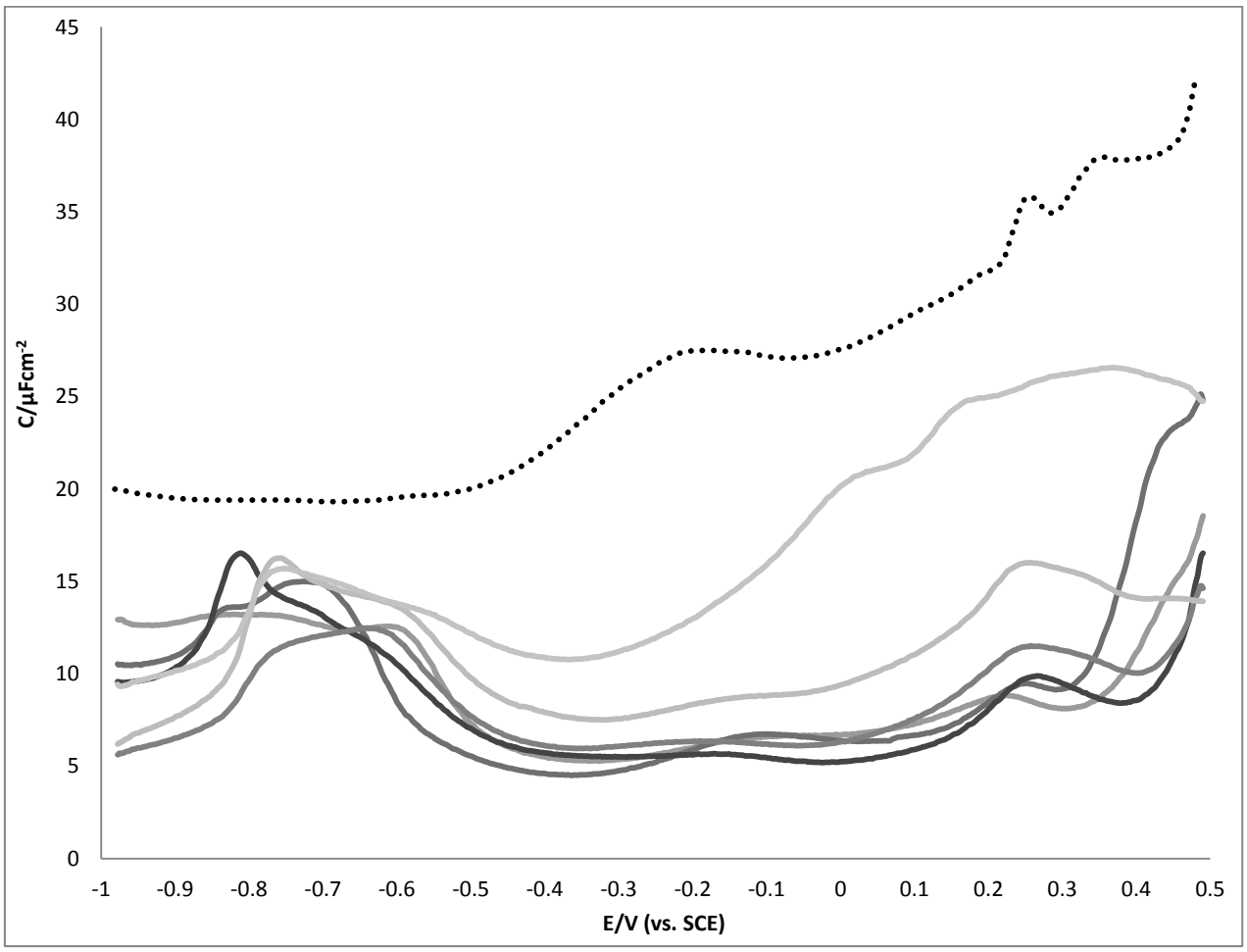

Figure 5.15B Differential capacity curves of the positive-going sweep, recorded for Au (111) in 0.1 M NaF solution without BDAC (black dotted line) and with BDAC (grey lines) after Additions 2-8 (1/64 of the CMC to the CMC of BDAC in 0.1 M NaF solution; 0.00008-0.00255 mM). The CV curves acquire progressively lighter shades of grey as the bulk concentration of BDAC increases.

Sweep rate 5 mV s^{-1}

In Figure 5.15A, the blue arrow points to the pronounced shoulder in the CV curve appearing at the CMC of BDAC. This shoulder is probably caused by the lifting of the Au (100)-(hex) reconstruction. All the Au (100)-(hex) reconstruction is likely to be lifted in this potential range because the only other current maximum in the positive-going sweep is the peak at

140 mV representing the phase transition of the surfactant film. This big shift in potential of the main reconstruction peak (from 180 mV at half CMC to -30 mV at CMC 8) is a result of more molecules, being specifically adsorbed on the Au (100)-(hex) surface as the bulk concentration of BDAC increases, thus allowing the surface fully to unreconstruct as a result of specific adsorption. These specifically adsorbed molecules are most likely to be benzyl groups, and not Cl^- ions. This is because such a prominent shoulder is not observed in the CV of Au (100) in CTAC solution at the same concentration, and the BDAC layer is likely to be less permeable than the CTAC layer owing to the strong N^+ interactions with the quadrupole moments of the benzyl groups.

In Figure 5.15B, between -400 and 100 mV, the differential capacitance values when the concentration of BDAC are between 1/64 and ¼ of the CMC, are similar, and are between the narrow range of 4 and 6.5 µF cm^{-2}. However, when the concentration of BDAC is at ½ the CMC and the CMC, the differential capacitance of the DC minimum increases to 8 µF cm^{-2} and then to 10.5 µ Fcm^{-2}. This shows a possible change in the surfactant adlayer structure as the bulk concentration of BDAC increases, due perhaps to 3D aggregation of surfactants occurring at these higher concentrations. It is noteworthy that no such pattern is observed for DC curves of Au (111) in BDAC solution, Figure 4.23B, doubtless because the aggregation of BDAC molecules when the concentration is at half the CMC and at CMC is specific only to the Au (100) surface. This is likely to be because BDAC molecules have more thermodynamically favourable interactions with the Au (100) surface than with the Au (111) surface, thus providing a more stable base for aggregation to occur on at higher concentrations. It could also be different chloride behaviours. It is possible the Cl^- can

penetrate the surfactant adlayer structure on Au (100) more easily, althrough the influence the Cl^- counter-ion has on the adlayer structure is unclear.

5.8 Summary and Conclusion

Less information can be obtained for the adsorption of surfactants on Au (100) than on Au (111) because chronocoulometry measurements are impossible to carry out, owing to the potential-induced inter-conversion between the energetically different unreconstructed Au (100)-(1 × 1) and reconstructed Au (100)-(hex) structures. However, DC and CV measurements show that the Au (100) surface provide fewer ideal sites with which the surfactant alkyl tail groups can interact by means of van der Waals interactions. As there is no stable 2D adlayer structure for CTAC and CTAF when the electrode is negatively charged or uncharged, the surfactant layer is less stable. The surfactant coverage for CTAC and CTAB greatly increases once a Cl^- and Br^- layer is adsorbed on the Au (100) surface. At higher bulk concentrations relative to the CMC, a bilayer structure is likely to form similar to that on Au (111). On account of the weaker alkyl tail group substrate interactions, halide ions probably permeate the surfactant layer on the Au (100) surface more easily than on the surfactant layer on the Au (111) substrate.

[1] Kolb D.M. and Schneider, J. (1986), *Electrochim Acta*, 31, p. 929.
[2] Schneider J. and Kolb, D.M. (1988), *Surf Sci*, 193, p. 579.
[3]Kolb D.M and Schneider,.J (1985) *Surf Sci*, 162, p. 764.
[4] Hayden, B.E., Prince, K.C., Dale, P.J., Paoluzzi G. and Bradshaw, A.M. (1983), *Sol St Commun*, 48, p.325.
[5] Gao, X., Edens, G.J., Hamelin A. and Weaver, M.J. (1993), *Surf Sci*, 296, p. 333.
[6] Kolb, D.M., Dakkouri, A.S. and Batina, N. (1995), in: *Nanoscale Probes of the Solid/Liquid Interface*, Gewirth A.A. and Siegenthaler H. (eds.), NATO AS1, Vol. E, 288, Dordrecht: Kluwer, p. 263.
[7] Kolb, D.M. (1993), in: *Structure of Electrified Interfaces*, Lipkowski J. and Ross P.N. (eds.), VCH, New York p. 65.
[8] Magnussen, O.M., Hotlos, J., Behm, R.J., Batina N. and Kolb, D.M. (1993), *Surf Sci*, 296, p. 310.
[9] Kolb, D.M. (1993), in: *Structure of Electrified Interfaces*, Lipkowski J. and Ross P.N. (eds.), VCH, New York p. 65.
[10] Wandlowski, Th., Wang, J.X., Magnussen, O.M. and Ocko B.M. (1996), *J Phys Chem*, 100*,* p. 10277.
[11] Kolb, D.M., Schneider, D. (1986), *Electrochim Acta*, 31, p. 929.
[12] Cuesta, A. and Kolb, D.M. (2000), *Surf Sci*, 465, p. 310.
[13] Ocko, B.M., Magnussen, O.M., Wang, J.X. and Wandlowski, Th. (1996), *Phys Rev*, B53 p. 7654.
[14] Kolb, D.M. (1996), *Prog Surf Sci*, 51 p. 109.
[15] Skoluda, P. (2003), *Electrochem Commun*, 5, p. 142.
[16] Vivek, J.K. and I.J. Burgess, (2010), *J Electroanal Chem*, 649, p. 16.
[17] Binning, G., Rohrer, H., Gerber Ch. and Stoll, E. (1984), *Surf Sci*, 144, p. 321.
[18] Lipkowski, J. and Ross P.N. (eds.), (1992), *Adsorption of Molecules at Metal Electrodes*, New York: VCH Publishers.
[19] Richer, J. and Lipkowski, J. (1986), *J Electrochem Soc*, 133 (1), p. 121.
[20] Stolberg, L., Lipkowski, J. and Irish, D.E. (1987), *J Electroanal Chem*, 238, p. 333.
[21] Prado. C., Prieto. F., Rueda. M., Feliu. J. and Aldaz. A. (2007), *Electrochim Acta* 52 p. 3168.

6. The Electrochemistry of Platinum-Gold Nanorods.

6.1 Characterisation of Au NRs

Figure 6.1 presents a high angle annular dark field (HAADF) STEM image of Au NRs, prepared using the seed-mediated growth method.[1]

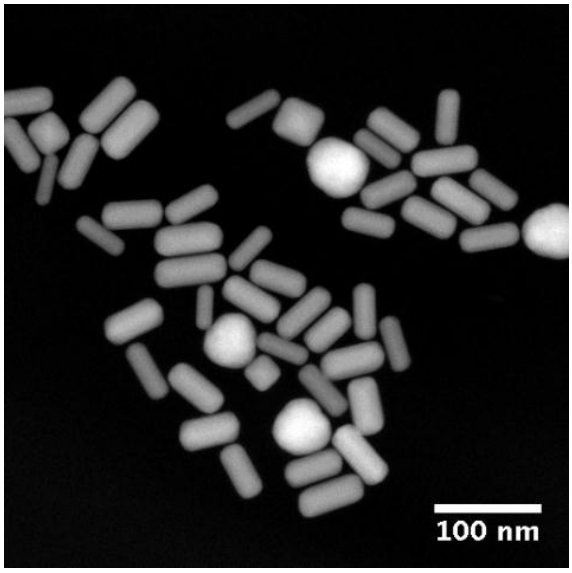

Figure 6.1. HAADF-STEM image of Au NRs

The Au NRs in Figure 1 are sphero-shaped cylinders. The average length of the Au NRs is 35 nm and the width is 10 nm. The aspect ratio (length: width) is 3.5. The solution has a high monodispersity, with mostly nanorods and a low proportion of nanocubes and nanospheres.

The temperature during nanorod synthesis is important for the monodispersity of the Au NRs. When the temperature of the growth solution for Au NR synthesis was at 15°C, a high

proportion of spherical and cube-shaped particles was produced because the temperature was not high enough for there to be a sufficient collision frequency between the CTA-$AuCl_2$ complex and the Au seeds to allow all the seeds to grow into rod-shaped particles. When the temperature of the growth solution for Au NR synthesis was at 40°C, the resulting Au NRs were wider on the sides than in the middle, hence their 'dog bone' structure. This is because the temperature was not low enough for there to be effective confinement of growth in the width of the Au NRs. The temperature used for the synthesis of Au NRs presented in this section was always 25°C.

$AgNO_3$, present in the growth solution during synthesis, confines the longitudinal growth of the Au NRs to 35 nm with an aspect ratio of 3.5. When Ag^+ is absent from the solution, Au NRs can grow to lengths of over 100 nm.[2] Silver ions in the solution allow for a finer control of the nanorod aspect ratio and a higher yield of rod-shaped particles than when no Ag^+ is present.[3]

Figure 6.2 gives the UV/vis absorption spectrum of a sample from the same set of Au NRs as used for the TEM image in Figure 6.1.

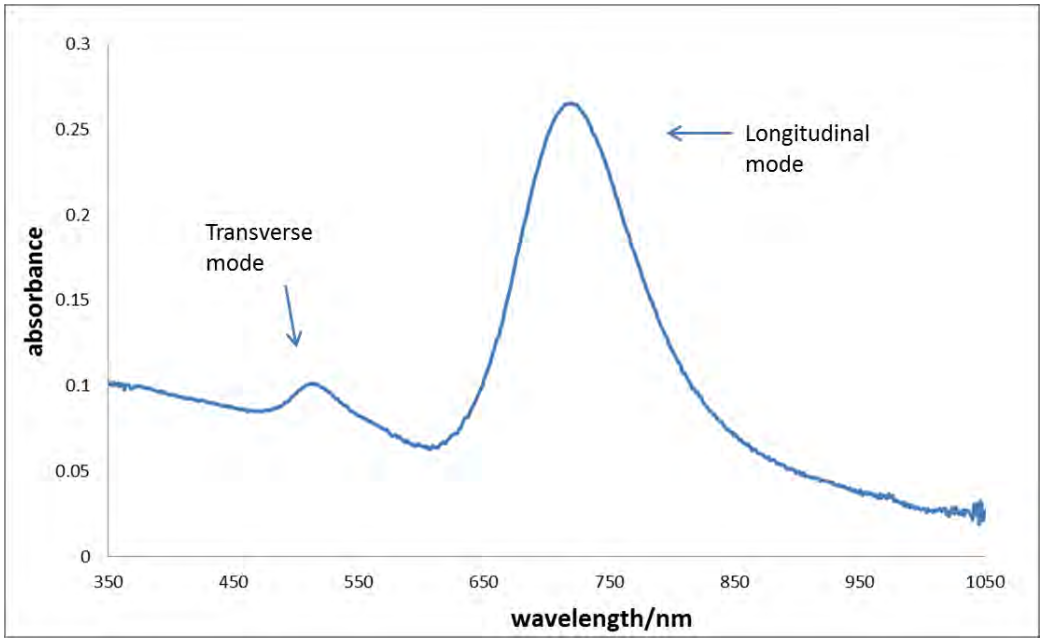

Figure 6.2 UV/vis absorption spectrum of a sample of the same set of Au NRs presented in the STEM image in Figure 6.1

The spectrum in Figure 6.2 represents the two expected absorption bands found in a UV/vis absorption spectrum of Au NRs: the transverse and longitudinal surface plasmon resonance bands. The absorption peak corresponding to the transverse mode is at a wavelength of 525 nm; the absorption peak caused by the longitudinal mode is at 740 nm. These two peaks are predicted by Gans theory, which was developed for the explanation of optical properties of ellipsoidal particles based on a dipole approximation.[4] The wavelength of the LSPR mode absorption peak at 740 nm is a result of Au NRs having a relatively small aspect ratio of 3.5. By comparison, a UV-vis spectrum of previously synthesised Au NRs with a higher aspect ratio of 4.0 had an LSPR peak at 818 nm. [5]

The transverse mode indicates the width of the nanorod. Whenever Au by-products such as nanospheres or nanocubes are produced during the synthesis of AuNRs, there is

additional absorption of between 500 and 600 nm.[5] In this region, Figure 2, there is no additional peak other than that caused by the transverse resonance of the Au NRs. However, the peak is not symmetrical. A small proportion of nanosphere and nanocube by-products may cause the higher wavelength tail.

6.2 The deposition of Pt on Au NRs

The aim of this work is to develop Pt-coated Au NRs as an electrocatalyst for the oxygen reduction reaction. Firstly, there must be controlled deposition of Pt on the Au NRs. Using the Cu_{UPD} and Pt redox replacement (see Section 1.8.2), it was found through experiments that a controlled sub-monolayer of Pt can be deposited on a polycrystalline gold surface. However, it is difficult to observe the morphology of the underpotentially deposited Cu layer and the subsequent redox replacement Pt adlayer on gold nanoparticles using electron microscopy.[6] The exact nature of the Pt monolayer on Au is therefore still unclear. Moreover, Cu_{UPD} requires electrochemical equipment, and the Pt deposition on the Au nanoparticles is restricted to just the Au nanoparticles immobilised on an electrode. In this study, Pt is deposited on the Au NRs directly, by reducing Pt ions onto the gold surface using a reducing agent. Direct deposition does not require electrochemical equipment and Au NRs coated by Pt through direct deposition can be observed by means of electron microscopy.

The weak reducing agent ascorbic acid (AA) was used to reduce the Pt ions onto the Au surface. When Pt deposition was attempted with a stronger reducing agent, $NaBH_4$, the Pt^{2+} ions reduced to Pt (0) before reaching the Au surface. Moreover, there was evidence that BH_4^- ions contaminated the gold by leaving a residue on its surface.

Solutions of K_2PtCl_4 and AA were added to an Au NR solution to form Pt-coated Au NRs. During the Pt deposition, the Au NR solution was kept at a temperature of 40°C. When lower temperature of 25°C was used, full deposition of Pt on the Au NRs did not occur because the collision frequency between the Pt salt micelle complexes with the Au NRs was too low. A temperature of 25°C was used for the synthesis of Au NRs. However, it was apparent that more energy was required for Pt to stick to Au than for Au to stick to Au.

Figure 6.3 presents STEM images of Pt-coated Au NRs. Each set of NRs has a Pt: Au molar ratio of 0.1: 1. The molar ratio of AA: Pt varies. NRs in Figure A have an AA: Pt ratio of 1:1, in B of 10:1, C of 30:1 and in D of 100:1.

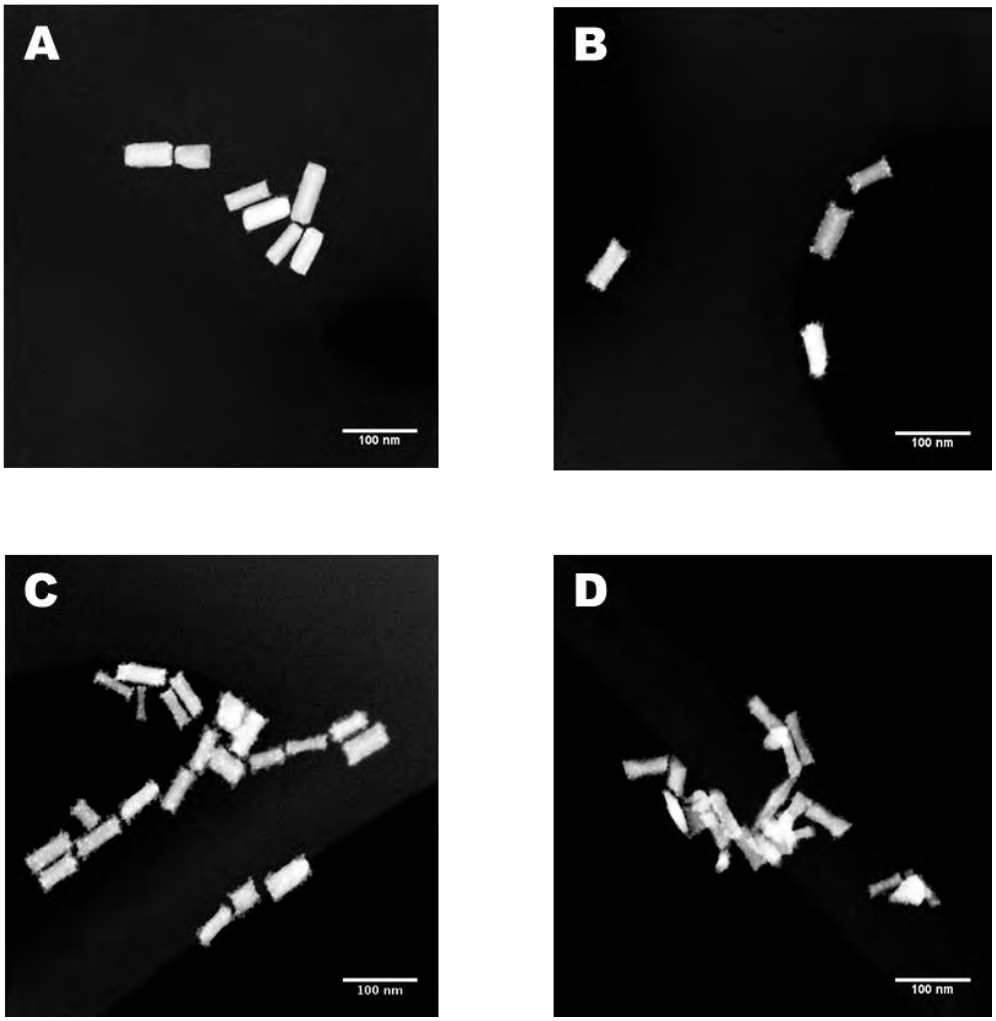

Figure 6.3. HAADF-STEM images of Pt-coated Au NRs with AA: Pt ratios of **A**. 1:1 **B.** 10:1 **C.** 30:1 **D.** 100:1. The Pt: Au ratio was 0.1: 1 for all samples

Figure 6.3 shows that Pt deposits on an Au NR surface in the form of nanodots which are 3-4 nm in size. There is no smooth Pt deposition. A factor is that Pt atoms have a higher cohesive energy with each other compared to an Au atom's cohesive energy with another Au atom. Pt has a cohesive energy of 5.84 eV/atom, whereas Au has a cohesive energy of 3.81 eV/atom.[7] Cu has a slightly lower cohesive energy than Au of 3.5 eV/atom and forms a smooth layer on Au.[8] Another factor could be the surface energy of Pt relative to Au. The surface energy of

Au has been found to be ca. 1.5 J m^{-2}, whereas the surface energy of Pt has a significantly higher value of ca. 2.5 J m^{-2}.[9 10] The Pt thus tries to minimise the total surface area to minimise the total surface energy. Any energy gained from the Au-Pt interaction is offset by the need to reduce surface energy.

In Figure 6.3, there is more Pt nanodot coverage on the Pt @ Au NRs when the ratio of AA: Pt is 10:1 than when the AA: Pt is 1:1. This is because, owing to the low concentration of the reducing agent when the AA: Pt ratio is 1: 1, not all the Pt salt-micelle complex collisions with the Au NRs result in formation of Pt (0) on the Au NR surface. Roughly the same amount of Pt nanodots deposit on each sample. However, there is more of an ordered, reproducible pattern of Pt nanodots on Au NRs if the AA: Pt ratio is 10:1, than for the AA: Pt ratios of 30:1 and 100:1. Thus in order to obtain controlled deposition of Pt on AuNRs, an AA: Pt ratio of 10:1 was used.

Pd also forms nanodots on an Au surface,[11] but they have a polycrystalline structure,[12] owing to a Au and Pd lattice mismatch, which induces the random nucleaction of the Pd nanodots. For Pt on Au NRs, instead of random nucleation, it is likely that there is an epitaxial Pt layer on the surface of the Au NR. Moreover, there is evidence that Pt has a single-crystalline structure. Figure 6.4 shows a magnified STEM image of a Pt nanodot on an Au NR particle.

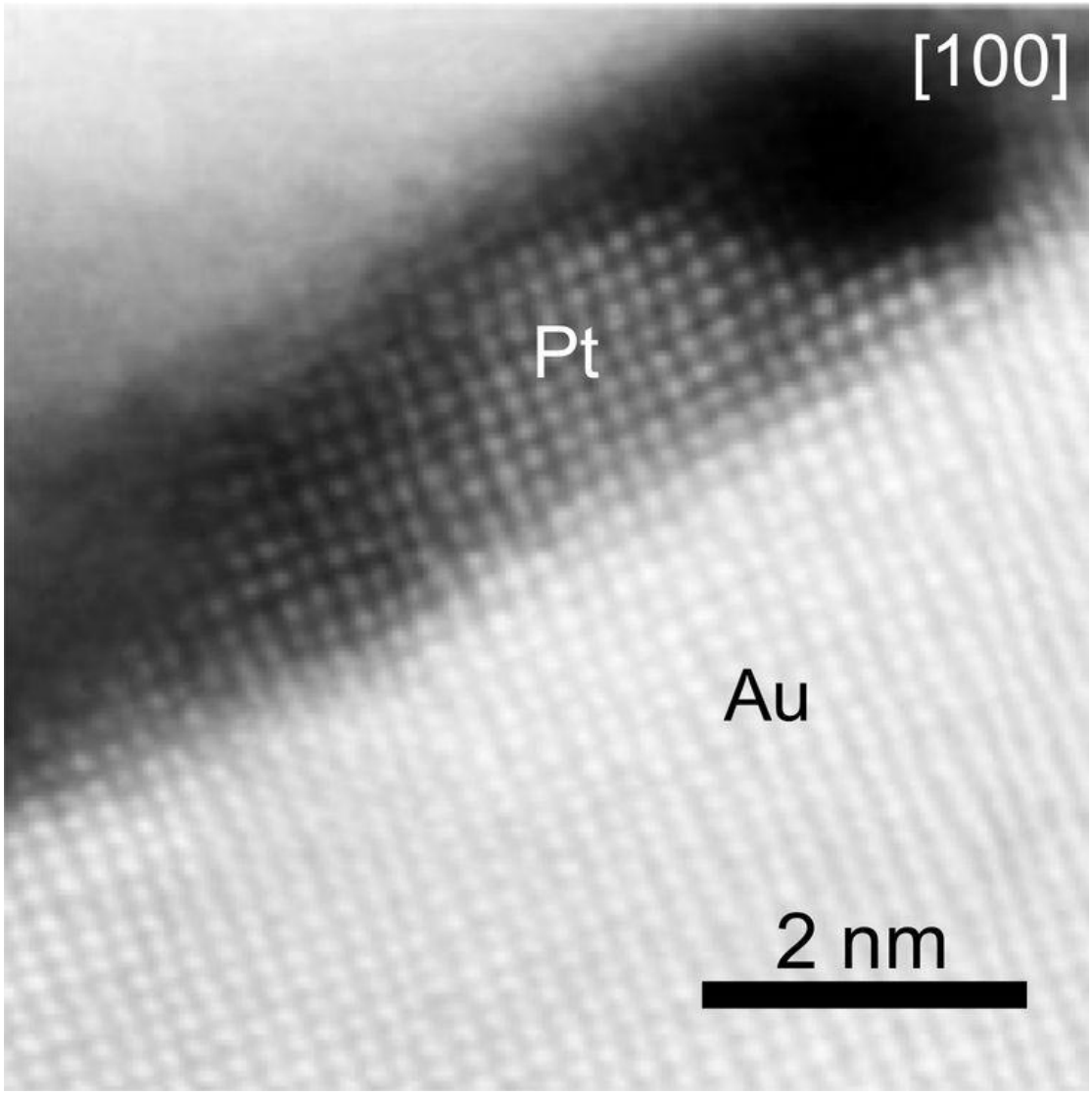

Figure 6.4 Atomic resolution HAADF-STEM images showing a Pt nanodot particle located on a side surface of an Au nanorod.

Figure 6.4 clearly shows that the Pt nanodot on the Au NR surface has a (100) - (1×1) single-crystalline structure, matching the underlying crystallographic surface of the Au NR.

Figure 6.5 gives STEM images of Pt-coated Au NRs with varying Pt: Au ratios. The Pt: Au ratios are A. 0.05, B. 0.25, C. 0.5 and D. 0.75. The AA: Pt ratio for all 4 sets of Pt-coated Au NRs is 10:1.

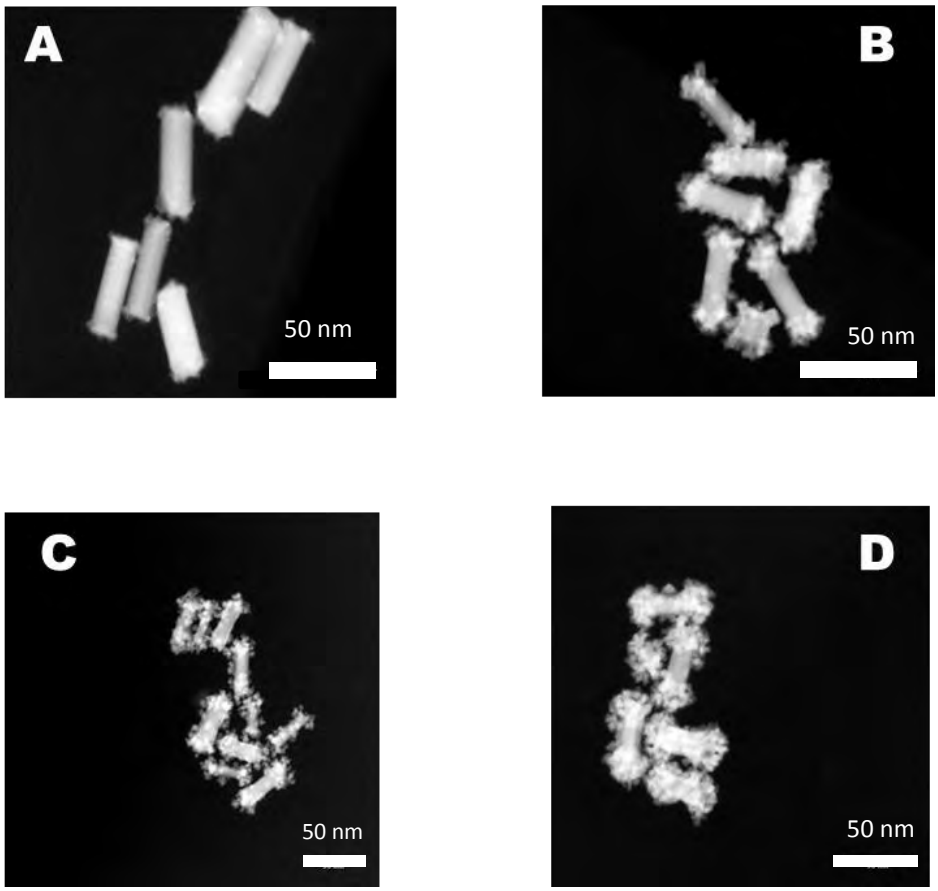

Figure 6.5 STEM images of Pt-coated Au NRs with Pt: Au ratio of A. 0.05, B. 0.25, C. 0.5, D. 0.75
The AA: Pt ratio used was 10:1

It is evident from the STEM images in Figure 6.5 that, especially for the higher Pt: Au ratios, the Pt nanodots appear mainly at the endcaps of the Au NRs. Pt deposits preferentially at the endcap of the Au NRs possibly because there are more structural defects and fewer orderly packed CTAB molecules in these areas.[13] Furthermore, the mass transport conditions are different at the ends and sides of the nanorods for collisions with the Pt-micelle complexes.

Ag or Ag species found in the growth solution during nanorod synthesis are said to form a more compact layer on the rod sides of the Au NRs and this could also be a factor in Pt

preferential deposition on the endcaps of the nanorods.[11] Since the Ag species could either block Pt from depositing on the rod sides or the Ag species on the Au NR surface could attract CTAB more strongly, the more strongly bound CTAB layer would lower the collision frequency with the Pt complexes and the gold nanorod surface on the sides. It has also been suggested that in the same way excess unreacted Ag^+ plays a significant role in determining the final Au NR dimensions by making the reaction kinetically controlled.[14] A similar mechanism could determine preferential deposition of Pt at the tips of gold nanorods in the presence of excess ions in solution.[11] This is less likely to be a major factor because, before Pt deposition, the Au NRs were centrifuged then redispersed in CTAB, so it is likely that most of the unreacted Ag^+ ions will have been absent during Pt deposition.

Figure 6.6 shows a UV-visible absorption spectrum of 0.05 Pt @ Au NRs, 0.25 Pt @ Au NRs, 0.5 Pt @ Au NRs and 0.75 Pt@ Au NRs. The spectra correspond to the same samples used for Pt STEM images as shown in Figure 6.5.

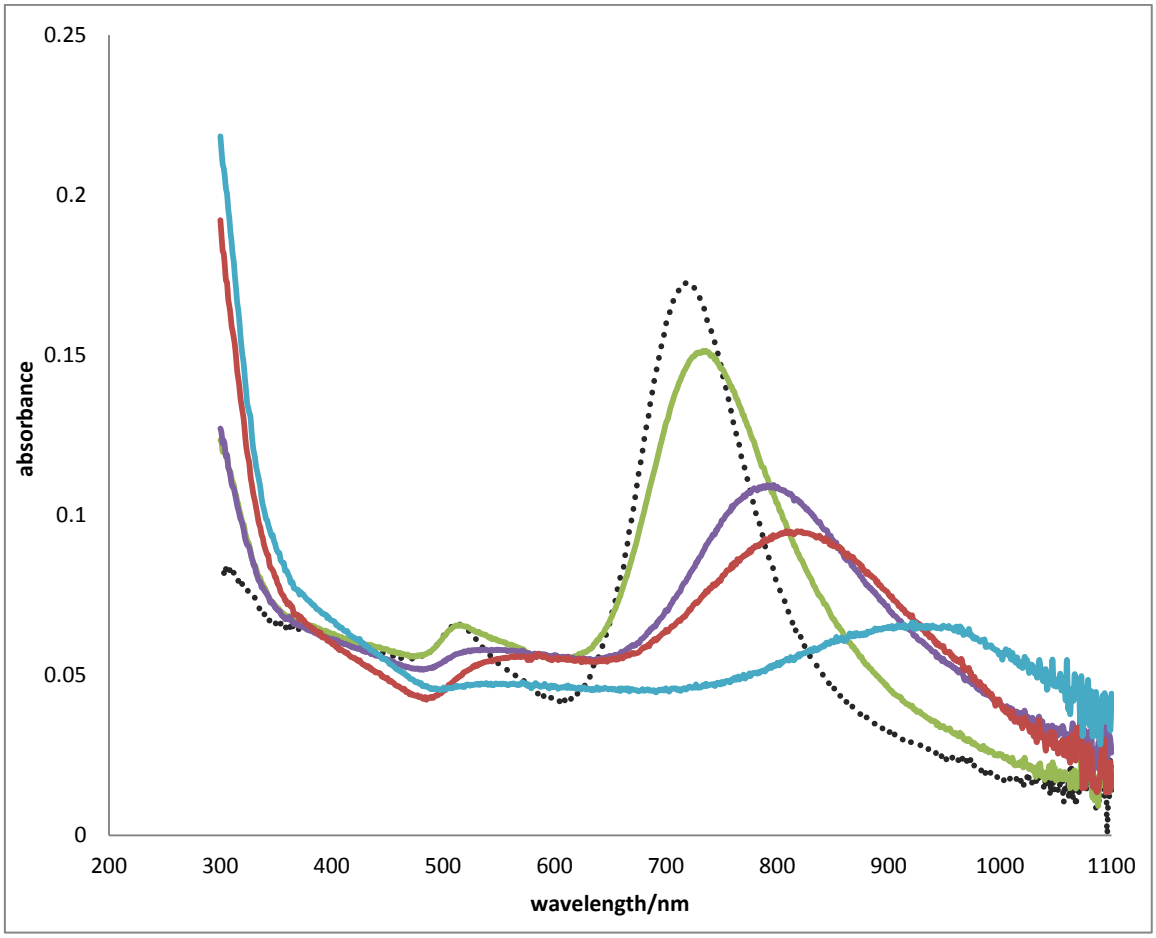

Figure 6.6 UV-visible absorption spectra of Pt-coated Au NRs with Pt: Au ratios of ratios of 0.05 (green line), 0.25 (purple line), 0.5 (red line) and 0.75 (blue line). A UV-vis sprectra of Au NRs is also included as reference (black dotted line)

When Pt was deposited on the Au NR surface, the absorbance of the longitudinal and transverse peaks decreased as more Pt was deposited on the Au surface: Pt, unlike Au, shows broad and weak surface plasmon resonance bands in the UV region. This effect is known as damping caused by Pt.[11] Consequently, the LSPR peaks become broader and their absorbance decreases as the amount of Pt on the Au NRs increases.

It is important also to note the wavelength of the LSPR peaks. The LSPR peaks of the Pt-coated Au NRs increase in wavelength (red shift) as the Pt: Au ratio increases. The

wavelengths and absorbances of the LSPR peaks of the Pt-coated Au NRs are presented in Table 6.1.

Table 6.1. LSPR peak wavelength and absorbance for UV-visible absorption spectrum presented in **Figure 6.5** for Pt-coated Au NRs with varying Pt: Au ratios.

Pt: Au ratio	LSPR Peak wavelength	LSPR Peak absorbance
0 (Au NRs only)	726	0.171
0.05	741	0.148
0.25	803	0.107
0.5	829	0.094
0.75	953	0.065

In the STEM images (Figure 6.5) corresponding to the UV-visible abosorption spectra in Figure 6.6, Pt is clearly coated on the end of the Au NRs more than in the middle; hence, while the Au NRs grow longer owing to the Pt deposition, their change in width is much smaller. This lack of homogeneity leads to an increase in aspect ratio of the rods. An increase in the aspect ratio of the Au NRs leads to a red shift in the LSPR peak.[15] However, another factor influencing the red shift could be the close proximity of the Pt-coated Au NRs to each other. This could cause a smaller surface plasmon resonance frequency, which would increase the wavelength of the LSPR band if the rods also associate with one another in solution.

It is noteworthy that the Pt-coated Au NRs used in this study were stable in solution for up to one-and-a-half years under ambient conditions. However, if the nanoparticles were stored on the TEM grid for the same amount of time in air and at room temperature, or were heated at 200°C in vacuum of 10 mbar for 3 hours, the Au NRs (underneath the Pt nanodot structure) seemed to dissolve or diffuse, possibly to form Pt-Au alloyed or Pt (core) Au (shell) nanoparticles.[16] Owing to their lack of stability, the nanorods are not suitable as electrocatalysts in practical devices.

6.3 Addition of a second Pt layer onto Pt-coated Au NRs

Figure 6.7A gives a STEM image of Pt-coated Au NRs after an Additional layer of Pt has been deposited onto them in the solution.

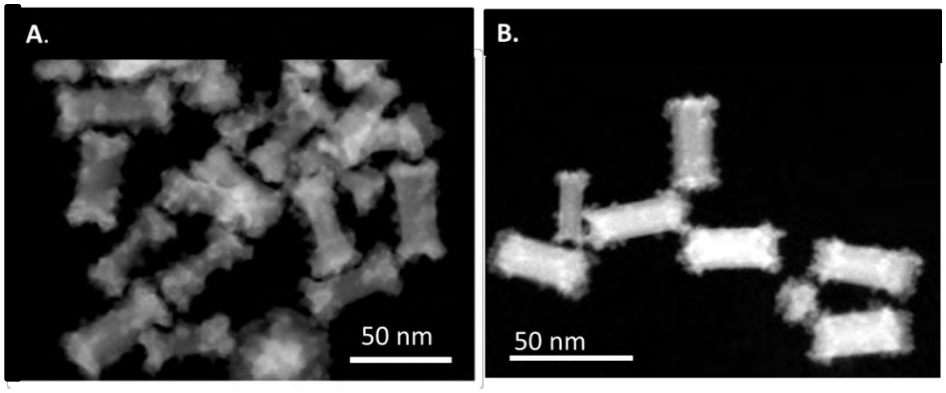

Figure 6.7 STEM images of Pt-coated Au NRs, with a Pt: Au ratio of 0.5. **A** is after an Additional layer of Pt has been added. In **B**, CO has been used as a blocking agent before the second deposition of Pt.

Figure 6.7A shows that the Pt nanodots on the endcaps grow larger, whereas hardly any more Pt coats in the middle of the nanords after an Additional Pt layer has been deposited.

Owing to the higher cohesive energy of Pt than Au, when an Additional Pt layer is added to a Pt-coated Au NR, Pt is more likely preferentially to deposit on other Pt sites rather than Au sites, causing the Pt nanodots to agglomerate. Moreover, according to a computational study on the structure of Au/Pt bimetallic clusters, a Pt-Pt bond is formed mainly through the overlap of s-d hybridised orbitals of the two Pt atoms, whereas a Pt-Au bond originates primarily from the overlap of the s-d hybridised orbitals of Pt with the 6s orbitals of Au. Through hybridised orbitals, there is maximum overlap between atomic orbitals.[17]

A more even distribution of Pt on the Au NRs after the second Pt deposition can be obtained if a blocking agent is used to block the already deposited Pt. The blocking agent chosen in this study was carbon monoxide. CO is able to adsorb strongly on all the Pt sites,[18] whereas CO very weakly adsorbs onto Au,[19] with low coverage. Figure 6.7B gives an STEM image of Pt-coated Au NRs (Pt: Au ratio of 0.5:1) where CO has been used as a blocking agent before a second deposition of Pt. This image shows that, as predicted, there is a more even distribution of Pt and higher Pt coverage on the nanorod surface. Moreover, it is clear that no Pt nanodot agglomeration occurs after the second Addition of Pt.

The CO-blocked nanorods were also found to be more stable on the TEM grid over an extended period of time than the non-CO-blocked nanorods. Overall, the blocking method improves the Pt coverage and has an impact on the stability of the particles.

For the remainder of this study, the Au NRs pictured in Figure 6.7A are denoted 0.5 Pt @ Au NRs + 0.5 Pt, and the Au NRs in Figure 6.7B are denoted 0.5 Pt@ Au NRs + CO + 0.5 Pt. The Au NRs in Figure 6.5C are denoted 0.5 Pt @ Au NRs. This nomenclature is summarised in Table 6.2.

Table 6.2: Nomenclature of all Pt-coated Au NR with details of Pt: Au molar ratio, and AA: Pt

Name of Pt-coated Au NR	Overall Pt: Au molar ratio	AA: Pt molar ratio	Additional notes
0.5 Pt @ Au NRs	0.5 : 1	10 : 1	-
0.5 Pt @ Au NRs + 0.5 Pt	1 : 1	10 : 1	0.5 Pt @ Au NRs with a second Pt layer deposited on the surface. The Pt/Au molar ratio of the additional Pt layer is 0.5. The overall molar ratio of Pt/Au is 1.0.
0.5 Pt @ Au NRs + CO + 0.5 Pt	1 : 1	10 : 1	0.5 Pt @ Au NRs with a CO layer deposited on it as a blocking agent. This is followed by an additional 0.5 Pt/Au layer. The overall molar ratio of Pt/Au is 1.0.

A UV -visible absorption spectrum of samples of 0.5 Pt@ Au NRs, 0.5 Pt @ Au NRs + 0.5 Pt and 0.5 Pt @ Au NRs + CO +0.5 Pt is given in Figure 6.8.

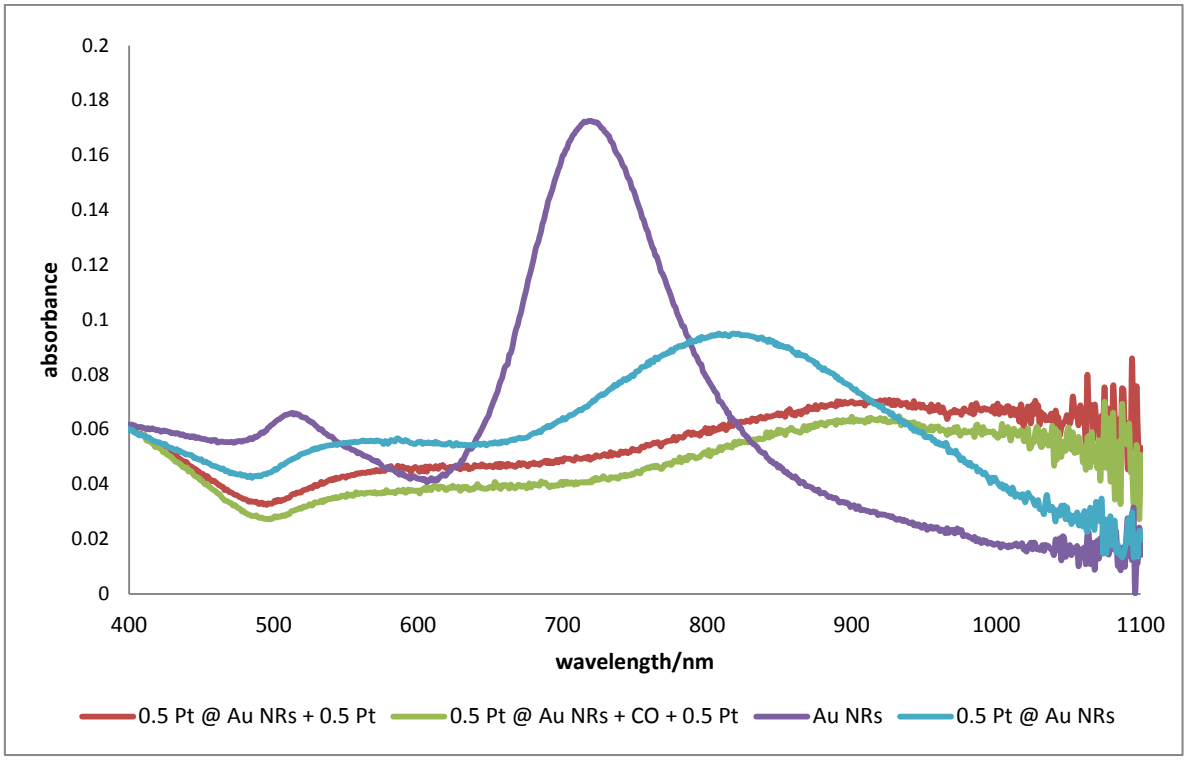

Figure 6.8 UV/visible absorption spectra samples of AuNRs, 0.5 Pt @ Au NRs, 0.5 Pt @ Au NRs + 0.5 Pt, 0.5 Pt @ Au NRs +CO + Pt.

For 0.5 Pt @ Au NR + 0.5 Pt and 0.5 Pt @ Au Nr + CO + 0.5 Pt, there is a higher Pt coverage with the Pt: Au molar ratio of 1:1. The resultant damping is so great that the LSPR peaks of the UV-vis spectra are very broad and have a low absorbance; hence the LSPR peak positions are difficult to interpret. For 0.5 Pt @ Au NRs + CO + 0.5 Pt, the absorption values of the surface plasmon resonance (SPR) peaks are lower than for 0.5 Pt @ Au NRs +0.5 Pt. This indicates that there may be more damping caused by Pt on the 0.5 Pt @ Au NRs + CO + 0.5 Pt, and hence greater Pt coverage.

6.4 Cyclic voltammetry of nanorods

The nanorods were immobilised onto a supported glassy carbon electrode. Before electrochemical measurements were carried out, the nanorod electrode surfaces were fully cleaned using CO and Cu_{UPD}, full details on this cleaning procedure are given in the Appendix, Section B.

6.4.1 Cyclic voltammetry of Au NRs

Figure 6.9 presents a cyclic voltammogram of a glassy carbon electrode containing immobilised Au NRs (purple line). A CV of polycrystalline Au (black dotted line) is included as a comparison.

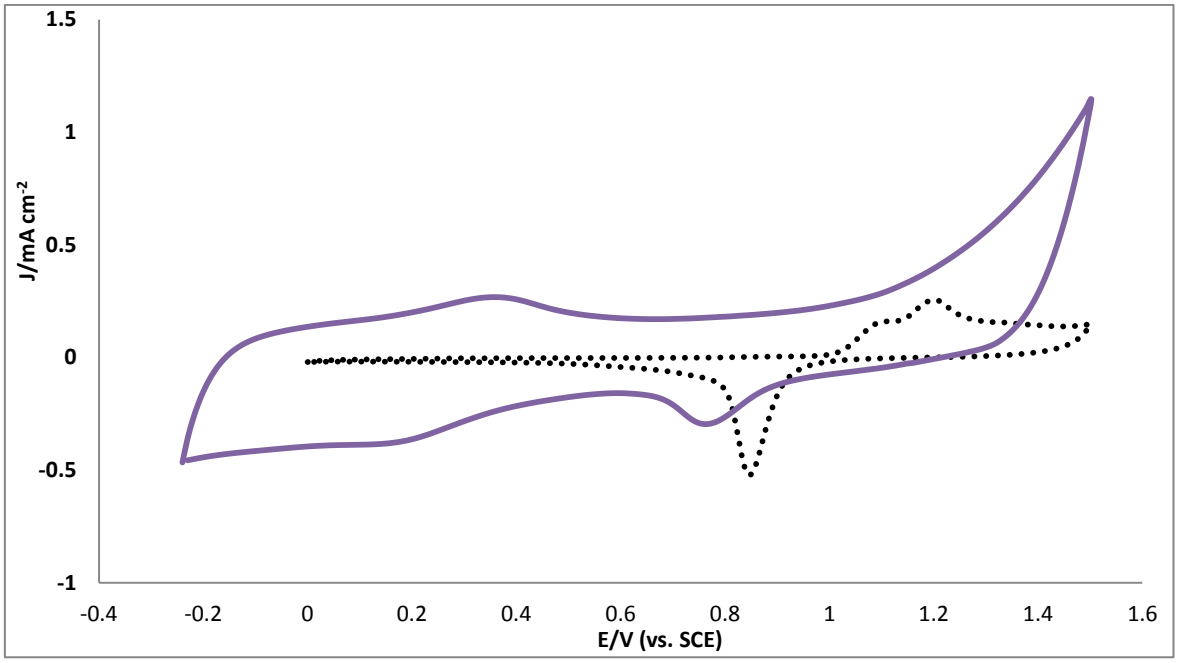

Figure 6.9 Cyclic voltammograms in Ar-saturated 0.05 M H_2SO_4 for thin film AuNRs/C electrode (purple line) and a polished polycrystalline gold disc electrode (black dotted line). Both surfaces are normalised according to real electrode surface area.
Sweep rate 100 mV s^{-1}

A comparison of the CV of the Au NRs with the CV of polycrystalline gold shows that there is a large background current, mostly due to the supporting carbon powder.[20] On the CV of the Au NRs, there is a pair of reversible peaks at around 0.3 V on the cathodic and anodic scans. These correspond to the oxidation and reduction of functional groups, which are found on the carbon surface and are probably types of quinones.[21] The oxidation of the carbon surface cause a slight increase in these peaks after the first few cyclic voltammetry sweeps.

The anodic peak at E > 1.1 V vs. SCE is due to the formation of Au surface oxides as with the polycrystalline Au surface. The cathodic peak at ca. 0.78 V, caused by the reduction of these oxides,[22] is at a more negative potential than that of polycrystalline gold, which has a corresponding peak at 0.85 V. Smaller gold nanoparticles of 10-15 nm in diameter produce a gold oxide reduction peak at ca. 0.89 V vs. SCE.[20] The peak being at a more positive potential on the Au NR surface shows that the Au NR system has more irreversibility in the kinetics of the Au oxide reduction. Au NRs have Au (110) faces on the sides, and Au (100) faces at the ends. The lack of strong SO_4^{2-} adsorbing trigonal Au (111) sites on the Au NRs mean that there would be less sulphate layer formed on the Au NR surface. Partially desorbed sulphate ions are said to help the reversible reduction of Au oxide.[22] A shift in the potential of Au oxide peaks of Au nanoparticle surfaces (compared with polycrystalline Au) has previously been ascribed to Au NPs having a different surface oxide adsorption affinity[23] and surface oxide stability layer.[24]

The total theoretical surface area of gold on the gold nanorods deposited on the carbon surface was calculated to be 0.75 cm^2 from the loading (assuming that the all the gold nanoparticles on the electrode were gold nanorods, and were all 35 nm in length and with an aspect ratio of 3.5). The charge of the gold oxide reduction peak was determined by integration, and was 236 μC. If the charge for the reduction of a gold oxide monolayer is 400 μC cm^2, [22] the electroactive surface area of the gold must be 0.59 cm^2. This value is similar to the theoretical, and shows that the Au NR surface was effectively cleaned and the nanoparticle loading was accurate.

6.4.2 Cyclic voltammetry of Pt-coated nanorods

Figure 6.10 presents cyclic voltammograms of glassy carbon electrodes containing thin films of Au NRs, 0.5 Pt @ Au NRs, 0.5 Pt @ Au NRs + 0.5 Pt and 0.5 Pt @ Au NRs + CO + 0.5 Pt on the surface. A CV of polycrystalline Pt (dotted line) is also added as a reference. Since the catalyst loading for all four nanorod electrode surfaces is identical (42 μg cm^{-2} of Au), all the nanorod CVs are normalised according to the calculated electroactive surface area of gold on Au NRs (0.59 cm^2). The numbers represent different potential regions to be discussed.

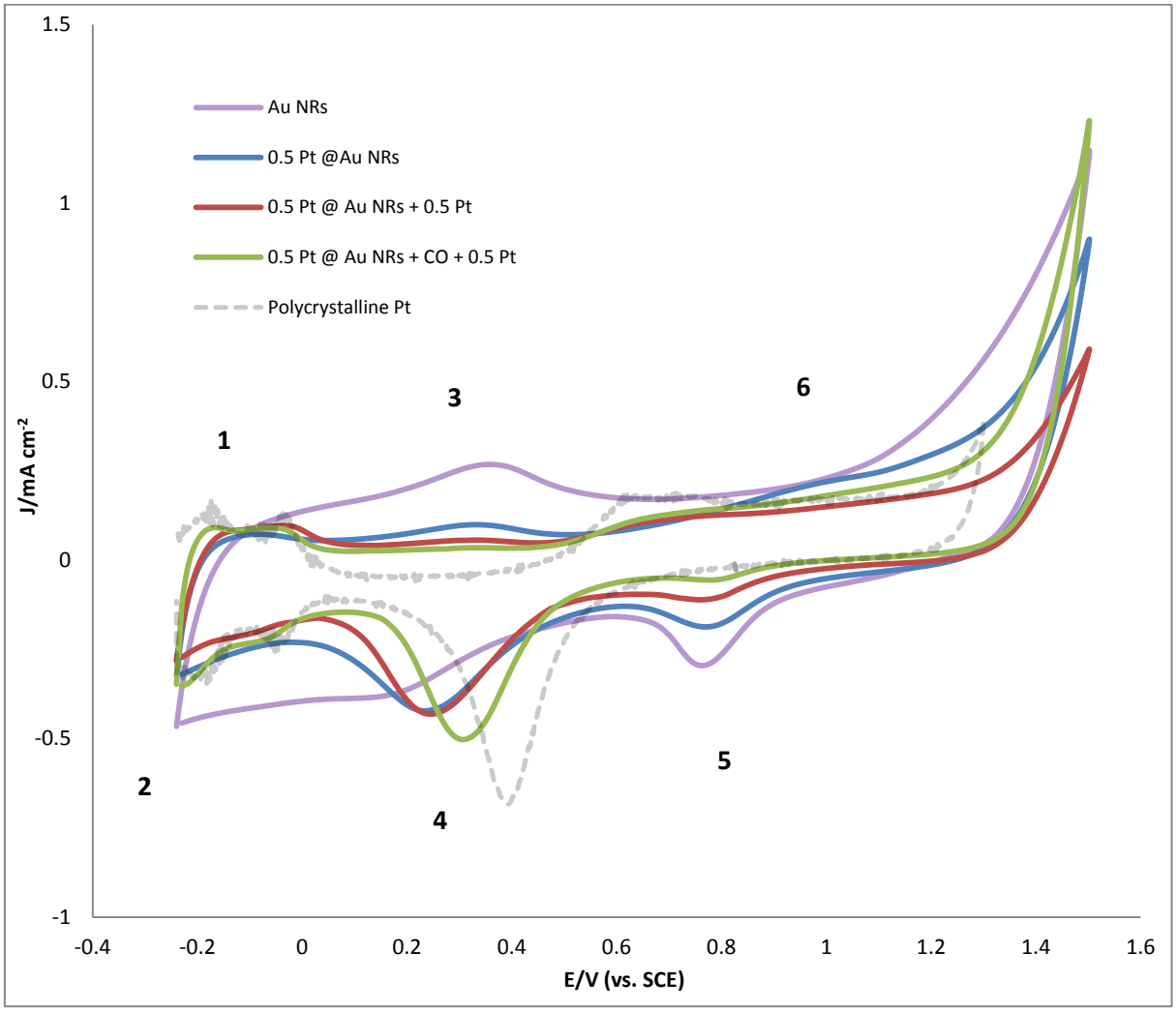

Figure 6.10 Cyclic voltammograms in Ar-saturated 0.05 M H_2SO_4 for thin film nanorod/C electrodes of Au NRs (purple line), 0.5 Pt @ Au NRs (purple line), 0.5 Pt @ Au NRs (blue line), 0.5 Pt @ Au NRs + 0.5 Pt (red line) and 0.5 Pt @ Au NRs (green line). A CV of polycrystalline Pt (grey dashed line) is also added for reference.
Sweep rate 100 mV s^{-1}

The increase in current and the peaks observed for the Pt-coated Au NRs between the potentials of -0.24 V and 0.1 V are caused by hydrogen desorption on the cathodic sweep (1) and hydrogen adsorption on the anodic sweep (2). There would also be a contribution from the tail of the quinone oxide/reduction which causes an increase in current in this potential region on the Au NR surface. This is particularly apparent on the 0.5 Pt @ Au NR surface

because no peak is observed in the hydrogen adsorption Region (1). There is a more evident contribution from quinones on the 0.5 Pt@ Au NR surface because it has less Pt deposited onto it, and consequently it has a greater surface area of Au exposed.

On the four nanorod surfaces, the background current due to the supporting carbon powder evidently decreases as the surface coverage of Pt increases. This can be seen in the current density peak caused by the quinone oxidation peak in the anodic sweep at ca. 0.35 V (3). The current density caused by quinone oxidation decreases in the order Au NRs < 0.5 Pt @ Au NRs < 0.5 Pt @ Au NRs + 0.5 Pt < 0.5 Pt @ Au NRs + CO + 0.5 Pt. This is in general because Pt nanoparticles have a low double-layer charging current in this potential region.[25]

In potential Region (4), Figure 6.10, there is a Pt oxide reduction peak present on the polycrystalline Pt electrode at 0.4 V and a peak on the Au NR surface representing the reduction of quinone species at ca. 0.2 V. As the Pt-coated Au NRs have peaks between these two potentials, one can infer that the cause of these peaks is a combination of Pt – oxide reduction (caused by Pt) and quinone reduction (caused by C). The Pt-coated Au NRs all display peaks from Au oxide reduction (5) at a similar potential to the peak found on the Au NRs at ca. 0.78 V. The Pt oxide and Au oxide on the nanorod surfaces is formed on the anodic sweep between 0.6 V and 1.5 V (6).

The CV of 0.5 Pt @ Au NRs + CO + 0.5 Pt has a slightly lower current caused by the double-layer charging in potential Region 3, characteristic of a Pt nanoparticle surface. In addition, the CV representing 0.5 Pt @ Au NRs + CO + 0.5 Pt has a peak in potential Region (4) that is closer in potential and current density to that observed for bulk Pt oxide reduction than that of the CV representing 0.5 Pt @ Au NRs + 0.5 Pt. This implies that the peak on the

CV of 0.5 Pt @ Au NRs + CO + 0.5 Pt has a larger contribution from Pt oxide reduction and is less influenced by the quinone species (found on the Au NR only surface) than the corresponding peak on the CV of 0.5 Pt @ Au NRs + 0.5 Pt. At the Au oxide reduction potential Region (5), the CV of 0.5 Pt @ Au NRs + 0.5 Pt has a visibly larger charge than the CV of 0.5 Pt @ Au NRs + CO + 0.5 Pt, indicating that there is a higher Au surface area and consequently less Pt coverage on the 0.5 Pt @ Au NRs. In the surface oxide formation Region (6), the CV of 0.5 Pt @ Au NRs + CO + 0.5 Pt has a slightly higher current corresponding to Pt-OH formation, and there is a large increase in the current of this CV between 1.2 V and 1.5 V arising from oxygen evolution on a Pt surface. A similar increase in current is not observed on the CV of 0.5 Pt @ Au NRs + 0.5 Pt.

The charges under hydrogen desorption (1) and under Au oxide reduction (5) are used to establish the active surface area of Au and Pt, respectively, on the Pt-coated Au NRs.

Table 5 presents the charges of the peaks corresponding to Au oxide reduction found in the CVs of each type of nanorod surface in Figure 6.10.

Table 6.3: Column 1: Gold oxide reduction peak charges from thin film AuNRs/C and Pt-coated Au NR/C electrodes. Column 2: calculated gold surface coverage (from Au oxide reduction peak charge), assuming charge to remove gold oxide monolayer is 400 μC cm^{-2}. Column 3: percentage area of gold on Pt-coated Au NRs assuming total surface area of Au NRs is 0.59 cm^2.

Nanorod type	Charge due to Au oxide reduction/μC	Active surface area of Au on nanorod surface/cm^2	% area of Au on nanorod surface
Au NRs	236	0.59	100
0.5 Pt @ Au NRs	184	0.46	78
0.5 Pt @ Au NRs + 0.5 Pt	123	0.31	53
0.5 Pt @ Au NRs + CO + 0.5 Pt	81.2	0.20	34

The results in Table 6.3 show that the surface area of Au on the nanorod surfaces decreases in the following order: 0.5 Pt @ Au NRs > 0.5 Pt @ Au NRs + 0.5 Pt > 0.5 Pt @ Au NRs + CO + 0.5 Pt. According to these results, there is an estimated 19% less Au surface on 0.5 Pt @ Au NRs + CO + 0.5 Pt, compared with 0.5 Pt @ Au NRs + 0.5 Pt.

Table 6.4 presents the calculated charges corresponding to hydrogen desorption from the CV of the Pt-coated Au NR surfaces in Figure 6.10, with the subsequently calculated surface coverage and per cent coverage of Pt on the nanorod surface also given.

Table 6.4 Column 1: charge caused by hydrogen desorption on Pt-coated Au NRs; b) calculated surface area of Pt on nanorod surface, assuming charge to remove monolayer of H on Pt is 209 μC cm^{-2}; c) per cent coverage of Pt on nanorod surface, assuming total surface area of Au NRs is 0.59 cm^2

Nanorod type	Charge due to hydrogen desorption/μ C	Surface area of Pt on Au NR surface/cm^2	% area of Pt on nanorod surface
0.5 Pt @ Au NRs	31.2	0.15	22
0.5 Pt @ Au NRs + 0.5 Pt	54.6	0.26	47
0.5 Pt @ Au NRs + CO + 0.5 Pt	75.6	0.36	67

The results in Table 6.4 indicate that the coverage of Pt on the Au NRs increases in the following order: 0.5 Pt @ Au NRs < 0.5 Pt @ Au NRs + 0.5 Pt < 0.5 Pt @ Au NRs + CO + 0.5 Pt, with 0.5 Pt @ Au NRs + CO + 0.5 Pt having a 20% higher surface area of Pt than 0.5 Pt @ Au NRs + 0.5 Pt.

The voltammetric profile for the desorption of hydrogen from Pt also presents different peaks, depending on the crystallographic planes exposed.[26] The lower potential peak is associated with weakly bonded hydrogen from (110) types of sites, and the peak at a higher potential arises from weakly bonded hydrogen on (100) types of surface, with (111) sites contributing to both peaks.

In Figure 6.11, larger scale CVs of Pt-coated nanorod electrode surfaces in the potential region where hydrogen desorption occurs are given.

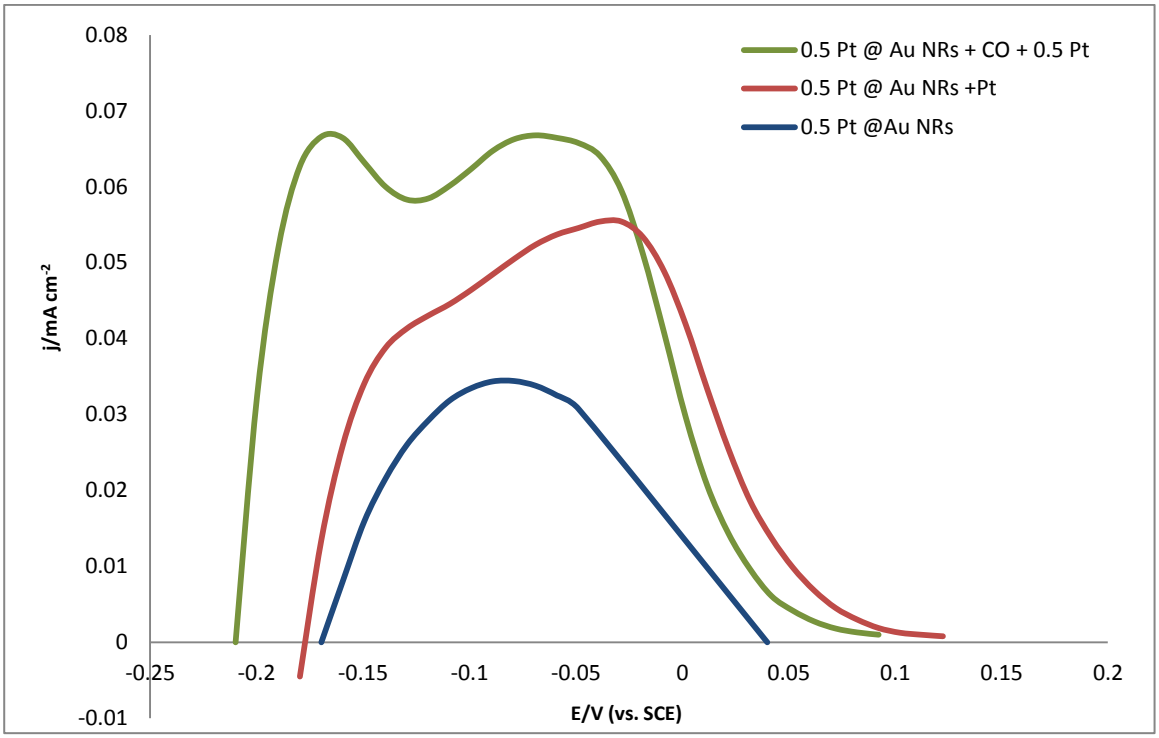

Figure 6.11 Voltammetric profile for the desorption of hydrogen from the Pt sites on glassy carbon electrodes containing thin films of 0.5 Pt @ Au NRs (green line), 0.5 Pt @ Au NRs + 0.5 Pt (blue line) and 0.5 Pt @ Au NRs + CO + 0.5 Pt (red line), in an Ar-saturated H_2SO_4 electrolyte.
Sweep rate 100 mV s^{-1}

The atomic resolution STEM image in Figure 6.4 clearly shows that there is epitaxial growth of Pt nanodots on the Au NR surface, with the (100)-(1×1) structure of the Pt nanodots being identical to the underlying Au NR (100)-(1×1) surface structure. It would therefore follow that Pt nanodots would have a (110) structure if grown on a (110) side face of an Au NR. There is evidence of this in Figure 6.11, where the H desorption peak of 0.5 Pt @ Au NRs + CO + 0.5 Pt has a pronounced peak representing (110) surface sites. As can be seen in Figure 6.7B, there is an abundance of Pt nanodots on the Au NR (110) side faces. 0.5 Pt @ Au NRs, which have fewer Pt nanodots on the Au NR (110) Side faces, have no peak in Figure 6.11 representing (110) sites. However, the larger Pt nanodots on this nanorod surface means that epitaxial growth is less likely to extend to the Pt surface atoms. There has thus

far been no evidence of extended planar faces on Pt nanoparticles, and the position and shape of hydrogen desorption peaks in CVs of Pt nanoparticle electrodes has been attributed to a family of energetically similar sites. [27] [28] [29] [30]

6.5 CO electro-oxidation on nanorods

Figure 6.12A gives CO oxidation voltammograms of 0.5 Pt @ Au NRs, 0.5 Pt @ Au NRs + 0.5 Pt and 0.5 Pt @ Au NRs + CO + 0.5 Pt. Figure 6.12B gives a comparison of each CO oxidation voltammogram (in Figure 24A) with a clean, CO-free surface.

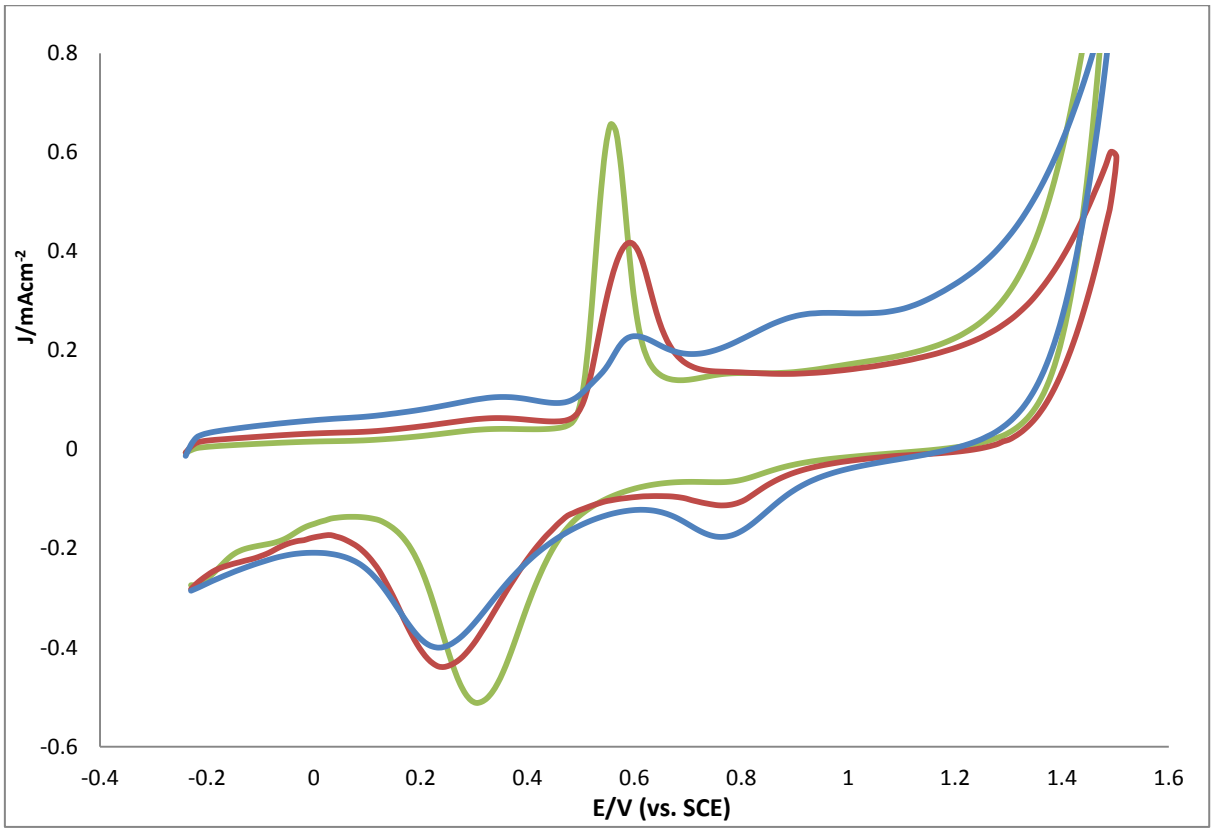

Figure 6.12A Cyclic voltammograms of oxidative desorption of CO in Ar-saturated 0.05 M H_2SO_4 electrolyte on 0.5 Pt @ Au NRs (green line), 0.5 Pt @ Au NRs + 0.5 Pt (red line) and 0.5 Pt @ Au NRs + CO + 0.5 Pt (blue line).
Sweep rate 100 mV s^{-1}

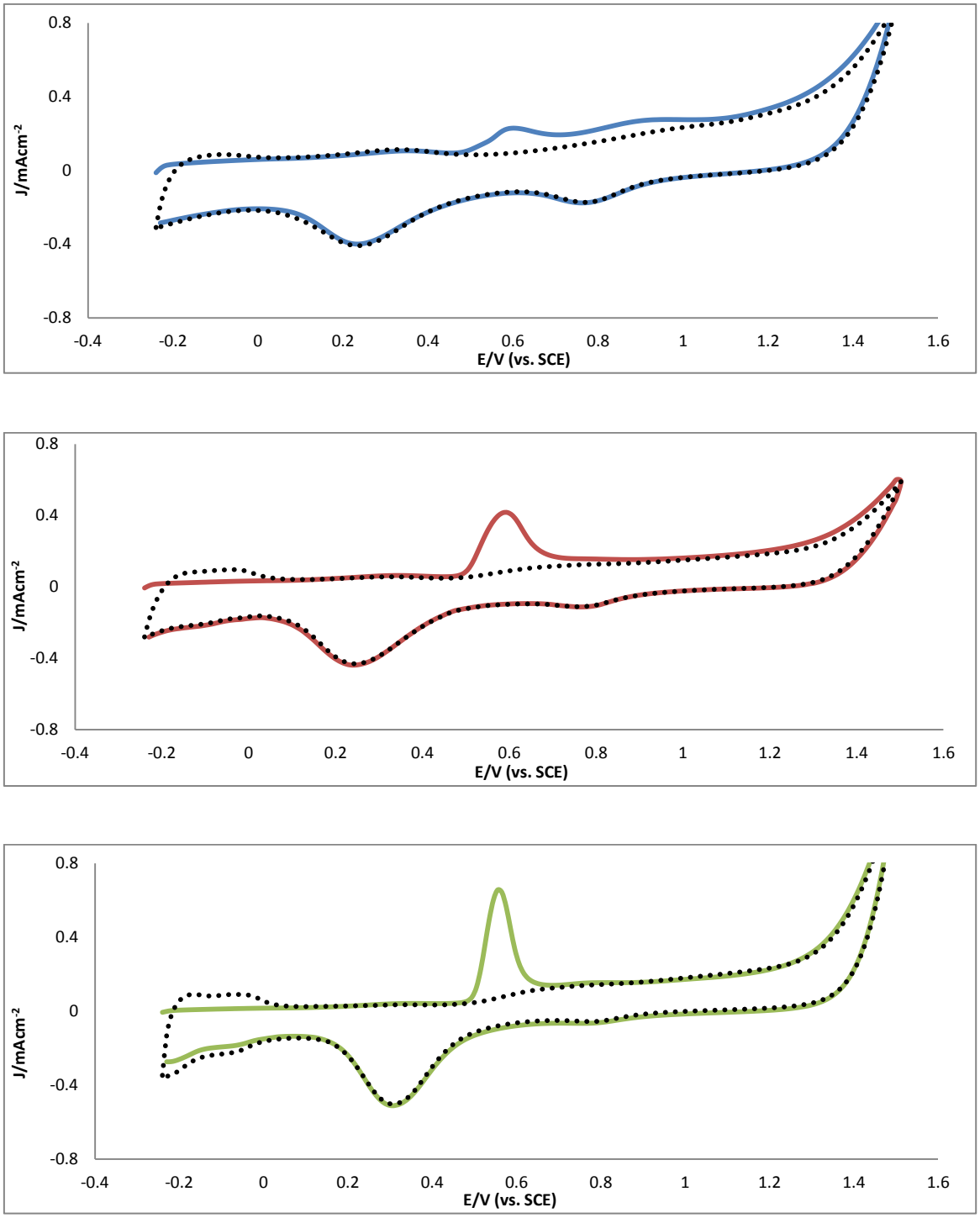

Figure 6.12B Comparison of CVs of oxidative desorption of CO in Ar-saturated 0.05 M H_2SO_4 electrolyte on 0.5 Pt @ Au NRs (blue line), 0.5 Pt @ Au NRs + 0.5 Pt (red line) and 0.5 Pt @ Au NRs + CO + 0.5 Pt (green line), with CVs of the same surfaces which are clean and CO-free (black dotted lines).
Sweep rate 100 mV s^{-1}

Owing to the bimetallic nature of the 0.5 Pt @ Au NR surface, there is a broad wave corresponding to CO oxidation between 0.7 and 1.11 V (see Section 1.11 for the proposed mechanism of CO oxidation on a Pt-Au bimetallic surface).

Table 6.5 gives a comparison of the potential, width and charge of the CO oxidation peaks of the 0.5 Pt @ Au NRs + 0.5 Pt and the 0.5 Pt @ Au NRs + CO + 0.5 Pt surfaces. The charge to remove a monolayer of CO when the coverage of CO on platinum (θ_{CO}) = 1.0 is 537 μC cm^{-2}.[31] However, voltammetric determination of the amount of CO on polycrystalline Pt shows that the saturated layer of CO on Pt is 90% of a monolayer.[32] Accordingly, the estimated charge to remove a monolayer of CO from the Pt surface is 480 μC cm^{-2}.

Table 6.5 The width, potential and charge of the CO oxidation peaks of 0.5 Pt @ Au NRs + 0.5 Pt, and 0.5 Pt @ Au NRs + CO + 0.5 Pt in Figure 6.12. The active surface area of Pt is given Column 5, assuming that the charge to oxidise a monolayer of CO off a Pt surface is 480 μC cm^{-2}.

Nanorod type	Potential of CO oxidation peak/V (vs. SCE)	Width of CO oxidation peak/ V	Charge of CO oxidation peak/ μC	Active surface Pt surface area according to charge of CO oxidation peak/cm^2
0.5 Pt @ Au NRs + 0.5 Pt	0.586	0.211	232	0.48
0.5 Pt @ Au NRs + CO + 0.5 Pt	0.556	0.145	275	0.57

Table 6.5 shows that the active surface area of Pt is 19 % greater on 0.5 Pt @ Au NRs + CO + 0.5 Pt than on 0.5 Pt @ Au NRs + 0.5 Pt. This is consistent with what was found from the charges of the hydrogen desorption. It is noticeable, though, that the active surface area of

Pt according to the CO oxidation charge is higher than the active Pt surface area of Pt according to the hydrogen desorption charge. In order to determine the charge caused by CO oxidation, correction is required of the total charge measured from other contributions, such as charge due to the double-layer (non-faradaic charge) and the faradaic components of the background charge (metal oxide).[33] The difficulty here is that the double layer has been found to be different with CO both present and absent.[31] Another uncertainty is due to an overlap of CO oxidation with other faradaic processes, such as hydroxyl deposition or metal oxidation.[33] For the Pt-coated AuNRs, the electric charge involved in Pt oxidation in the absence of CO was subtracted from the voltammogram with a CO peak. This did not take into account the effect of the CO being oxidised at the same time as the formation of oxygen-containing species.

The relative values for the potentials of the two CO oxidation peaks in Table 6.5 show that the 0.5 Pt @ Au NR + CO + 0.5 Pt is more active towards the oxidation of CO than 0.5 Pt @ Au NRs + 0.5 Pt. This could be because some Pt nanodots on the 0.5 Pt @ Au NRs + CO + 0.5 Pt surface have expitaxially grown and have a (110) surface structure or the Pt nanodots on the nanorod surface a surface structure energetically similar to Pt (110). It has been found that the activity of electro-oxidation for Pt single-crystal surfaces increases in the order {100} ≅ {111} < {110}.[18] The CO could adsorb less strongly on the Pt (110) surface.[34] Another reason is that the increased activity is due to the stepped nature of the Pt (110) surface.[35] Studies in ultra-high vacuum environments have shown that on Pt (110), CO ad-atoms preferentially chemisorb on the terrace sites, with OH_{AD} adsorbing on the step sites.[36] This configuration means that OH_{AD} is ideally situated, relative to CO_{AD}, for CO electro-oxidation to occur.

The smaller size of the Pt nanodots on 0.5 Pt @ Au NRs + CO + 0.5 Pt (3-4 nm), compared with those on 0.5 Pt @ Au NRs + 0.5 Pt (4-8 nm), could also contribute to the shift in the CO oxidation peak position. On Pt single-crystal surfaces, it has been found that under-coordinated Pt ad-islands (0.5 to 4 nm), from lifting surface reconstruction, are more active for CO oxidation than pure step sites.[18] This is because OH competes better with CO for adsorption sites on ad-islands than on other surface features.

Table 6.5 and Figure 6.12 show that the CO oxidation wave produced by the 0.5 Pt @ Au NRs + 0.5 Pt electrode surface is broader than that of the 0.5 Pt @ Au NRs + CO + Pt surface. It has been found that as the proportion of linear-to-bridge-bonded CO on Pt increases, the current peak broadens.[37] This could be because the deprotonation of the COOH intermediate happens less readily if the COOH is bridge-bonded; thus the CO oxidation process happens over a larger potential range. According to previous studies of CO adsorption on Pt using FTIR, there are bands representing bridge-bonded CO on Pt (111)[38] and Pt (100)[39] single-crystal faces. For similar studies on Pt (110), on the other hand, no bridge-bonded CO was observed.[40]

The surface of the Pt-coated Au NR electrocatalyst is a dynamic system; it is assumed that CO on the Pt surface is not rigid it is and said to move rapidly over the Pt surface, possibly though interconversions of linear and bridged CO.[34] It has been found that on a Pt surface during electro-oxidation of CO, bridge-bonded CO increases from 10% to 30%.[37] This interconversion would be more likely on the 0.5 Pt @ Au NRs sites where the Pt nanodots are bigger because there are more adjacent Pt sites to which a linearly bonded CO molecule can bridge-bond.

6.6 The oxygen reduction reaction on nanorod surfaces

6.6.1 Polarisation curves of nanorod electrodes

The oxygen reduction reaction was investigated with the rotating disc electrode (RDE) technique for the cleaned Au NR, 0.5 Pt @ Au NRs, 0.5 Pt @ Au NR + 0.5 Pt, and 0.5 Pt @ Au NRs + CO + 0.5 Pt electrodes used for cyclic voltammetry and CO oxidation voltammetry in Section 6.5.

The RDE polarisation curves measured for the reduction of oxygen on the Au NR surface are presented in Figure 6.13. Rotation rates of 400, 900, 1600 and 2500 rpm were used.

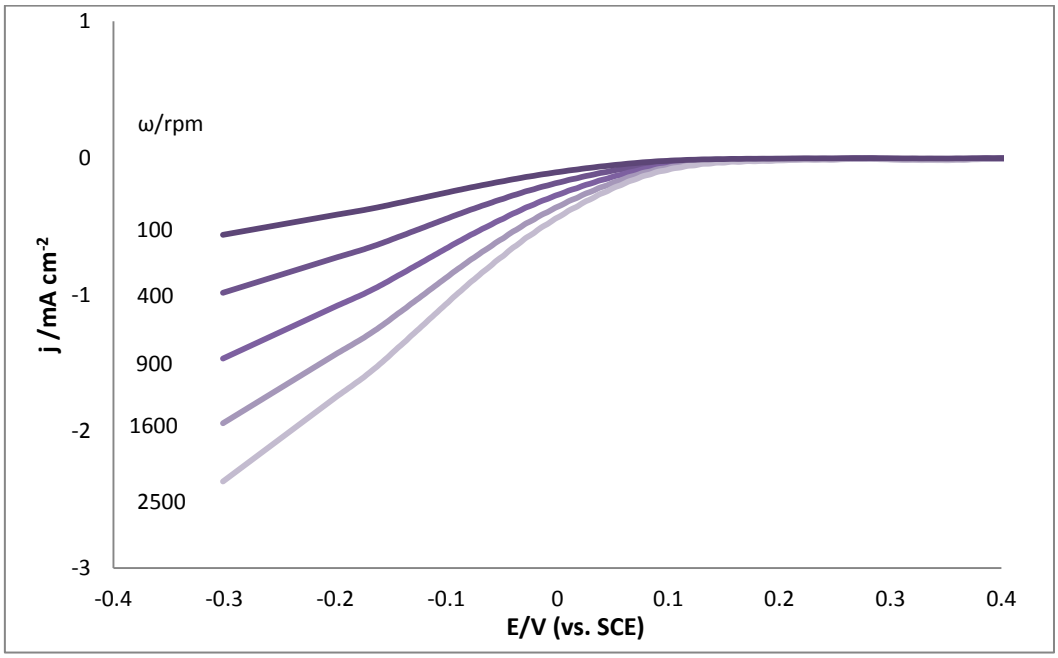

Figure 6.13 Rotating disc electrode (RDE) curves of thin film Au NR on glassy carbon electrode in O_2-saturated 0.05 M H_2SO_4 solution, using rotation rates of 400 rpm, 900 rpm, 1600 rpm and 2500 rpm.
Sweep rate 2 mV s^{-1}

In Figure 6.13, the shape of the polarisation curves produced by the Au NR electrode is identical to the polarisation curves produced by other Au surfaces.[41 20] This indicates that O_2 is reduced on Au NRs with similar mechanism to that of other Au surfaces. In Figure 27, and in previous studies of the ORR on Au surfaces in acidic electrolytes, no limiting current plateau is observed in the polarisation curves. This shows that the kinetics of the ORR on gold surfaces is slow.

The onset of the increase in current density caused by oxygen reduction is at ca. 0.15 V (vs. SCE). The onset of the increase in current density caused by ORR can also be observed at a similar potential on RDE polarisation curves for polycrystalline Au and single-crystal Au surfaces,[41] and thin film smaller Au nanoparticle/carbon electrodes where the nanoparticles are 10-15 nm in diameter.[20] This shows that the strength of the O_2 interaction with the Au NR surface is similar to that of other Au surfaces. When the RDE is rotated at 2500 rpm, the current density of the polarisation curve of the Au NRs at -0.3 V vs. SCE reaches -2.6 mA cm^{-2}. At the same rotation speed and equivalent potential, the current density of the polarisation curves produced by pure Au (110) and Au (100) electrodes in the 0.05 M H_2SO_4 solution is -3.5 mA cm^{-2}.[41] Thin film Au nanoparticle (ca. 15 nm in diameter)/C electrodes produced ORR polarisation curves with higher current density (when the electrode is rotated 2500 rpm, at -0.3 V vs. SCE) of -4.5 mA cm^{-2} [23]. On these other Au surfaces, more electrons are transferred to the oxygen atoms per cm^2 than on the Au NR electrode surface. This is most likely because the other Au nanoparticle surfaces have a higher electrochemical surface area.

Figure 6.14 gives representative RDE polarisation curves of O_2 reduction on (a) 0.5 Pt @ Au NRs, (b) 0.5 Pt @ Au NRs + 0.5 Pt and (c) 0.5 Pt @ Au NRs + CO + 0.5 Pt, for the same rotation rates of 100 rpm, 400 rpm, 900 rpm, 1600 rpm and 2500 rpm.

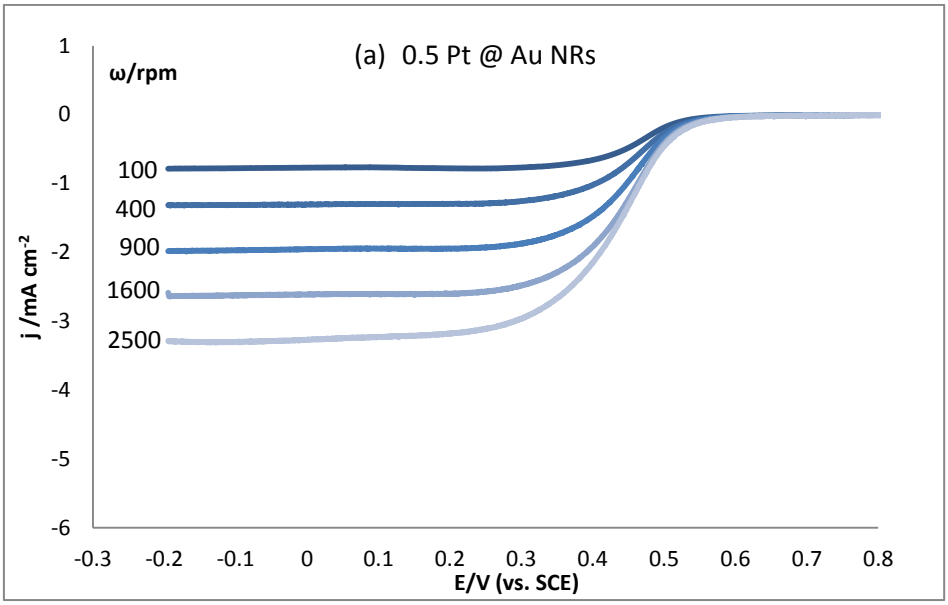
(a) 0.5 Pt @ Au NRs
ω/rpm
100
400
900
1600
2500
j /mA cm-2
E/V (vs. SCE)

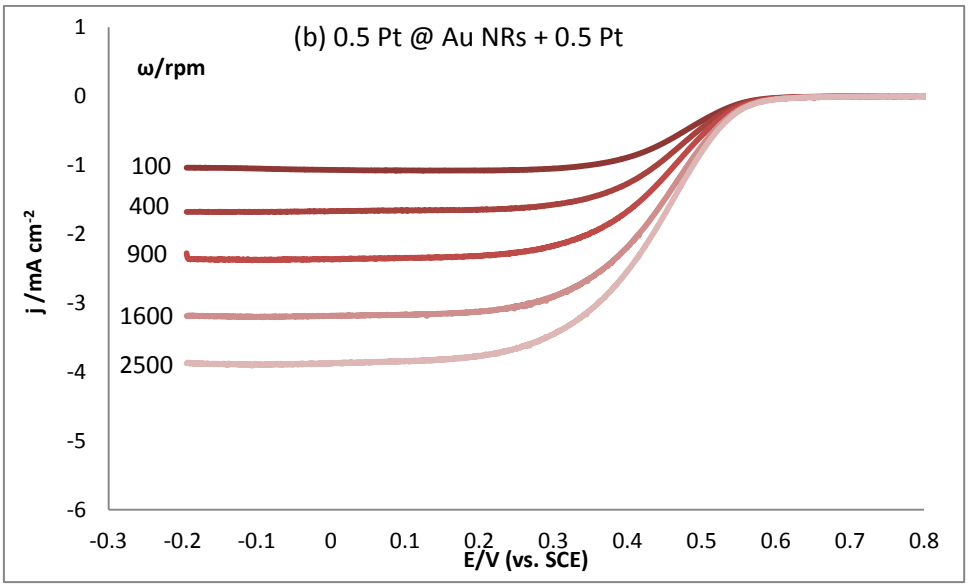
(b) 0.5 Pt @ Au NRs + 0.5 Pt
ω/rpm
100
400
900
1600
2500
j /mA cm-2
E/V (vs. SCE)

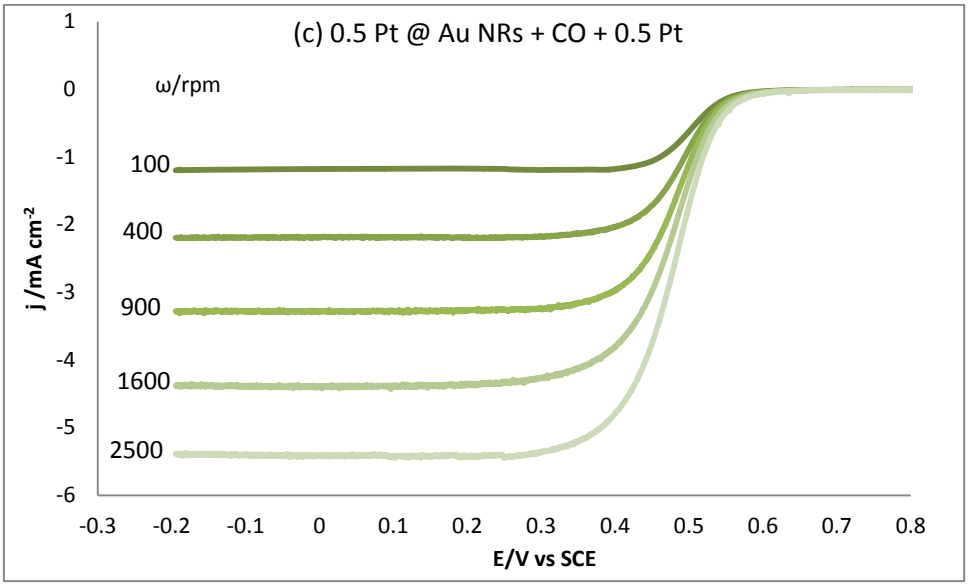

Figure 6.14 RDE voltammetry results for O_2 reduction on: (a) 0.5 Pt @ Au NRs, (b) 0.5 Pt @ Au NRs + 0.5 Pt, (c) 0.5 Pt @ Au NRs + CO + 0.5 Pt in O_2 saturated 0.05 M H_2SO_4 solution. Electrode rotation speeds of 100 rpm, 400 rpm, 900 rpm, 1600 rpm, and 2500 rpm are used. Sweep rate 2 mV s^{-1}.

The diffusion-limited current plateau is reached for all three of the nanorod surfaces because the kinetics is faster on the Pt than on Au. The polarisation curves are a similar shape to those recorded for polycrystalline Pt electrodes and Pt nanoparticle/C electrodes, also in O_2-saturated H_2SO_4 electrolytes.[42] According to the polarisation curves in Figure 6.14, the potential of the current onset caused by the reduction of oxygen for the Pt-coated Au NRs is at 0.645 V vs. SCE. The potential at which the current starts to increase is more positive for other Pt electrode surfaces. For polycrystalline Pt, it is 0.685 V (vs SCE);[42] for small Pt nanoparticles (1-10 nm in diameter) immobilised on a glassy carbon electrode, with a similar loading (mass of NPs) to that of the nanorod electrodes used in this work, it is 0.705 V (vs SCE).[43] The Pt/Au bimetallic nature of the Pt-coated Au NR surfaces could be a reason for the lower onset potential.

A direct comparison of the polarisation curves of the differential nanorod derivatized electrode surfaces at a rotation rate of 2500 rpm is provided in Figure 6.15.

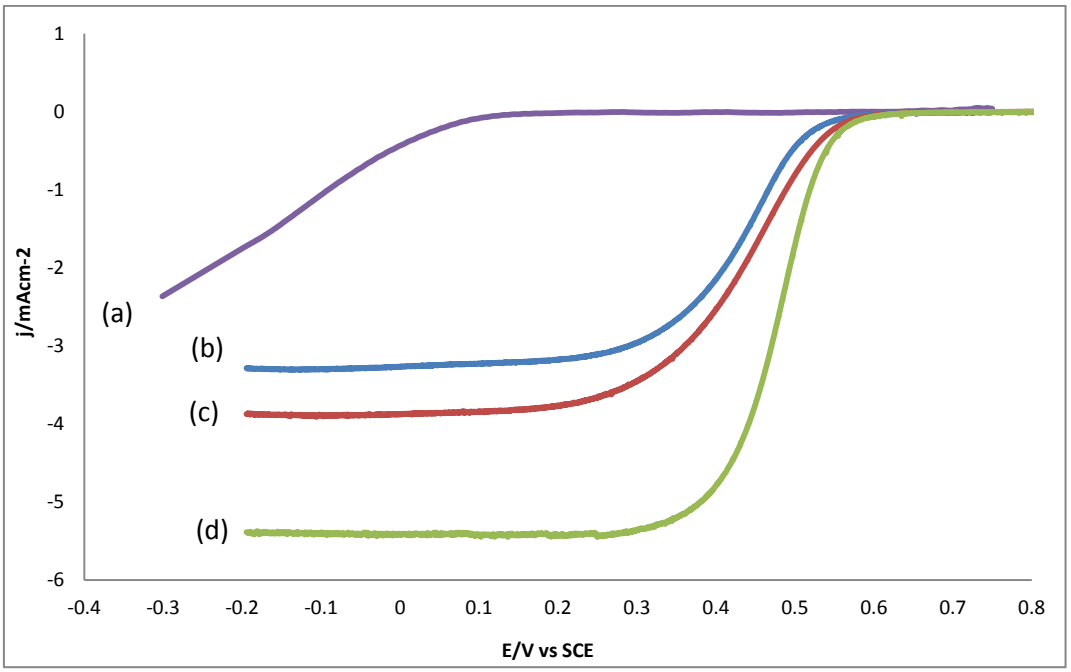

Figure 6.15 Comparison of polarisation curves produced by (a) Au NRs, (b) 0.5 Pt @ Au NRs, (c) 0.5 Pt @ Au NRs + 0.5 Pt, (d) 0.5 Pt @ Au NRs + CO + 0.5 Pt electrode surfaces when the RDE is rotated at 2500 rpm, in O_2 saturated 0.05 M H_2SO_4. Sweep rate 2 mVs^{-1}.

Figure 6.15 gives a clear comparison of the onset potentials of the current increase caused by the ORR on the Pt-coated Au NRs. The onset of the ORR current is at a more positive potential on 0.5 Pt @ Au NRs + 0.5 Pt and 0.5 Pt @ Au NRs + CO + 0.5 Pt than on 0.5 Pt @ Au NRs. This implies that O_2 forms a weaker interaction with the surface of 0.5 Pt @ Au NRs because there is a more negative potential for O_2 adsorption to occur. The weaker interaction of O_2 with the 0.5 Pt @ Au NR surface would be because this nanorod has a higher surface area of gold. The slow kinetics of the ORR on an Au surface compared with Pt is discussed in Section 1.12.

It should be noted that the onset of the oxygen reduction current on 0.5 Pt @ Au NRs + 0.5 Pt and 0.5 Pt @ Au NRs + CO + 0.5 Pt is at an almost identical potential. This may be because initially the adsorption energy of O_2 is similar on either surface. However, the shapes of both polarisation curves differ. The potential at which the current plateaus and thus forms a limiting current on 0.5 Pt @ Au NRs + 0.5 Pt is 0.17 V; however, on 0.5 Pt @ Au NRs + CO + 0.5 Pt, it is at a more positive potential of 0.27 V, reaching its limiting current density in a smaller potential range. This could indicate that the rate of electron transfer is faster on this surface.

The limiting current density of 0.5 Pt @ Au NRs + CO + 0.5 Pt of the ORR polarisation curve, when the electrode rotates at 2500 rpm, is 5.4 mA cm^{-2}. The polarisation curve of a glassy carbon electrode with Pt nanoparticles in the same electrolyte (0.05 M H_2SO_4) at the same rotation rate (2500 rpm) has a limiting current density of 5.5 mA cm^{-2}.[42] Under similar conditions, polycrystalline Pt has a higher limiting current density of the ORR polarisation curve of 7.5 mA cm^{-2}.[42]

The 0.5 Pt @ Au NRs + 0.5 Pt and 0.5 Pt @ Au NRs electrodes have polarisation curves when the electrode is rotated at 2500 rpm with limiting current densities of 3.9 mA cm^{-2} and 3.3 mA cm^{-2}, respectively. These limiting current densities are lower than those of 0.5 Pt @ Au NRs + CO + 0.5 Pt because the two nanorod surfaces have fewer Pt sites. Thus fewer O_2 molecules are reduced on Pt atoms while more O_2 molecules are reduced on Au atoms.

6.6.2 Koutecky-Levich analysis of the four nanorod surfaces

The polarisation curves of the four nanorod surfaces in Figure 6.15 are analysed using the Koutecky-Levich (K-L) equation:

$$\frac{1}{j} = \frac{1}{j_k} + \frac{1}{j_d} = -\frac{1}{nFkC_{O_2}^b} - \frac{1}{0.62nFD_{O_2}^{2/3}v^{-1/6}C_{O_2}^b\omega^{1/2}} \quad (1)$$

In this equation, j is the recorded current density, j_k is the kinetic current per geometric electrode surface area, j_d is the diffusion limited current, n is the average number of electrons transferred per molecule of O_2, k is the rate constant of oxygen reduction reduction, F is the Faraday constant (96, 485 C mol^{-1}), ω is the rotation rate of the RDE, $C_{O_2}^b$ is the concentration of oxygen in the bulk electrolyte solution (1.26×10^{-6} mol cm^{-3}),[44] D_{O_2} is the diffusion coefficient of oxygen (1.96×10^{-5} cm^2 s^{-1}) [44], and v is the kinematic viscosity of the solution (1.009×10^{-2} cm^2 s^{-1}).[45]

If $1/j$ is plotted against $1/\sqrt{\omega}$, the gradient of the resulting straight line of this plot allows the number of electrons transferred in the overall reduction of oxygen per O_2 molecule to be calculated, using the K-L equation (Equation (3)). The plots are referred to as Koutecky-Levich (K-L) plots. K-L plots of 0.5 Pt @ Au NRs, 0.5 Pt @ Au NRs + 0.5 Pt and 0.5 Pt @ Au NRs + CO + 0.5 Pt are given in Figure 30. The potential at which the K-L slopes are calculated in this Figure is -0.1 V. At this potential, the polarisation curves of the Pt-coated Au NRs reach a limiting current density. The dotted line above the K-L plots has the same

gradient as a K-L plot if n = 2, and the dotted line below the K-L has the same gradient as a K-L plot if *n* = 4.

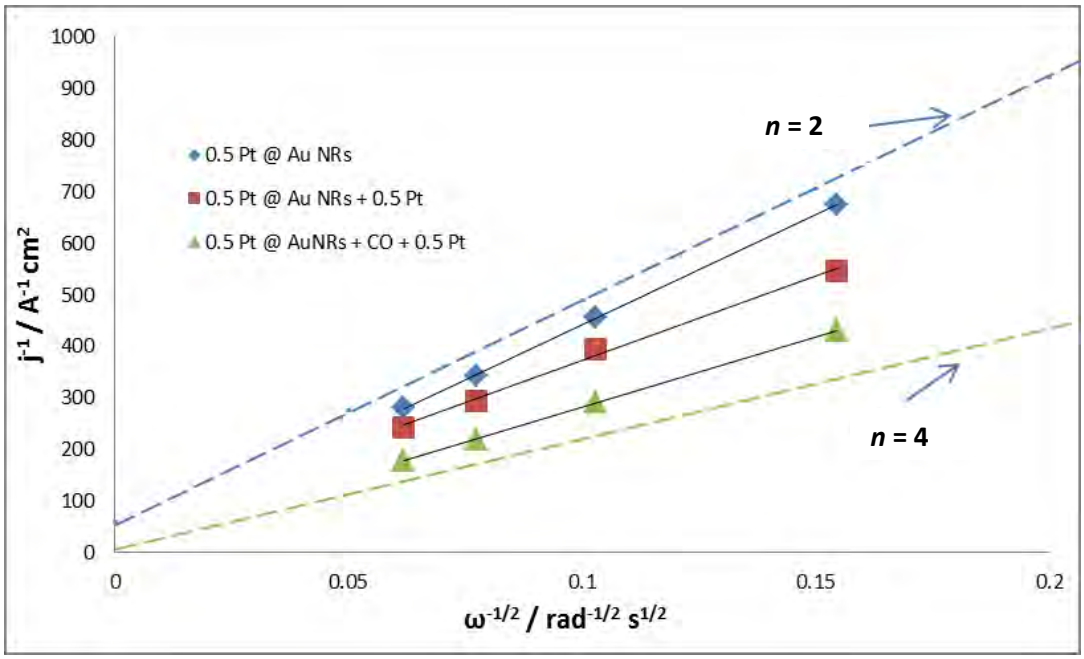

Figure 6.16. K-L plots for O_2 reduction of 0.5 Pt @ Au NRs (blue squares), 0.5 Pt @ Au NRs + 0.5 Pt (red squares) and 0.5 Pt @ Au NRs + CO + 0.5 Pt (green triangles). The plots are taken from the polarisation curves in Figure 28 when the potential is 0.1 V. At this potential, the polarisation curves of each of the three surfaces reaches a limiting current density. The dotted line above the K-L plots is a theoretical K-L plot if *n*=2; the green dotted line below the K-L plots is a theoretical K-L plot if *n*=4.

The gradients of the K-L slopes presented in Figure 6.16 are given in Table 6.6. The reciprocal of the gradients gives the number of electrons transferred per O_2 molecule on each of the nanorod surfaces. These values are given in column 3, Table 6.6. A K-L plot was taken for Au NRs at -0.3 (vs. SCE). At this potential, a maximum current is reached. The gradient of this K-L plot, and subsequently calculated values of *n* are also included in Table 6.6.

Table 6.6 K-L analysis of polarisation curves nanorods. The gradients of Tafel plots from polarisation curves of Au NRs when the potential is -0.3 V (vs SCE), and 0.5 Pt @ Au NRs, 0.5 Pt @ Au NRs + 0.5 Pt and 0.5 Pt @ Au NRs + CO + 0.5 Pt when the potential is 0.1 V are given in column 2. The numbers of electrons transferred per O_2 molecules, calculated from these values is given in column 3.

Nanorod	**K-L slope gradient**	**Number of electrons transferred per O_2 molecule**
Au NRs	6296	1.40
0.5 Pt @ Au NRs	4253	2.08
0.5 Pt @ Au NRs + 0.5 Pt	3291	2.69
0.5 Pt @ Au NRs + CO + 0.5 Pt	2689	3.29

According to the values in Table 6.6, for 0.5 Pt @ Au NRs and 0.5 Pt @ Au NRs + 0.5 Pt, the number of electrons transferred per O_2 molecule (n) is close to 2 at the limiting current, and for the 0.5 Pt @ Au NRs + CO + 0.5 Pt n is closer to 4 at the limiting current. For Au NRs, at the maximum current of the polarisation curves, $n < 2$.

A K-L plot was plotted for each surface, every 50 mV between 0.5 V and -0.3 V. From these plots, the number of electrons was calculated. Figure 6.17 gives a graph where *n* is plotted against potential for each of the four nanorod surfaces.

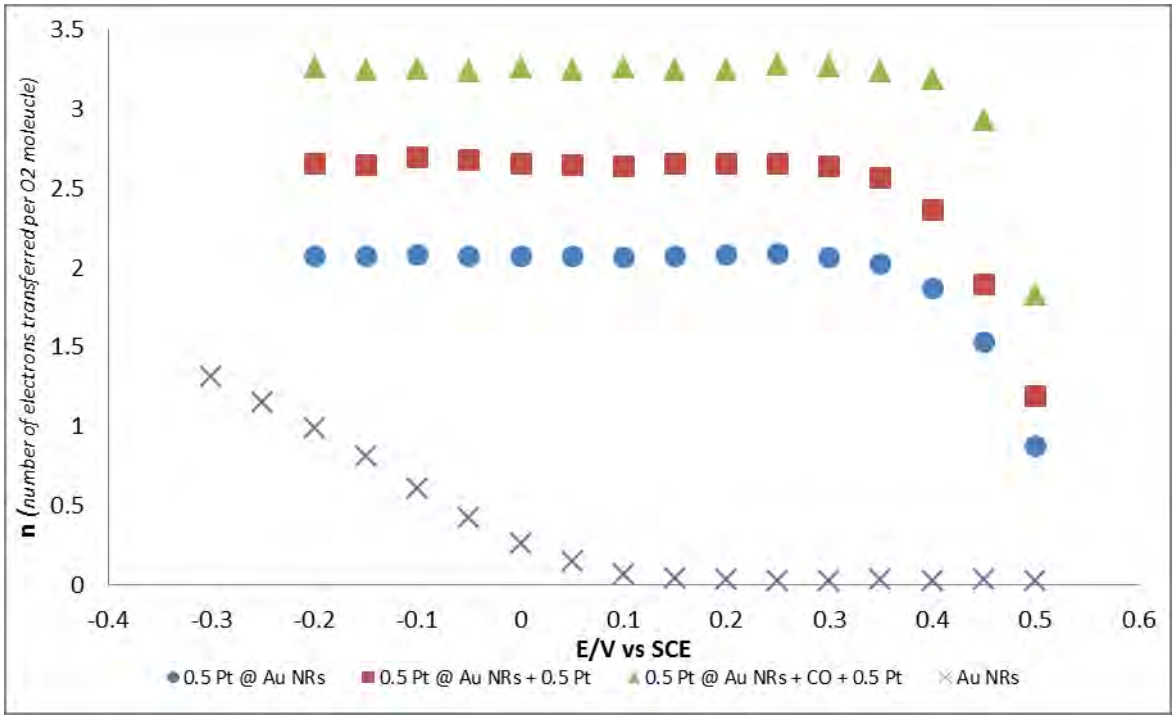

Figure 6.17 The number of electrons transferred per O_2 molecule during the ORR, calculated from K-L plots at given potentials, for Au NRs (crosses), 0.5 Pt @ Au NRs (blue circles), 0.5 Pt @ Au NRs + 0.5 Pt (red squares) and 0.5 Pt @ Au NRs + CO + 0.5 Pt (green triangles). Data for K-L plots are taken from same data that provided ORR polarisation curves in Figures 6.15 and 6.16.

The value of the number of electrons transferred during oxygen reduction on Au NRs at -0.3 V of 1.35 is lower than the number of electrons transferred per O_2 molecule on other Au surfaces. On pure Au (110) and Au (100) electrodes in the same electrolyte, the value of *n* was found to be 2.1 by Adzic et al.[41] However, on Au (111), they found that the value of *n* was 1.7. The low value of *n* for Au NRs could be due to some Au (111) sites on the AuNR surface. In previous literature, nanostructured Au electrodes were found to be more electro-catalytically active than bulk Au, although the origin of the effect remains unclear.[46 47] Values of $3 \geq n \geq 2$ have previously been reported for thin film Au nanoparticle-glassy carbon electrodes in acidic medium.[23 20] As with the reduction of oxygen on pure Au surfaces, the reduction of O_2 on gold nanoparticles involves the formation of H_2O_2 (via the $2e^-$ reduction),

although after -145 mV (vs. SCE), the H_2O_2 is said to be able to be reduced further to H_2O.[48] Some of the H_2O_2 produced on the Au NRs may also be further reduced to H_2O at potentials more negative than -0.145 V. In Figure 6.16, the polarisation curves of the ORR on Au NRs become less steep after -0.15 V, indicating a further reduction of H_2O_2 could also occur on this surface. The slight change in polarisation curve slopes can also be observed in the polarisation curves of electrodes containing smaller nanoparticles (5-20 nm in diameter) [23] and the change in gradient of the slope occurs at the same potential where surface peroxides are said to be further reduced to water. Perhaps, as with other Au nanostructures, the same 2 e^- and 4 e^- reductions of O_2 occur on Au NRs, although on fewer Au sites as other Au surfaces.

On 0.5 Pt @ Au NRs, an average of 2.08 electrons is transferred to an O_2 molecule adsorbed on the surface. On average, there are more electrons transferred per O_2 molecule because of the Pt present on the surface. On a clean Pt surface, O_2 is reduced to H_2O via a 4-electron mechanism.[49] On the 0.5 Pt @ Au NRs + 0.5 Pt electrode surface, there is a higher average number of electrons transferred per O_2 molecule of 2.66 because the Au surface area is lower on this electrode and the Pt area is higher. Hence, there are more O_2 molecules reduced with 4 electrons on this electrode surface than on 0.5 Pt @ Au NRs.

On the 0.5 Pt @ Au NR + CO + 0.5 Pt, the value of 3.25 indicates that there are more sites capable of reducing O_2 via the 4-electron mechanism than on the 0.5 Pt @ Au NR + 0.5 Pt sample. This is because the coverage of Pt on this nanorod surface is greater, and hence there are more adjacent Pt atoms leading to more O-O splitting.

6.6.3 Analysis of the Electrode Kinetics Using the Tafel Equation

Electrode kinetics can be obtained from the mass transport-corrected Tafel equation:[50]

$$\eta = \frac{2.303\ RT}{\alpha n_a F}\log j_o + \frac{-2.303\ RT}{\alpha n_a F}\log\left[\frac{j_d j}{j_d - j}\right] \quad (2)$$

Here, η is the overpotential ($E - E^O$), R is the gas constant, T is the absolute temperature, α is the transfer coefficient (or symmetry factor), n_a is the number of electrons transferred in the slowest step of the ORR, known as the rate determining step (RDS), and j_d is the diffusion-limited current density and $j_o$is the exchange current density. Values for $\log\left[\frac{j_d j}{j_d - j}\right]$ can be plotted against overpotential, η. This gives a mass transport-corrected Tafel plot. According to the Tafel equation, Equation (4), the slope of the plot would give information on the type of mechanism that occurs in the rate-determining step of the reduction of oxygen on the particular electrode surface. The intercept of the Tafel slope on the current axis gives the exchange current density. Exchange current density is an important kinetic parameter representing the electrochemical reaction rate at equilibrium. For the electrochemical reaction

$$O + ne^- \leftrightarrow R \quad (1)$$

both forward and backward reactions can occur. At equilibrium, the net current density of the reaction is zero. The current density of the forward reaction equals that of the backward reaction.[50 51] The current here is called the exchange current density. The magnitude of the exchange current density shows how rapidly the reduction of oxygen occurs. Unlike with the K-L analysis, where the current is related to the geometric area of the electrode, the

exchange current density is related to the real surface area of the electrode surface. As calculated in Section 4.8, the real surface area of all four nanorod surfaces is 0.59 cm^2. Since the geometric surface area of the electrode is 0.0706 cm^2, the roughness factor of the electrode is 8.34.

All the current densities used in Equation (2) are calculated relative to the real surface area of the working electrode, although it is also possible to use geometric areas initially and then correct the j_o values obtained by dividing by the roughness factor. Both methods give exactly the same Tafel slopes, α coefficients (transfer coefficients) and values of exchange current density.

Figure 6.18 gives mass transport-corrected Tafel plots of (a) Au NRs, (b) 0.5 Pt @ Au NRs, (c) 0.5 Pt @ Au NRs + 0.5 Pt and (d) 0.5 Pt @ Au NRs + CO + 0.5 Pt. For the x-axis values of $\log\left[\frac{j_d j}{j_d - j}\right]$, j is taken from the current density (in terms of real surface area) of the polarisation curves of each surface when the RDE is rotated at 1600 rpm. The value of j_d for each surface is calculated according to the K-L equation.

In order to obtain the overpotential values, η, for the y-axis, the thermodynamic electrode potential under standard conditions (E^0) for the 4 e^- reduction of O_2 on Pt in an O_2 saturated 0.05 M H_2SO_4 electrolyte is 0.93 V vs. SCE.

$O_2 + 4H^+ + 4e^- \rightarrow 2\ H_2O$ $\qquad E^0 = 0.93$ V $\qquad$ (2)

This value of E^0 is subtracted from all the applied potential values (vs. SCE) of the Pt-coated nanorods to give η. The Tafel plots of the Pt-coated Au NRs in Figures 6.18(b), (c) and (d),

and the resulting values of the exchange current density are calculated in terms of this overpotential.

Gold primarily catalyses oxygen reduction to peroxide via the two-electron mechanism. The E^0 of this reaction in an O_2 saturated 0.05 M H_2SO_4 electrolyte is 0.4 V (vs. SCE).

$$O_2 + 2H^+ + 2e^- \rightarrow H_2O_2 \qquad E^0 = 0.4\ V \qquad (3)$$

The Tafel slope for Au NRs in Figure 6.18 is plotted with the overpotential according to the standard electrode potential of reaction (3).

Table 6.6 gives the values of the Tafel slopes and the exchange current densities calculated from the current axis intercepts of the Tafel slopes. On the Au NR surface, one Tafel slope is obtained. For the Tafel plots of the Pt-coated nanorods, there are two slopes. The first is from the low current density (lcd) region; the second, from the high current density (hcd) region of the polarisation curves.

In Table 6.6, the Tafel slope and the exchange current density of Pt nanoparticles, which are ca. 3 nm in diameter on a glassy carbon electrode, are included. These values are taken from Stassi et al.[62]

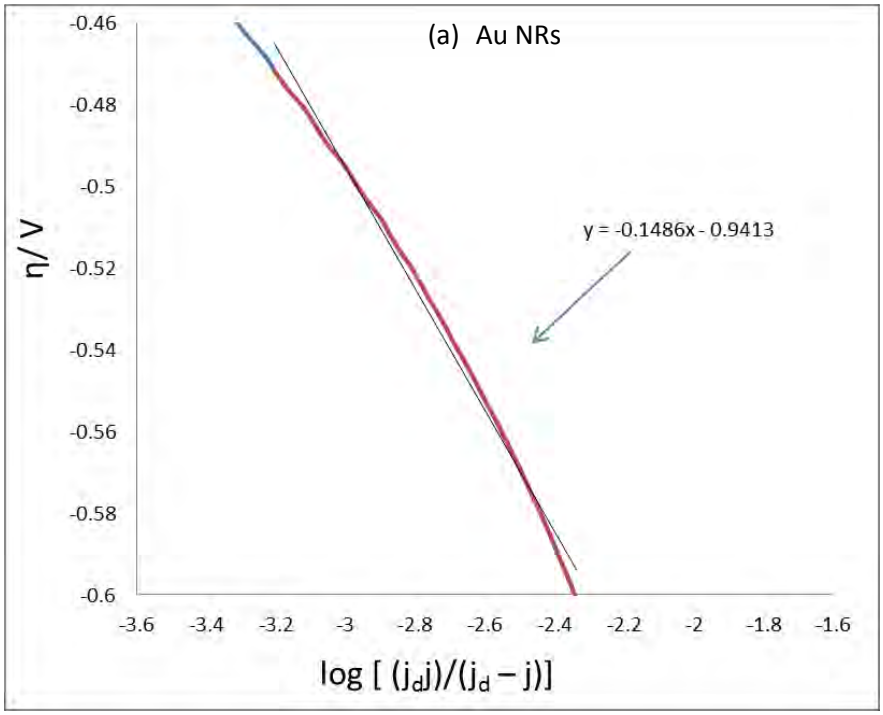
(a) Au NRs
y = -0.1486x - 0.9413
η/ V
log [(jdj)/(jd – j)]
-0.46
-0.48
-0.5
-0.52
-0.54
-0.56
-0.58
-0.6
-3.6
-3.4
-3.2
-3
-2.8
-2.6
-2.4
-2.2
-2
-1.8
-1.6

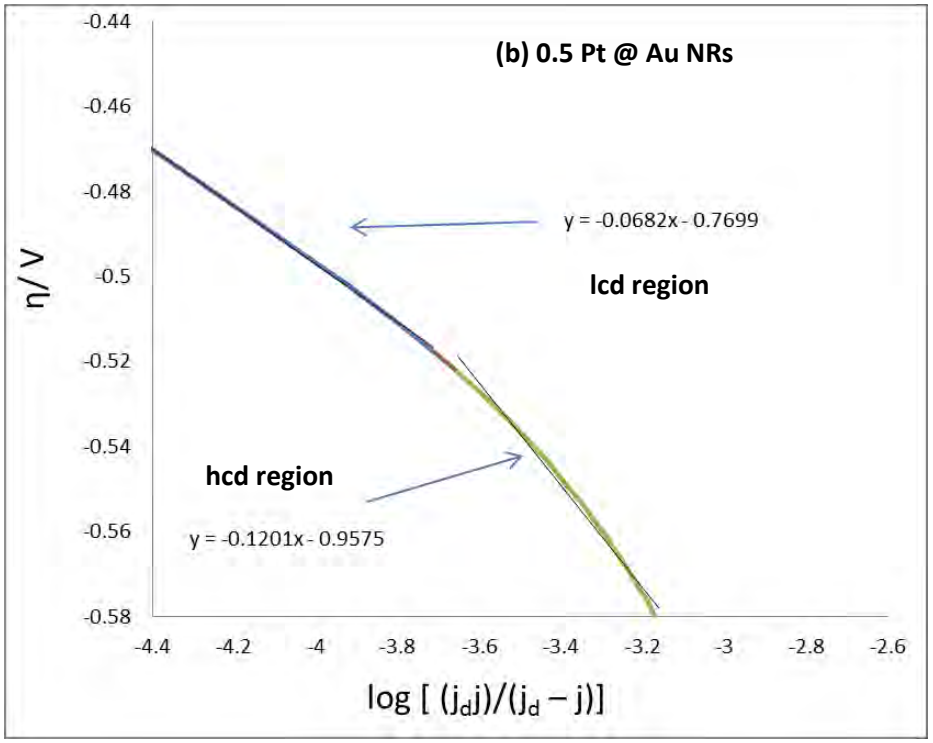
(b) 0.5 Pt @ Au NRs
y = -0.0682x - 0.7699
lcd region
hcd region
y = -0.1201x - 0.9575
η/ V
log [(jdj)/(jd – j)]
-0.44
-0.46
-0.48
-0.5
-0.52
-0.54
-0.56
-0.58
-4.4
-4.2
-4
-3.8
-3.6
-3.4
-3.2
-3
-2.8
-2.6

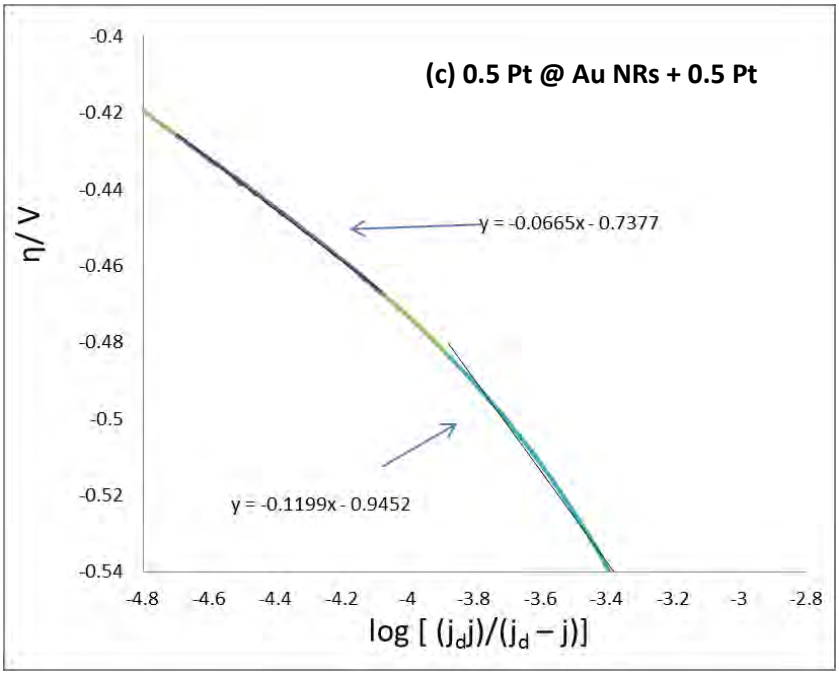

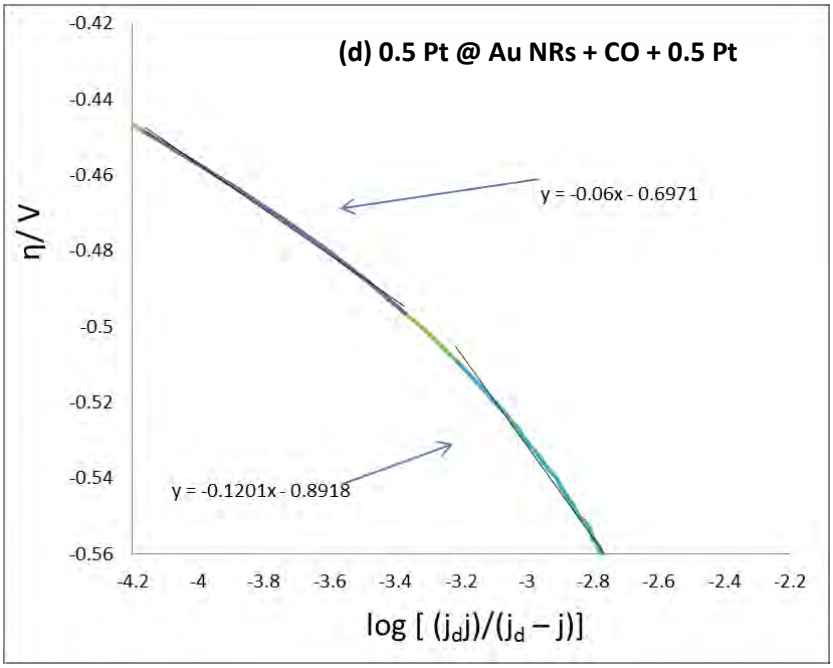

Figure 6.18 Mass-transport corrected Tafel plots for (a) Au NRs (a) 0.5 Pt @ Au NRs, (b) 0.5 Pt @ Au NRs + 0.5 Pt and (c) 0.5 Pt @ Au NRs + CO + 0.5 Pt. Equations for all the lines are included. The Tafel slope in Figure (a) for Au NRs gives one line and the Tafel slope for Pt-coated NRs in Figures (b), (c) and (d) gives 2 lines: one in the low current density (lcd) region, the other in the high current density (hcd) region. The polarisation curves in Figure 29 are used; the current used is in terms of real surface area of the nanorods on the electrode surface.

Table 6.6 Kinetic parameters: Tafel slope and exchange current density Au NRs in the first row, where $\mathbf{j_o}$ is the exchange current density for the 2 e^- reduction of oxygen to peroxide.

Rows 2-4 give the kinetic parameters of 0.5 Pt @ Au NRs, 0.5 Pt @ Au NRs +0.5 Pt and 0.5 Pt @ Au NRs + CO + 0.5 Pt. The Tafel slopes and the exchange current densities are given for the low current density (lcd) and high current density (hcd) regions. The kinetic parameters in Table 8 are calculated from the Tafel plots in Figure 32.

Row 5 gives Tafel slope and exchange current density values in the (hcd) region of Pt nanoparticles which are ca. 3 nm in diameter supported on a glassy carbon electrode. These values are taken from Stassi et al. [66].

Nanorods	Slope/ mV	j_o (2 e^- reduction)/Acm^{-2}		
Au NRs	-149	4.62×10^{-7}		
	Slope (lcd)/mV	j_o (lcd)/Acm^{-2}	Slope (hcd)/mV	j_o(hcd)/Acm^{-2}
0.5 Pt@AuNRs	-68	5.14×10^{-12}	-120	1.04×10^{-8}
0.5 Pt @ Au NRs + 0.5 Pt	-67	8.07×10^{-12}	-120	1.33×10^{-8}
0.5 Pt @ Au NRs + CO + 0.5 Pt	*-60*	2.41×10^{-12}	-120	3.70×10^{-8}
Pt nanoparticles from literature			*-120*	*1.66×10^{-8}**

*values taken from Stassi et al. [66]

For bulk Au (110) and Au (111) surfaces, Tafel slope values of around -120 mV dec^{-1} have previously been found.[41] The Tafel slope value indicates that the transfer of the first electron from the gold surface to the oxygen is the rate-determining step if $\alpha = 0.5$. The Tafel slope produced by the Au NR surface, Figure 32, has a higher value of -149 mV $decade^{-1}$. Higher Tafel slope values than -120 mV dec^{-1} have also been obtained previously from other gold electrode surfaces. The Tafel slope from an Au (111) electrode is -175 mV dec^{-1},[41] and electrodes containing Au NPs with are ca. 15 nm in diameter have given Tafel slopes of around -160 mV dec^{-1}.[20] Tafel slopes higher than -120 mV dec^{-1} have been explained by a potential distribution at the interface affected by the accumulation of peroxide.[52] This could arise from a higher degree of sulphate adsorption on Au (111). The high Tafel slope value for the Au NRs could be further evidence that there are some Au (111) sites on the Au NR surface. Another possible cause for the higher Tafel slope value for the Au NRs is the two-barrier model caused by an oxide layer.[53] In the potential region where oxygen reduction occurs on the Au NR electrode surface (0.15 to -0.3 V vs. SCE), there is no Au oxide layer. However, the kinetics of the ORR are slow on Au in acidic conditions.

For the three Pt-coated nanorod surfaces, there are two well-defined linear Tafel regions. One corresponds to the region in the polarisation curves where the potential is greater than 0.5 V (vs. SCE), known as the low current density (lcd) region; the other, to the region in the polarisation curves where the potential is less than 0.5 V (vs. SCE), known as the high current density (hcd) region. These two regions have also been observed for Pt surfaces in acidic electrolytes,[43] and for electrodes with a Pt|Nafion® interface.[54] [55]There are two regions because the electrode potential plays an important role in changing the Pt surface structure in the presence of O_2. For the nanorods at higher potentials (>0.5 V vs. SCE), the electrode

surface is a mixture of Pt and PtO (Pt with surface oxides). Thus the kinetics of the O_2 reduction on Pt changes in different potential regions.

In the lcd region, (Temkin conditions where there is high coverage of adsorbed oxide-containing species), the slope for the Tafel plot (-2.303 RT/αnF) should be -60 mV decade^{-1} for a Pt surface.[56] The Pt surface oxide is said to inhibit the adsorption of O_2 and the reaction intermediates.[57] According to density functional theory (DFT) calculations based on electronic structure, the mechanism of oxygen reduction is different in the low current density region from the high current density region.[58] In the low current density region, O_2 is said to dissociate before electrons are transferred from the electrode surface to the oxygen molecule. This mechanism is similar to the direct 4e$^-$ mechanism, and is known as the dissociative mechanism. Through this mechanism, the O_2 would dissociate less readily, so the rate of this reaction would be slower than it is for the ORR on a clean Pt surface. At the hcd region, when the coverage of oxygen-containing species is low, (Langmuirian conditions), a slope of -120 mV/decade should be observed for Pt.[59] The rate-determining step for the reduction of oxygen in the low and high current density regions is the transfer of the first electron to oxygen.[60] Thus the slope for the Tafel plots (-2.303 RT/αnF) in both current density regions would have a value of n=1. The difference between the slopes in both regions would therefore be the symmetry value, α, which is 1 and 0.5 for the high-low density region and low and high-current density regions, respectively.

In the lcd region, the 0.5 Pt @ Au NRs + CO + 0.5 Pt surface gives a Tafel slope of -60 mV dec^{-1}, which is the same slope as with all the other Pt surfaces. This shows that there is a similar extent of Pt-oxide coverage on this surface as for pure Pt surfaces. However, in Table

9, the surfaces of 0.5 Pt @ Au NRs + 0.5 Pt and 0.5 Pt @ Au NRs have higher Tafel slope values than 0.5 Pt @ Au NRs + CO + 0.5 Pt. These higher values could indicate that there is less Pt-oxide layer on the two surfaces because the two surfaces have a higher surface area of exposed gold. According to the CVs in Figure 22, the Au oxide reduction gives rise to a peak between 0.9 and 0.7 V and the peak arising from Pt oxide reduction is at a more negative potential between 0.5 and 0.1 V. Consequently, in the potential range of the lcd region (0.6-0.5 V), there would be less surface oxide on the 0.5 Pt @ Au NRs and 0.5 Pt @ Au NRs + 0.5 Pt surfaces than on a 0.5 Pt @ Au NRs + CO + 05 Pt (which has a higher coverage of Pt).

The values for the exchange current densities of the three Pt-coated nanorod surfaces, Table 9, show that the Pt oxide layer inhibits the reduction of oxygen on 0.5 Pt @ Au NRs + CO + 0.5 Pt more than on the other two Pt-coated nanorod surfaces. In the lcd region, the 0.5 Pt @ Au NR and 0.5 Pt @ Au NRs + 0.5 Pt surfaces have exchange current densities over twice higher than the corresponding exchange current density value of 0.5 Pt @ Au NRs + CO + 0.5 Pt. These values could be consistent with the previously mentioned DFT calculations by Nørskov et al;[58] where it was found that Pt oxide coverage causes a change in the mechanism of oxygen reduction. More O_2 molecules being reduced via the kinetically slower dissociation mechanism on the 0.5 Pt @ Au NRs + CO + 0.5 Pt could be a reason that the exchange current density for this surface in the lcd region is significantly slower than in the same region of the other two surfaces.

All three Pt-coated nanorod surfaces give the expected Tafel slope of -120 mV decade^{-1} in the surface oxide-free hcd region. The activity of the nanorod surfaces is measured by the

exchange current density found from the hcd region. According to the values given in Table 9, the 0.5 Pt @ Au NRs and 0.5 Pt @ Au NRs + 0.5 Pt have similar exchange current density values, which are slightly lower than those of a glassy carbon electrode containing Pt nanoparticles of ca. 3 nm in diameter.[62] The slightly lower exchange current density values for the Pt-coated Au NRs is probably a combination of a lower surface area of Pt and the exposed Au surface on these nanorods.

Table 6.6 shows that the surface of 0.5 Pt @ Au NRs + CO + 0.5 Pt has an exchange current density in the hcd region nearly three times higher than that of the 0.5 Pt@ Au NR + 0.5 Pt surface, even though, according to the charges of the H_{UPD}, Au oxide reduction and CO oxidation peaks on both surfaces (Section 4.8), there is only a 20 % greater Pt coverage on 0.5 Pt @ Au NRs + CO + 0.5 Pt than on 0.5 Pt @ Au NRs + 0.5 Pt. Moreover, the exchange current density of 0.5 Pt @ Au NRs + CO + 0.5 Pt is twice higher than that of Pt nanoparticles, which are ca. 3 nm in diameter [62]. The high value for the exchange current density of the 0.5 Pt @ Au NRs + CO + 0.5 Pt surface in the hcd region indicates that the increased surface area of Pt is not the only reason why the 0.5 Pt @ Au NRs + CO + 0.5 Pt surface has a high ORR activity. The closer proximity of the Pt nanodots to each other on the 0.5 Pt @ Au NRs + CO + 0.5 Pt could also be a factor. Jiang et al. found that as the particle-particle distance of Pt nanoparticles on an electrode decreases, there is more structured diffusion of the adsorbed reagent species, increasing the electrocatalytic activity of the particles.[61]

The morphology and electronic structure of Pt nanodots on this surface need also to be considered. There could be a small alloying effect of the small Pt nanodots on the Au NR surface, similar to that found on other Pt- M alloy systems.[62] The slight alloying effects on

the Pt nano dots could change their electronic structure, allowing for an increase in Pt d-band vacancies. This increase would produce a stronger Pt-O_2 interaction, which would in turn cause better weakening of the O-O bond. The epitaxial growth of the Pt nanodots on the Au NR surface could also cause a geometric effect with a slight lattice expansion, leading to a more favourable Pt-Pt distance for the dissociative adsorption of O_2.

6.7 Summary and Conclusions

The Au NRs used in this work were synthesised using $AgNO_3$. $AgNO_3$ was used because it enhances the monodispersity of the Au NRs in the solution. However, when $AgNO_3$-synthesised AuNRs are coated with Pt, the Pt deposits on the Au surface as nanodots on the endcaps. When solutions of Pt-coated Au NRs were saturated with CO before a second coating of Pt was applied, STEM images showed a more even distribution of Pt all over the Au NR. Electrochemical measurements showed that Pt-coated Au NRs prepared using CO-blocking techniques also more effectively oxidise CO and have higher activity towards the oxygen reduction reaction. A more detailed summary is given in section 7.1.

[1] Nikoobakht, B. and El-Sayed, M.A. *Chem Mater* (2003), 15, p. 1957.
[2] Murphy, C.J., Sau, T.K., Gole, A.M., Orendrorff, C.J., Gao, J.X., Gou L. and Hunyadi, S.E. (2005), *J Phys Chem*, 109, p. 13857.
[3] Sau T.K. and Murphy, C.J (2004). *Langmuir*, 20, p. 6414.
[4] Gans, R. *Ann Phys* (1915), 47, p. 270.
[5] Jiang, X.C., Brioude, A. and Pileni, M.P. (2006), *Colloids and Surfaces A: Physicochem Eng Aspects*, 277 p. 201.
[6] Yu, Y., Hu, Y., Liu, X., Deng, W. and Wang X. (2009), *Electrochimica Acta*, 54, p. 3092.
[7] Brewer, L. (1977), *Lawrence Berkeley Laboratory Report*, N° LB-3720 (unpublished),.
[8] Delley, B., Ellis, D.E. and Freeman J. (1983), *Phys Rev* B27, p. 2132.
[9] Tyson, W.R. and Miller, W.A. (1977), *Surf Sci*, 62, p. 267.
[10] Vitos, L., Ruban, A.V., Skriver, H.L. and Kollar, J. (1998), *Surface Science*, 411 p. 186.
[11] Grzelczak, M., Pérez-Juste, J., Rodriguez-Gonzalez, B. and Liz-Marzán, L.M. (2006), *J Mater Chem*, 16, p. 3946.
[12] Song, H., Kim, F., Kim, D. and Yang, P.D. (2005), *Chem Eur J*, 11, p. 910.
[13] He, W., Wu, X., Liu, J., Zhang, K., Chu, W., Feng, L., Hu, X., Zhou, W. and Xie, S. (2009), *J Phys Chem C*, 113, p. 105005.
[14] Orendorff, J. and Murphy, C.J. (2006), *J Phys Chem* B, 110, p. 3990.
[15] Huang, X., Neretina, S. El-Sayed, M.A. (2009), *Adv Mater,* 21, p. 4880.
[16] He, D.S., Han, Y., Fennell, J., Horswell S.L and Li, Z.Y. (2012), *Appl Pys Lett*, 101, p. 113102.
[17] Wang, F., Liu, P. and Zhang, D. (2011), *J Mol Model* 17, p. 1069.
[18] Strmcnik, D.S., Tripkovic, D.V., van der Vliet, D., Chang, K.C., Komanicky, V., You, H., Karapetrov, G., Greeley, J.P., Stamenkovic, V.R. and Markovic, N.M. *J Am Chem Soc*, (2008), 130, p. 46.

[19] Radnik, J., Mohr, C. and Claus, C.P. (2003), *Phys Chem,* 5, p. 172.
[20] Erikson, H., Jürman, G., Sarapuu, A., Potter, R.J. and Tammeveski, K. (2009), *Electrochimica Acta*, 54, p. 7483.
[21] Alexeyeva, N. and Tammeveski, K. (2007), *Electrochem S Lett*, 10, F18.
[22] Angerstein-Kozlowska, H., Conway, B.E., Hamelin, A. and Stoicoviciu, A. (1986) *Electrochimica Acta*, 31, p. 1051.
[23] Jirkovsky, J.S., Halasa, M. and Schiffrin, (2010), D.J. *Phys Chem Chem Phys*, 12, p. 8042.
[24] Bayati, M., Abad, J.M., Bridges, C.A., Rosseinsky M.J. and Schiffrin, D.J. (2008), *J Electroanal Chem*, 19, p. 623.
[25] Schmidt, T.J., Gasteiger, H.A., Stüb, G.D., Urban, P.M., Kolb D.M. and Behm, R.J. (1998), *J Electrochem Soc*, 145, p. 2355.
[26] Will, F. (1965), *J Electrochem Soc*, 112, p. 451.
[27] Markovic N.M., Marinkovic, N.S. and Adzic, R.R. (1991), *J Electroanal Chem*, 314, p. 289.
[28] Markovic, N., Grugur, B. and Ross, P. (1997), *J Phys Chem B*, 101, p. 5405.
[29] Lopez-Cudero, A., Cuesta, A. and Gutierrez, C. (2003), *J Electrochem*, 548, p. 109.
[30] Clavilier, J., Rodes, A., El Achi, K. and Zamakhchari, M.A. (1991), *J Chim Phys*, 88, p. 1291.
[31] Orts, J.M., Fernandez-Vega, A., Feliu, J.M., Aldaz, A. and Chavilier, J. (1992), *J Electroanal Chem*, 327, p. 261.
[32] Gasteiger, H.A., Markovic, N., Ross Jr, P.N. and Cairns, E.J. (1994), *J Phys Chem*, 98, p. 617.
[33] Weaver, M.J., Chang, S.-C., H., L.-W., Leung, Jiang, X., Rubel, M., Szklarczyk, M., Zurawski, D. and Wieckowski, A. (1992), *J Electroanal Chem*, 327, p. 247.
[34] McGrath, P., Fojas, A.M., Reimer, J.A. and Cairns E.J. (2009), *Chemical Engineering Science*, 64, p. 4765.
[35] Lebedeva, N.P., Rodes, A., Feliu, J. M., Koper, M.T.M. and van Santen, R.A. (2002), *J Phys Chem*, B106, p. 9863.
[36] Xu, J. and Jates, J.T. (1993), *J Chim Phys*, *99*, p. 725.
[37] Rush, B.M., Reimer, J.A. and Cairns, E.J. (2001), *J Eletrochem Soc*, 148 (2), A137-A148.
[38] Villegas, I., and Weaver, M.J. (1994), *J Chem Phys*, 101, p. 1648.
[39] Chang, S.C. and Weaver, M.J. (1990), *J Phys Chem*, 94, p. 5095.
[40] Zhou, S., Gomes, R. and Weaver, M.J. (1998), *Surf Sci*, 399, p. 270.
[41] Adzic, R.R., Strbac, S. and Anastasijevic, N. (1989), *Materials Chemistry and Physics*, 22, p. 349.
[42] Higuchi, E., Adachi, K., Nohara, S. and Inoue, H. (2009), *Res Chem Intermed*, 35, p. 985.
[43] Maillard, F., Martin, M., Gloaguen, F. and Leger, J.-M. (2002), *Electrochim Acta*, 47, p. 3431.
[44] Markovic, N.M., Gasteiger, H.A. and Ross, P.N. (1995), *J Phys Chem*, 99 p. 3411.
[45] Gottesfeld, S., Raistrick, I.D. and Srinivasan, S. (1987), *J Electrochem Soc* 134, 1455.
[46] Gao, F.F., El Deab, M.S., Okajima, T. and Ohsaka, T. (2005), *J Electrochem Soc*, 152A, p. 1226.
[47] Zhang, Y., Suryanarayanan, V., Nakazawa, I., Yoshihara, S. and Shirakashi, T. (2004), *Electrochim Acta*, 49, p. 5235.
[48] El-Deab, M.S. and Ohsaka, T. (2002), *Electrochim Acta*, p. 474255.
[49] Liang, C.C. and Julliard, A.L. (1967), *Nature*, p. 629.
[50] Bard, A.J. and Faulkner, L.R. (1980), *Electrochemical Methods: Fundamentals and Applications*, New York: Wiley.
[51] Song, C. and Zhang, J. (2008), 'Electrocatalytic Oxygen Reduction Reaction' in *PEM Fuel Cell Electrocatalysts and Catalyst Layer: Fundamentals and Applications*, New York: Springer.
[52] Yeager, E. (1984), *J Electrochem Soc*, 128, p. 160 C.
[53] Meyer, R.E. (1960), *J Electrochem Soc*, 106, p.847.
[54] K. Kinoshita, (1992), *Electrochemical Oxygen Technology*, New York: Wiley.
[55] Beattie, P.D., Basura, V.I. and Holdcroft, S. (1999), *J Electroanal Chem*, 468, p. 180.
[56] Damjanovic, A. and Brusic, V. (1967), *Electrochim Acta*, 12, p. 615.

[57] Adzic, R. in: Lipkowski, J. and Ross, P.N. (eds.), (1998), *Electrocatalysis*, New York: Wiley-VCH, (Ch. 5),.
[58] Nørskov J.K., Rossmeisl J., Logadottir A., Lindqvist L., Kitchin J.R., and Bligaard T. (2004), *J Phys Chem*, B108, p. 17886.
[59] Damjanovic, A. and Genshaw, M.A. (1970), *Electrochim Acta*, 15, p. 1281.
[60] Sepa, D.B., Vojnovic, M.J., Vracar, L.M. and Damjanovic, A. (1984), *Electrochim Acta*, 29, p. 1169.
[61] Jiang, J. and Yi, B. (2005), *J Electroanal Chem*, 577, p. 107.
[62] Stassi A., D'Urso C., Baglio V., Di Blasi A., Antonucci, V. and Arico, A.S. (2006), *J Appl Electrochem*, 36, p. 1143.

7. Summary, Conclusions and Future Work

7.1 Summary and Conclusions

This work provides a better understanding of the adsorption of the cationic surfactants CTAF, CTAC, CTAB and BDAC on Au (111), and Au (100). Therefore role surfactants play in the synthesis of Au NRs can now be better understood.

According to the electrochemical results in Chapters 4 and 5, it is questionable whether CTAB forms a more densely packed bilayer structure on the Au (100) surface than on that of Au (111). However, the results indicate that the interactions of the Br^--CTA^+ layer are probably stronger on the Au (100) surface. As discussed in Section 1.5.2, Br^- ions do not adsorb onto the stable four-fold hollow sites found on the Au (100) surface, because this structure does not minimise the unfavourable halide-halide interactions (adsorbate-adsorbate interactions dominate over adsorbate-surbstrate interactions). If, however, CTA^+ is adsorbed onto the Br^- adlayer, the unfavourable halide-halide interactions can be reduced. As a result, the Br^- ions (with CTA^+ molecules bonded on top of them) may be able to adsorb onto these energetically favourable four-fold hollow sites. This principle explains perhaps why Au seeds grow into nanorod particles when CTAB is present in the solution. Au nanorods (synthesised without $AgNO_3$ in the growth solution) have Au (111) end-caps and Au (100) side faces (Figure 1.16). During Au NR synthesis, the strongly bonded CTAB on the Au (100) facet of the Au seed is therefore harder to displace than the CTAB bonded on the Au (111) facet. It is therefore likely that there will be more successful collisions between the

CTA^+AuCl_2 and the Au (111) facet than with the Au (100) facet. This leads to unidirectional growth and hence the formation of rod-shaped nanoparticles.

If CTAF were used as a surfactant instead of CTAB in nanorod synthesis, collisions would readily occur on all facets of the seed because the van der Waals-substrate interactions are considerably weaker than Br^--substrate interactions. There would therefore be no confinement of seed growth, and the resulting nanoparticles would probably be large non-mono-disperse nanocubes and nanospheres. If CTAC were to be used as a growth-directing agent in nanorod synthesis, unidirectional growth of the seed particles would be unlikely: Cl^- ions seem to displace the alkyl tail groups from the surface less easily than Br^- and as a result the resulting CTA^+-halide layer structure interacts more weakly with the particle's surface. The CTAC bilayer structure is therefore more permeable than the CTAB layer to CTA^+-$AuCl_2$ collisions on all facets of the seed particles. When previously, instead of CTAB, CTAC was used for the seed-mediated growth method to synthesise Au NRs, STEM images showed that only spherically shaped particles are produced. [1]

Electrochemical studies of Au substrates in solutions containing BDAC show that the benzyl group found in the head group of BDAC molecules has a strong, stable interaction with the Au surface. One of the main conclusions to be drawn from comparing the adsorptive behaviours of Au (100) with Au (111) is that the benzyl group probably interacts more strongly with the Au (100) surface than with that of Au (111): the Au (100) surface lattice has four-fold hollow adsorption sites for the benzyl group, rather than the three-fold sites found on Au (111). Owing to this interaction, the adsorption of BDAC on Au is probably an even more surface-specific process than the adsorption of CTAC on Au. When Au NRs

were previously synthesised in a solution containing CTAB and BDAC, longer, narrower and more monodisperse (higher-yield) Au NR particles were produced.[2] Interestingly, however, when only BDAC was used to synthesise Au NRs, rod-shaped particles are not produced.[1] It is unclear why BDAC mixed with CTAB increases the monodispersity and aspect ratio of the synthesised nanorods, and no universally agreed explanation has hitherto been proposed. Perhaps BDA^+ combines with the Br^- counter-ions of the CTAB molecules to form a densely packed adlayer structure, especially on the Au (100) facets of the seed. Alternatively, the presence of the CTA^+ molecules might bring about a rod-shaped micelle, thus helping direct rod-shaped growth. Further experiments are needed to investigate this.

One of the main findings of this work in Chapter 6 is that, according to atomic resolution STEM images, Pt nanodots grow epitaxially on the Au NR surface. The nanodots have the same crystallographic orientation as the underlying Au substrate.

The proposed CO-blocking method, whereby solutions of Pt-coated Au NRs are saturated in CO before a second coating of Pt was applied, was found not only to increase the coverage of Pt nanodots on the Au nanorod surface but also to improve the stability of the nanorod particles, which are thus made more suitable as electrocatalysts. Electrochemical measurements of electrode surfaces containing immobilised nanorods showed that when CO blocking is used the Pt nanodots of the nanorods have enhanced electrocatalytic activity.

Firstly, CO-blocked nanorods (after being immobilised on a supported glassy carbon electrode) more effectively electro-oxidise CO than nanorods on which the CO blocking is not used. CO tolerance is enhanced because the Pt nanodots seem to be energetically similar to CO-tolerant step- and terrace-rich Pt (110). Moreover, because of the narrowness

of the CO oxidation peak of the CO-blocked nanoparticle surface there are few CO bridge-bonding sites. As a result, the product of the CO oxidation process (CO_2) desorbs from the surface faster.

The CO-blocked nanorods also have enhanced activity for the oxygen reduction reaction. As the small size of the epitaxially grown Pt nanodots could mean that there is lattice strain of the Pt, or that Pt-Au alloying is possible, the Pt d-band vacancies would increase. In addition, the close proximity of the Pt nanodots to each other could enhance diffusion of the adsorbed O_2.

7.2 Future Work

Currently, polarisation modulation infrared reflective adsorption spectroscopy (PM-IRRAS) studies are being carried out on CTAB and CTAC on Au (111). The results have hitherto shown that both CTAB and CTAB molecules change their orientation on the Au (111) surface as the potential becomes more positive, with a greater change observed for CTAB. These experiments need to be repeated in order to obtain consistency. PM-IRRAS will also be carried out on Au (111) in CTAF solution. The data from these experiments will act as a corroboration of the conclusions drawn from the electrochemical measurements of Section 4. The effect of the Cl^- and Br^- counter-ions on the adsorption of CTAC and CTAB on Au (111) could be more clearly seen if electrochemical measurements are carried out with variable concentrations of CTAF molecules in a solution containing an excess of NaCl and NaBr.

In Section 5, potential-induced reconstruction prevented chronocoulometry measurements on the unreconstructed Au (100)-(1 × 1) surface. More data is therefore required to back up the findings from the DC and CV curves of Section 5. Potential-induced reconstruction during chronocoulometry could be remedied by extensive electrochemical annealing of the Au (100) electrode before it is placed in the cell. It has been found in previous experiments by Kolb that after holding the potential of an Au (100)-(1 × 1) electrode at 0.6 V (vs. SCE) for an hour in NaCl solution, potentially induced reconstruction is no longer observed even after the electrode has been kept at negative potentials in an electrolyte solution for 30 min.[3] PM-IRRAS measurements of surfactant molecules on electrochemically annealed Au (100)-(1 × 1) can easily be carried out in the potential range positive of the pzc, thus eliminating the possibility of potential-induced reconstruction.

There are also greater possibilities of studying BDA^+ adsorption on Au surfaces. The effect of the halide counter-ion can be more clearly seen by carrying out electrochemical and IR measurements on synthesised BDAF and BDAB molecules (synthesised using a similar technique used for CTAF synthesis, see Section 4.1), and by comparing these results with the measurements obtained for BDAC.

Generally, further information of CTAF, CTAC, CTAF and BDAC adsorption on Au (111) and Au (100) can be gained from neutron scattering techniques and in situ STM images. With appropriate isotope contrast, neutron reflectivity would give information on the surfactant layer thickness and solvent content, which could shed light on the type of aggregate structures formed at the interface. STM provides molecular resolution topographical information on structures formed by molecules on the surface. Both techniques can be used under potential control.

Another possible set of surfactant measurements should also be carried out on Ag (110) and Ag (100), as these are the facets of Au NRs when they are synthesised with $AgNO_3$ in the growth solution.

There can be further control of how much Pt goes on the surface of Pt-coated Au NRs by means of several small depositions of Pt: for example, a small amount of Pt (e.g. Pt: Au molar ratios of 0.1:1) can be deposited on the Au NR surface, followed by CO blocking, then the same small amount of Pt is again added, followed by CO blocking, etc. This procedure would allow not only for a smoother Pt nanodot coverage, but also for the optimum coverage or loading of Pt on the nanorod surface for catalytic reactions to be found by testing various nanoparticles with different amounts of Pt deposited on them using the CO-

blocking techniques. The possibility of expitaxial Pt nanodot growth on the Au NRs is interesting; it needs to be explored further with atomic resolution STEM.

Overall, once there is a better understanding of the role of surfactants in Au NR synthesis, the length and even the crystallographic surface of a gold nanorod can be controlled. If, furthermore, there is a possibility of controlled deposition of epitaxially grown nanodots on an Au NR surface, a wide range of tuneable Pt-Au nanorod electrocatalysts can be developed in the future.

[1] Sharma, V., Park K. and Srinivasarao, M. (2009), *Mater Sci and Eng R*, 65, pp. 1
[2] Nikoobakht, B. and El-Sayed, M.A. (2003), *Chem Mat*, 15, p. 1957
[3] Kolb, D.M. (1996), *Progress Surf Sci*, 51, p. 109

APPENDIX

A. Cyclic Voltammetry of polycrystalline Au and Pt

Cyclic voltammetry on Au and Pt electrodes without active species present in the electrolyte results in current peaks at certain potentials that are characteristic for the electrode material used.

Figure A.1 presents a cyclic voltammogram of polycrystalline Au in 0.05 M H_2SO_4 solution. The arrows on the voltammogram indicate the direction in which the potential is being swept.

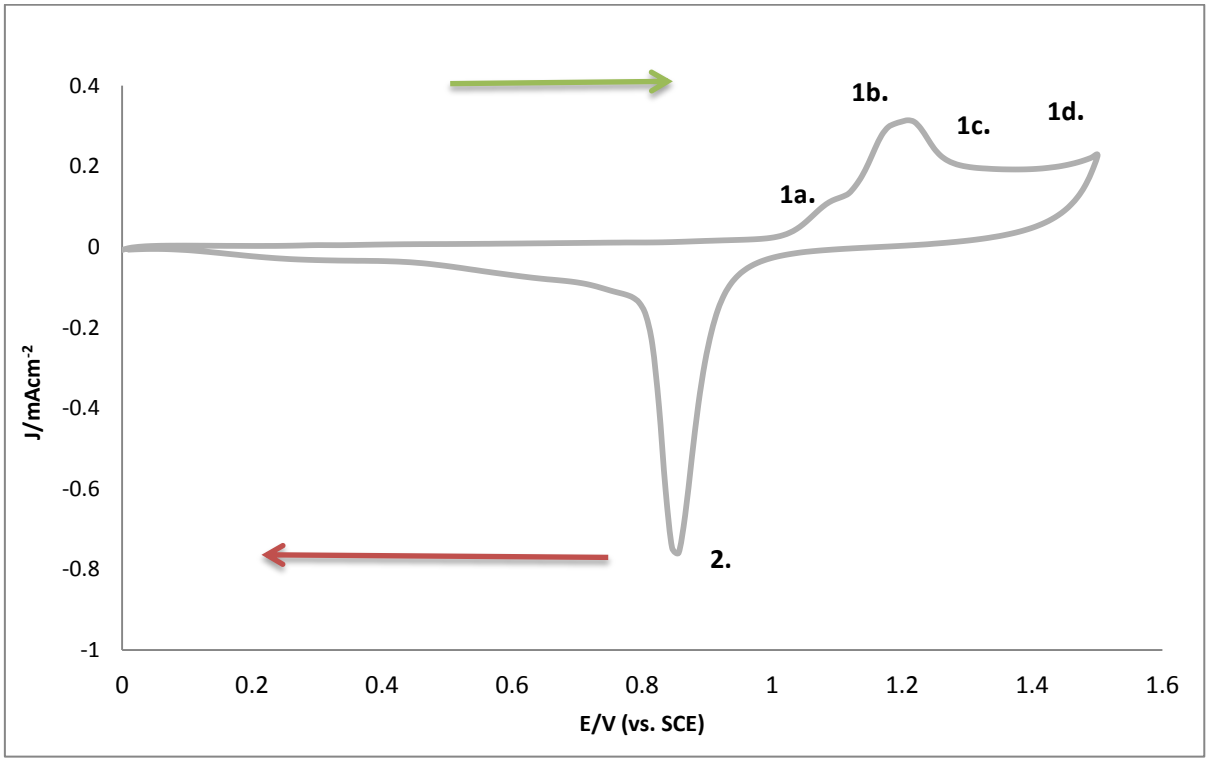

Figure A.1 Cyclic voltammogram of polycrystalline Au in Ar saturated 0.05 M H_2SO_4 electrolyte. 1. Indicates the formation of Au oxide layer. 2. Indicates the Reduction of the Au oxide layer

Sweep rate 100 mV s^{-1}.

On the positive potential sweep, an oxide layer from the double layer region is formed on the Au surface. This is shown by the increase in current between 1.0 V and 1.5 V (1). The following discussion of the mechanism for the Au-oxide formation is based on a study by Conway et al.[1]

Between 1.0 V and 1.1 V **(1a)** there is an initial increase in the current corresponding to the formation of the first sublattice of OH deposited between specifically absorbed sulphate anions (from the H_2SO_4 electrolyte).

$[Au_x – SO_4^{2-}]Au + H_2O \leftrightarrow [Au_x – SO_4^{2-}]\ Au\text{-}OH + H^+ + e^-$ (A.1)

Between 1.1 and 1.2 V **(1b)**, a peak in the current is observed for polycrystalline Au because of the deposition of OH on the Au surface accompanied by desorption of the sulphate anions.

$Au_x – SO_4^{2-} + H_2O \rightarrow Au_{x-1} + Au\text{-}OH + SO_4^{2-} + H^+ + e^-$ (A.2)

The processes in **(1a)**, and **(1b)** represent the deposition of the first and second sublattices of the Au-OH species. This submonolayer of Au-OH is reconstructed according to equation (3):

Au-OH-Au-OH → Au-OH-OH-Au (A.3)

After a slight initial decrease, the current is constant, between 1.25 V and 1.3 V, **(1c).** This is caused by the formation of the third sublattice, completing the Au-OH monolayer:

$[MOH]_{x-1}M + H_2O \rightarrow {}_xMOH + H^+ + e^-$ (4)

Between 1.25 and 1.5 V **(1d)**, the Au-OH monolayer is oxidised to Au-O:

$Au\text{-}OH \rightarrow Au\text{-}O + H^+ + e^-$ (5)

In the cathodic scan, the peak between 1.0 V and 0.7 V **(2)** represents the reduction of the Au oxide layer. The peak occurs at a more negative potential than the Au oxide formation because the Au oxide layer is reconstructed before it is reduced. [1] After the main peak, further reduction of the OH sublattice occurs on patches of anion-free surface.[1]

Figure A.2 shows a cyclic voltammogram of polycrystalline Pt in a 0.05 M H_2SO_4 solution.

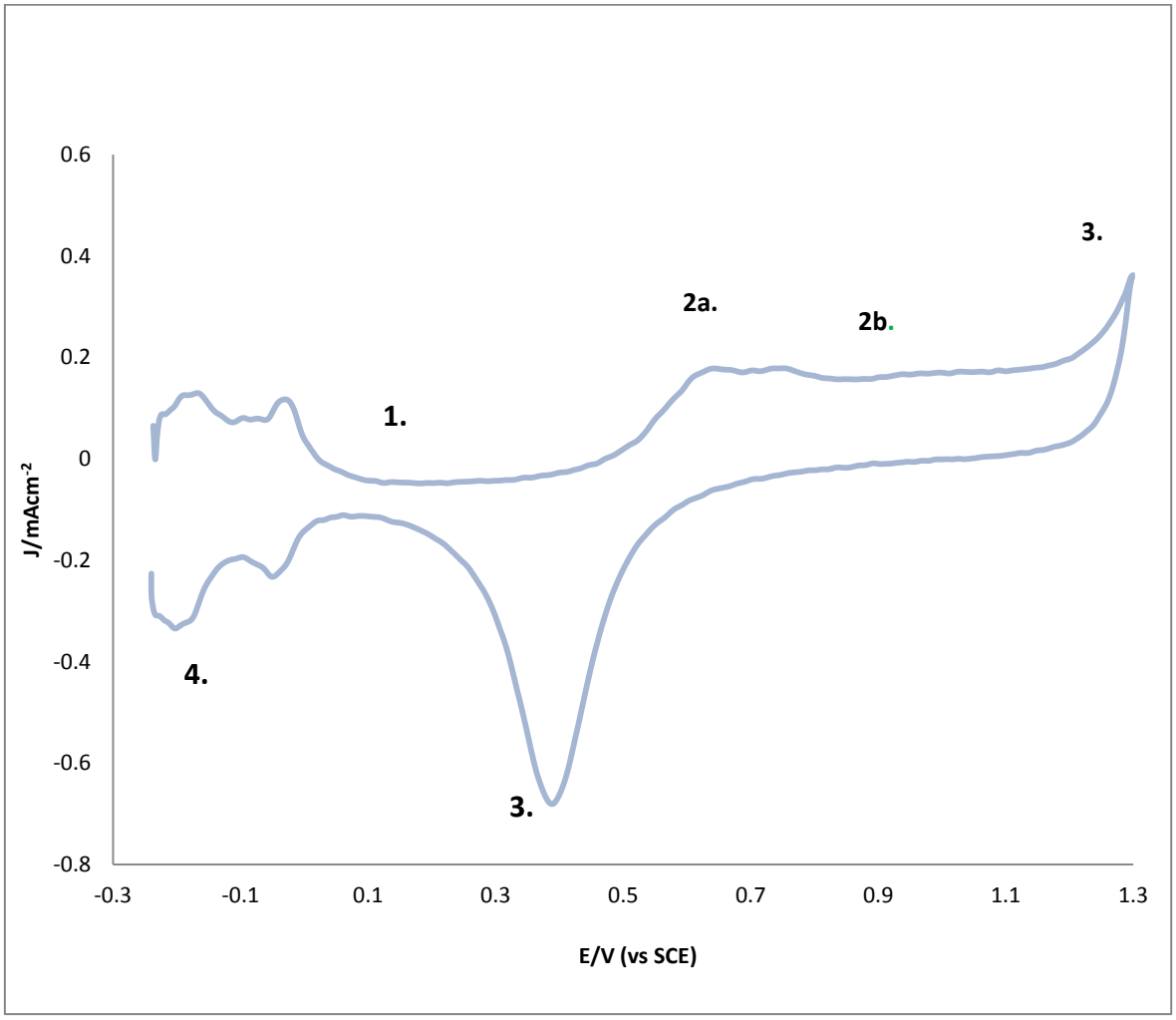

Figure A.2 Cyclic voltammogram of polycrystalline Pt in 0.05 H_2SO_4 electrolyte

Sweep rate 100 mVs^{-1}

On the positive sweep at potentials between 0 V and 0.45 V (1), the only current flowing is the one necessary to charge the electrolytic double layer. The increase in current between 0.45 V and 1.1 V **(2)** represents the formation of the Pt oxide layer.[2] The steep increase in current from 0.475 V and 0.6 V **(2a)** represents Pt-OH formation.

$$Pt + H_2O \rightarrow Pt\text{-}OH + H^+ + e^- \qquad (A.6)$$

Above the potential of ca. 0.65 V **(2b.),** a Pt-O layer is formed, according to the equation 2.

$$Pt\text{-}OH + H_2O \rightarrow Pt\text{-}O + H_3O^+ \qquad (A.7)$$

On the negative sweep, between 0.63 V and 0.18 V **(3)**, the peak is caused by the chemisorbed Pt oxide layer becoming completely desorbed through electrochemical reduction.

$$Pt\text{-}O + 2e^- + 2H^+ \rightarrow Pt + H_2O \qquad (A.8)$$

Following a small double layer region between 0.17 V and 0.05 V, there is an underpotential deposition of hydrogen atoms on Pt **(4)**. The double peak on the negative sweep is due to hydrogen adsorption, and the double peak in the same potential region on the positive sweep to the hydrogen desorption.

B Cleaing procedure for Pt-coated Au NR electrodes

Figure B.1 presents a CV of a Pt- Au surface that was prepared in Pt-coated Au NR reaction conditions. A polycrystalline Au electrode was left in a solution of CTAB, $AgNO_3$ and AA to mimic the conditions used in Au NR growth. After a subsequent Pt deposition on the Au surface, the electrode was left in a CTAB solution for 24 hours because Pt deposition on Au NRs is carried out in a CTAB solution over 24 hours. The electrode was rinsed before cyclic voltammetry. A CV of a fully clean Pt-Au surface is shown by the dotted line for reference.

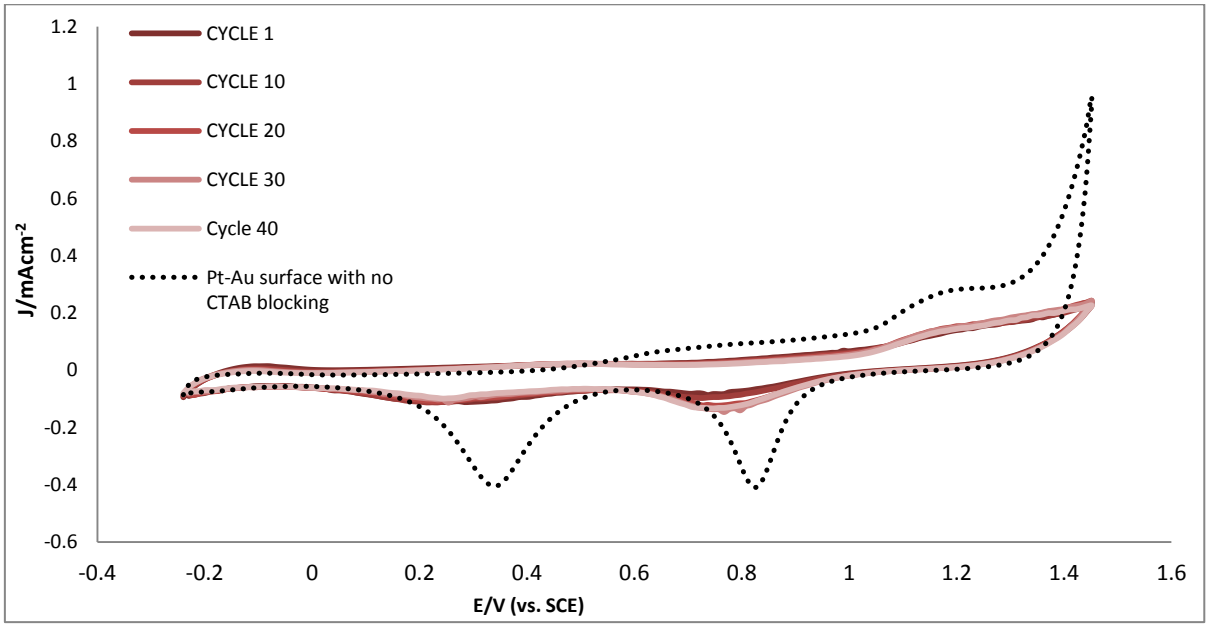

Figure B.1. Cyclic voltammogram of Pt-Au surface left in conditions that mimic Pt-coated Au NR synthesis, in an Ar-saturated 0.05 M H_2SO_4 electrolyte. The CVs are presented a progressively lighter shade of red as the number of cycles increases. The dotted line represents clean Pt-Au surface as a reference.

Sweep rate 100 mV s^{-1}.

It is clear from Figure B.1 that the CTAB species block the Au sites because the Au oxide formation and reduction peaks have a visibly lower current density than the clean Pt-Au

surface, shown with the dotted line. During synthesis of Au NRs, CTAB forms a micelle structure around the nanoparticle. Molecular level interactions of CTAB with the Au NR surface has yet to be completely understood. It is generally accepted that the surfactant is bound to the surface through electrostatic interactions between the cationic head group (quaternary ammonium) and anion sites on the Au surface.[3] It is unclear exactly what these anion sites are, whether they are bromide counter ions, bromide-related species or silver-related species.

During nanorod growth, ascorbic acid (AA) does not reduce Ag^+ (from $AgNO_3$) to bulk silver. However, it has been suggested that a monolayer or submonolayer of bulk Ag can underpotentially deposit on the Au surface. EXAFS studies[4] have detected the presence of Ag (0) on the Au surface. According to atomic emission spectroscopy, up to four monolayers of silver could be on the Au surface[5], though this technique does not distinguish between Ag (I) and Ag (0). It has been proposed that Ag(I) is present on the Au NR surface in the form of AgBr[6]. XPS data suggests that detectable silver is present as Ag (I)[7] on Au NRs, though though CTAB and $AgNO_3$ from synthesis could also be responsible for that observation. $AgBr_2^-$ and $AgBr_2^-$ species have been detected on a rigorously purified Au NR surface by another group through a laser desorption/ionisation mass spectrometry technique[8]. Ag-Br pairs are said to decrease the charge density of bromide ions, thus decreasing the repulsion between neighbouring CTA^+ headgroups.[1] This would allow the formation of a more densely packed CTAB layer on the Au NR surface.

It is evident from Figure B.1 that the CTAB species also block the Pt surface. After 40 cycles, there is no indication of the Pt-Au surface becoming much cleaner because the the Pt

and Au oxide formation and reduction peaks do not increase significantly in current. The Au oxide reduction peak does slightly increase, while the Pt oxide reduction peak decreases slightly in current, which could imply that during cycling, the CTAB species on Au defect to the Pt sites.

Cyclic voltammetry alone apparently does not sufficiently clean the Pt-Au bimetallic surface. An effective cleaning procedure for Au nanoparticles involving underpotentially depositing Pb on an the Au surface has been used by Hernandez et al. [9] The same procedure was carried out on the Pt-Au surface blocked by CTAB species. Figure B.2 shows subsequent cycles of the CTAB blocked Pt-Au surface after a Pb underpotential deposition.

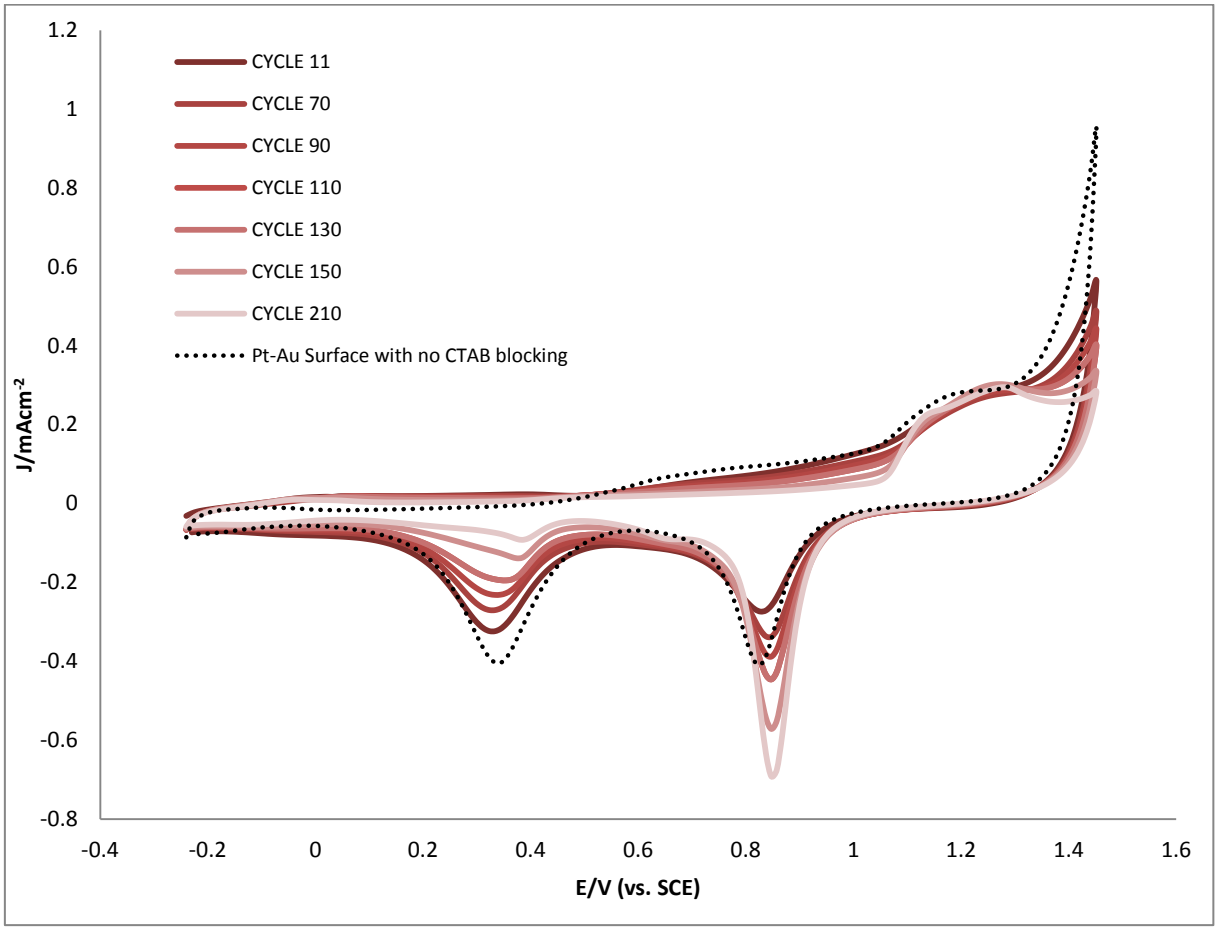

Figure B.2 Cyclic voltammogram of CTAB-blocked polycrystalline Pt-Au surface after a layer of Pb was underpotentially deposited onto it in Ar-saturated 0.05 M H_2SO_4 electrolyte. The CV is presented a progressively lighter shade of red as the number of cycles increased. The clean Pt-Au surface is used as a reference (dotted line)

Sweep rate 100 mV s^{-1}

It is clear from Figure B.2 that initially the Pb $_{UPD}$ layer cleans both the Pt and the Au sites on the Pt-Au bimetallic surface; however, after several cycles, the Pt oxide reduction peak decreases in current, while the Au oxide reduction peak increases in current. It can be concluded that while the Pb $_{UPD}$ technique effectively cleans the Au surface, it also irreversibly displaces the Pt from the surface. According to the CV, after 200 cycles most of the Pt has left the Pt-Au surface, and the remaining surface is polycrystalline Au.

A CTAB-blocked Pt-Au was cleaned instead using underpotential deposition of copper. The resulting CV is presented in Figure B.3 (dark red line). The initial CTAB-blocked surface (light red line) and the fully clean Pt-Au surface (dotted line) are included for reference.

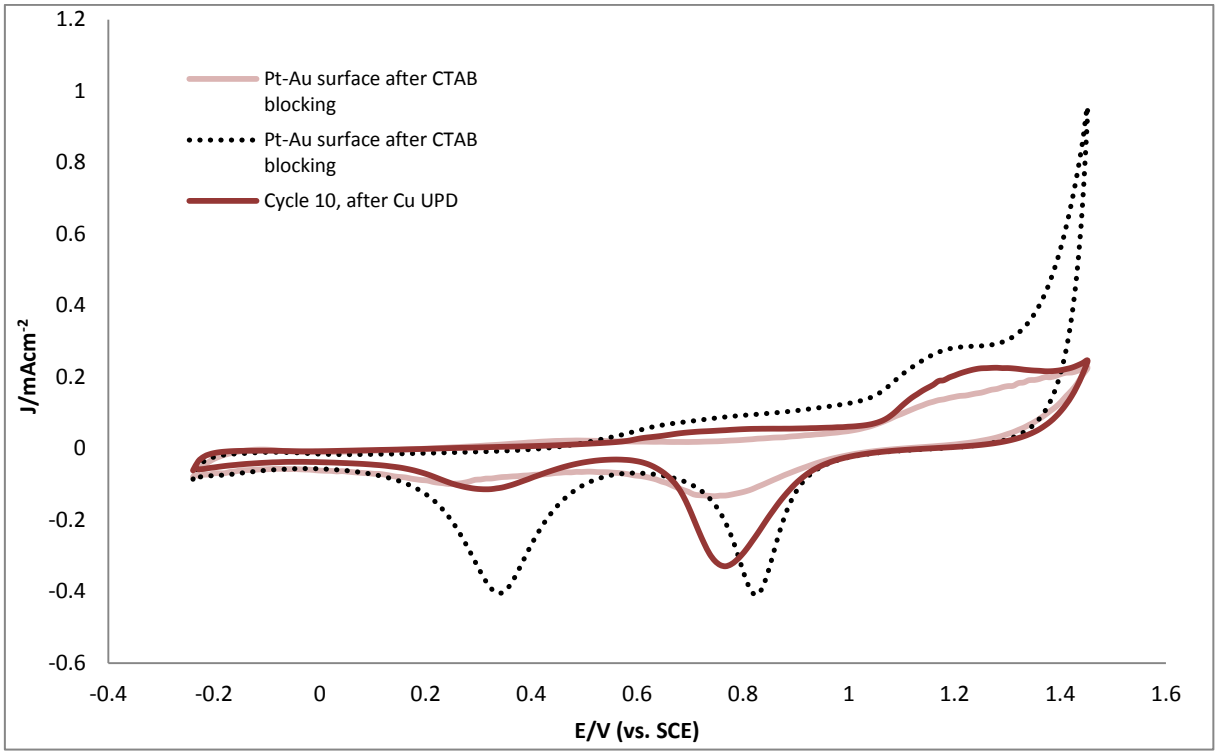

Figure B.3 Cyclic voltammogram in Ar-saturated 0.05 M H_2SO_4 electrolyte of CTAB-blocked polycrystalline Pt-Au surface, after underpotential deposition of Cu (dark red line). The initial CTAB blocked polycrystalline Pt-Au surface (light red line) and the cleaned Pt-Au surface (dotted line) are used as a comparison.

Sweep rate is 100 mV s^{-1}

Figure B.3 shows that after Cu_{UPD}, an increase in the Au oxide reduction peak is observed, which shows that Cu can effectively displace the CTAB species from the Au surface. However, there is no a significant increase in the Pt oxide reduction peak. It is likely that the Cu underpotentially deposits on the Au surface and effectively displaces the CTAB species, but does not deposit on the Pt surface as effectively; therefore CTAB species remain on the Pt areas of the surface.

CO was subsequently deposited on the electrode surface, in order to displace the CTAB species from the Pt sites. A cyclic voltammogram of the Pt-Au surface after CO

adsorption and Cu $_{UPD}$ is presented in Figure B.4. The voltammograms become progressive darker shades of red as the number of cycles increase.

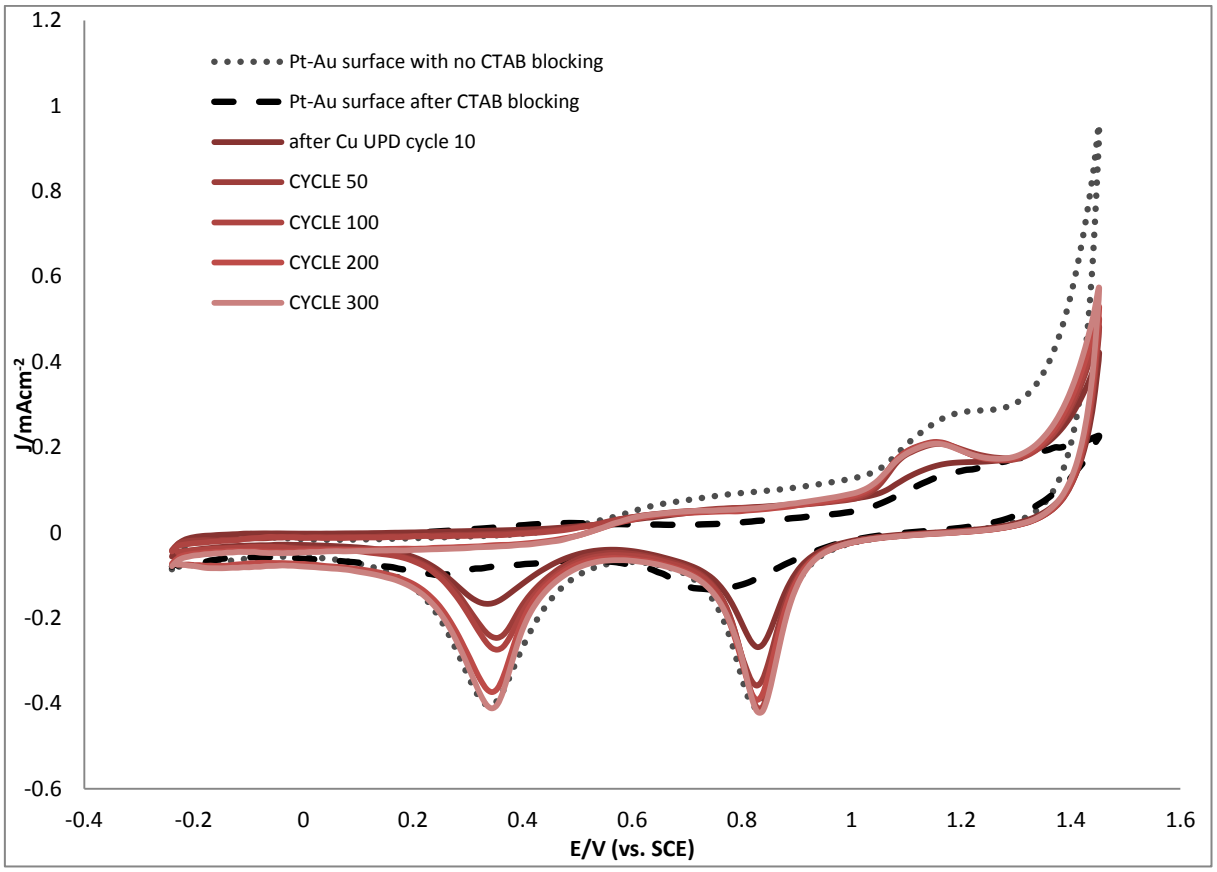

Figure B.4 Cyclic voltammogram of CTAB-blocked polycrystalline Pt-Au surface after cleaning using Cu $_{UPD}$ and CO adsorption in Ar-saturated 0.05 M H_2SO_4 electrolyte. The progressive darker shades of red represent an increase in number of cycles The initial CTAB-blocked polycrystalline Pt-Au surface (dashed) and the cleaned Pt-Au surface (dotted line) are used as a reference.

Sweep rate 100 mV s^{-1}

According to Figure B.4, after 300 cycles, the Pt oxide and Au oxide reduction peaks have the same current as the original clean surface (dotted line). This proves that the CTAB species have been removed from the Pt and Au sites. Figure 19 shows that the CTAB species are displaced from the Au at a faster rate than from the Pt sites. This is evident because the Au oxide reduction peak increases after fewer cycles than the Pt oxide reduction peak.

Based on these results, the overall cleaning method to be used on the nanorods was Cu_{UPD} then cycling, followed by CO electrodepostion, followed by cycling. This sequence was to be repeated three times.

Pt-coated Au NRs were immobilised onto a glassy carbon electrode and then cleaned using the Cu_{UPD} and CO adsorption method. The resulting CVs are given in Figure B.5.

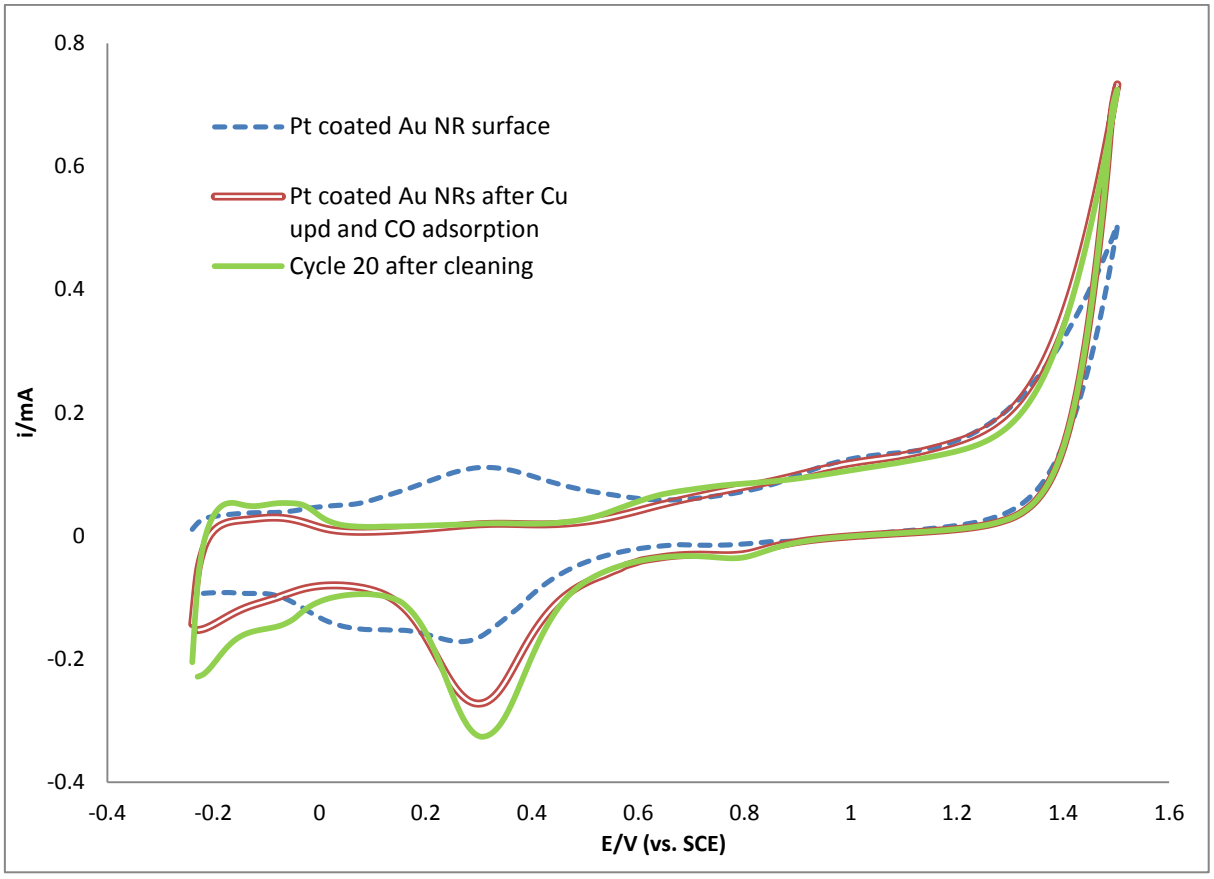

Figure B.5 Cyclic voltammogram of Pt-coated Au NRs in Ar-saturated 0.05 M H_2SO_4 electrolyte of initial Pt-coated Au NR surface (blue dotted line, Pt-coated Au NRs after cleaning using Cu UPD and CO adsorption (red double line) Pt-coated Au NRs, 20 cycles after cleaning procedure (green solid line)

Scan rate 100 mV s^{-1}

It is clear from Figure B.5 that initially after CO oxidation and Cu_{UPD}, most of the impurities were displaced from the Au NR suface. After further cycling the remaining impurities seem to be displaced, especially off the Pt surface. The Pt oxide reduction peak increases in current, and the hydrogen adsoption peaks noticeably increase, showing that there are more Pt sites available for hydrogen adsorption.

[1] Angerstein-Kozlowska, H., Conway, B.E., Hamelin, A. and Stoicoviciu, A. (1986) *Electrochimica Acta*, 31, p. 1051.
[2] Hamann, C.H., Hamnett, A. and Vielstich, W. (1998) *Electrocatalysis*, Weinheim: Wiley-VCH.
[3] Orendorff, C.J., Alam, T.M., Sasaki, D.Y., Bunker, B.C. and Voigt, J.A. (2009) *ACS Nano*, 3, p. 971.
[4] Giannici, F., Placido, T., Curri, M.L., Striccoli, M., Agostiano, A. and Comparelli, R. (2009) *Dalton Trans*, 46, pp. 10367–10374.
[5] Orendorff, C.J. and Murphy, C.J. (2006) *J Phys Chem*, B, 110, p. 3990.
[6] Hubert, F., Testard, F. and Spalla, O. (2008) *Langmuir*, 24, p. 9219.
[7] Habenicht, A., Olapinski, M., Burmeister, F., Leiderer, F.P. and Boneberg J. (2005) *Science*, 309, p. 2043.
[8] Niidome, Y., Nakamura, Y., Honda, K., Akiyama, Y., Nishioka, K., Kawasaki, H. and Nakashima, N. (2009) *Chem Commun*, p. 1756.
[9] Hernández, J., Solla-Gullón, Herrero, E., Aldaz, A. and Feliu, J.M. (2007) *J Phys Chem C, 111,* p. 14083.